

NORTHWESTERN UNIVERSITY

Advancements in our Understanding of the Yucatán Platform: Sedimentary Geology and  
Geochemistry, Speleogenesis, Chicxulub Ring of Cenotes, and Tectonic Stability

A DISSERTATION

SUBMITTED TO THE GRADUATE SCHOOL

IN PARTIAL FULFILLMENT OF THE REQUIREMENTS

for the degree

DOCTOR OF PHILOSOPHY

Field of Earth and Planetary Sciences

By Emiliano Monroy-Ríos

EVANSTON, ILLINOIS

December 2020

© Copyright by Emiliano Monroy Ríos 2020  
All Rights Reserved

## Abstract

Carbonates constitute Earth's largest carbon (C) reservoir, with most shallow marine deposition occurring on the low-latitude carbonate platforms covering  $\sim 800,000$  km<sup>2</sup>. The Yucatán Platform situated between the Western Caribbean and Gulf of Mexico basins, is one of the largest present-day carbonate platforms. As with post-Paleozoic carbonates generally, it is readily weathered and karstified, as these retain primary porosity and remain close to the surface, with dissolution leading to order of magnitude permeability increases. This addresses questions of the Yucatan geological history using a combination of literature research, geophysical and geodetic data, and geochemical analyses, along with field observations.

The genesis and hydrogeological function of the surface expressed Ring of Cenotes remains an active question in the Yucatán geological understanding. A genetic model for the formation of the Chicxulub Ring of Cenotes (ROC) is presented based on the published geology and stratigraphy, geophysical surveys, and general carbonate platform hydrogeology and hydrogeochemistry. Hydrogeothermal circulation of marine water through the platform pre-dates the impact, with density-driven fluxes exiting the sub-marine platform top, and dolomitization and anhydritization along the platform flow paths from the platform sides. Platform scale circulation continued post-impact, but enhanced vertical fluxes constrained around the perimeter of the hot and low-permeability melt plug. The numerous impact ring fault sets provide likely flow paths, but it is the fracture set circumscribing the perimeter of the impact melt plug that is significantly karstified by bottom-up hypogene processes to produce the observed Ring of Cenotes. Epigene karstification was only in the Late Miocene (<10 Ma) with exposure of the Yucatán Peninsula to meteoric inputs.

The Yucatán Block (YB) has been considered to be tectonically stable. Geodetic data from UNAVCO (DAI v2) stations with 5+ year records show the present-day motion to include NW direction and counterclockwise rotation, along with N and NE coastal subsidence of  $\sim 1$  m / 1000 year. Major fault systems are now considered here as a continuous bank-marginal fracture system subjected to rotation. Coastal ecology, geomorphology, and archeological observations are consistent with the observed vertical motions and cast to at least the Late Holocene. The YB is tectonically rigid in the strict sense, without apparent deformation, yet block tilting and rotation is of broad significance in interpretation of the karst hydrogeology, paleoenvironmental records, and coastal adaptation to sea level rise.

This work delivers a significant 30 element geochemical atlas of the Pleistocene and Holocene of the NE Yucatán Peninsula. Comparison of the bulk rock geochemistry to ocean chemistry helps constrain diagenetic post-depositional processes such as leaching, dolomitization and pedogenic pathways, including the origin of *terra rossa* formed on karst.

The knowledge provided by this thesis provides the foundation for (re) assessing and the significance of vertical motion in the interpretations of sea level records and coastal adjustments including under already rising sea levels, depth stratification of epigene speleogenesis, and the hydrogeological function of bank marginal fracture sets, and the Chicxulub ring faults and the Ring of Cenotes.

## **Acknowledgements**

Monroy-Ríos gratefully acknowledges graduate research fellowship support from the Mexican National Science and Technology Council (CONACyT). This research was possible through funding to Beddows from the Institute for Sustainability and Energy at Northwestern (ISEN), and the National Science Foundation (NSF-1530345).

*Dedicated to Michelle and Martina, for all the love.*

*To my parents, Henriette D and Mario B.*

*To my beloved families in México and Puerto Rico.*

*To all the people who taught me the underwater and underground worlds.*

*To Trish & Ed.*



II-3	GEOTHERMAL CONVECTIVE CIRCULATION .....	53
II-3.1	DIAGENESIS: EARLY BURIAL DOLOMITIZATION AND COUPLED ANHYDRITIZATION .....	56
II-3.1.1	Burial anhydrite: Refutation of Evaporite Origin.....	58
II-3.2	HYPOGENE KARSTIFICATION DURING SUBMARINE STAGE .....	58
II-3.3	EPIGENE KARSTIFICATION DURING SUBAERIAL REGIME .....	61
II-4	HYPOGENE HYDROGEO THERMAL MODEL FOR GENESIS OF THE RING OF CENOTES .....	63
II-5	DISCUSSION.....	65
II-6	CONCLUSIONS .....	70
<b>III</b>	<b>On the Tectonic Stability of the Yucatán Block: Tilt and Rotation.....</b>	<b>72</b>
	ABSTRACT .....	72
III-1	INTRODUCTION .....	73
III-1.1	TECTONIC SETTING AND FEATURES OF THE YUCATAN PLATFORM AND PENINSULA .....	73
III-1.2	WESTERN CARIBBEAN SEA LEVEL RISE (SLR) .....	82
III-1.3	UPPER PLEISTOCENE RIDGES.....	83
III-2	DATA AND METHODS .....	83
III-3	RESULTS.....	84
III-3.1	GPS/GNNS STATIONS .....	84
III-3.2	MAYA COASTAL SITES .....	86
III-3.2.1	Additional Sites - North & Gulf Coast Maya Sites .....	88
III-3.3	COASTAL MANGROVE .....	88
III-4	INTERPRETATION & DISCUSSION.....	90
III-4.1	GEODETIC DATA – TILT.....	90
III-4.2	COASTAL GEOMORPHOLOGY, ECOLOGY, AND ARCHAEOLOGY .....	91

III-4.3	DURATION AND PERSISTENCE OF OBSERVED MOTIONS.....	92
III-4.4	ROTATION – REFLECTED IN MAJOR FAULTS, RIDGE AND SWALE COMPLEXES, AND PLATFORM TERRACE CHRONOSEQUENCES .....	93
III-4.5	MASS BALANCE – WEATHERING AND BANK TOP SEDIMENT LOADING.....	97
III-4.6	COMPARISON TO FLORIDA AND BAHAMAS .....	98
III-5	CONCLUSIONS .....	99
<b>IV</b>	<b>Geochemical Characterization of Pleistocene-Holocene Carbonate Rocks from Northeastern Yucatán Peninsula, México .....</b>	<b>100</b>
	ABSTRACT .....	100
IV-1	INTRODUCTION .....	101
IV-1.1	STUDY AREA .....	103
IV-1.2	GEOLOGICAL SETTING.....	104
IV-1.3	DENSITY STRATIFIED COASTAL KARST AQUIFER.....	109
IV-2	METHODS.....	114
IV-2.1	FIELDWORK.....	114
IV-2.1.1	Rock Sampling .....	116
IV-2.2	ICP-OES GEOCHEMICAL ANALYZES.....	118
IV-2.2.1	Sample and standard preparation.....	119
IV-2.2.2	Comparison between analytical runs.....	120
IV-3	RESULTS & BULK ROCK GEOCHEMISTRY OVERVIEW .....	123
IV-3.1	BULK ROCK GEOCHEMISTRY.....	123
IV-3.1.1	Major elements: Ca and Mg .....	126
IV-3.1.2	Intermediate elements: Al, Ba, Be, Fe, K, Li, Na, P, S, Si, Sr .....	128
IV-3.1.3	Metals forming carbonates and oxides: Fe and Mn.....	134
IV-3.1.4	Aluminosilicates: Al and Si.....	136
IV-3.1.5	Minor elements: Ba, Cd, Co, Cr, Cu, Mo, Ni, Pb, V.....	140
IV-3.1.6	Trace elements: Ag, Be, Bi, Cs, Ga, In, Rb, Tl, Zn.....	144

IV-4	BULK GEOCHEMISTRY COMPARED TO MODERN OCEAN WATER .....	144
IV-5	GEOGRAPHICAL DISTRIBUTION .....	152
IV-6	STRATIGRAPHIC DISTRIBUTION.....	157
IV-6.1	VADOSE / PHREATIC ZONE DISTRIBUTION .....	157
IV-6.2	CHEMOSTRATIGRAPHY .....	161
IV-6.2.1	Outcrops and quarries.....	163
IV-6.2.2	Phreatic caves and cenotes .....	172
IV-7	DIAGENETIC PROCESSES .....	183
IV-7.1	DOLOMITIZATION .....	183
IV-7.1.1	Mg:Ca ratio.....	187
IV-7.2	RESIDUAL ELEMENTS AND SOILS .....	192
IV-7.2.1	SAF Plots.....	199
IV-7.2.2	Assessment of Saharan dust input .....	203
IV-7.2.3	Fe:P ratio.....	205
IV-7.2.4	Assessing anthropic inputs in surface rocks.....	210
IV-8	CONCLUSIONS .....	211
<b>V</b>	<b>References .....</b>	<b>213</b>
<b>VI</b>	<b>Appendix A .....</b>	<b>245</b>
	UNAVCO DATASETS USED.....	245
<b>VII</b>	<b>Appendix B .....</b>	<b>250</b>
	ROCK COMPOSITION TABLES.....	250
<b>VIII</b>	<b>Vita .....</b>	<b>260</b>

## List of Figures

Figure I-1	The World Karst Aquifer Map (WOKAM) demarking karstifiable carbonate and evaporite rocks that represent potential karst aquifers. From Goldscheider et al. (2020). .....	27
Figure I-2	<b>a.</b> Three-dimensional conceptual model of a karst geology aquifer, with a 3D matrix, 2D planar fractures, fissures, and bedding planes, and 1D linear conduits housing turbulent flow. <b>b.</b> Table of four representative karst aquifers, with data on the proportion of the total water that is held in the 3D matrix storage, and the proportion of the total flux that occurs in the 1D conduits. From Worthington et al. (2000). .....	28
Figure I-3	Hydrogeological interpretations reflecting the actual state-of-knowledge reported in different sources: <b>a.</b> interpretation of groundwater flow from the Mexican National Water Commission (CONAGUA, 2010); <b>b.</b> Exercise on interpretation of hydrogeological features of the Yucatán Peninsula aquifer by different research groups (Amigos de Sian Ka'an A.C., 2003).....	30
Figure II-1	Grouping of cenote morphologies showing their vertical scale dimensions.....	42
Figure II-2	The Yucatán Platform relative to North and South America (upper inset) and between the Gulf of Mexico and the Western Caribbean (main panel). The 200 m isobaths delineate the platform, with the offset subaerial peninsula on the east margin. Bouguer gravity anomalies overlain on main Connors et al. (1996) show the multi-ring Chicxulub Impact Structure in the center of the platform, and cross cutting the northwest modern coastline. Transect line A–A' shows the cross section used in Figure II-3 and Figure II-5. Bathymetry redrawn from Dirección General de Oceanografía, Secretaría de Marina using data from Oregon State University YUCATAN '85. Overlay colored SRTM elevation model of the Yucatán Peninsula NASA/JPL (2000), overlain by cenote locations (white dots) showing only those considered to be part of the ROC from Hildebrand et al. (1995) and Connors et al. (1996). .....	44

- Figure II-3 Cross-section showing core correlation reflecting core logs from Ward et al. (1995): Yucatán 1, 2, 4, 5, and 6 (Y1, Y2, Y4, Y5, Y6); Chicxulub 1 (C1), near the center of the impact structure; and Ticul 1 (T1). Note the predominant anhydrite and dolomite in the Cretaceous beds overlying the granodiorite basement of the Yucatán Peninsula. Vertical exaggeration of x100. ....48
- Figure II-4 A) Global sea level data from the K-Pg to present from Haq et al. (1988). Regular subaerial exposure of the Yucatán Platform and development of a meteoric lens was only possible from 10 Ma onwards; B) Prior to the K-Pg, the platform elevation was at ~-500 mbs; C) Post-10 Ma, subaerial exposure and development of a thick freshwater lens. Fresh-saline mixing corrosion along the base of the lens leads to karstification; D) Upwards stoping of the hypogene deep seated dissolution voids formed around the low-permeability and high thermal conductivity melt plug (below lower boundary of cartoon); E) Stacked levels of karstification tied to sea level, with many of the deep hypogene voids stope upwards, breaching the surface to create pit cenotes along the perimeter of the ROC. The overall increase in permeability thins the freshwater lens. ....53
- Figure II-5 General geology and hydrogeology cross-sections of the Yucatán Platform based on the published literature on drill core and geophysical surveys undertaken by Pemex, UNAM, and IODP/ICDP from Ward et al. (1995). Deep crustal interpretation is from Christeson et al. (2009). ....56
- Figure III-1 Features of the Yucatan Platform. The major fault systems are the Ring of Cenotes, the Sierrita de Ticul fault line, the Holbox fracture zone, the Rio Hondo block fault zone and the La Libertad fault zone. The Chemax – Catoche Faults are also shown and discussed in text. Sources: Bauer-Gottwein et al., 2011; Connors et al., 1996; Pope et al., 1993; Weidie, 1985. ....76
- Figure III-2 Features of the Yucatan Platform. Terrace geomorphology shown with 10 m contour (using 15 m pixel resolution base; INEGI, 2013). Thicker black lines are visually interpreted contours showing terrace edges. White swales are topographic lows relative to surrounding terrains, overlying the Holbox Fracture Zone. ....77

- Figure III-3 Fracture and structurally guided karst features on the Caribbean coast of the Yucatán Peninsula. The “T” shaped rocky sided caletas, created by the collapse of conduits. **a.** Xel Ha. **b.** Yalku. **c.** The overall direction of the explored sub-horizontal phreatic conduits near Tulum are anastomotic at the passage scale, but the overall alignment of multiple drainage lines does not present obvious fracture guiding at 2-15 km from the coastline, from Smart et al. (2006). **d.** In some segment of conduits 1 km from the coast, the influence of the bank marginal fracture systems is obvious, as in Sistema Abejas adjacent to the coast. ....81
- Figure III-4 Motion vectors for stations with +5 years of geodetic data. **a.** East-West component, **b.** Vertical residual after un-tide function applied to remove earth tides. Geodetic derived data products from the UNAVCO (2018) Data Archive Interface v2.0 (DAI v2), with station data from PBO, COCONet, and TLALOCnet networks for the greater study area of the Caribbean and Gulf of Mexico. Reference frame dataset is IGS14 with plate motions relative to Earth's core. Vertical velocity vectors have been scaled by 2.....85
- Figure III-5 Summary direction of mid- to late Holocene vertical motion but with no representation of rate, including for geodetic GPS/GNSS stations (▲), archeological sites (■), and mangrove ecology (●).....86
- Figure III-6 Sea level rise has a rapid and direct effect on ecosystems in the intertidal zone, such as mangroves. Mangrove coastal areas in **a.** the north coast, with wetlands remain connected to ocean and actively flush by tides; and **b.** the Caribbean coast, where wetlands seem to be perched and above sea level, including coastal mangroves decoupled form the ocean. ....89
- Figure III-7 Vertical velocity (mm/year) of four stations on the eastern Yucatán Peninsula: CN23 (Belmopan), CN24 (Felipe Carrillo Puerto), CNC0 (Cancun), and UNPM (Puerto Morelos). Results plotted as station distance to CNC0. ....91

- Figure III-8 Eustatic sea level since the Cretaceous. Composite from the work of Abreu & Anderson (1998). A blue line shows the proposed uniform subsidence of the Yucatan Peninsula linearly approximated which tracks the elevation of the highest altitude geomorphic surface at an elevation of about 200 m to their present elevation of about 25 m. The parallel curve, 25 m lower, approximates the elevation through time of the carbonate rocks at the present-day shoreline, from Kinsland et al. (2000). .....93
- Figure III-9 Geomorphic features of the north-east Yucatan Platform. Terrace geomorphology shown with 10 m contour (using 15 m pixel resolution base; INEGI, 2013). Thicker black lines are visually interpreted contours showing terrace edges. White swales are topographic lows relative to surrounding terrains, overlying the Holbox Fracture Zone (WGS84-UTM). .....96
- Figure IV-1 Eustatic global sea level variations over the last 800,000 yrs, for the Holocene and Upper Pleistocene. LGM - Last Glacial Maximum; LFI - Last Full Interglacial. Sea-level data from Siddall et al. (2007). Grey bands mark sea levels -50 m or lower, and where the near-surface rocks in this study have likely been sub-aerially exposed assuming no vertical displacement of the platform. ....105
- Figure IV-2 Regional scale fracture features with surface expression are: Ring of Cenotes (Perry et al., 1995), the Sierrita de Ticul fault line, the Holbox fracture zone, the Rio Hondo block fault zone, and the La Libertad fault zone (south of figure extent). The five recognized physiographic regions with variable degrees of distributed fracturs are: the coastal zone that spans 1-10 km of the peninsula perimeter (not marked), the northwestern coastal plain (NWCP) that broadly overlaps with the Chicxulub basin demarcated by the Ring of Cenotes, the northeastern coastal plain (NECP), the central hill district (CHD), and the eastern block fault district (EBFD). .....107
- Figure IV-3 Hypothetical cross section perpendicular to northeastern coast of the Yucatán Peninsula, showing stratigraphic relationships of older Pleistocene units and caliche horizons. Modified from Ward & Halley (1985). .....108

- Figure IV-4 Calcium equilibrium concentration as a function of carbon dioxide pressures. Different pathways for solutions towards their equilibrium values are shown. In open systems, dissolution proceeds along horizontal (solid) lines, while in closed systems dissolution proceeds along sloping (solid) lines. The effect of mixing two saturated solutions equally (black circles), results in a new undersaturated solution (grey circle), which again can dissolve calcium. From Kaufmann (2009)..... 111
- Figure IV-5 Schematic conceptual diagram showing the ‘freshwater lens’ (FWL); saline water zone (SWZ); mixing zone (MZ), also called halocline; submarine groundwater discharge (SGD) and cave formations in a coastal density stratified carbonate aquifer. With sea level changes, the whole system including the intruding marine water, the mixing zone, and the freshwater lens, all move coherently, upward during sea level rise, and downward when sea level falls. .... 113
- Figure IV-6 Location of sampling sites, where phreatic zone samples obtained by cave diving marked in blue; vadose zone samples are marked in red, for a total of 385 samples in 38 different sites. .... 117
- Figure IV-7 Comparison of results (mmol/kg) 8 selected elements (Al, Ba, Fe, Mn, P, S, Si, Sr) for the 75 samples that were run initially with 10 element standards in the first batch, and then repeat analyzed with the 30-element standard in two analytical runs. .... 121
- Figure IV-8 The 30 elements considered in this study for quantification by ICP-OES methods. .... 122
- Figure IV-9 Global average bulk rock composition (n=385) for all elements considered in this study, grouped in a) Major elements (Ca, Mg); b) Intermediate elements (Al, Ba, Fe, Mn, P, S, Si, Sr); c) Minor elements (Ba, Cd, Co, Cr, Cu, Ni, Pb, V); and Trace elements (Ag, Be, Bi, Cs, Ga, In, Rb, Tl, Zn), those below detection limit, not shown. Each panel excludes elements of other panels so % is not over the total. For total percentages see Table IV-5. Label values in mmol kg<sup>-1</sup> of dry rock (upper) and mol % (lower). .... 124

Figure IV-10	Depth-average representation of Ca and Mg concentration in mol %. Mg/Ca molar ratio is also shown. Note that the elevation bin sizes are not equally sized, based on the number of samples available for each bin. Distribution statistics for each elevation bin not shown.....	127
Figure IV-11	Regional distribution of Ca and Mg, excluding all other elements. Concentration values given in mmol kg <sup>-1</sup> . .....	128
Figure IV-12	Depth-average concentration profiles for alkali and alkaline earth metals considered in this study (Ba, K, Li, Na), excluding all other elements. Concentration values given in mmol kg <sup>-1</sup> and percentages are in mol %. Note the log scale on the left plot.....	130
Figure IV-13	Geographic distribution of K, Li, Na, excluding all other elements. Concentration values given in mmol kg <sup>-1</sup> . .....	131
Figure IV-14	Ternary plot showing molar composition of rocks; normalized to mol % (n = 290). Spreadsheet for creating tri-plots from Graham & Midgley (2000).....	133
Figure IV-15	Geographic distribution of Ba and Sr excluding all other elements. Concentration values given in mmol kg <sup>-1</sup> . .....	134
Figure IV-16	a) Mass CaCO <sub>3</sub> – MgCO <sub>3</sub> – (Fe+Mn)CO <sub>3</sub> ternary plot assuming all elements are present as their corresponding carbonate minerals; normalized mol % (n = 290); b) Molar composition Ca–Mg–[Al+Fe+Mn+Si], normalized mol %.....	136
Figure IV-17	Geographic distribution of Al, Fe, Mn, and Si, excluding all other elements. Concentration values given in mmol kg <sup>-1</sup> .....	138
Figure IV-18	Total Aluminum (Al) and Silicon (Si) content (mmol kg <sup>-1</sup> ) in 290 sample rocks from eastern coastal Quintana Roo, illustrating the chemical composition of bulk samples. Linear regression (red line) approximately represents 1:1 molar ratio for Al and Si. When forcing intercept to zero, regression equation is $y = 0.9027x$ with $R^2=0.6852$ .....	139
Figure IV-19	Mass SiO <sub>2</sub> – Al <sub>2</sub> O <sub>3</sub> – Fe <sub>2</sub> O <sub>3</sub> (SAF) ternary plots illustrating the chemical composition of bulk samples. Calculations assuming Al, Fe, Si are all present as their oxide, normalized mol %; n = 290. ....	140

Figure IV-20	Depth-average concentration values for Minor elements in decreasing order of concentration: Cr, Co, Ba, V, Cu, Ni, Pb, Cd, and Mo; <b>a)</b> values in mmol kg <sup>-1</sup> ; <b>b)</b> normalized to 100 mol %. Note that the elevation bin sizes are not equally sized, based on the number of samples available for each bin. Distribution statistics for each elevation bin not shown. ....	142
Figure IV-21	Geographic distribution of Ba, Cd, Co, Cr, Cu, Mo, Ni, Pb, and V, excluding all other elements. Concentration values given in mmol kg <sup>-1</sup> . ....	143
Figure IV-22	log-log solubility diagram and generated evaporation line, taking into account the most abundant cations and anions and their solubility product constants ( $K_{sp}$ ) at 20 °C and 1 atm. ....	148
Figure IV-23	Geographically distributed transects, two perpendicular (A and B) to the north and Caribbean coast, respectively; and one running parallel (C) to the Caribbean coast. This configuration was intended to capture hypothesized patterns explained in text. ....	153
Figure IV-24	Distribution of a) Ca, Mg and b) Fe, P contribution to rock composition along the three transects A, B and C. Values given in mmol kg <sup>-1</sup> .....	154
Figure IV-25	Distribution of Intermediate (Al, Fe, Mn, Si) and Minor (Ba, Cd, Co, Cr, Cu, Mo, Ni, Pb, V) elements on rock composition along transects A, B and C. Values given in mmol kg <sup>-1</sup> .....	156
Figure IV-26	Bulk rock composition. Average concentration values distribution for the most abundant elements in the vadose and the phreatic zone. Values in mmol kg <sup>-1</sup> . Phreatic zone is underrepresented due to cave diving limitations.....	160
Figure IV-27	Mass SiO <sub>2</sub> – Al <sub>2</sub> O <sub>3</sub> – Fe <sub>2</sub> O <sub>3</sub> (SAF) ternary plots illustrating the chemical composition of rocks in: <b>a)</b> Vadose zone, sampled in outcrops, quarries and dry caves; and <b>b)</b> Phreatic zone, sampled in underwater caves and cenotes. Data is in normalized weight %. Calculations assuming all Al, Fe, Si are present as their oxides.....	161

Figure IV-28	Sedimentary record for an outcrop located west to Akumal Pueblo, approximately 1 km inland; SedLog software was used to generate the sedimentary records. A simple lithological description at the right. ....	165
Figure IV-29	Geochemical profiles for selected elements in Outcrop 1 located in Akumal Pueblo, Quintana Roo, Mexico. ....	166
Figure IV-30	Sedimentary record for Quarry 2 near Tulum, located 2 km inland; SedLog software was used to generate the sedimentary records. Sampling depths are marked with a black cross and a simple lithological description is shown at the right.....	167
Figure IV-31	Depth profile concentrations—in decreasing concentration order— of Si, Al, S, Sr, Fe, P, Mn, and Ba for Quarry 2 near Tulum, located 2 km inland. Concentration values in mmol kg <sup>-1</sup> . SedLog software was used to generate the sedimentary records. ....	168
Figure IV-32	Sedimentary record for Quarry 4 located 55 km inland; SedLog software was used to generate the plots. A digital image of the site is shown to the left and a simple lithological description at the right. Rock samples also shown.....	169
Figure IV-33	Geochemical profiles for selected elements in Quarry 4, located 55 km inland. ....	169
Figure IV-34	Sedimentary record for Quarry 6 located 43 km inland; SedLog software was used to generate the plots. A simple lithological description shown at right. Size of the wall allowed subsampling on Unit 2 and Unit 6. ....	171
Figure IV-35	Geochemical profiles for selected elements in Quarry 6, located 43 km inland from the north coast.....	171
Figure IV-36	Geochemical profiles for selected elements in Quarry 8.....	171
Figure IV-37	Location of outcrops and quarries from which SedLog profiles were sketched. Associated geochemical profiles are also shown. Detailed individual profiles are found in previous figures.....	172

Figure IV-38	Cross section of Cenote Zapote (Hell Bells) modified from Stinnesbeck et al. (2018). Position of the halocline is shown. Elevation in meters relative to water table. ....	173
Figure IV-39	Location of cenotes around the area of Puerto Aventuras. Sistema Ponderosa, Chac Mool and Minotauro discharge fresh groundwater to the Caribbean coast. Lithology from Servicio Geológico Mexicano; underwater caves from Atlas Nacional de Riesgos (Mexican National Risk Atlas, CENAPRED, 2018; data from QRSS, 2020).....	177
Figure IV-40	Location of cenotes around the area of the largest underwater cave systems of planet Earth around Tulum. Sac Aktun and Ox Bel Ha discharge fresh groundwater to the Caribbean coast. Lithology from Servicio Geológico Mexicano (2018), Underwater caves from Atlas Nacional de Riesgos (CENAPRED, 2020), although displacement of 7+ km has been detected. ....	178
Figure IV-41	Location, cross sections, and geochemical (Al, Ba, Fe, Mn, P, S, Si, Sr) depth profiles of two pit-cenotes: a) Angelita, b) El Pit. Cross sections modified from Octavio del Río. Elevation in meters relative to water table. ....	180
Figure IV-42	Depth geochemical profiles of selected of the intermediate concentration elements (Al, Ba, Fe, Mn, P, S, Si, Sr) in rock samples from 19 cenotes located in the eastern Caribbean coastal Yucatán Peninsula, from the Puerto Morelos area, Sistema Ponderosa, Sistema Sac Aktun and Sistema Ox Bel Ha. Depth relative to water table. All values in mmol kg <sup>-1</sup> . ....	181
Figure IV-43	Overall distribution of Major (Ca, Mg), Intermediate (Al, Fe, K, Li, Mn, Na, P, S, Si, Sr), and Minor (Ba, Cd, Co, Cr, Cu, Mo, Ni, Pb, V) elements in rock samples distributed along the extensive underwater cave systems around Tulum, eastern coastal Quintana Roo. All values in mmol kg <sup>-1</sup> .....	182
Figure IV-44	Bulk distribution of Ca, Mg and Mg:Ca ratio by depth average (n = 290). ....	191
Figure IV-45	Regional distribution of Ca and Mg composition on rock samples. ....	191

- Figure IV-46 Calcite – Magnesite – Siderite ternary plot illustrating chemical composition of bulk samples; normalized to mol % (n = 290). Spreadsheet for creating tri-plots form Graham & Midgley (2000). ..... 193
- Figure IV-47 Elevation plots showing Al, Fe, Si, and Mn average concentration in the rock column. Same plot on the right with different scale to observe less abundant Mn. Units are in mmol of element per kilogram of dry rock ( $\text{mmol kg}^{-1}$ ). ..... 196
- Figure IV-48 Average bulk rock composition for two sections of the rock shown in Figure IV-49 a) very well indurated reddish clay; b) a white very fine-grained limestone with gastropods crosscut at the contact with the red infill clay. Values by elements are  $\text{mmol kg}^{-1}$  concentrations. The Ca and Mg are not plotted, and these are the intermediate and minor elements. .... 197
- Figure IV-49 Geochemical assessment of the contrasting and intercalated and cross cutting white fossil bearing limestone and red infill indurated sediment. Concentration of Al, Ba, Fe, Mn, P, S, Si and Sr in the two sections of the rock shown above, from Quarry 2. Rock sample shows secondary calcite deposition in both phases, and abundant bivalve fossils into the white matrix; a) and b) at left panel correspond to Figure IV-48. .... 198
- Figure IV-50 Mass  $\text{SiO}_2 - \text{Al}_2\text{O}_3 - \text{Fe}_2\text{O}_3$  (SAF) ternary plots illustrating the chemical composition of rocks and different degrees of alteration experienced; recalculated to 100% w. Calculations assuming all Al, Fe, Si are present as their oxides. All surface rock samples are plotted as small grey circles and sets of samples taken in depth sequences from select quarries and phreatic caves plotted in colors according to the legend. .... 200
- Figure IV-51 Mass  $\text{SiO}_2 - \text{Al}_2\text{O}_3 - \text{Fe}_2\text{O}_3$  (SAF) ternary plots showing the range and mean (n = 290) reported in this work; values reported for soil-pockets infilled with pedosediments, Akumal rendzina, and Maya Block granite (Cabadas-Báez et al., 2010); Saharan dust (Castillo et al., 2008); and El Chichón Holocene eruptions (B. J. Andrews et al., 2008); normalized weight %. Calculations assuming all Al, Fe, and Si are present as their oxide in bulk samples. .... 202

Figure IV-52	Ternary plot showing distribution of three biologically relevant elements present in the young carbonate rocks of the Yucatán Peninsula: Fe, P, and S; normalized mol % (n=290).....	207
Figure IV-53	Regional distribution of iron (Fe) and phosphorous (P) relative composition on rock samples (mmol kg <sup>-1</sup> ).....	209

## List of Tables

Table I-1	The Yucatán Peninsula most prominent hydrogeological/physiographic features from Perry et al, 2002. ....	32
Table II-1	Physical properties of different rock types. Hydraulic conductivity values are from Domenico & Schwartz (1997) and thermal conductivity values from Eppelbaum et al. (2014).....	46
Table II-2	Yucatán Platform hydrogeological regimes pre- and post- Chicxulub impact. ....	67
Table III-1	Yucatán Platform summary of historically published faulty and fracture features. The table is ordered from the north to the south.....	79
Table IV-1	Pleistocene and Holocene stratigraphic relationships of carbonates on islands and the main land coast of northeastern Yucatán. From Ward (1997).....	108
Table IV-2	ICP-OES wavelengths used and limits of detection (LOD) for selected elements under simultaneous multi-element conditions with axial view and a concentric nebulizer. Source: US EPA Method 200.7; Martin et al. (1994).....	118
Table IV-3	The three standard solutions concentration range (ppm) for selected elements used for calibration curve in ICP-OES analyses.....	119
Table IV-4	The 30 elements considered in this study for quantification by ICP-OES methods and their atomic numbers. ....	122

Table IV-5	Global average bulk rock composition showing mean, minimum, maximum, and standard deviation values obtained by ICP-OES quantification in rock samples (n = 385). Concentration values given in mmol per kg of dry rock ( $\text{mmol kg}^{-1}$ ). .....	125
Table IV-6	Concentration of studied elements in young carbonate rocks, n = 290 (this work); and in modern mean seawater, data from Libes (2009) and Millero (2013). .....	149
Table IV-7	Aqueous solubility values at 20 ° C and 1 atm for common compounds, containing some selected elements studied in this work. Data from Libes (2009) and Millero (2013). .....	150
Table IV-8	Aqueous product solubility constants for common mineral compounds associated with carbonates containing some selected elements studied. ....	150
Table IV-9	Concentration of studied elements in young carbonate rocks, n = 290 (this work); and in modern mean seawater, data from Libes (2009) and Millero (2013). On the right side, calculations on apparent accumulation/leaching as explained in text. Table is ordered top down for elements most in excess or accumulated and descending to scarcity or leached. ....	151
Table IV-10	Principal distinctions between vadose and phreatic zone rock samples. This table employs less data than previous one .....	159
Table IV-11	Comparison of average concentration values for the most abundant elements in the vadose and the phreatic zone. Values in $\text{mmol kg}^{-1}$ . Phreatic zone is underrepresented due to cave diving limitations. ....	159
Table IV-12	Summary table of phreatic cenote and cave sites sampled, grouped from north to south along the Caribbean coast, Quintana Roo. ....	174
Table IV-13	Comparison of two different dolomitization mechanisms operating as function of depth and their specific requirements. ....	187
Table IV-14	Cation composition of carbonate rocks from the shallow subsurface on the northeastern coast of the Yucatán Peninsula. Data from Ward & Halley (1985). ....	189
Table IV-15	Pedogenetic hypotheses on terra rossa formation. ....	194

Table IV-16	Chemical formulas and stoichiometric coefficients of limestone components and naturally occurring Al, Fe, Mn, Si minerals common in carbonate settings. ....	201
Table IV-17	Major (wt% oxides) element analyses determined by means of ICP–OES in rocks from the Yucatán Peninsula (this work) and in Western Saharan dust (Moreno et al., 2006). Assuming all elements are present as their oxides. ....	204
Table IV-18	Mean concentrations of some Minor Elements: cadmium (Cd), chromium (Cr), copper (Cu), lead (Pb), and vanadium (V) sampled in vadose and phreatic rocks, and from sand at a public beach. All values in $\text{mmol kg}^{-1}_{\text{rock}}$ . ....	210
Table VI-1	Geodetic data for the 40 GPS/GNNS stations considered in this study within the greater Caribbean area. Location, data temporal range and calculation of velocities are shown. Displacements in $\text{mm yr}^{-1}$ . Data from UNAVCO (2018). ....	248
Table VII-1	Average bulk rock composition showing mean, minimum, maximum, and standard deviation values obtained by ICP-OES quantification in rock samples ( $n = 185$ ) grouped in three areas: beach sand vadose zone and phreatic zone. Concentration values for 22 elements given in $\text{mmol per kg}$ of dry rock ( $\text{mmol kg}^{-1}_{\text{rock}}$ ). Depth means meters above ground for vadose sample rocks, and meters below water table for phreatic zone sample rocks. ....	251
Table VII-2	Information on geography, characteristics of sites, coordinates, and weight (mg) used in the multi-elemental quantification by ICP-OES analyzes for a selection of 185 samples. Depth means meters above ground for vadose sample rocks, and meters below water table for phreatic sample rocks. ....	256

# **I           General Introduction**

## **I-1    PREFACE**

This work has been separated into four main sections. First, an Introduction to acquaint the reader with the broad context of the topics covered in this research. Following the Introduction are three topical Chapters, each of which constitutes a separate research package with discussion and conclusion sections.

Although chapters can be read independently of each other, the order of this thesis aims to guide the reader in a journey across different spatial and temporal scales, intentionally reflected in the structure of this document. In this way, the chapters are presented in the order that starts with platform-scale considerations and spanning broad timescales on the order of  $10^7$  yr, then progressing to mechanisms which operate on sea level changes with temporal scale on the order of  $10^5$  yr. The final body chapter examines the processes happening today leading to insights on the modern configuration of the platform based on geochemical characterization of young carbonate rocks spanning the Pleistocene-Holocene Epochs.

The thesis combined literature research, geophysical, geodetical and geochemical data analyses, along with field observations to address questions on the Yucatán platform geological history, with implication in the present-day Peninsula.

## I-2 CONTEXT AND MOTIVATION

Earth's global carbon cycle includes major carbon sinks and sources. Over the last decades, a growing wealth of long-term atmosphere, ocean, and ecosystem observations has provided essential insights into how climate change affects the ways that carbon moves through Earth's environment, yet many fundamental questions remain unanswered. The most challenging and societally relevant question might well be whether the rate at which the land and ocean can sequester carbon will continue to keep pace with rising anthropogenic carbon dioxide (CO<sub>2</sub>) emissions. Warmer temperatures drive longer and more destructive fire seasons, shifting precipitation patterns cause flooding in some areas and drought in others, ocean acidification threatens marine life across the globe, and induced sea level rise (SLR).

Atmospheric pCO<sub>2</sub> exhibits natural variations over scales that range from 100 kyr glacial-interglacial frequencies to millions of years. The changes in pCO<sub>2</sub> (and links to climate) are controlled by weathering reactions involving carbonic acid and its role as a reactant during weathering of silicate and carbonate minerals (Berner, 2003; Kump et al., 2000). Weathering of silicate minerals involves carbonic acid originates through hydration of atmospheric CO<sub>2</sub> which reactions are commonly referred to as “weathering” rather than dissolution because they may be incongruent (Martin, 2017).

Carbonate minerals constitute Earth's largest carbon (C) reservoir. Over long periods of time  $>10^6$  yr, this reservoir is considered unimportant to the global C cycle because it provides balanced sources and sinks of atmospheric CO<sub>2</sub> as carbonate minerals precipitate and dissolve from carbonic acid (Herman, 2019; White, 2003). However, over time scales  $10^2 - 10^5$  yr, the carbonate mineral reactions may impact the carbon cycle at particularly when atmospheric pCO<sub>2</sub>

changes by several hundred ppm, as exemplified by the Paleocene-Eocene Thermal Maximum, at transitions between glacial-interglacial times, and over the past century from anthropogenic inputs.

Most carbonate minerals form in the ocean as calcite and its polymorph aragonite, two minerals in a group of around 60, of which calcite and dolomite are sufficiently abundant to be rock forming. Deposition in epeiric seas and tectonic uplift has resulted in limestone, marble and dolomite exposures covering 15 to 20% of the terrestrial landscape (Dürr et al., 2005; Ford & Williams, 2007). At present-day, carbonate minerals are deposited about equally in the shallow and deep ocean and most shallow deposition occurs on carbonate platforms that cover around 800,000 km<sup>2</sup> of low latitude ocean (Milliman, 1993). The Yucatan Platform is one of the largest present-day carbonate platforms globally.

Carbonate mineral dissolution contributes around 50% of the global river Ca and Mg loads (Meybeck, 1987). Flux rates are likely higher from karst landscapes that form on carbonate terrains, where focused dissolution causes internal drainage through air and water-filled caves through sinkholes (Ford & Williams, 2007). Post-Paleozoic carbonates are more readily weathered, since they typically remain closer to the surface and retain more of their primary porosity, leading to order of magnitude permeability increases by dissolution along flow paths. The development of organized, and increasingly efficient drainage networks principally by dissolution, is karstification, and a dissolution weathering process that results in widespread mass loss through the aquifer system.

Karst resurgences include numerous first order magnitude springs globally, and these make them ready water supplies. While ~16% of the earth's surface is carbonates, their hydrogeological functions lead them to provide some 25% of the world's drinking water supplies (Ford & Williams,

2007). At the same time, the triple porosity natures of the aquifers make them challenging to understand hydrogeochemically, and also subject to great risk from impact and contamination. In all karst systems, the majority of the water in the system is held in the 3D rock matrix leading to high rates of water rock interaction, while the flux is principally in the turbulent flow conduits (Figure I-2). The increasing exploitation of karst resources, such as water and building material, is leading to severe environmental impacts and unsustainable situations. The number of karst areas affected by water pollution, landscape degradation and other impacts is growing very rapidly, unfortunately. Furthermore, the damage caused by hazardous karst processes, especially subsidence sinkholes (De Waele et al., 2011; A. C. Waltham et al., 2005), will most likely continue an increasing trend.

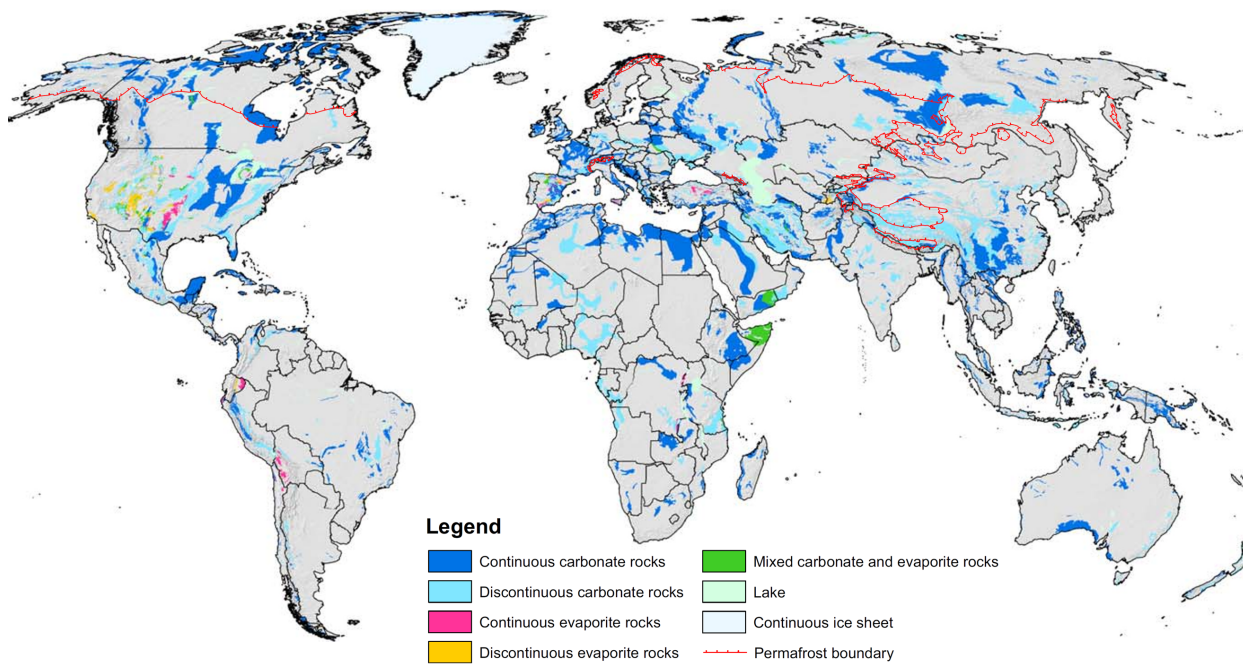
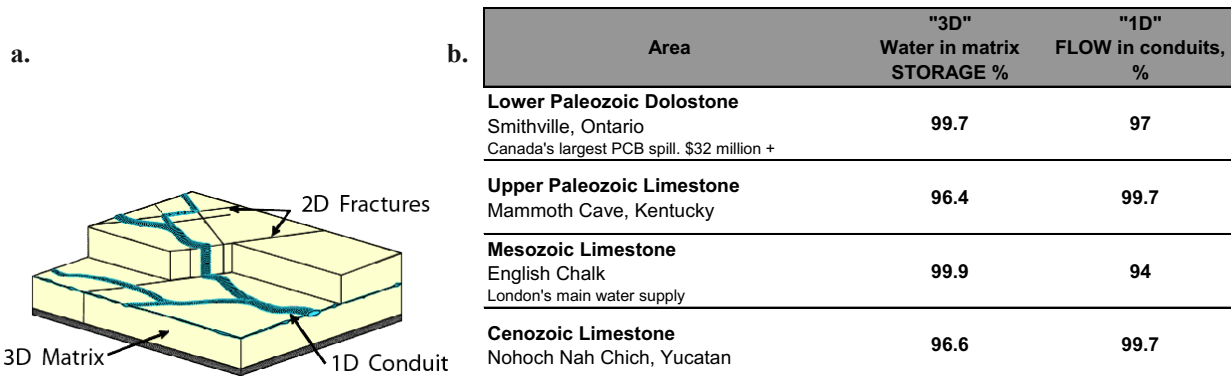


Figure I-1 The World Karst Aquifer Map (WOKAM) demarking karstifiable carbonate and evaporite rocks that represent potential karst aquifers. From Goldscheider et al. (2020).



*Figure I-2 a. Three-dimensional conceptual model of a karst geology aquifer, with a 3D matrix, 2D planar fractures, fissures, and bedding planes, and 1D linear conduits housing turbulent flow. b. Table of four representative karst aquifers, with data on the proportion of the total water that is held in the 3D matrix storage, and the proportion of the total flux that occurs in the 1D conduits. From Worthington et al. (2000).*

The most distinctive aspect of shallow marine carbonate platforms is the predominant role of organisms in producing, processing and trapping carbonate sediment, which confers the complexity of biogenic and abiotic interactions imprinted and overlapped over time. Over geological time scales, the sub-marine shelf can be understood as a surface of dynamic equilibrium (Wright & Burchette, 1996) controlled by the variables of relative sea level changes, the rate and characteristics of sediment input, and the rate of sediment transport. With sea level fluctuations, platforms may partially or completely be sub-aerial, with marine carbonate deposition interrupted, and the surface then subject to hydrochemical processes including dissolution by meteoric waters and any biological weathering tied to ecosystem development. Surface weathering and internal dissolution both remove mass from the sub-aerial platform (now peninsula or island) and may lead to surface lowering.

Diagenesis is any physical and chemical process that affects a sedimentary earth material after initial deposition, during or after lithification, exclusive of weathering and metamorphism. The study of diagenesis in rocks is used to understand the geologic history they have undergone and the nature and type of fluids that have circulated through them. Two important post-depositional processes affecting the Yucatán Peninsula carbonate rocks are considered in this work: dolomite formation, or dolomitization, and pedogenetic transformation of rock to soils, which includes the geochemical paths of a number of residual elements.

Many aspects of the hydrogeology and geology of the Yucatán carbonate platform remain underdeveloped, with simplistic and sometimes contradictory interpretations being used for management purposes. As is common with karst geology, the surface topography does not effectively demonstrate the distribution and pathways of the underground drainage, and consequently topography alone is highly ineffective at determining drainage basins, and drainage divides (Ford & Williams, 2007). Many of the *Comisión Nacional del Agua* (CONAGUA – Mexican Water Commission) documents include a simple, but likely somewhat effective approach of straight-line drainage from the recharge interior to coastal drainage (Figure I-3a). The compiled “expert” position coordinated by the NGO *Amigos de Sian Ka'an* in 2004 shows many conflicting ideas on broad peninsula scale drainage (Figure I-3b). It is evident that the platform scale karstification processes must be substantially advanced, in order to inform the platform scale understanding of the hydrogeology, if there is hope of arriving at effective regional, or site-specific water and waste management strategies.

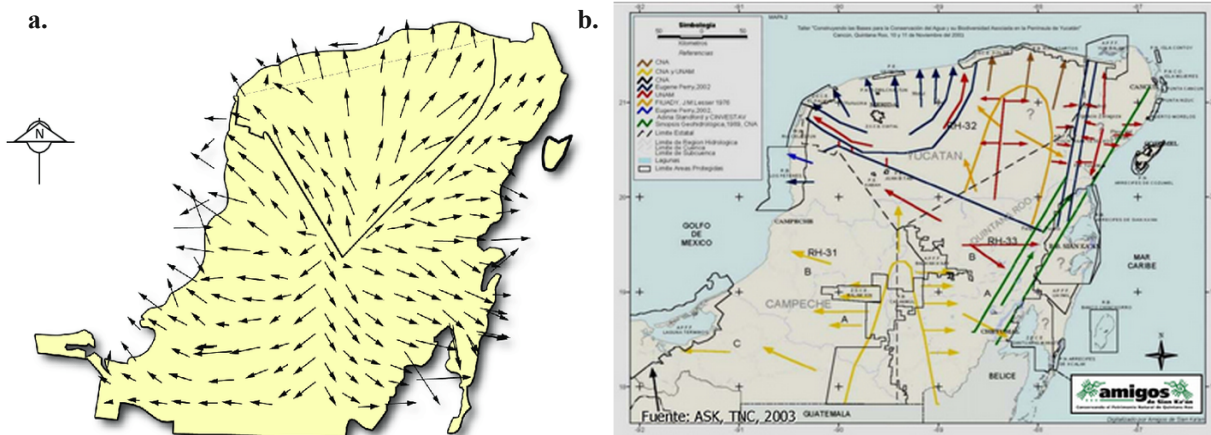


Figure I-3 Hydrogeological interpretations reflecting the actual state-of-knowledge reported in different sources: **a.** interpretation of groundwater flow from the Mexican National Water Commission (CONAGUA, 2010); **b.** Exercise on interpretation of hydrogeological features of the Yucatán Peninsula aquifer by different research groups (Amigos de Sian Ka'an A.C., 2003).

The largest identified Phanerozoic bolide impact on Earth ~66 Ma, became a site of deposition of dominantly marine carbonate sediments during most of the Cenozoic Era. The actual understanding of Chicxulub impact crater and associated structures has been expanded in recent years through significant investment in lithologic, bio-stratigraphic, petrographic, geochemical, and geophysical exploration and interpretation, including with onshore and off-shore drilling and geophysics. The so-called Chicxulub Sedimentary Basin (Lefticariu et al., 2006; Perry et al., 2002) is coincident with the impact crater and circumscribed by the Ring of Cenotes (ROC), which is a surficial expression consisting of an arc-alignment of karst sinkhole coincident with the perimeter of the deep-buried crater structure. The ROC is often considered to have high permeability developed in Tertiary carbonate rocks, separating it from other outside features with long exposure history (Marín & Alcocer, 2002; Perry et al., 1995). A robust understanding of the karstification of the Chicxulub Basin and the Ring of Cenote is required, in order to establish a robust understanding of its influence on the hydrogeology of the northwestern peninsula.

Geomorphological and hydrogeological research can play a decisive role in natural disasters prevention and mitigation in karst areas, particularly those induced by human activities; dams, mines and tunnels affected by flooding and subsidence, high-speed railways built in sinkhole-prone areas (Guerrero et al., 2008) or development of sinkholes at elevated rates induced by water table drawdown (Sprynskyy et al., 2009). The importance of properly managing karst areas and mitigating the detrimental effects caused by anthropic activities on these inherently sensitive and vulnerable environments must not be underestimated.

Sea level reconstruction requires sites with well-constrained tectonic histories. Accurate paleo-sea-level benchmarks for Quaternary sea levels are important for many reasons, including to monitor the magnitude of climate and sea level changes in the past and present; to establish the concordance or discordance of astronomical, isotopic and climatic events; and to provide benchmarks from which the magnitude of uplift or subsidence in tectonically unstable zones can be calculated. To date, the Yucatán Platform has been consistently considered tectonically stable, principally based on the initial and limited work of Szabo et al. (1978). Robust understanding of the degree of stability, or variance from that, is required in order to consider development of quality far-field sea level records from the peninsula which affords wide ranging opportunities to contribute to western Caribbean Sea level records that at present require significant expansion. Insight on the tectonic rigidity of the Yucatán Platform also has direct relevance to the (re-) interpretation of geological history, speleogenesis, and hydrogeology and water resource management, and the consideration of the long-term prospects for coastal developments that at present advance at an extreme rate, driven by tourism.

### I-3 OUTLINED ORGANIZATION

This section briefly describes each one of the three main Chapters composing this work. Each Chapter is presented in journal-style structure, with their own discussion and conclusion sections.

In support of the reader accessing the body chapters, Table I-1 is presented here to outline the most prominent hydrogeological and physiographic features of the Yucatán Peninsula, and to offer a quick overview of the carbonate platform principal geological features.

*Table I-1 The Yucatán Peninsula most prominent hydrogeological/physiographic features from Perry et al, 2002.*

<b>FEATURES</b>	<b>INTERPRETATION</b>
<b>Holbox Fracture Zone</b>  <b>aka Xel Ha Fracture Zone in the southern expression near Tulum</b>	The extensive bank marginal coastal-parallel fracture system and horst and graben system of the Yucatan Peninsula is overlain by elongated seasonally flooding swales, or poljes, in the north, and locally called the Holbox Fracture Zone (HFZ) continuing south to Xel Ha Zone, and west to horst and graben complex for Cozumel Island and the Cozumel channel parallel to the faulted east coast. These fault systems are probably related to Eocene tectonic events in the Caribbean, manifested by elongated cenotes often connected by broad “swales,” some of which are 100 km long chains of elongated solution depressions locally known as <i>sabanas</i> . Water movement is northward (Lesser & Weidie, 1988; Weidie, 1985).
<b>Rio Hondo Fault Zone</b>	The bank marginal fracture system continues near to Tulum and southwards, with the surface expression including the orientation of coastal caletas, alignment of Chetumal Bay and the parallel Laguna Bacalar complex, with additional features south into Belize, where it is called the Rio Hondo Fault Zone (RHFZ) (see Bauer-Gottwein et al., 2011; Gondwe et al., 2010). It consists of normal faults identified as the onshore continuation of an extensive horst and graben block system located sub-parallel to the southern Caribbean coast (Weidie, 1985).
<b>Ticul Fault Zone</b>	A prominent ridge thrust up to south, which surface expression is an escarpment trending WNW for about 100 km called Sierrita de Ticul. Cenozoic gypsum-anhydrite bearing K/Pg impact breccia closer to surface in upthrust block (Perry et al., 1995).
<b>Ring of Cenotes</b>	Semicircular system of deep listric faults (Gulick et al., 2013). The surface expression known as the Ring of Cenotes (ROC) developed in Cenozoic rocks overlying the 66 Ma K/Pg Chicxulub Impact Structure. Separates internal Chicxulub Sedimentary Basin from Pockmarked Terrain and other external features with long exposure history. The ROC is a zone of very high permeability.

<i>FEATURES</i>	<i>INTERPRETATION</i>
<b>Chicxulub Sedimentary Basin</b>	Cenozoic Basin of subsidence formed after impact and lasting during much of Paleogene. With lower permeability, it contains fewer cenotes than areas outside the Ring of Cenotes. Groundwater chemistry dominated by mixing with saline intrusion.
<b>Pockmarked Terrain</b>	Underlying Tertiary evaporite and K/T gypsum-anhydrite-bearing breccia may have been exposed to karstification, especially during Paleogene uplift and erosion. High permeability evidenced by many cenotes.
<b>North Coast</b>	Dune ridge almost continuous except where crossed by ROC, HFZ, and Ria Lagartos (another permeable zone of relatively high discharge). Groundwater beneath dune and inland from dune is confined by a thin, impermeable caliche layer.
<b>Northern East Coast</b>	Fault-bounded coast. Mixing-zone dissolution causes rapid erosion along fractures to produce embayments or <i>caletas</i> . Steeper water table gradients than on the north coast, partly because of greater recharge. Extensive development of caves along fractures.
<b>Typical ground surface</b>	Pervasive caliche layer up to about 3 m thick with little soil cover. Particularly well developed in Chicxulub Sedimentary Basin. This layer is highly impermeable and forms a narrow coastal aquitard (Perry et al., 1995).

## **Chapter II: Hypogene Hydrogeothermal Convective Circulation Model for the Formation of the Chicxulub Ring of Cenotes in the Yucatán Peninsula, Mexico**

The genesis of the surface expressed Ring of Cenotes remains an active question in the Yucatán geological understanding. The first Chapter begins with an overview of the geological history of the Yucatán Peninsula, in order to provide a conceptual model for the formation of the Chicxulub Ring of Cenotes (ROC), based on published evidence on geology and stratigraphy, onshore and offshore geophysical surveys, general knowledge of carbonate platform circulation, reactive transport modeling, and aqueous geochemical data.

It is proposed that deep-seated hypogene driven circulation and dissolution in the Yucatán Platform pre-dates the impact, while the platform was submarine. Post-impact, continued hypogene circulation and dissolution influenced by non-evaporitic anhydrite, heat of impact, and

the geometry of the pre-existing submarine platform groundwater circulation patterns, combined with the geometry of the low permeability impact melts, all result in the aligned spatial concentration of deeply penetrating pit cenotes, which over time stope upwards through overlying carbonate sequences, in places breaching the modern surface, and now forming the ROC. This chapter provides a genetic model for how the impact topography mantled in km's of overlying sediments has a surface expression, due to hydrogeothermal epigene convective circulation in the post-impact carbonate sequences, leading to spatially focused dissolution at depth, with voids concentrated around the perimeter of the impact plug and crater edge. Fracturing associated with the Chicxulub impact provides numerous preferential flow paths, however it is specifically the fractures aligned with the perimeter of the impact melt plug that are significantly karstified by bottom-up hypogene processes to produce the observed Ring of Cenotes. Hydrogeological interconnection between the vertical pit cenotes is not specifically indicated, although the ring fractures may channel water.

### **Chapter III: On the Tectonic Stability of the Yucatán Block: Tilt and Rotation**

Sea level reconstruction requires sites with well-constrained tectonic histories. The Yucatán Block (YB) is understood to be tectonically stable, with some subsidence since the Eocene. This second Chapter presents the use of geodetic data from UNAVCO (DAI v2) stations with 5+ year records, to show the present-day YB motion is NW counterclockwise rotation, along with subsidence rates of 1 m / 1000 year on the N and NE peninsula coastlines. An argumentation is made for persistence of the measured vertical motions from the mid-Holocene to present, based on coastal geomorphology, ecology, and archeological observations.

The present vertical rates are 3-orders of magnitude faster than the previously indicated subsidence since mid/late Eocene. The YB is tectonically rigid in the strict sense, without apparent deformation, yet block tilting and rotation is of broad significance in interpretation of the karst hydrogeology, paleoenvironmental records, and coastal adaptation to sea level rise.

#### **Chapter IV: Geochemical Characterization of Pleistocene-Holocene Carbonate Rocks from Northeastern Yucatán Peninsula, México**

The third and final body chapter treats the geochemistry of Paleocene-Holocene carbonate rocks from the Yucatán Peninsula (YP) with the aim of providing substantive insight on the geochemical composition, distribution and its relation to the geological evolution of the platform. The focus of the research is to investigate the geochemical composition of young carbonate rocks aged Pleistocene to Holocene by ICP-OES methods and to explore on water-rock interactions within the aquifer, with potential downstream impacts on coastal water chemistry.

Water-rock interactions through time are key to understand present chemo-stratigraphic setting, and geochemical evolution of shallow coastal environments, where the mixing zone plays a fundamental role. Neither clear geographical distribution, nor depth distribution patterns are evident, likely due to the inherent patchiness of coastal shallow marine facies, and also because overlapping of geomorphological and diagenetic processes driven by sea level changes. Insight is gained on the recalcitrant origin of *terra rossa* formed on karst, with examination of the residual elements leading to accumulation of pedogenetic Al, Fe and Si oxides in reddish clays in the soils, and sometimes lithified, as part of the landscape of the Yucatán Peninsula. An exploration of the bulk rock geochemistry in relation to modern ocean chemistry helps constrain diagenetic post-depositional processes such as leaching, dolomitization and pedogenic pathways.

## **II Hypogene Hydrogeothermal Convective Circulation Model for the Formation of the Chicxulub Ring of Cenotes in the Yucatán Peninsula, Mexico**

### **ABSTRACT**

The Ring of Cenotes in the Yucatán Peninsula, Mexico, is an aligned arc of sinkholes (locally called cenotes), which is the surface expression of the deeply buried multi-ring Chicxulub Impact Crater. A pending question remains the formation processes for the initial deep voids, and also their upwards propagation cross cutting over 1,000+ m of supra-deposited submarine Cenozoic carbonate sequences. The cenotes overlying the crater are 100+ m deep shafts commonly breaching the surface. The pit geomorphology indicates a bottom-up genesis. We argue for the formation of the Ring of Cenotes by hydrogeothermal epigene convective circulation in the post-impact carbonate sequences, leading to spatially focused dissolution at depth, with voids concentrated around the perimeter of the impact plug and crater edge. Fracturing associated with the Chicxulub impact provides numerous preferential flow paths, however it is specifically the fractures aligned with the perimeter of the impact melt plug that are significantly karstified by bottom-up hypogene processes to produce the observed Ring of Cenotes. In contrast, the popular cenotes and sub-horizontal caves systems along the Caribbean coast are formed by epigene processes, which have only been possible over the last 10 Ma once regular subaerial exposure occurred allowing for the formation of a meteoric water lens.

## II-1 INTRODUCTION

It has been almost four decades since the discovery of an underwater arc with "extraordinary symmetry" by Camargo & Penfield, at that time working for a Mexican oil-drilling company, PEMEX, in the northern Yucatán Peninsula, of Mexico (Penfield & Camargo-Zanoguera, 1991, 1981). At the same time, Alvarez et al. (1980) hypothesized that a large extraterrestrial body had struck Earth at the end of the Cretaceous causing a global mass extinction. Evidence of the large *Chicxulub* crater quickly accumulated, despite it being buried under Cenozoic carbonate deposits (Camargo-Zanoguera & Suárez, 1994; Hildebrand et al., 1991, 1995, 1998; Morgan et al., 1997; Pope et al., 1991, 1993; Sharpton et al., 1996). Most recent scrutiny includes the 2017 onshore and shallow marine coring campaigns, combined with sub-surface mapping using geophysical methods (Gulick et al., 2017; Morgan et al., 2017). The *Chicxulub Impact Structure* is currently understood to result of a 10–12 km diameter bolide that impacted  $65.55 \pm 0.3$  Ma at the Cretaceous/Paleogene (K/Pg) boundary. An estimated of  $325 \pm 130$  Gt of sulfur and  $425 \pm 160$  Gt  $\text{CO}_2$  were ejected and produced severe changes to the global climate (Artemieva & Morgan, 2017). Proposed kill mechanisms for the K/Pg mass extinction include: short-term cooling and darkness produced by aerosol dust, soot, and sulfur (Bardeen et al., 2017; Brett, 1992; Brugger et al., 2017; Kaiho et al., 2016; Pierazzo et al., 2003); long-term warming from the release of massive volumes of  $\text{CO}_2$  (Gupta et al., 2001; Shen et al., 2003; Yang & Ahrens, 1998); ocean acidification (Maruoka & Koeberl, 2003; Ohno et al., 2014); and global firestorms ignited by heated ejecta reentering Earth's atmosphere (Morgan et al., 2013; Robertson et al., 2013; Wolbach et al., 1985).

Thousands of sinkholes, locally called cenotes, are found across the Yucatán Peninsula. A distinct semi-circular high-density alignment of cenotes forms the *Chicxulub Ring of Cenotes* (ROC). Coastal springs occur along the modern coast where the ROC intersects the Holocene northwest coastline (Hernández-Terrones et al., 2011; Null et al., 2014; Perry et al., 2002). Geophysical data shows that the ROC overlies the peak ring (PR) of a multi-ring impact basin (Gulick et al., 2013). There are at least three series of semi-continuous, deep concentric, listric *ring faults* around the peak ring structure, radially reaching distances of up to 130 km from the crater center. The recently acquired IODP-ICDP Expedition 364 offshore cores provide detail of the structure, and advance the estimates of ejecta and total energy released during the impact (Gulick et al., 2013, 2017).

The genesis of the surface expressed Ring of Cenotes is now even more enigmatic. How does a topographic surface mantled in km's of overlying sediments have a surface expression? This paper provides a novel conceptual model for the formation of the *Chicxulub Ring of Cenotes*, based on published evidence of the Yucatán geology and stratigraphy, onshore and offshore geophysical surveys, general knowledge of carbonate platform circulation, reactive transport modeling, and aqueous geochemical data. We propose that deep-seated hypogene driven circulation and dissolution in the Yucatán Platform pre-dates the impact. Post-impact, continued hypogene circulation and dissolution influenced by non-evaporitic anhydrite, heat of impact, and the geometry of the pre-existing submarine platform groundwater circulation patterns, combined with the geometry of the low permeability impact melts, all result in the aligned spatial concentration of deeply-penetrating pit cenotes, which over time stope upwards through overlying

carbonate sequences, in places breaching the modern surface, and now forming the *Chicxulub Ring of Cenotes*.

## II-2 KARSTIFICATION

Karstification is the assemblage of processes, which includes dissolution of soluble substrate, leading to orders of magnitude increase in permeability (Ford & Williams, 2007). Karst landscapes and aquifer develop on the full range of carbonate deposits. These include diagenetically immature eogenetic carbonates, which are those that remain close to their depositional environment and typically retain the majority of their primary porosity, and also, telogenetic carbonate formations that burial, compaction, and cementation has reduced or eliminated primary porosity (Vacher & Mylroie, 2002). Structural features controlling the geometry of karstification include bedding planes and fractures, which can significantly guide incipient groundwater flow paths, particularly in lower porosity telogenetic karst.

The process of karstification requires undersaturated waters, and flux through the formation to remove the dissolution products. Epigene karstification is driven "top down" by meteoric water flowing principally under the force of gravity. Hypogene karstification occurs where the source and drive of water circulation is geogenic in nature, and decoupled from the atmosphere, such as from hydrothermal or volcanic sources.

Low latitude karstified platforms such as the Yucatán, Bahamas, and Florida, are eogenetic as seen in their location, retention of high primary porosity, and lack of telogenetic characteristics associated with burial (Vacher & Mylroie, 2002). The karstification is typically conceived of as epigene, with meteoric waters being a principal component of the concept, mostly with fresh-saline mixing zone corrosion leading to dissolution at the base of the meteoric lens (Smart et al., 2006;

Whitaker & Smart, 2007; Wigley & Plummer, 1976), but also with an increasing appreciation for remineralization of organic matter at the meteoric water table (Gulley et al., 2013, 2014). Truly hypogene concepts for karstification in these young carbonate platforms is rarely considered. Hypogene contributions to the development of distributed, non-spatially organized karst features both onshore and offshore in the Florida Platform have been indicated, tied to exceptional porosity development and high hydraulic conductivity in deep Cenozoic and Paleocene/Eocene strata bounded by gypsum/anhydrite, and in deeper Cretaceous strata tied to  $H_2SO_4$  dissolution. There is evidence that collapse zones in these deeper strata have migrated upwards to the modern land surface (Upchurch et al., 2019). In contrast, similar hypogene karstification in the Yucatán would be geometrically constrained and organized by the buried Chicxulub structure.

## II-2.1 CENOTES - MORPHOLOGY AND GENESIS

The Yucatán Peninsula is a type location for bedrock-exposed sinkholes, locally called cenotes, of which more than ~10,000 have been estimated to exist on the Peninsula (Aguilar-Duarte et al., 2016). Sinkholes require a pre-existing subterranean void for their development (Ford & Williams, 2007).

Cave diving exploration mostly concentrated along the Caribbean coast has revealed ~1,500 km of mostly flooded sub-horizontal anastomotic conduits, with average maximum passage depth of only -21 m below the water table (QRSS, 2020). The cenotes providing access to these shallow underwater cave systems within 10 km of the coast are predominantly 1–20 m diameter collapses of the thin rock ceiling (Figure II-1 Upper Row; (Beddows et al., 2007; Smart et al., 2006). The speleogenesis of these sub-horizontal shallow anastomotic networks is argued to be driven by enhanced dissolution rates at the fresh-saline interface (*aka* mixing zone, or halocline)

of the density stratified coastal aquifer (Smart et al., 2006). Research in similarly shallow and sub-horizontal caves in Florida point to remineralization of organic matter at the water table as also being a significant endogenous drive for undersaturation and thus dissolution (Gulley et al., 2013, 2014). The extensive karstification at the halocline and/or at the water table has led to increased permeability, as shown by an extremely flat-water table gradient of  $10^{-5}$  (which is cm:km) that corresponds closely to sea level (Bauer-Gottwein et al., 2011; Beddows, 2004; Marín et al., 2000; Perry et al., 1995). These Caribbean caves which lie at and below the water table include abundant phreatic speleothems, demonstrating formation during subaerial phases tied to lower aquifer and global sea levels during glacial maxima (Moseley et al., 2013, 2015).

In contrast, the cenotes of the ROC overlying the buried Chicxulub Impact Structure in the northwest of the Peninsula are geomorphological distinct from those of the Caribbean coast (Figure II-1). These “pit cenotes” (Figure II-1 Lower Row) span 20–100 m at the water table, are bounded by near-vertical walls and overall present bell-shaped cross sections (Beddows, 2004). The vertical extent includes the 10–20 m drops from ground surface, and the few surveys reach 120 m below the water table, which is also the limit of even the most advanced technical cave diving explorers. The cenote basins are mantled in sediment with some exposed breakdown blocks, but the majority of the pit void is open water indicating dissolution removal of the breakdown blocks. A number of these pit cenotes retain intact rock ceilings spanning across the void and are nearly - “entranceless” with access only possible via small fractures or holes created by tree roots (See Ucil in Figure II-1 Lower Row). The vertical expanse of the pit cenotes indicates a bottom-up genesis, with deep-seated initiation at depths of at least 120 m below the modern water table.

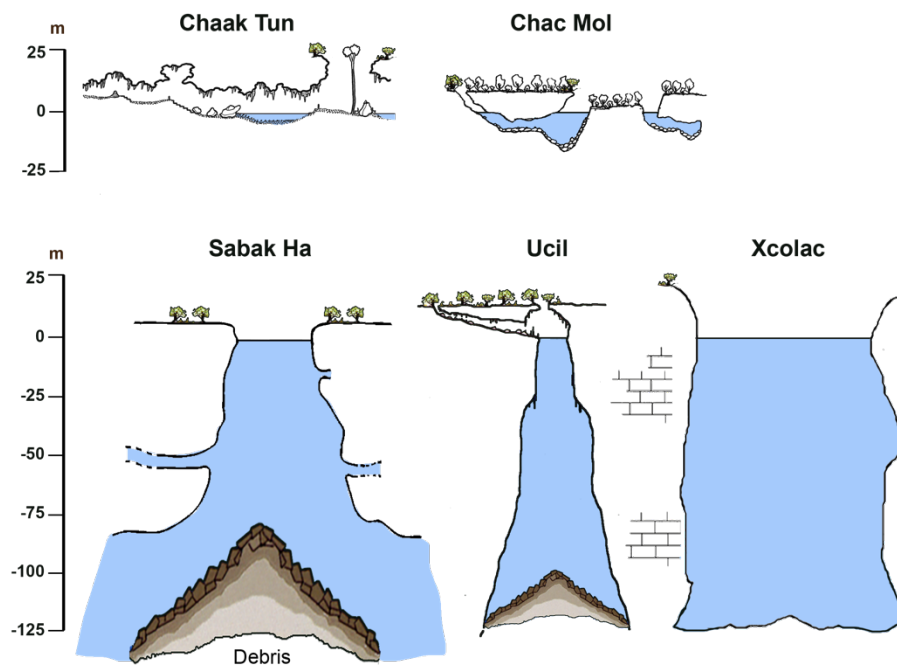


Figure II-1 Grouping of cenote morphologies showing their vertical scale dimensions.

Upper Row – Shallow Cenotes – Thousands of cenotes mostly along the Caribbean coast present shallow depth profiles. Often easy connectivity to the long distance (100–1000's m) near horizontal often flooded conduit. Cross sections from: Chac Mol – Matthes (2000); Chaak Tun – Lace et al. (2008).

Lower Row – Pit Cenotes – Vertical bell-shaped sinkholes reaching to 120+ m below local water table, with sediment and breakdown piles in the base. General absence of significant horizontal conduits. Often incomplete breaching of the ground surface. Cross sections from: Ucil – Lazcano & Knab in: Thomas (2011); Xcolac – Socki et al. (2002).

## **II-2.2 THE YUCATÁN PLATFORM OVERVIEW**

The Yucatán Platform spans 900 km N-S by 750 km E-W separating the Caribbean and Gulf of Mexico basins. The platform is composed of 3.7 km of massive carbonate sequences down to a granodiorite basement (Gulick et al., 2013; Pope et al., 1996; Sharpton et al., 1996; Ward et al., 1995), and is broadly rectangular and with a relative flat surface reflecting the sub-horizontal marine depositional topography. The platform edge delimited by the 200 m isobaths lies ~200 km offshore of the north and north-west shoreline, with a drop to full marine depth (~3,500 m) in the Gulf of Mexico and western Atlantic. The platform scarp lies within ~10 km east from the Caribbean coast (Figure II-2).

The present subaerially exposed Yucatán Peninsula spans 400 km E-W by 450 km N-S, but global sea level records indicate that the platform was fully submarine through to at least <30 Ma in the Oligocene, and with longer persistent subaerial exposure only possible after 10 Ma (Haq et al., 1988).

### **II-2.2.1 Paleozoic Granodiorite Basement**

Geophysical surveys using combined reflection and seismic velocity data, and 3D wide-angle tomographic analyses, show that the basement rock in the center of the peninsula is at a depth of ~3.7 km below modern surface (Gulick et al., 2013; Morgan et al., 1997). It is topographically near planar, but with a steepening down to the east to 5.5–6.0 km (Collins et al., 2008; Morgan et al., 2006).

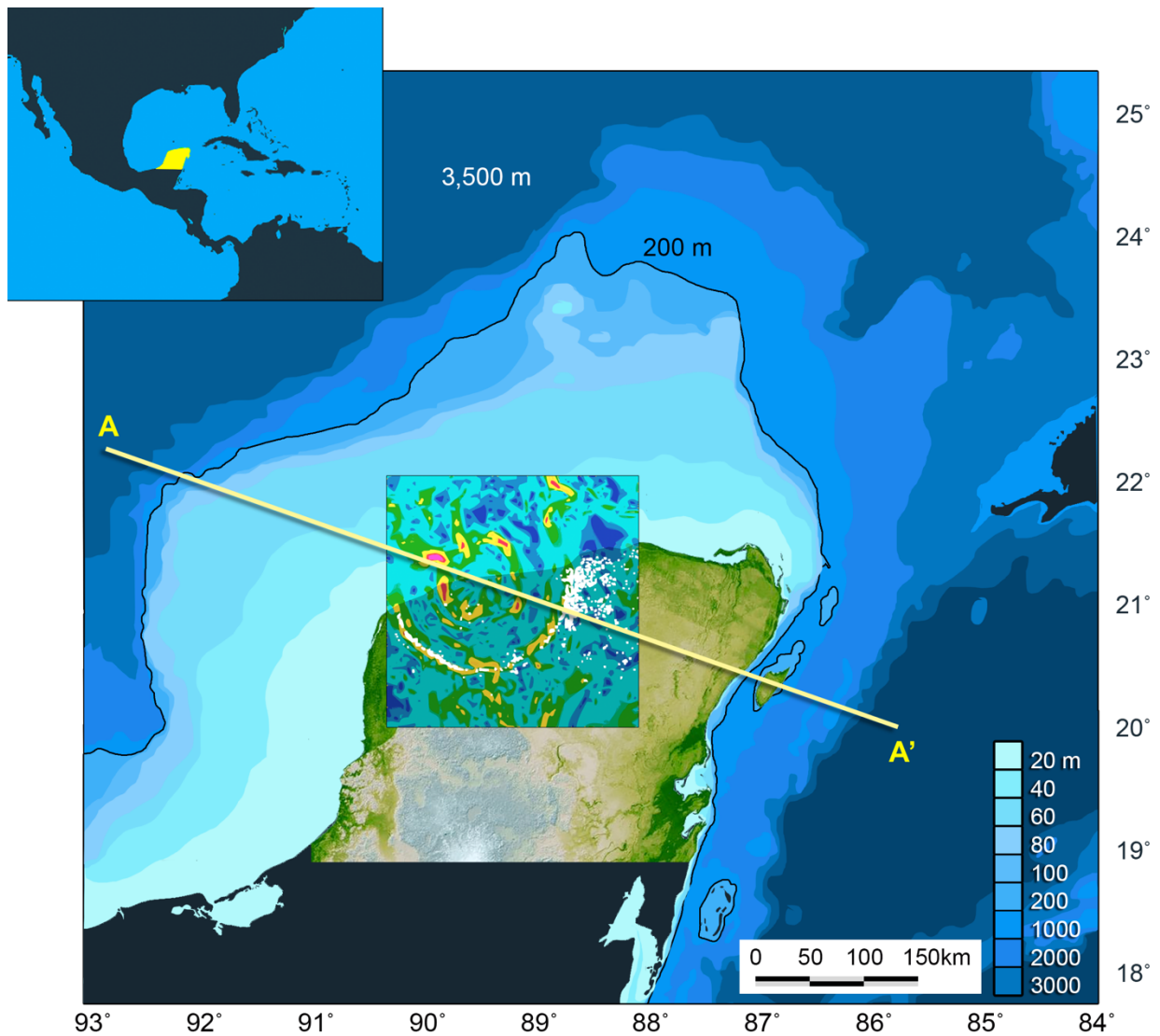


*Figure II-2 The Yucatán Platform relative to North and South America (upper inset) and between the Gulf of Mexico and the Western Caribbean (main panel). The 200 m isobaths delineate the platform, with the offset subaerial peninsula on the east margin. Bouguer gravity anomalies overlain on main Connors et al. (1996) show the multi-ring Chicxulub Impact Structure in the center of the platform, and cross cutting the northwest modern coastline. Transect line A–A' shows the cross section used in Figure II-3 and Figure II-5. Bathymetry redrawn from Dirección General de Oceanografía, Secretaría de Marina using data from Oregon State University YUCATAN '85. Overlay colored SRTM elevation model of the Yucatán Peninsula NASA/JPL (2000), overlain by cenote locations (white dots) showing only those considered to be part of the ROC from Hildebrand et al. (1995) and Connors et al. (1996).*

Evidence for the age and composition of the Yucatán crystalline basement rock comes from samples of impactites obtained from drilling projects (Nelson et al., 2012), and ejected impact event material found globally (Hildebrand et al., 1998; Kring et al., 2004; Sharpton et al., 1996; Urrutia Fucugauchi et al., 1996). The clasts found in the brecciated material show the basement rock to be granodiorite (Dressler et al., 2003), which is an igneous rock with essential quartz, plagioclase and alkali feldspar, and minor mafic minerals, which are typically hornblende and biotite. The zircon age of the recovered samples is  $546 \pm 5$  Ma (Keppie & Keppie, 2014).

The bulk porosity of the crystalline granodiorite basement rock is arguably low. The relative tectonic stability (See CHAPTER II) and lack of volcanic activity of the platform furthermore indicate limited pre-impact fracturing of the basement (Urrutia-Fucugauchi et al., 2011), however recent geophysical surveys map lineaments extending deep into the basement (Gulick et al., 2013).

We generalize bulk physical characteristics of the basement granodiorite (Figure II-3) with hydraulic conductivities of  $10^{-14}$ – $10^{-10}$  m/s for un-fractured and  $10^{-9}$ – $10^{-4}$  m/s for fractured rocks, permeability of  $10^{-16}$ – $10^{-13}$  cm<sup>2</sup> for un-fractured and  $10^{-11}$ – $10^{-8}$  cm<sup>2</sup> for fractured, porosity of 0–5% for dense rock and 0–10% for fractured crystalline rock, and thermal conductivity ranging over 2.3 – 2.8 Wm<sup>-1</sup>K<sup>-1</sup> (Eppelbaum et al., 2014). Corresponding values for carbonates are several orders of magnitude higher for conductivity, permeability, and porosity (Table II-1, lower section).

Table II-1 Physical properties of different rock types. Hydraulic conductivity values are from Domenico & Schwartz (1997) and thermal conductivity values from Eppelbaum et al. (2014).

Rock type	Hydraulic conductivity (m/s)	Permeability (m <sup>2</sup> )	Porosity (%)	Thermal conductivity (Wm <sup>-1</sup> K <sup>-1</sup> )
Un-fractured igneous and metamorphic rock	3×10 <sup>-14</sup> to 2×10 <sup>-10</sup>	10 <sup>-18</sup> to 10 <sup>-13</sup>	0–5	2.8
Fractured igneous and metamorphic rock	8×10 <sup>-9</sup> to 3×10 <sup>-4</sup>	10 <sup>-15</sup> to 10 <sup>-12</sup>	0–10	2.3
Karst and reef limestone	1×10 <sup>-6</sup> to 2×10 <sup>-2</sup>	10 <sup>-7</sup> to 10 <sup>-5</sup>	30–40	1.9
Dolomite, Limestone	1×10 <sup>-9</sup> to 6×10 <sup>-6</sup>	5×10 <sup>-15</sup>	15	2.1–2.2
Anhydrite	4×10 <sup>-13</sup> to 2×10 <sup>-8</sup>	10 <sup>-18</sup>	10–30	5.4
Water	---	---	---	0.6

### II-2.2.2 Mesozoic Pre-Impact – Upper Jurassic, Lower Cretaceous, and Upper Cretaceous

The granodiorite basement is overlain by thickly bedded carbonate marine facies that reach 3.7 km at the deepest point around the central crater (López-Ramos, 1975). Basal accretion began with Upper Jurassic deposits, only observed in deeper basin sections towards the Gulf of Mexico. This is overlain with 1.7 km thick Lower Cretaceous unit that is in direct contact with the granodiorite basement over most of the platform, then a 1 km thick Upper Cretaceous unit, which is then capped by 1-km thick Cenozoic Paleogene-Neogene-Quaternary units (Figure II-3). Cross correlation from cores show that the strata above the basement are laterally extensive, and of relatively even thickness (Figure II-3). The mineralogy of the platform is mostly limestone, dolomite, and so-called evaporites (Figure II-3; Ward et al., 1995). The cores outside the Chicxulub Impact Structure show a complex of Cretaceous anhydrite, dolomite, limestone, minor

conglomerate, lithic breccias, and several layers of oil-bearing shale (Kenkmann et al., 2004; Tuchscherer et al., 2006; Wittmann et al., 2004).

In the Lower Cretaceous from basement at ~3.5 up to ~1.6 km depth, the thick and massive dolomite and anhydrite deposits account for >90% of the cores and span the width of the platform (Figure 3). The anhydrite has been widely described as evaporitic (Perry et al., 1995, 2009; Rebolledo-Vieyra et al., 2000; Urrutia-Fucugauchi et al., 2008, 2011; Ward et al., 1995), but without enough detail to argue for this formation environment. The considerable thickness of *anhydrite* (CaSO<sub>4</sub>) of the impact target rock, is part of the argument for massive volatilization of SO<sub>2</sub> and hundreds of billions of tons of aerosol sulfuric acid, causing significant shifts in global climate-ocean states (Bardeen et al., 2017; Brett, 1992; Brugger et al., 2017; Pierazzo et al., 1998, 2003).

Through the Upper Cretaceous from ~2 km up to ~1 km depth, the bulk composition changes to dolomite accounting for ~20–50% of cores, with some minor anhydrite deposits, all intermixed with limestone (Figure II-3).

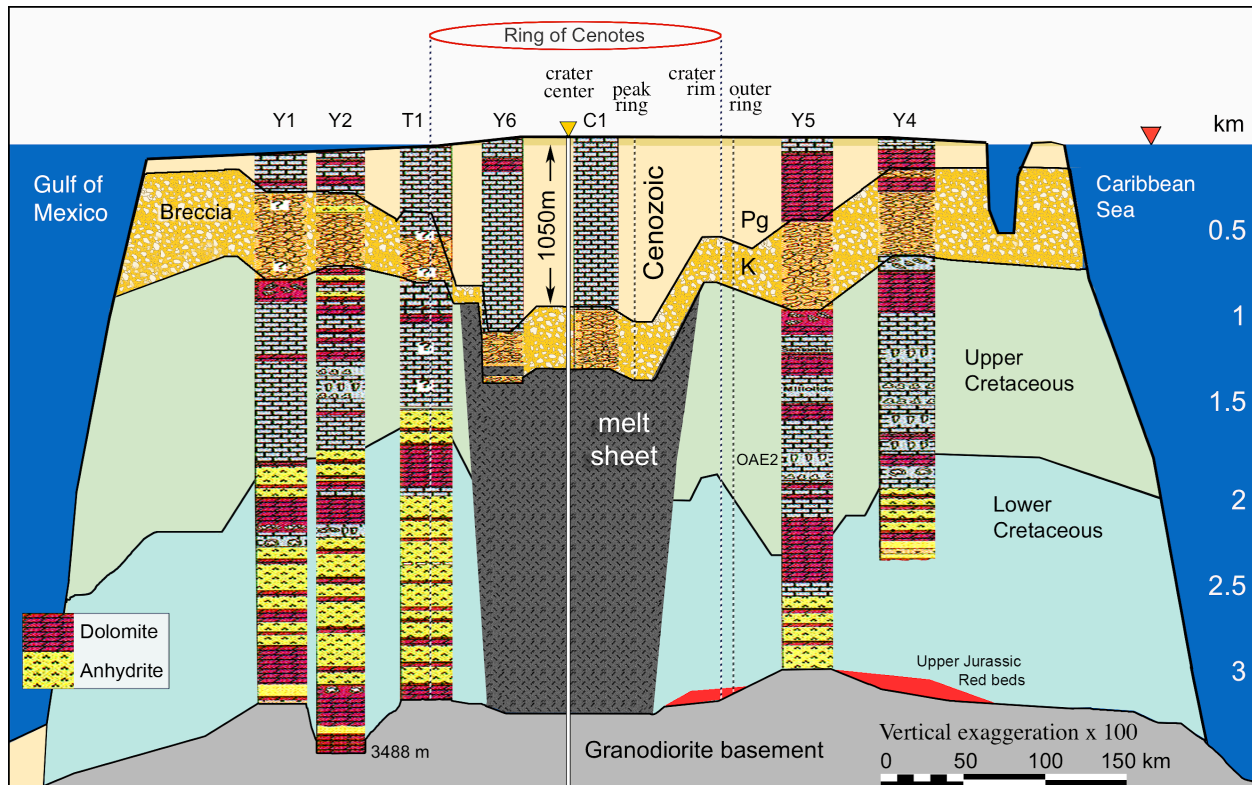


Figure II-3 Cross-section showing core correlation reflecting core logs from Ward et al. (1995): Yucatán 1, 2, 4, 5, and 6 (Y1, Y2, Y4, Y5, Y6); Chicxulub 1 (C1), near the center of the impact structure; and Ticul 1 (T1). Note the predominant anhydrite and dolomite in the Cretaceous beds overlying the granodiorite basement of the Yucatán Peninsula. Vertical exaggeration of  $\times 100$ .

### II-2.2.3 K-Pg Chicxulub Impact, Breccia Blanket, and Melt Plug

The Chicxulub meteorite impacted on the pre-existing submarine Lower and Upper Cretaceous deposits. The meteorite is currently understood as a large bolide of 10–12 km of diameter that impacted  $65.55 \pm 0.3$  Ma at the Cretaceous/Paleogene (K/Pg) boundary (Kring, 2007; Morgan et al., 1997; Urrutia-Fucugauchi et al., 2008). The impact energy is calculated to be  $5 \times 10^{23}$  J (Morgan et al., 1997), creating a crater of ~180 to 200 km (Kring, 1995; Morgan et al.,

1997). Significantly more than  $10^4$  km<sup>3</sup> of the crust was ejected from the crater (Kring & Durda, 2002; Schwenzer & Kring, 2013). Although the mantle was not melted or excavated, the rebound from the impact is argued to have temporarily uplifted the Moho by ~1 km beneath the crater (Christeson et al., 2001).

It is highly notable that, by circumstance, the impact location coincides with the platform geographic center (Figure II-2).

The ~0.5 km thick breccia ejecta blanket is deepest in the center of the platform at ~1.5 km below the surface, and grades shallower with the upper boundary being only ~0.3 km or less depth towards the platform perimeter (Figure II-3). The breccia consists of chaotically mixed rock fragments, with abundant sand- to gravel- sized, angular to sub-rounded fragments of dolostone, anhydrite, and lesser limestones that are suspended in a dolomicrite matrix (Parnell et al., 2010), and anhydrite fragments typically make up 15%–20% of the breccia in the form of tiny angular cleavage splinters (Ward et al., 1995). Secondary constituents of the breccia are fragments of melt rock and basement rock (Schuraytz et al., 1994). The Cretaceous mega-block breccia has high heterogeneity of all properties, particularly mineral composition, thermal conductivity, and density (Mayr et al., 2008).

The force and heat of impact combined with the uplifted crystalline basin created a central melt plug that now spans from 1.5 km depth below surface, down to the granodiorite basement (Figure II-3). The plug is suevitic and quasi-metallic, and arguably has low hydraulic permeability, but high thermal conductivity. It has been buried by breccia and the overlying Cenozoic carbonates.

#### **II-2.2.4 Cenozoic Post-Impact – Paleogene, Neogene, Quaternary**

The Chicxulub Sedimentary Basin is the collection of Cenozoic carbonate deposits with a maximum thickness of 1.1 km decreasing upward and outward the center.

Paleogene formations are much thicker inside the basin due to the depth of the impact breccia. Sequences include pelagic carbonates during the Paleocene and Eocene, Early Oligocene and filled during the Middle Miocene. Oldest formations mapped at the surface are Eocene epoch showing shallow-water marine facies, being more abundant outside the basin. Formation of replacive dolomite, dissolution, and precipitation of calcite cement have been more common outside the basin than inside (Lefticariu et al., 2006; Perry et al., 2002).

The Cenozoic carbonates above ~1 km depth retain high primary porosity (González-Herrera et al., 2002; Perry et al., 2002), and have permeability through structural features, and dissolution channels, presenting a classic “triple porosity” karst system (Worthington, 2007). The porosity and permeability of the deeper carbonates (>1 km) have not been reported.

The modern now subaerial surface includes classic off-lapping fringes of progressively younger sequences, from Paleocene-Eocene in the central peninsula, out to Quaternary-Holocene modern coastlines (Ward et al., 1995). The diagenetically immature carbonates lack allochthonous insoluble material particularly across the northern plain, leading to little insoluble residue after dissolution; acid digestion of samples from cores ~30 km inland on Mio-Pliocene rocks showed a silica-containing insoluble residue less than ~20% in weight (Gmitro, 1987).

### II-2.3 THERMAL ANOMALY & HYDROTHERMAL FLUX IN IMPACT STRUCTURES

The kinetic energy of hypervelocity bolide impactors is primarily converted into heat and mechanical energy (Sanford, 2005). In addition to the creation of the crater and the melt plug, the transfer of kinetic energy to the target creates long-lived thermal anomalies in shallow areas of the crust (Naumov, 2005; Osinski et al., 2013). The Chicxulub Impact Structure has a major positive heat flow anomaly persistent today of  $\sim 80 \text{ mW/m}^2$ , attributed to the combined effect of: 1) central uplift of the crystalline basement; 2) concentration of radioactive element due to impact below the impact structure; 3) local lower crust higher thermal conductivities (Espinosa-Cardena et al., 2016).

Active hydrothermal systems develop in impact structures associated with convective circulation of hydrothermal fluids and seawater (Osinski et al., 2013 and references therein). This circulation tied to the residual heat of impact occurs at any impact site where water is present in the target rock (Naumov, 2005). Hydrothermal flux can be found in a number of meteorite impact craters, ranging from large 200–250 km structures, such as the Sudbury (Ames et al., 2004), medium structures such as the Ries at 24 km diameter (Arp et al., 2013), to smaller craters such as the 1.8 km diameter Lonar crater (Hagerty & Newsom, 2003). Evidence is derived from mineral veins, altered impactites, and altered post-impact sediments (Escobar-Sanchez & Urrutia-Fucugauchi, 2010; Osinski, 2005; Osinski et al., 2013; Velasco-Villareal et al., 2011; Zürcher & Kring, 2004). Additionally, mantle deformation in the central uplift of deep crater structures causes vertical transport of deeper rocks (Christeson et al., 2009), thus bringing heat to the near surface.

## II-2.4 MULTIPLE SETS OF RING FAULTS

Gulick et al. (2008) reported sets of semi-continuous, arcuate ring faults and a topographic peak ring (PR) in the impact structure. To the east and northeast around the crater structure, they describe them as concentric listric faults at distances up to 130 km from the crater center. They group the ring faults in three series, each in turn associated with the inner-ring, peak ring and outer ring of the buried impact structure (and not referring to the surficial expression of the ROC). These fractures penetrate the crater structure and extend down to the granodiorite basement under the carbonate platform (Collins et al., 2008; Gulick et al., 2008, 2013). However, it is not clear if the deep-reaching concentric fractures also extend fully upwards through the whole succession of post-impact Cenozoic carbonates. It is possible that any movement along the deeper faults would have propagated fractures upwards into the overlying carbonate beds at some point in geological time after the impact.

## II-2.5 SEA LEVEL HISTORY

From the Cretaceous until the Pleistocene, numerous marine transgressions submerged the Yucatán Platform under warm tropical waters. During this time, limestone strata were formed with the remains of ancient coral reefs and seashells, including the uppermost Miocene-Pliocene (23 Ma – 2.5 Ma) Carrillo Puerto Formation, a 15-meter thick deposit of almost pure calcium carbonate that hosts the shallow portions of present-day karst systems (Lesser & Weidie, 1988)

The evolution of the platform can be neatly divided into nearly persistent submarine conditions pre-10 Ma, and with cycling through subaerial and submarine phases post-10 Ma. All diagenesis including shallow karstification tied to the influence of a meteoric freshwater lens is therefore only possible post-10 Ma and recurrently dominating in the last 2 Myr.

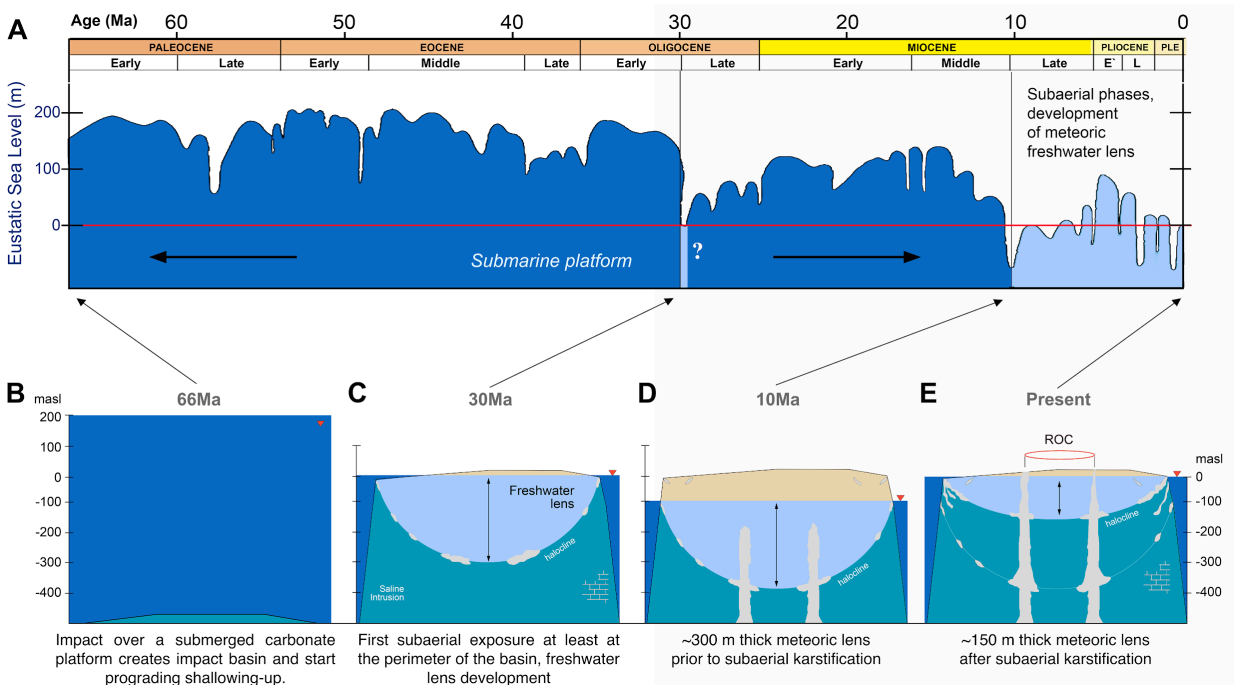


**Figure II-4** A) Global sea level data from the K-Pg to present from Haq et al. (1988). Regular subaerial exposure of the Yucatán Platform and development of a meteoric lens was only possible from 10 Ma onwards; B) Prior to the K-Pg, the platform elevation was at  $\sim$ -500 mbs; C) Post-10 Ma, subaerial exposure and development of a thick freshwater lens. Fresh-saline mixing corrosion along the base of the lens leads to karstification; D) Upwards stoping of the hypogene deep seated dissolution voids formed around the low-permeability and high thermal conductivity melt plug (below lower boundary of cartoon); E) Stacked levels of karstification tied to sea level, with many of the deep hypogene voids stope upwards, breaching the surface to create pit cenotes along the perimeter of the ROC. The overall increase in permeability thins the freshwater lens.

### II-3 GEOTHERMAL CONVECTIVE CIRCULATION

Geothermal heat creates a density contrast between cold seawater and warmed fluids within the platform, driving density-controlled convective circulation of saline groundwater through permeable carbonate platforms (Hughes et al., 2007; Kohout, 1960, 1965; Sanford et al., 1998; Wilson et al., 2001). Geothermal heating from the crystalline basement up into prograded high-permeability carbonate sequences provides a textbook environment for high upward flux at the

central maximum thermal gradient, which is broadly at the center of the Yucatán Platform (Figure II-5A). In simple square-sided submarine platforms including the Yucatán, the maximum upward discharge across the submarine top boundary is in the center over the maximum geothermal gradient. Influx of marine waters occurs on the margins. The density-controlled convective fluxes are independent of relative sea level, and thus expected to operate in all submarine permeable carbonate platforms (Hughes et al., 2007; Wilson et al., 2001).

With emergence of the platform and development of a meteoric lens, the bank-top discharge is impeded, and saline discharge is redirected to the platform margins at some depth below the meteoric lens. The shallowest saline water 1-5 m below the present meteoric lens, sampled in the diver-accessible conduits along the mid-section of the Caribbean coast, show warmer waters adjacent to and matching the Caribbean surface water temperatures at coastal sites, and decreasing with distance inland. The shallowest saline water at least in the conduits is decoupled and not entrained by flow and mixing with meteoric waters (Beddows et al., 2007). Deep temperature profiles to 400 m depth in Yaxcopoil-1 demonstrate robust geothermal gradient persists in the middle of the platform, indicating Kohout style circulation (Šafanda et al., 2009), even though it does not extend to the base of the meteoric lens (Beddows et al., 2007).

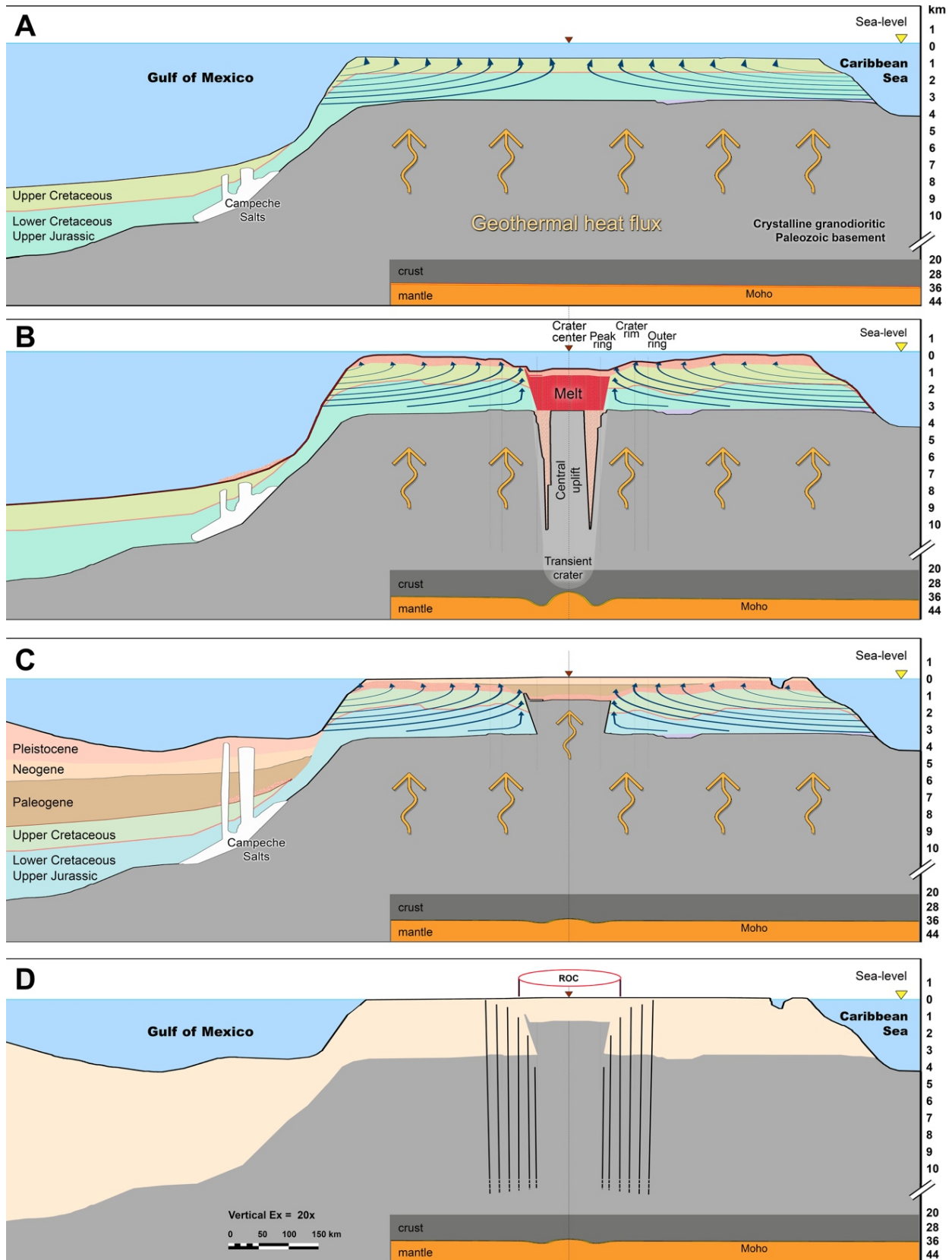


*Figure II-5* General geology and hydrogeology cross-sections of the Yucatán Platform based on the published literature on drill core and geophysical surveys undertaken by Pemex, UNAM, and IODP/ICDP from Ward et al. (1995). Deep crustal interpretation is from Christeson et al. (2009).

*A. Pre-Impact* Geothermal heat flux from the granodiorite basement into the overlying carbonate strata establishes platform-scale circulation drawing marine water in from the margins and exiting through the submarine platform top.

*B. Post-Impact* A deeply penetrating crystalline melt plug with high thermal conductivity and low permeability is created by the impact near the geometric north center of the platform.

*C. Present:* The now sub-aerial platform includes peripheral sets of fractures around the now deeply buried melt plug, which provide preferential vertical flow paths. Specifically, the one fracture that aligns with the perimeter of the melt plug is overlain by the ROC.

*D.* Fracture sets from (Gulick et al., 2013).

### II-3.1 DIAGENESIS: EARLY BURIAL DOLOMITIZATION AND COUPLED ANHYDRITIZATION

Carbonate diagenesis includes reactive mineralization and chemical compaction (Milliken, 2014). In addition to anhydrite deposition in evaporitic environments (Twenhofel, 1950), in carbonate platforms subject to the flux of near-normal marine water, early burial replacement dolomitization and coupled anhydritization are important diagenetic processes along geothermal convective circulation flow-paths (Babel & Schreiber, 2014; Kendall & Walters, 1978; Warren, 2016). Massive dolomites commonly form during early burial, sourcing magnesium from near-normal seawater (Land, 1985). Reactive transport models (RTM) show that dolomitization initially occurs as kinetic limitation are overcome with near-marine  $Mg^{2+}$  concentration waters on the flank margins exposed to geothermally elevated temperatures. Dolomitization releases calcium into solution, resulting in down-flow precipitation of anhydrite cement where temperatures exceed 50 °C (Wilson et al., 2001), which further depletes sulfate and elevates  $Mg^{2+}/Ca^{2+}$  ratios, driving

further burial dolomitization (Al-Helal et al., 2012). According to coupled hydrological-geochemical models, dolomitization is likely limited by large-scale mass transport where high enough temperatures occur and not by kinetic rates, and, anhydrite precipitation should accompany dolomitization where adequate sulfate is available (Al-Helal et al., 2012; Whitaker & Xiao, 2010; Wilson et al., 2001).

The coupled dolomitization-anhydritization diagenesis has hydrogeological implications due to the alteration of bulk porosity and permeability. Dolomitization creates up to 8–10% of vuggy porosity due to the mole-for-mole replacement of the smaller  $Mg^{2+}$  for  $Ca^{2+}$  ions (Machel, 2004), however some porosity is then occluded by the precipitation of anhydrite cement (Al-Helal et al., 2012; Kendall & Walters, 1978). The interplay between porosity generation by dolomitization and porosity occlusion by anhydrite cementation influences subsequent fluid flow and diagenesis in the further development of the platform.

The prevalence and distribution of dolomite and anhydrite in Lower and Upper Cretaceous strata pre-dating the Chicxulub impact (Figure II-2) reflects the diagenetic cascade of *early burial dolomitization* and coupled *anhydritization*, and in particular the exceptional deposits in the earlier strata overlying the basement rock where geothermal heating drives circulation of magnesium ( $Mg^{2+}$ ) and sulfate ( $SO_4^{2-}$ ) ion-rich marine water (Figure II-5).

The cores T1, Y2, and Y1 located in the platform center have lower occurrence of dolomite and anhydrite compared to the more platform peripheral cores Y5 and Y4, which have a much higher proportion of dolomite exceeding 75% above 1,600 m. Furthermore, depth-gradients are also present. The Upper Cretaceous includes a lower occurrence of dolomite and much lesser amounts of anhydrite, in a pattern consistent with younger strata being less diagenetically evolved.

There is a higher prevalence of dolomite on the eastern side of the platform in both the Upper Cretaceous as well as the post-impact Cenozoic, accounting for more than 75% of the cores Y4 and Y5 above 1600 m (Figure II-3). This distribution indicates greater dominance of east-to-west cross platform flow, with greater influx of Caribbean marine waters at least in the Upper Cretaceous and Cenozoic.

### **II-3.1.1 Burial anhydrite: Refutation of Evaporite Origin**

The anhydrite/gypsum salts in the Yucatán cores are commonly referred to as “*evaporites*” (Hildebrand et al., 1998; López-Ramos, 1975; Pope et al., 1993; Rebolledo-Vieyra et al., 2000; Sharpton et al., 1996; W. Stinnesbeck et al., 2004; Ward et al., 1995), and yet the submarine history of the platform through to ~10 Ma, combined with the depth and east-west co-placement of anhydrite and dolomite argue against a true shallow water evaporitic origin of the extensive anhydrite deposits. Most recovered dolomite samples have negative  $\delta^{18}\text{O}$  and positive  $\delta^{13}\text{C}$  indicating that replacement dolomitization involved a high geothermal gradient (Lefticariu et al., 2006; Perry et al., 2009). These isotopic values may also result from the presence of a fluid dominated by meteoric circulation, however the submarine state of the platform through to the Oligocene refutes that process happening during that stage. In the least, the Yucatan anhydrites might be considered “secondary evaporites” (per the nomenclature of Machel, 2004; Schreiber & El Tabakh, 2000) as their primary genesis is unlikely shallow marine evaporation, and they have likely undergone burial-related diagenetic processes.

### **II-3.2 HYPOGENE KARSTIFICATION DURING SUBMARINE STAGE**

The geological history of the Yucatán Peninsula can be separated in pre-10 Ma when it was under a full submarine regime and when geothermal gradients lead to the establishment of

platform-scale circulation patterns. The Yucatán Platform was fully submarine prior to the Chicxulub impact and through to 30 Ma at the earliest. The geothermal gradient radiating up from the crystalline basement into the porous overlying carbonates drives circulation of marine waters through the platform with the greatest heating occurring at the center of the platform, and waters rising upwards to exit across the submerged surface. Because the submarine regime we would expect to find no desiccation cracks and other features indicative of subaerial exposure as the case of well indurated epikarst bedrock layers known as caliche at this stage in the carbonate parasequences reported for the area.

Cave formation by deep-seated groundwater is recognized as a common process of subsurface water–rock interaction. The formation of solution-enlarged permeability structures by waters ascending to a cave-forming zone from below, is called *hypogene speleogenesis*, where deeper groundwater in regional or intermediate flow systems interact with shallower and more local groundwater flow systems where a number of dissolution mechanisms can operate either in combination or sequentially (Klimchouk & Ford, 2009; Palmer, 2011) This is in contrast to more familiar epigene speleogenesis, which is dominated by shallow groundwater systems receiving recharge from the overlying or immediately adjacent surface.

Hypogene speleogenesis creates solution porosity which distribution and patterns, in area and cross-section, are quite distinct from porosity created by epigene speleogenesis. Hypogene caves are identified in various geological and tectonic settings, and in various lithologies (Djidi et al., 2008; Forti et al., 2002; Palmer, 2011; Spötl et al., 2016; Tisato et al., 2012).

The karstification of hypogene systems commonly involves upwards flows, but always a geological drive to the circulation that is decoupled from the climate and meteoric waters. Most

hypogene systems are disconnected from the surface at least during early development (Sendra et al., 2014). In these systems, several processes contribute to the creation of porosity, including retrograde calcite solubility, mixing corrosion induced by cross-formational flow, and dissolution by deep-sourced geogenic acids, which enhances limestone dissolution (Goldscheider et al., 2010). For instance, collapse dolines with hypogene speleogenesis caused by geogenic CO<sub>2</sub> are reported for *Sistema Zacatón* in Mexico caused by volcanogenic CO<sub>2</sub> (Gary & Sharp, 2006), and the *obruks* in Turkey, involving the upward migration of deep-seated CO<sub>2</sub> attributed to asthenosphere rise (Bayari et al., 2009). Furthermore, other geogenic acids can cause karstification such as H<sub>2</sub>S resulted from microbial or thermal reduction of sulfates (Hill, 1990).

During the submarine stage, deep hypogene voids may have formed by chemical and thermal density differences producing upward-pointed dissolution (Klimchouk, 2009) acting on both the deep dolomite and anhydrite facies from early burial processes.

### II-3.3 EPIGENE KARSTIFICATION DURING SUBAERIAL REGIME

It is only < 10 Ma that extended periods of subaerial exposure of the Yucatán Platform was possible based on the global sea level curve (Haq et al., 1988), and consequently the earliest time horizon when a meteoric lens would have formed on the now exposed peninsula. The saline circulation driven by the geothermal gradients first, and then combined with the superimposed additional drive for circulation from the heat of impact would persist and be particularly focused around the vertical wall perimeter of the melt plug. Due to the impermeable nature of the melt plug, the groundwater circulation directly over this now buried surface would be limited.

Epigene karstification is the process of organized porosity generation leading to orders of magnitude of permeability increase at the aquifer scale (Ford & Williams, 2007). Under-saturated meteoric waters may drive dissolution of the carbonates in subaerial aquifer systems and mixing corrosion can generate in-situ under-saturated water within the aquifer itself. In coastal aquifers, mixing corrosion along the fresh-saline interface is recognized as contributing dissolution potential. Groundwater circulation is a necessary component of karstification as it removes the dissolution products, allowing for further void development.

The maximum depth of epigene karstification occurring along the meteoric-saline interface would be no more than 350 m below modern sea level (SL; see Figure II-4). Global sea level ranged down to -150 m below modern SL. The current base of the fresh-water lens in the middle of the peninsula is ~100 m below SL. However, in the early time of freshwater lens, the platform scale permeability would be lower prior to the development of horizontally extensive conduit networks that add significantly to the overall permeability. Thus, the freshwater lens may have been double, or ~200 m thick, in the early time of subaerial exposure.

A geochemical consequence of the geothermal heated circulation is dolomitization by  $Mg^{2+}$  replacement with the circulation of near-normal seawater and subsequent coupled anhydritization. This significant diagenetic alteration is observed in the prevalence of dolomite and anhydrite across the platform in cores >1,600 m depth. The dolomitization reduces bulk volume of the carbonates due to the tighter crystalline mineral structure, leading to greater porosity up to 13% with mole-to-mole replacement (Land, 1985). However, anhydritization occludes pore spaces thus limiting increases in porosity and/or permeability. The cores provide clear evidence for massive coupled dolomitization-anhydritization diagenetic alteration due to the geothermal driven platform scale circulation, but the extent of permeability increase – e.g., karstification – at this stage pre-impact is not presently determinable.

The Chicxulub impact occurred near the geographical center of the Yucatán Platform (Figure II-3), and therefore superimposed on top of the center of the pre-existing geothermal driven circulation patterns. Even once marine carbonate sedimentation resumed no later than early Paleocene, the centroid of the platform circulation remained in the same geographical region. The creation of the impact melt plug with high thermal conductivity will effectively bring the geothermal gradient upwards in elevation within the platform, and also in magnitude of  $W/m^2$  flux. Furthermore, the massive heat of impact will be centered in the same location. The radial fracturing around the impact site, and the radial distribution of thick and disorganized massive breccia block deposits, provides for increased permeability. Thus, despite the massive physical interruption of the impact, the net hydrogeological result of the Chicxulub impact is to reinforce the geographical pattern of platform scale circulation of marine waters through the still submarine platform, with inflows deeper along the margins, and rising waters exiting the center of the platform.

Post-impact in the still-submarine platform, the ongoing circulation continues to drive dolomitization and anhydritization, with now also greater circulation along radial fracture patterns. Any movement of mega-blocks surrounding the impact site furthermore provide for deep-seated mechanical generation of extensional faults that form concentric rings (Gulick et al., 2013) surrounding the crater center (ring faults) and fissures up through the overlying marine carbonates. Post-impact, the vertical permeability through the platform is arguably greatly increased, and specifically organized through mechanical fractures around the perimeter of the uplifted crystalline melt *plug*.

#### **II-4 HYPOGENE HYDROGEO THERMAL MODEL FOR GENESIS OF THE RING OF CENOTES**

The ROC may have formed by dissolution associated with *geothermal-driven vertical deep-water circulation* around the crater structure and channelized through the adjacent fractures, at least for those fractures not obstructed by the meteorite remnants. The strongest vertical components of geothermal circulation, around the crater structure at the center of the platform, fed the concentric fractures close to the structure and dissolution was spatially enhanced there. Also, this process circulates deep water close to shallower areas in localized regions around the crater, those overlying the concentric fracture groups reported. These *deep fluids bring cations and anions to the surface*, in ratios not commonly found in the shallow groundwater in inland areas, promoting diagenetic, dissolution and precipitation processes. Also, recrystallization can occlude fractures, passages, conduits or voids as seen in other hydrothermal systems.

If there is a strong vertical component at the center of the platform, and if it has been enhanced through vertical concentric fractures, it is possible to postulate that this ion rich,

principally in  $\text{Ca}^{2+}$  and  $\text{Mg}^{2+}$  in different ratios from its marine origin, circulation, channeling towards the top will promote localized dissolution around the buried crater structure.

The argumentation for the proposed mechanism goes as follows:

1. At the center of the Yucatan Platform, there is a *strong vertical component* of geothermal convective flow that pre-dates the impact.
2. The meteoritic metallic "*plug*" is located near the middle of the platform, resting over impact-uplifted deep strata. It is suevitic, quasi-metallic, low hydraulic permeability, and high thermal conductivity. The melt plug has been buried by deposition of Cenozoic carbonates to a modern depth of  $\sim 1$  km.
3. There are at least *three concentric fracture sets* called *ring faults* (Gulick et al., 2008, 2013) surrounding the impact structure, classified as inner-faults, peak ring-faults and outer ring-faults or fracture sets.
4. Post-impact, *the maximum vertical flow will be* through the peak ring-faults close to the center of the structure and overlying the edge of the low permeability melt plug.
5. *Hydrogeothermal convective circulation* continues in submarine post-impact carbonate sequences, leading to focused dissolution at depth at the halocline, initiated along the edges of the now buried crater structure.
6. With subaerial exposure only post-10 Ma, the shallow *karstification along base of thick meteoric lens effectively expands voids*, with many stopping upwards, with some, but not all breaching the surface to create pit cenotes.
7. Independent of the deep dissolution, *extensive shallow horizontal discharge channels* have formed along the coast.

## II-5 DISCUSSION

At least one group of fractures (*ring faults*) reported by Gulick et al. (2013) coincide on a geographical projection with the surficial expression of a condensed belt of vertically developed collapsed karstic sinkholes, called the ROC. These fractures could have provided deep-fluids circulation path vertically upward the surface needed for the diagenetic, post-depositional processes observed in the geological cores (Ward et al., 1995) and to promote hypogene excavation of the cylindrical, dome-intact, deep shaft voids observed at surface along the ROC.

This deep fluid vertical circulation might also explain the high concentration (relative to Caribbean seawater) of ions such as soluble reactive silica (measured as soluble reactive silicon, SRSi by Hernández-Terrones et al., 2011) in groundwater from the shallow aquifer in groundwater in the oriental coast of the Peninsula. Following this model, excess Si in the shallow groundwater points to a convective circulation with strong vertical components geochemically linking either the granodiorite basement rock to the surface, or by contact with the remnant meteoritic material on top of the buried impact structure, from which some ions are dissolved and carried away by the geothermal circulation fluids upwards near the center and spreading out at the surface of the platform, in the spatial patterns suggested by RTM models on carbonate shelves and islands (Whitaker & Xiao, 2010).

In a distributed sampling of 350+ near surface rocks, the bulk composition determined by ICP-OES showed maximum Si –measured as soluble reactive silicon (SRSi)– concentration of 131.3  $\mu\text{mol SRSi/g}$  with an average value of 22.5  $\mu\text{mol SRSi/g}$  of rock. Also, there is low biogenic marine stock of Si around 2 mM (Hernández-Terrones et al., 2011). Thus, the SRSi of the younger rock formations indicates that the primary SRSi concentration from diatoms in these shallow

marine carbonates is low. The geothermally driven circulation might have carried upwards deep-seated SRSi from metamorphic materials buried or transported near to the surface by the impact, and once mixed with meteoric waters, discharging to the ocean through epigenetic karst conduits and passages.

Why is there one pronounced *Ring of Cenotes*, and not a series of rings following the zonal pattern of reported platform-scale internal fractures? Inner rings are obstructed by meteorite material remnants. Maybe outer "rings" are just faded out. Maybe at far distance from the center the geothermal flow is insignificant and there is no strong flow enough of deep fluids to drive reactions. In this model, "central ring fractures" correspondent to those *ring faults* are preferred (*available; i.e. not obstructed*) proposed for upward vertical deep-fluids circulation to reach close to the surface.

The earliest potential full subaerial exposure of the platform (Figure II-4; Table II-2) occurred during the marine regression in the Oligocene, at the least the northern part some ~30 Ma, and documented (Perry et al., 1995) only post-10 Ma, occurring in two phases during the Miocene (see Figure II-5) as a semicircular embayment remained inside the crater until at least the Pliocene (Pope et al., 1996). Halocline depth at the time of first subaerial exposure was estimated using the equations from *Dupuit-Ghyben-Herzberg*, based on a combination of the continuity equation and Darcy's Law with the *Ghyben-Herzberg* Principle and the *Dupuit* assumptions of horizontal flow (Myroie & Myroie, 2007). Also, (Beddows et al., 2007) mapped the average halocline depth along a horizontal transect from the oriental coast of the Peninsula going inland to the center of the platform and reaching 150 m of maximum depth.

Table II-2 *Yucatán Platform hydrogeological regimes pre- and post- Chicxulub impact.*

	<i>PRE-IMPACT Mesozoic</i>		<i>POST-IMPACT Cenozoic</i>	
	Submarine		Subaerial	
<b>Geologic Time</b>	> 65.5 Ma Upper Jurassic – Cretaceous		65.5 – 10 Ma Paleogene	
<b>Predominant platform-scale flow regime</b>	Geothermal convective		Geothermal convective + Heat of Impact	
<b>Predominant process</b>	Accretion / Early burial dolomitization and anhydritization		Erosion / Karstification	
<b>Predominant karstification type</b>	Hypogene		Hypogene + Epigene	
<b>Surface processes</b>	No exposed surface		Development of low-permeability subaerial surfaces (caliche); stratigraphic sequence boundary.	
<b>Void formation</b>	Bottom-up (hypogene)		Top-down (epigene) (water table + halocline)	
<b>Cenotes (sinkholes)</b>	Incipient hypogene voids		Stopping upwards with occasional breaching of the surface Pit cenotes.  Shallow cave systems and collapse cenotes. Intersection between shallow + pit formation	

At the center of the Peninsula the halocline reaches its maximum depth, conservatively estimated around ~300 m prior to subaerial karstification. After subaerial karstification along the base of thick meteoric lens effectively expands voids, with many stepping upwards, breaching the surface to create pit cenotes. Halocline depth at this stage was estimated at ~150 km deep as freshwater-saline interface depth decreases because the thickness of the freshwater lens decreases, according to the equations. Also, shallow horizontal water discharge channels formed. Extensive underground systems were carved through the carbonate rock by subaerial karstification processes,

effectively connected inland groundwater reservoirs with coastal discharge systems where marine-groundwater exchange takes place.

It is postulated that such horizontal circulation pattern exists beneath the subaerial semi-circular feature that we see as the ROC on the modern surface, and allows groundwater to circulate through this path either north to the Gulf of Mexico (*Bocas de Dzilám*) or west towards the lagoon of *Celestún* (Escolero et al., 2002; Steinich et al., 1996; Young et al., 2008), arguing for a very large groundwater connectivity along the ROC at least in the exposed portion over the platform.

Despite the lack of direct evidence for this platform-scale deep circulation pattern, the collected observations support the genesis of the ROC as being principally driven by hydrogeothermal hypogene circulation patterns leading to geospatially concentrated karstification:

- Geological cores (Ward et al., 1995) show extended areas of deep dolomite and anhydrite (called evaporite in that work) that are a possible product of early burial dolomitization and anhydritization.
- Dolomite core-samples ranging from surface to 540 m deep from inside the Cenozoic basin are very different from that outside the Chicxulub Sedimentary Basin (Lefticariu et al., 2006). Freshwater diagenesis has been extensive especially outside and at the edge of the ring basin and replacive dolomite most common outside the Basin than inside. Due to its negative  $\delta^{18}\text{O}/\delta^{16}\text{O}$  and positive  $\delta^{13}\text{C}/\delta^{12}\text{C}$  isotopic values, they suggested that dolomitization involved the presence of a fluid dominated by freshwater and/or an anomalously high geothermal gradient.

- High concentration of SRSi in groundwater in the area, extended to the whole northern Yucatán Peninsula as different research reported (Hernández-Terrones et al., 2011) provided diatom-sourced SRSi is quantitatively smaller, may be also indicative of deep-seated SRSi brought to surface by vertical geothermal circulation.
- Platform scale Reactive Transport Models (RTM) show unequivocal patterns of marine water intrusion, geothermal circulation arrows, and spatially distributed diagenetic products over the carbonate platform (Whitaker & Xiao, 2010). Near-surface meteoric circulation may be influenced locally in part by these deep-seated features, but is likely decoupled as has been demonstrated for the decoupling of the modern shallow fresh and saline circulations (Beddows et al., 2007).
- A valuable test of this conceptual model for the ROC based on hypogene geothermal convective circulation would involve close examination of the anhydrite pre- and post-impact in available cores, including examination of more recent drilling campaigns. Microscopic examination should effectively indicate the formation environment as truly evaporitic in origin, or the identification of diagenetic processes, such as early burial anhydritization, by identifying size and geometry of possible mega-nodules (Ortí et al., 2012) or by mineral characterization of replacive anhydrite spar (Warren, 2016; after Kendall & Walters, 1978), and by examination of distribution of euhedral, subhedral, anhedral or vug microfabrics (Machel, 2004) with depth.
- This hypogene model provides a plausible explanation for the formation of the Chicxulub ROC in the northern Yucatán Peninsula, Mexico. It provides a mechanism including both a hypogene component and epigene karstification processes.

## II-6 CONCLUSIONS

The submarine Yucatán Carbonate platform was impacted by a ~10 km diameter bolide at the K/Pg boundary ~66 million years ago. The impact created a central basin, with a low permeability and higher thermal conductivity melt plug reaching down to the granodiorite basement. Subsequent deposition resulted in overlain carbonates sequences, with the submarine platform only having significant periods of subaerial exposure post-10 Ma, when a meteoric fresh-water lens developed.

Geophysics has revealed multiple closely spaced concentric sets of slump block faults and more deeply penetrating peripheral sets of ring faults. A single set of these ring-faults at ~85 km from the impact center has striking surface expression with a dense concentric ring of vertically developed dissolution sinkholes, forming the ROC.

The vertical flux in the center is inhibited by the low permeability melt plug and breccia, while vertical flux and thus deep-seated dissolution karstification around the perimeter of the impact fill is enhanced by the presence of the first deeply penetrating ring fault, which furthermore focuses the geothermally driven circulation in this first “open” pathway.

Deep seated mixing-zone dissolution hypogene karstification beginning in the late Miocene at the base of the meteoric lens may extend to ~350 m depth, tied to low sea level stands and a thicker meteoric lens in the as-yet un-karstified platform. Progressively shallower karstification from the Late Miocene to present is tied to a thinning meteoric lens as bulk platform permeability increases with the development of coastal conduit drainage networks.

While there are a great number of pit cenotes/blue holes globally in massive carbonate platforms, the interplay of the Chicxulub impact and the first ring fault line of the multiple fracture sets, provided hypogene karstification tied to sea level could explain the development of such a dense and spatially organized concentration for the ROC.

### **III        On the Tectonic Stability of the Yucatán Block:              Tilt and Rotation**

#### **ABSTRACT**

Sea level reconstruction requires sites with well-constrained tectonic histories. The Yucatán Block (YB) is understood to be tectonically stable, with some subsidence since the Eocene. Using geodetic data from UNAVCO (DAI v2) stations with 5+ year records, we show the present day YB motion is in NW direction and counterclockwise rotation, along with subsidence rates of  $1 \text{ mm yr}^{-1}$  on the N and NE peninsula coastlines. We argue for persistence of the measured vertical motions from the mid-Holocene to present, based on coastal geomorphology, ecology, and archeological observations. The present vertical rates are 3-orders of magnitude faster than the previously indicated subsidence since mid/late Eocene. The YB is tectonically rigid in the strict sense, without apparent deformation, yet block tilting and rotation is of broad significance in interpretation of the karst hydrogeology, paleoenvironmental records, and coastal adaptation to sea level rise.

### **III-1 INTRODUCTION**

The Yucatán Block (YB) is a 450,000 km<sup>2</sup> continental microplate, covering southeast Mexico, northern Guatemala, and Belize. It has been a structural entity since at least 230 Ma (Steiner, 2005). In the late Middle Jurassic time (~165 Ma), the initial seafloor spreading in the Gulf of Mexico (Martini & Ortega-Gutiérrez, 2018) combined with intra-continental extension in western equatorial Pangea, followed by a two-step counter-clockwise rotation of the YB to its present position (Bird et al., 2005). The subaerial carbonate Yucatán Peninsula (YP) on the YB has been broadly understood to be tectonically stable, and volcanically inactive (Kambesis & Coke, 2013; Szabo et al., 1978; Urrutia-Fucugauchi et al., 2011; Zúñiga et al., 2000), and glacio-hydro-isostatic stability (Potter & Lambeck, 2004), but postulated to have some subsidence since the Early/Middle Eocene (Kinsland et al., 2000). The northern YP is presently an expansive shallow marine bank and a textbook example of modern marine carbonate factory, experiencing undoubtedly substantial but presently unquantified mass loading by carbonate deposition.

#### **III-1.1 TECTONIC SETTING AND FEATURES OF THE YUCATAN PLATFORM AND PENINSULA**

The Yucatán Platform extends to the borderland of the western Caribbean Yucatán Basin (López-Ramos, 1975; Rosencrantz, 1990; Ward et al., 1995), and the eastern flank includes notable expressions of bank marginal tectonic and structural features.

Cozumel Island and Cozumel Channel are on the southern end of a horst of the block-faulted continental margin, which extends NE to the submerged Arrowsmith Bank (Lesser & Weidie, 1988). Movement along these normal faults likely began in the Cretaceous, continuing through most of the Paleogene (Dillon & Vedder, 1973). This complex of horst and graben-basin

province may be a faulted margin related to *sphenochasmic* rifting of the Yucatán Peninsula out of the present site (Donnelly et al., 2015), or a left-lateral transform margin of probable Late Cretaceous-Paleogene age between western Cuba and Guatemala-Honduras, or a fault block margin associated with Paleogene subsidence of the Yucatán Basin (Case & Holcombe, 1980). Comparison of upper Pleistocene facies on the Yucatan Peninsula and adjacent Cozumel Island 17 km east off the Caribbean shore indicates that there has been no differential movement of these two areas during the late Quaternary (Spaw, 1977; Ward, 1997).

The Chicxulub meteorite ~66 Ma impacted the already accreting carbonate platform, penetrating to the basement rocks of the crust (Camargo-Zanoguera & Suárez, 1994; Hildebrand et al., 1995; Kring, 2007; Kring & Durda, 2002; Morgan et al., 1997; Pilkington & Grieve, 1992). Pilkington The offshore segments of the impact ring faults correlate with an onshore arc of large diameter sinkholes, forming the Ring of Cenotes (Pope et al., 1996). Most of the faults show no motion during the Cenozoic (Gulick et al., 2008). The lack of apparent motion during the Cenozoic indicates no large-scale ongoing expansion / relaxation, no evidence of compression, although block slippage along the ring faults has been broadly indicated (Gulick et al., 2008, 2013; Schulte et al., 2010; Urrutia-Fucugauchi et al., 2011). The Yucatán Basin has expanded eastward through the Late Paleocene to Middle Eocene due to Caribbean plate movements (Rosencrantz, 1990), by crustal relaxation, and/or basin loading following the Cretaceous–Paleogene (K/Pg) impact in the northwest (Perry et al., 2002).

The most prominent onshore tectono-physical features are bank-marginal to the Caribbean coast, and progressively rotating from NE in the south, to even slight west in the north (Figure

III-1). The features presented on Figure 1 are a best visual representation from previous publications as indicated in Table III-1.

Beginning in the south of the Peninsula at the Maya Mountains of Guatemala/Belize is the Rio Hondo Fault Zone (RHFZ), seen in the bank-margin alignment of the Chetumal Bay inner backshore, and the parallel and ~70 km landward Bacalar Lake complex, both trending 35°.

In the mid-section of the Caribbean coast near Tulum and extending to the north coast, is the combined surface expression of the Holbox Fracture Zone (HBFZ), and some portions sometimes called the Xel Ha Fracture Zone (XHFZ) considered here to be the southern expression of the HBFZ (see Bauer-Gottwein et al., 2011; Szabo et al., 1978; Tulaczyk et al., 1993). Near Tulum, surface expressions of the HBFZ are seen in the aligned open water basins of Chunyaxche, Muyil, Union, and others, running 5-10 km inland of Tulum and trending 24°. The HBFZ influence on conduit development around Tulum is seen in the notably T shape of rock sided coastal caletas, with the heads of the T also trending at 24°, and with the conjugate leg of the T at 140° (Figure III-3). Moving northwards, the HBFZ is seen in a series of low-lying swales/poljes with sawgrass and some with persistent water hosting inland freshwater mangroves, which then become very overt and numerous >100 km long broadly parallel seasonally flooded poljes orientated 5° to 10°, typically considered the main features of the HBFZ (white swales in Figure III-2). Remote sensing data indicate that development of regional dissolution features was strongly influenced by the HBFZ and result in high permeability and groundwater drainage at the intersection with the north coast (Pérez-Ceballos et al., 2012; Southworth, 1984; Tulaczyk et al., 1993).

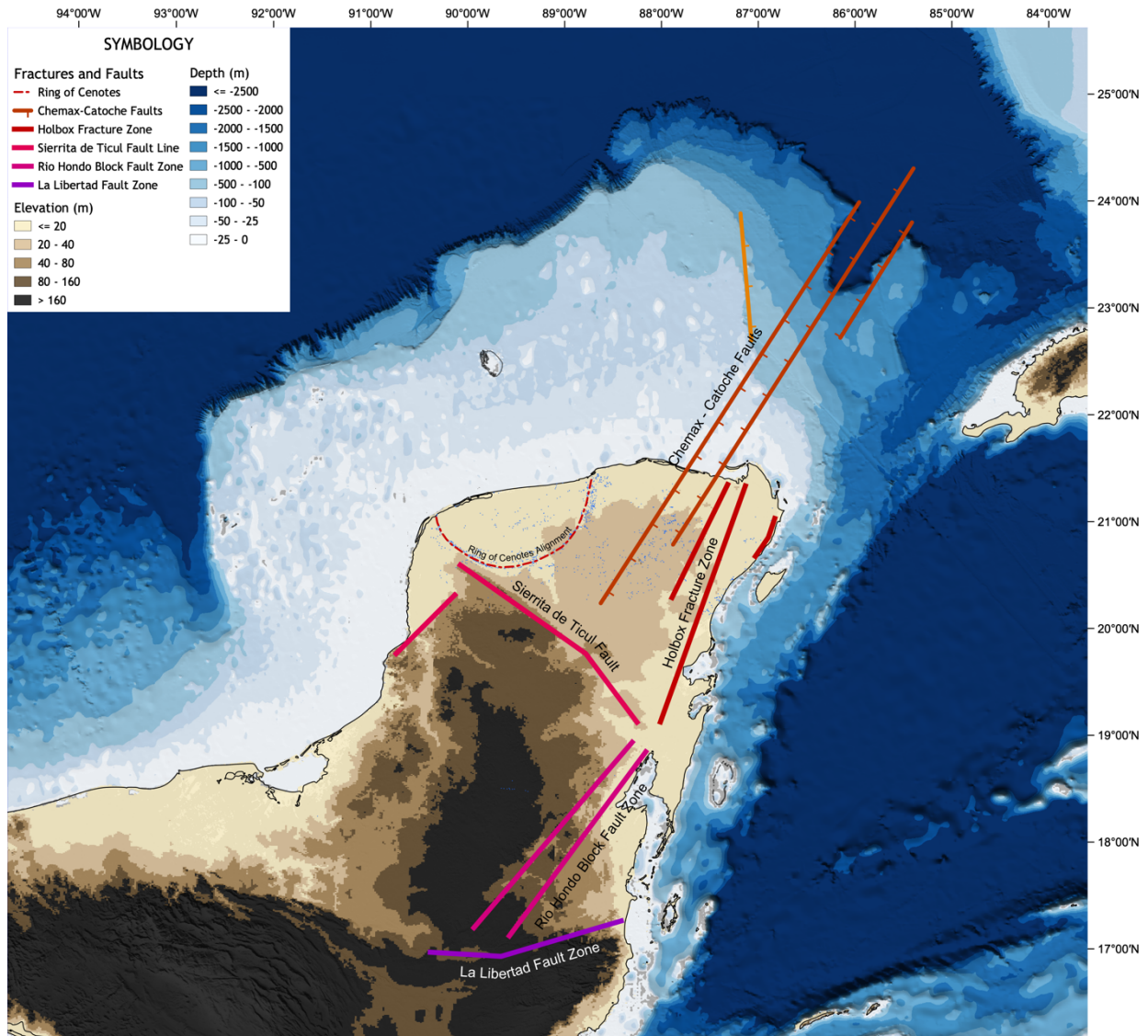
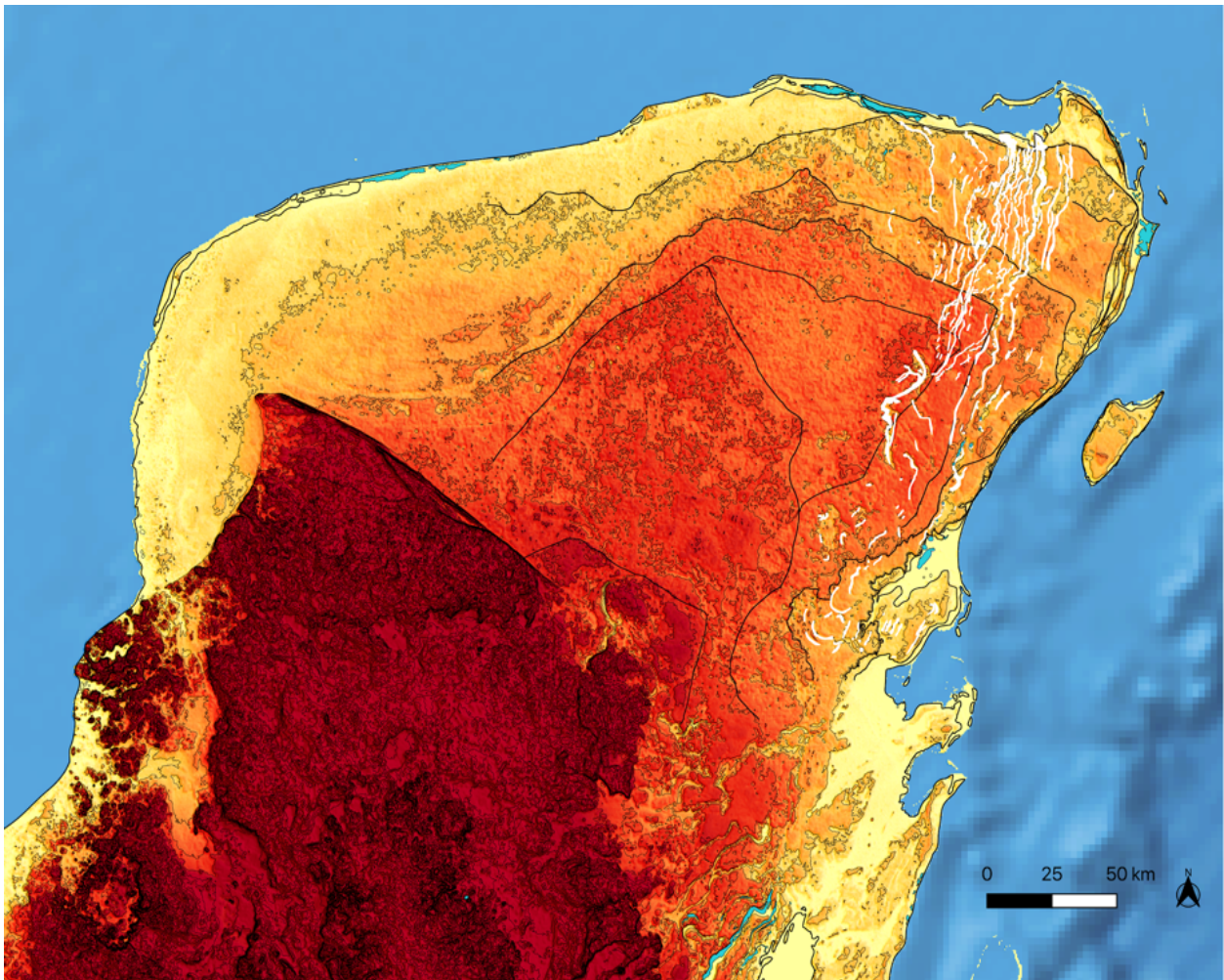


Figure III-1 Features of the Yucatan Platform. The major fault systems are the Ring of Cenotes, the Sierrita de Ticul fault line, the Holbox fracture zone, the Rio Hondo block fault zone and the La Libertad fault zone. The Chemax – Catoche Faults are also shown and discussed in text. Sources: Bauer-Gottwein et al., 2011; Connors et al., 1996; Pope et al., 1993; Weidie, 1985.



*Figure III-2 Features of the Yucatan Platform. Terrace geomorphology shown with 10 m contour (using 15 m pixel resolution base; INEGI, 2013). Thicker black lines are visually interpreted contours showing terrace edges. White swales are topographic lows relative to surrounding terrains, overlying the Holbox Fracture Zone.*

Off the north-shore is a prominent sub-marine escarpment from 100 to 250 km offshore and at ~100 m water depth trending 355°. It shown in orange in Figure III-1, and to our knowledge is unnamed and does not appear in any of the indexed literature. Its orientation continues the progressively rotating bank-marginal fracture sets to the north bank margin, from 35°, 24°, 5-15°, and now 355°.

The prominent Catoche Tongue is also offshore at 200 km from the NE modern coastline. It is an incised SW-NE re-entrant, dropping the platform margin to full ocean depth of > 2500 m. Over the decades, the Catoche Tongue has been inferred to continue on-land as the Chemax-Catoche Fault, but plotted schematically and with low confidence, seen with several question marks, as in (Weidie, 1985) and subsequent works, and Pope et al. (1993).

Systematic review of seminal publications including geological field reports on the faults and fractures of the Yucatán Peninsula is presented in Table III-1. There is very limited direct geophysical or other primary data, and the majority of sources use observations of surface expressions pre-dating satellite data. In the case of the Chemax-Catoche Faults, there is comment by Shaub (1983) of a “prominent reflector underlying the carbonate bank section on either side of the Tongue” but the primary geophysics data is neither presented nor cited. Connors et al. (1996) also comment that the Holbox swale depressions are strongly correlated with gravity anomalies, but similarly the primary geophysics are not presented nor cited and most likely were an extension comment based on the gravity anomaly work of Hildebrand et al. (1995) even though that was centered on Chicxculub to the west. It is only in the 2000’s onwards with renewed efforts first by the ICDP and now also IODP, that large field campaign geophysics have advanced on the Yucatán Peninsula. However, the geophysical investigations continued to focus on the NW quadrant of the peninsula, primarily in and around the Chicxulub Impact sedimentary plain including offshore extension (Gulick et al., 2008, 2017; Urrutia-Fucugauchi et al., 2011). These works have not provided substantial new insight on the Caribbean coast bank marginal fractures, or on the motion and faulting at the platform scale at large.

The nature of the long-inferred Chemax-Catoche Fault that has no distinct surface expression on the sub-aerial peninsula remains enigmatic, and the sketched extent and orientation in numerous publications beginning in the 1980's (Connors et al., 1996; Lesser & Weidie, 1988; Pope et al., 1993; Weidie, 1985) and propagated in publications onwards requires reconsideration. Of the features with clear surface expression, these fracture systems collectively form a continuous bank marginal system. With some discounting of the Catoche-Chemax Fault, we see a progressive set of bank-marginal faults presently called by distinct names in the south-central-and northern expression including offshore, but that systematically indicate counter-clockwise rotation from south to north for the post Paleogene Yucatán Peninsula.

*Table III-1 Yucatán Platform summary of historically published faulty and fracture features. The table is ordered from the north to the south.*

<b>Fracture Zone</b>	<b>Observations/Features</b>	<b>Interpretation</b>	<b>References</b>
<b>Chemax (?)</b>	Consistent use of question marks on Figures of the offshore "extension" of Chemax-Catoche Fault Zones through the Catoche Tongue (Pope et al., 1993; Weidie, 1982; Weidie, 1985).	Offshore extension Chemax-Catoche Fault Zone (Pope et al., 1993).	<i>Figures by Weidie (1985) and Pope et al., 1993 include Chemax-Catoche Fault Zones with question marks.</i>
<b>Catoche Fault Zone</b>	"Submarine Catoche Fault Zone" (Connors et al., 1996).	YP Eastern Block Fault District that onshore includes the Rio Hondo Fault Zone (Lesser & Weide, 1988).	<i>Mentioned by Connors et al., 1996 (no further references). In figures by Weidie (1985) and Pope et al. (1993).</i>
<b>Catoche Tongue</b>	A major re-entrant in the Campeche Platform in the southeastern Gulf of Mexico (Shaub, 1987)	The Tongue is underlain by a block-faulted basin. The basement of the basin is correlated with a prominent reflector underlying the carbonate bank section on either side of the Tongue (Shaub, 1987).	
<b>Holbox Fracture Zone HBFZ</b>	Surface expressions of the Holbox fracture zone are large, flat-bottomed, elongated swales.	[HBFZ] guided the development of regional dissolution features [...] resulting in high permeability and groundwater drainage (Tulaczyk et al. 1993).	<i>Tulaczyk et al. (1993).  Connors et al. (1996)</i>

<i>Fracture Zone</i>	<i>Observations/Features</i>	<i>Interpretation</i>	<i>References</i>
		The swale depressions are strongly correlated with gravity anomalies (Connors et al., 1996). The Holbox Fracture Zone is part of the north-northeast trending Eastern Block Fault District that onshore includes the Rio Hondo Fault Zone (Lesser & Weidie, 1988) and the offshore extension Chemax-Catoche Fault Zone (Pope et al., 1993). Pope et al. (1993) related the curvature of the Holbox Fracture Zones to deeper impact structures.	<i>Pope et al. (1993)</i>  <i>Pope et al. (1993)</i>
<b><i>Ring of Cenotes ROC</i></b>	Coincide with maxima in horizontal gravity gradients and a topographic depression (Connors et al. 1996)	In the vicinity of the cenote ring the karst features are closely associated with gravity gradients interpreted as corresponding to peripheral faults of the buried crater (Hildebrand et al., 1995).	<i>Hildebrand et al. (1995)</i>
<b><i>Ticul Fault Line</i></b>	A sharp, NE facing escarpment along the northern edge of the Sierrita de Ticul.	Interpreted as a normal fault (Weidie, 1985). Based on groundwater geochemistry, interpreted as a zone of <b>high permeability</b> (Perry et al. 2002). Ticul Fault Line was implemented as a <b>flow barrier</b> in regional-scale numerical groundwater-flow model of NW Yucatán (Gonzalez-Herrera et al. 2002; Marín, 1990; Marín et al. 2004).	<i>Weidie (1985).</i>  <i>Perry et al. (2002).</i>  <i>Gonzalez-Herrera et al. (2002); Marín (1990); Marín et al. (2004).</i>
<b><i>Rio Hondo Block Fault Zone RHFZ</i></b>	The onshore continuation of an extensive horst and graben block fault system off the Caribbean coast of the southern YP (Weidie, 1985).	Created by distinct tectonic events over Late Cretaceous to Pliocene times (Lara, 1993). The Rio Hondo and nearby faults trend precisely at N35°E and are parallel to faults in the Yucatán channel and to the Guayape-Patuca faults of Chortis Block in Honduras (James, 1989) Regional-scale structures in southern Quintana Roo were identified, which are aligned E–W to NE–SW and possibly form part of the Rio Hondo fault zone (Bauer-Gottwein et al., 2011)	<i>Lara (1993)</i>  <i>Weidie (1985)</i> <i>James (1989)</i>  <i>Bauer-Gottwein et al. (2011)</i>
<b><i>La Libertad Fracture Zone</i></b>		The fault zone is caused by the anticlinal La Libertad arch which extends from the Rio Usumacinta in the west to the Maya mountains in the East (Burkart, 1994; Miller, 1996; Vinson, 1962).	<i>Burkart (1994); Miller (1996); Vinson (1962)</i>
<b><i>Polo chic and Motagua Fault Systems.</i></b>	A complex of sinistral faults and north- and south-verging thrusts regarded as a suture (James, 1989).	Lateral-moving transform faults caused by the movement of the Caribbean Plate relative to the North American Plate (Erdlac & Anderson, 1982; Lodolo et al. 2009; Schwartz et al. 1979).	<i>Erdlac &amp; Anderson (1982); Lodolo et al. (2009); Schwartz et al. (1979)</i>
<b><i>Eastern Yucatan Platform</i></b>		'Block Fault Zone' (Lesser & Weidie, 1988)	<i>Lesser &amp; Weidie (1988)</i>

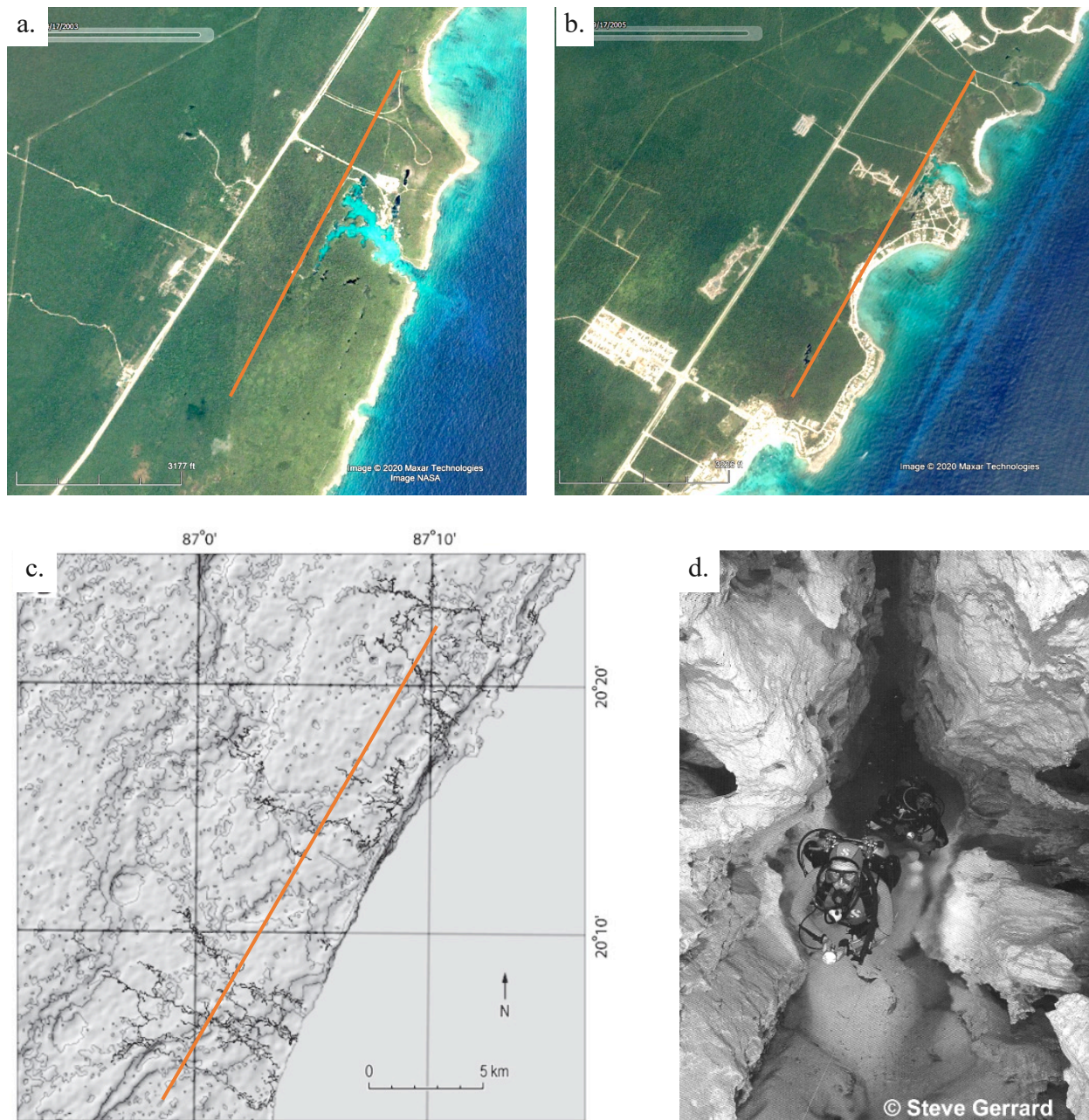


**Figure III-3** Fracture and structurally guided karst features on the Caribbean coast of the Yucatán Peninsula. The “T” shaped rocky sided caletas, created by the collapse of conduits. **a.** Xel Ha. **b.** Yalku. **c.** The overall direction of the explored sub-horizontal phreatic conduits near Tulum are anastomotic at the passage scale, but the overall alignment of multiple drainage lines does not present obvious fracture guiding at 2-15 km from the coastline, from Smart et al. (2006). **d.** In some segment of conduits 1 km from the coast, the influence of the bank marginal fracture systems is obvious, as in Sistema Abejas adjacent to the coast.

### III-1.2 WESTERN CARIBBEAN SEA LEVEL RISE (SLR)

Accurate paleo-sea-level benchmarks for Quaternary sea levels are important for many reasons: (1) to monitor the nature, magnitude and speed of climate and sea level changes in the past; (2) to establish the concordance or discordance of astronomical, isotopic and climatic events; (3) to provide benchmarks from which the magnitude of uplift or subsidence in tectonically unstable zones can be calculated (Hearty & Kindler, 1995).

Global sea level through the Holocene includes a rapid from Last Glacial Maximum ~14 ka to 7 ka, and then rising at a reduced rate since (Fairbanks, 1989; Lambeck & Chappell, 2001). Caribbean Sea-level broadly follows global trends, with ~+2 m over the last 3,000 years (Khan et al., 2017; Milne & Peros, 2013). Using back-stepping Pleistocene reef architecture, Blanchon (2010) identified a quick regional SL jump from +3 to +5 m during the Last Interglacial highstand (MIS 5e), similar to the Bahamian “over-shoot” (Blanchon et al., 2009; Hearty & Neumann, 2001).

Local Holocene sea-level curves are the combined function of eustatic effects of glacial melting and thermal expansion, meteorological changes, regional tectonics and isostatic rebound (Minor & Grant, 1996), sediment transport, erosion, deposition (Marriner et al., 2006), and local karst or anthropogenically induced collapse (De Waele et al., 2011; Guerrero et al., 2008; Waltham et al., 2005; Waltham, 2008). No comprehensive local SLR curve exists for the Western Caribbean, but observations include that the last inter-glacial sea level maximum peaked briefly at +5-6 m, and a series of beach ridges accreted along the Caribbean coastline. Subsequently, the strandplain prograded seaward with falling sea level at the end of the MIS 5e. Even when sea level fell several meters during the early stages of the last glacial period, production of carbonate sediment on the shallow ramp apparently remained high, because a series of carbonate eolian sand dunes built up

along the seaward margin that are now 9 m underwater (Ward, 1997; Ward et al., 1995; Weidie, 1985).

### **III-1.3 UPPER PLEISTOCENE RIDGES**

An Upper Pleistocene ridge-and-swale complex runs between Cancun and Tulum (Ward, 1997; Ward & Halley, 1985). More than 20 ridges run from Cancun to Playa del Carmen broadly parallel to the modern coast, and these narrow to a single ridge ~10 km north of Tulum. South of Tulum the ridges broaden substantially to span 25 km in the complex coastline dominated by tidal flats and vast mangrove wetlands, protected in the Sian Ka'an Biosphere Reserve, and the numerous and broadly distributed ridge-and-swales continue into Belize.

Ridge crests are locally 1-5 m above the intervening swales, spaced 50 to 200 m apart from Cancun and south to Tulum. Ridges reach 15 m asl, while the most prominent ridge is on the actual coastline in the archeological site of Tulum. The Maya walled maritime trading port city of Tulum is on the high ground of the coastal Pleistocene dune rocks, with a multi-functional structure serving also as a lighthouse for the coastal trade routes. Furthermore, Upper Pleistocene eolianites are the framework of the islands of Contoy, Mujeres, and Cancun.

## **III-2 DATA AND METHODS**

We use geodetic derived data products from the UNAVCO (2018) Data Archive Interface v2.0 (DAI v2) for GPS stations within the greater area Caribbean Sea and Gulf of Mexico region, including PBO, COCONet, and TLALOCnet networks to explore the present-day tri-axial Yucatan Block motion. The motions in the IGS14 reference frame are based on the global weighted average plate velocities relative to the Earth's core. Stations with 5+ years of data are used and trimmed to the longest full calendar to avoid seasonal bias from incomplete earth tide cycles. The linear slope

is calculated for the north and east components and plotted as a combined vector (Figure III-4a). For the vertical component, the prominent Earth tide solar annual (Sa) period of ~1 yr is removed using the “un-tide” function within T-Soft earth tide software package (Van Camp & Vauterin, 2005; Wahr, 1995). The linear slope of the un-tide residual is used here to approximate the present-day vertical motion (Figure III-4b). See Appendix A for supplemental materials on station details and data plots.

Published results from collected records of geoarchaeology, coastal geomorphology, and coastal ecology are also considered for interpretation of relative position now, compared to Holocene sea level. The Maya plied long-distance maritime trade routes from Honduras to the Gulf of Mexico, and out to numerous offshore islands. The development, location, and practices within their coastal settlements, now archaeological sites, provide the broad context for relative sea level change in the late Holocene, with some sites now flooded or perched relative to modern sea level (Andrews & Corletta, 1995; Jaijel et al., 2018b; Khan et al., 2017). Similarly, the condition and position of coastal geomorphology including beach and reef features, as well as the extensive mangrove swamps flanking the YP, allow for determining the direction of vertical motion relative to Holocene sea levels.

### **III-3 RESULTS**

#### **III-3.1 GPS/GNNS STATIONS**

Four stations on the northern lowland Yucatán Peninsula (YP) are principally considered: 1 in Cancun, 2 co-deployed in Puerto Morelos, and 1 in Felipe Carrillo Puerto. The YP current motion is consistently westward, at rates of 8-10 mm/year (Figure III-4a), along with



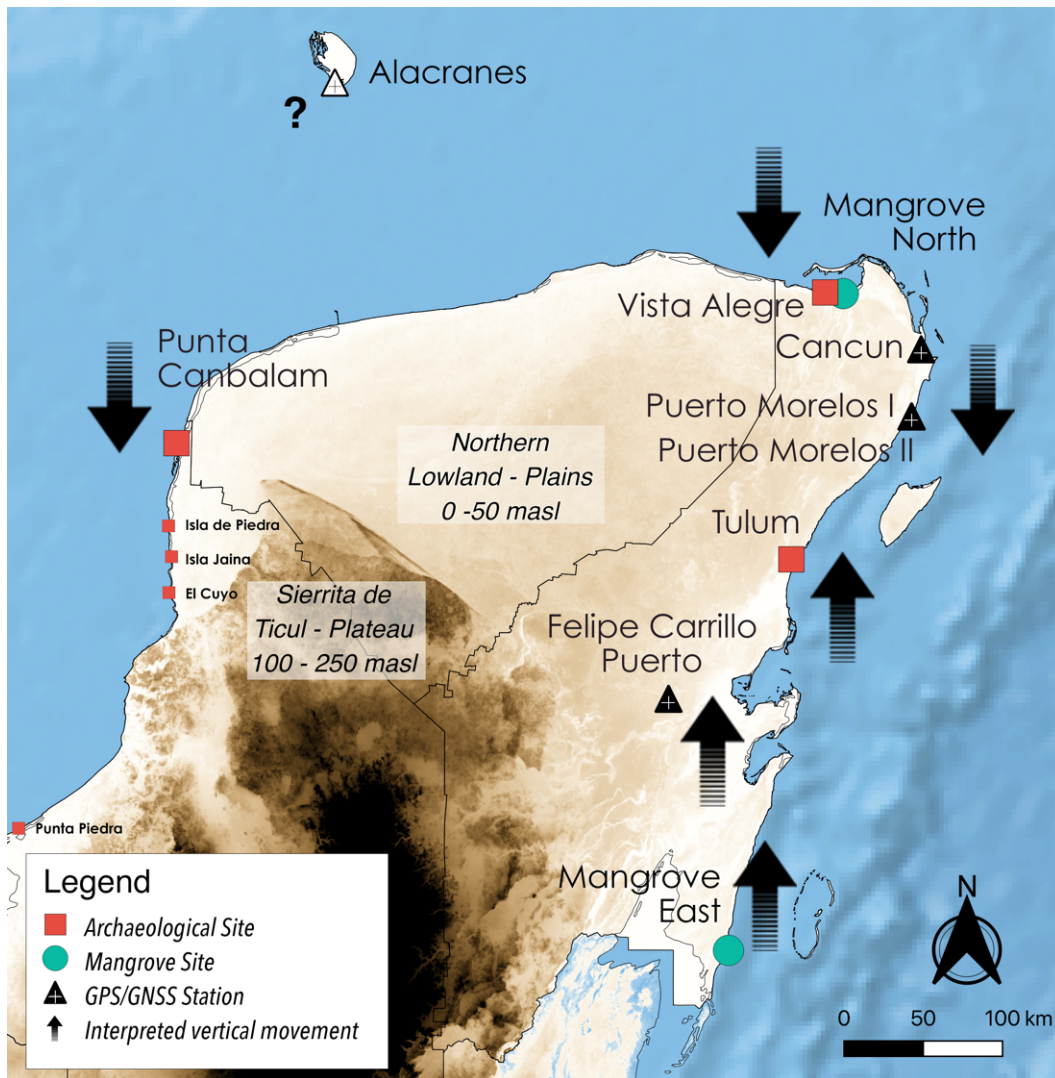


Figure III-5 Summary direction of mid- to late Holocene vertical motion but with no representation of rate, including for geodetic GPS/GNSS stations ( $\blacktriangle$ ), archeological sites ( $\blacksquare$ ), and mangrove ecology ( $\bullet$ ).

### III-3.2 MAYA COASTAL SITES

#### *Tulum*

The archaeological site of Tulum is the most prominent Maya port of the Caribbean coast, a walled city with its largest structure “El Castillo” on top of a +12 m asl prominent coastal ridge,

a cliff-like feature unique along the whole coastline, which is bounded to the north by a sandy beach area that extends 50 m inland, and is 20 m wide at the coast (Leal-Bautista et al., 2013; Sullivan, 2002). The intruding beach spit is also regionally unique and is of the same dimensions and orientation to the numerous rock sided caletas common northward along the coast and formed by collapse of dissolution conduits. Maya commonly used caletas as natural harbors for the sea-going trade canoes (Andrews & Corletta, 1995). A natural question that follows is if the beach at the Tulum archeological site is a perched sediment mantled caleta where groundwater used to discharge, which may also in part explain the water supply for inside the walled city. Stratigraphic confirmation is required.

### *Vista Alegre*

West of Cancun on the north coast, the first major archeological site is the Maya port of Vista Alegre, Yalahau Region, located in Holbox Lagoon inside the barrier island. Vista Alegre features a notably steep pyramid used as look out over Holbox Lagoon, in support of the Maya canoe routes along the northern coast. Inland of the sites are extensive wetlands associated with HBFZ, before reaching the higher elevation Pleistocene ridges some km's distant (Glover et al., 2011). Hydrogeology and sedimentology investigations of the site since 2010 have failed to identify any modern proximate fresh-water resources that could support the estimated population at the prime of the port (Beddows et al., 2016). Test pits show that intact floor at the occupation layer is 2.75 m below the ground surface, and just above the water table, which is within cm's offset of sea level in this region (Beddows, 2004; Jaijel, et al., 2018b). The  $^{14}\text{C}$  dates place the floor at the Terminal Pre-Classic / Early Classic, roughly ~250 CE (Jaijel et al., 2018a), a time when Late Holocene sea level should only have been within at most -1 m below present.

### *Punta Canbalam*

Punta Canbalam, on the NW corner of the YP, is close to a long sandbar off the southern tip of the Celestún Peninsula, about 500-1000 m offshore, now submerged to a depth of 1-2 m. Initial interpretation identified that the site level could not be explained solely by Holocene sea level rise, and suggesting instead highly active erosional processes (Dahlin et al., 1998).

#### **III-3.2.1 Additional Sites - North & Gulf Coast Maya Sites**

Virtually every coastal site along the northern coast of the Yucatan Peninsula point to at least a ~1 m lower *relative* sea level during the Late Classic period, or until ca. 800 CE, based on submerged architecture on the north coast (Andrews & Corletta, 1995; Dahlin et al., 1998), submerged archaeological features on Cozumel (Rathje, 1973), and a significant number of Gulf Coast sites also having submerged Late Classic architecture, including Isla Jaina, El Cuyo, Yukumbalam, Isla de Piedras and Los Guarixes on Isla del Carmen (Andrews & Corletta, 1995).

#### **III-3.3 COASTAL MANGROVE**

Sea level rise (SLR) or fall, directly affects ecosystems in the intertidal zone, with landward or seaward migration of species respectively (Jones, 1994). Mangroves are particularly good indicators of the effective coastline over time as they can adapt to rapid sea level changes including rises of 8-9 cm/100 years (Ellison & Stoddart, 1991).

A comparison of the north coast and Caribbean coastal geomorphology and ecology shows fundamental differences. The north coast wetlands remain connected to ocean and actively flush by tides (Figure III-6a). In stark contrast, the mangrove wetlands along the often-rocky mid-section

Caribbean coast are perched and, in some cases, categorically decoupled from active marine circulation by intact substantial beach ridges (Figure III-6b).

a.



b.



*Figure III-6* Sea level rise has a rapid and direct effect on ecosystems in the intertidal zone, such as mangroves. Mangrove coastal areas in **a.** the north coast, with wetlands remain connected to ocean and actively flush by tides; and **b.** the Caribbean coast, where wetlands seem to be perched and above sea level, including coastal mangroves decoupled form the ocean.

## III-4 INTERPRETATION & DISCUSSION

### III-4.1 GEODETIC DATA – TILT

The interpretation of the available geodetic data is that there is presently a significant counterclockwise rotation and north-northwest down tilt on the whole Maya Block, lowering the northern portion of the Yucatán Peninsula, and lifting the southern margin at the joint with the Maya Mountains in Belize.

The falling rates at the Puerto Morelos and Cancun stations all at the NE corner of the peninsula are highly inter-consistent and range narrowly from -1.68 to -1.79 mm/year with both station records spanning ~12.5 years. At Felipe Carrillo Puerto, ~90 km SW of Tulum, there is a falling rate of - 0.29 mm/yr over the ~5-year record, indicating that the hinge line for the tilting plate is located near Tulum or Felipe Carrillo Puerto. The linear relationship in vertical velocity in mm/year for the stations over the nearly 500 km from Cancun+Puerto Morelos, Felipe Carrillo Puerto, and Belmopan indicate that the Maya Block is tilting coherently as a block (Figure III-7)

The stations with 5+ years of data are spatially biased, being all along the Caribbean coastline. A geodetic station was installed on Alacranes Atoll, 120 km due north of the peninsula NW coastline, but this station has failed to deliver any substantial or usable data. Data from the west Gulf of Mexico coastline of the Yucatán Peninsula would be ideal for further testing the spatially biased data from the Caribbean site. Sites within the Chicxulub Sedimentary Basin should be included in addressing the motion of the whole of the Maya Block.

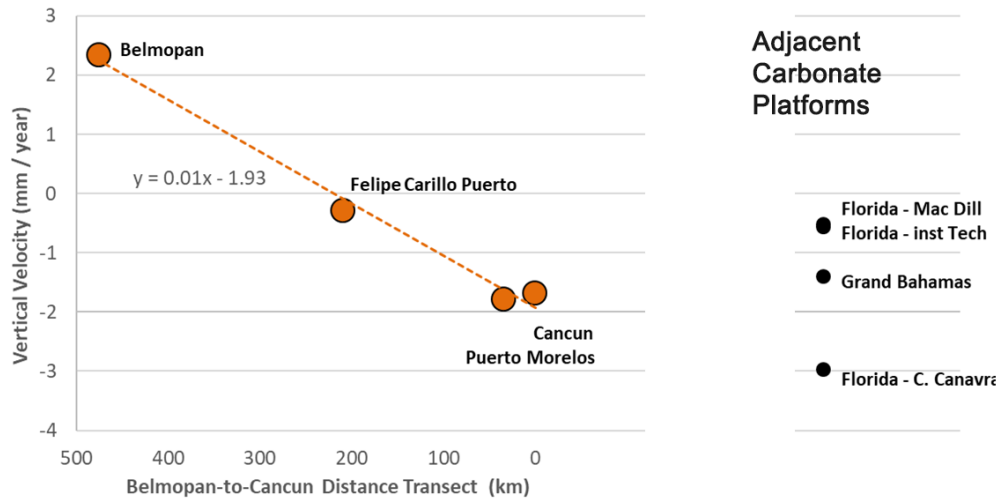


Figure III-7 Vertical velocity (mm/year) of four stations on the eastern Yucatán Peninsula: CN23 (Belmopan), CN24 (Felipe Carrillo Puerto), CNC0 (Cancun), and UNPM (Puerto Morelos). Results plotted as station distance to CNC0.

#### III-4.2 COASTAL GEOMORPHOLOGY, ECOLOGY, AND ARCHAEOLOGY

The combined observations of the drowning north coast mangrove, the numerous drowned archeological sites on the north and west coast, the perched Caribbean coast mangrove, the elevated coastal ridges notably near Tulum, all combine to support the tilting motion observed in the geodetic data. These observations are not explained well by the Late Holocene sea level rise (SLR), which is on the order of 1-2 m over the last 6 thousand years. And specifically, rising SL should result in drowning Caribbean mangroves and lower relative coastal ridges, not perched mangroves and excess elevation ridges. The Maya were a robust civilization and engaged in extensive long-distance trade over coastal avenues building numerous ports, and even still the Late Holocene SLR does not explain the degree of drowning of these sites. The field observations require additional vertical motion beyond Late Holocene SLR, such as provided by the observed Maya Block north coast subsidence.

Dahlin et al. (1998) invoke elevated erosion rates as a possible process for the additional vertical delta required to drown the coastal archeology. A low sea stand during major occupation of Punta Canbalam can hardly be doubted and suggests that a subsequent rise to modern SL might be responsible for the destruction of the site and the dispersion of its artifacts. Furthermore, this hypothesis is implicitly based on the assumption of strict tectonic rigidity for the platform/Maya Block. With the observation of north coast falling at an order of magnitude of 1 m / 1000 years, the additional vertical delta required to explain the drowned archeology is achieved. It is not SLR alone, but that the coastline is also falling at the same time, creating a large vertical delta.

#### **III-4.3 DURATION AND PERSISTENCE OF OBSERVED MOTIONS**

The geodetic data spans 5-10 years for most stations while the Cancun and Puerto Morelos stations reach ~12 years each. These records, while definitive of present motion, obviously are not to be considered persistent in rate or even direction over significant time. We infer from the combined coastal site observations for the current motions to be representative at least from the Late Holocene, which coincides with flooding of the northern platform bank (see Section III-4.5 for process discussion).

Consistent with the presently observed platform fall, Kinsland et al. (2000) proposed a uniform subsidence of the Yucatan Peninsula tracking the elevation of the highest altitude geomorphic surfaces defined by Pope et al. (1996) at an elevation of about 200 m, to their present elevation of about 25 m. The first documented subaerial exposure of the platform happened middle to late Eocene (Figure III-8). At that time, sea level was about 200 m above the present level.

This surface, which is today at about 25 m above sea level must have subsided since their emergence resulting in a net local relative sea level fall of only about 25 m and individual steps of emergence of other geomorphic surfaces are consistent with the sea level curve (Figure III-3).

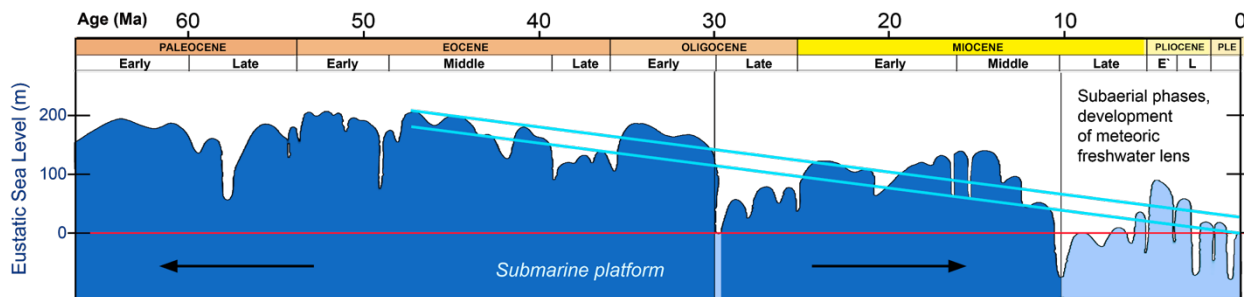


Figure III-8 Eustatic sea level since the Cretaceous. Composite from the work of Abreu & Anderson (1998). A blue line shows the proposed uniform subsidence of the Yucatan Peninsula linearly approximated which tracks the elevation of the highest altitude geomorphic surface at an elevation of about 200 m to their present elevation of about 25 m. The parallel curve, 25 m lower, approximates the elevation through time of the carbonate rocks at the present-day shoreline, from Kinsland et al. (2000).

#### III-4.4 ROTATION – REFLECTED IN MAJOR FAULTS, RIDGE AND SWALE COMPLEXES, AND PLATFORM TERRACE CHRONOSEQUENCES

##### *Process – Ongoing opening of the Caribbean Basin*

The rotation observed in the geodetic data, and the persistence of the westward motion may be driven by the motions of the Cocos and Caribbean plates tied to the development of the greater western Caribbean basin. The ongoing forces of the Caribbean basin (Figure III-4), pushing west include the *sphenochasmic* rifting of the Yucatán Peninsula out of the present site, and stretching of the easterly Yucatán Basin to the west. The whole fault block package looks to be moving coherently, with no relative motion between Yucatán mainland and Cozumel island. Geodetic data

(this work, Figure III-4) shows all stations east of the Cayman Through with strong east motion, and all stations on the eastern edge of the North American plate and the Yucatán Block, such as Cayman Island and Yucatán, are moving coherently in the west/north-west direction, consistently with the opening of the Cayman Trough (Rosencrantz, 1990).

#### *Pivot Point indicated by Ridge and Swale Complexes*

The expanded coastal ridge-swale complex in the NE corner of the peninsula, the reduction to a single ridge in the mid-coast section just north of Tulum, and then further south expanded sequences spanning more than 25 km. If the coastal processes through the Pleistocene were self-similar along the whole coastline, then the multiple successions forming the expanded sequences north and south, were overprinted in this mid-section near Tulum. The reduction to a single ridge near Tulum indicates this area as being the axis of rotation – or pivot – which is geographically close to the inferred hinge line based on the vertical motions.

#### *Rotation in major Fault Zones from S to N*

If as indicated, the differently named major bank-marginal fault systems to the Caribbean coast of the Yucatán Platform are one continuous fault system, then the progressive shift from NE in the south, to north-northwester at the north coastline, and finally slightly NW offshore, is evidence of the Maya Block rotation, consistent with the primary driver being the ongoing opening of the Caribbean.

#### *Chronosequences – Barrier Islands, HBFZ Swales, and Terraces*

Geomorphic age sequences, or chronosequence, are spatially distinct sites representing a temporal sequence. Since closure of the Caribbean Basin, the western loop impinges on the

Caribbean coast of the Yucatán Peninsula around Belize up to Tulum and is deflected northwards creating the Yucatán current that then flows up and around Cabo Catoche (aka Cancun). With persistent rotation driven by the opening of the Cayman Trough, *chronosequences* of geomorphs can be seen in the NW Yucatán Peninsula, in addition to the successive Pleistocene-Holocene beach and barrier island complexes prominent on the NW point of Cabo Catoche with Cancun and Isla Mujeres. Relative position of the ancient coastlines' fans counterclockwise, with the older ones to the SW, and the younger prograding NNE. At least through the Pleistocene, coastlines were prograding as a result of **a)** whole system moving west, and **b)** counterclockwise rotation of the block, in which the orientation of the coastline would fan progressively (Figure III-2).

Expanded chronosequences across the landscape in the NE peninsula may also be seen in the sequence of **marine terraces** in the central north of the peninsula, west of the HBFZ swales are marked by the black ~10 m contour lines in Figure III-2, supporting persistence of the counterclockwise motion at the least pre-Pleistocene, potentially of Middle Miocene or earlier with the peninsula being shallow marine, given sea level at ~+100 m (Figure III-8). It is also conjectured that the swales of the HBFZ (white in Figure III-9) may be another example, based on the counterclockwise rotation and westward movement.

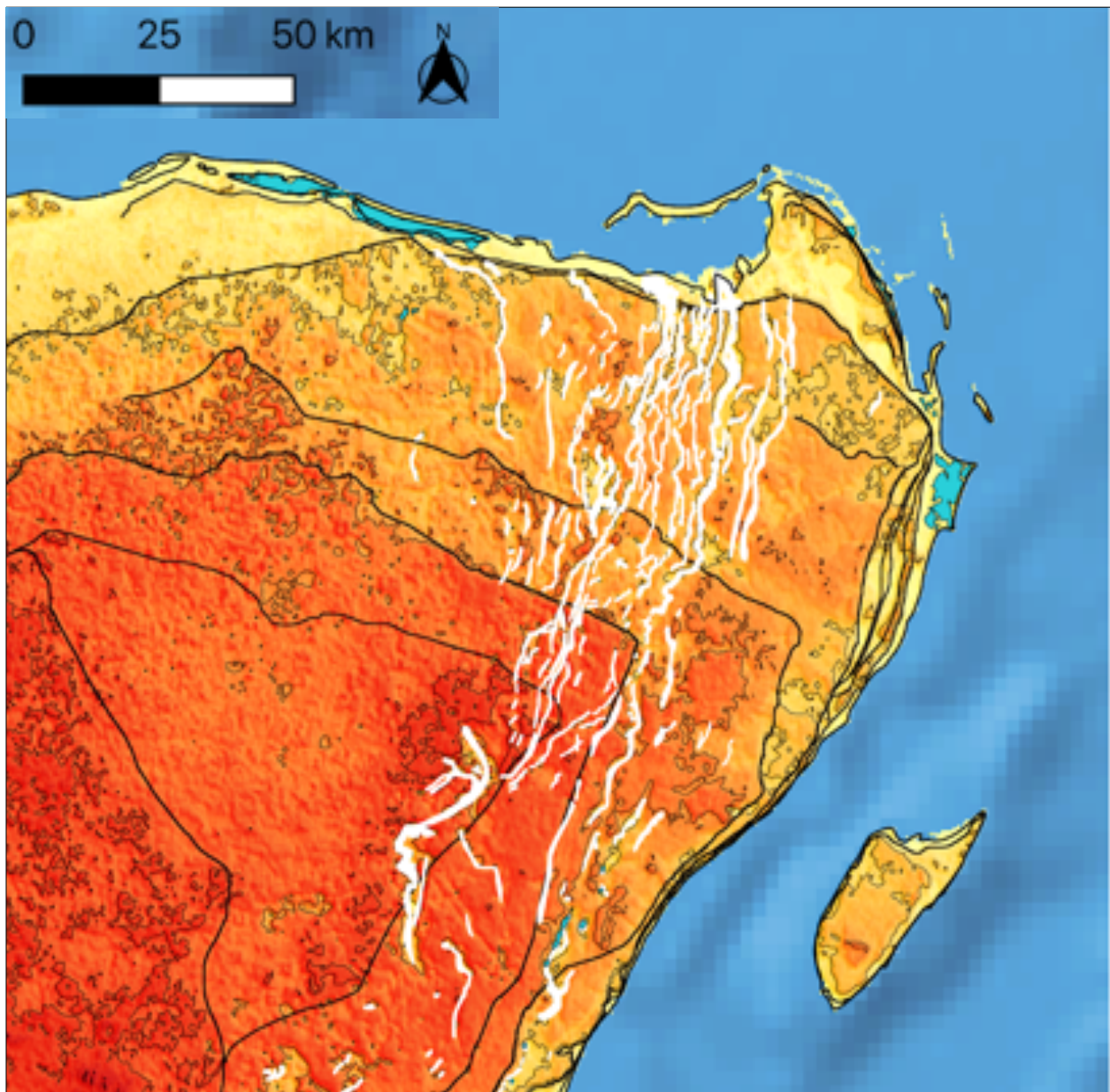


*Figure III-9* Geomorphic features of the north-east Yucatan Platform. Terrace geomorphology shown with 10 m contour (using 15 m pixel resolution base; INEGI, 2013). Thicker black lines are visually interpreted contours showing terrace edges. White swales are topographic lows relative to surrounding terrains, overlying the Holbox Fracture Zone (WGS84-UTM).

### III-4.5 MASS BALANCE – WEATHERING AND BANK TOP SEDIMENT LOADING

Karstification is pervasive over the Yucatán Peninsula, tied to the tropical climate, and rapid infiltration through the high-permeability eogenetic carbonate aquifer system (Beddows, 2004; Smart et al., 2006). Carbonate weathering conditions are optimal along the Caribbean coast, with peak rainfall of 1.5 m/year occurs on the Caribbean coast, and intensive cave exploration beginning in the 1980s has now documented over 1500 km of conduits, of which 1,450 km are phreatic (QRSS, 2020). Distributed dissolution of the surface, and phreatic dissolution notably along the typically undersaturated fresh-saline interface in this density stratified aquifer, leads to as yet unquantified mass offloading, which should result in some uplift. If similar to Florida where karst denudation rates are ~0.11 mm/year (Bahtijarević & Faivre, 2016), then Yucatán surface lowering may be on the same magnitude as the present observed vertical vector.

The timing and persistence of the vertical vector is harder to constrain compared to the westward movement and counterclockwise rotation argued here to be a long-standing influence on the Maya Block. The presently observed subsidence of the north coast may be tied to, or greatly increased during higher sea levels that progressively overtop the vast northern Campeche Bank platform. The flooded northern bank is mass loaded in some part by transported sediments, but also likely extremely so by autogenous sediment formation/deposition in this vast carbonate factory notably. The present observations cannot disambiguate if the whole platform experiences a background rise tied to mass unloading by weathering, and that tilt with north coast subsidence is only induced with high enough levels overlapping the northern bank leading to excess loading beyond the mass loss from karst denudation. At least some norm of uplift / rise is likely through the range of Pleistocene.

### III-4.6 COMPARISON TO FLORIDA AND BAHAMAS

The Bahamas and Floridian Platforms, like the Yucatán Platform, are all large carbonate environments and major modern example of carbonate platform (Upchurch et al., 2019). All three have the potential to provide paleo-sea level records, as long as tectonic motions are well constrained.

The Bahamian Archipelago extends 1400 km from near Florida Peninsula southeast to the Caribbean Plate boundary and contains 125,000 km<sup>2</sup> of shallow platform, and 11,407 km<sup>2</sup> of subaerially exposed islands (Meyerhoff & Hatten, 1973). The Bahamas is considered stable carbonate platforms, whose tectonic stability is assumed from equal-age marine deposits that show no significant differences in elevation. It has a quiescent history during at least the late Quaternary.

The Florida Platform is constructed of Middle Jurassic to Quaternary evaporite, carbonate, and siliciclastic sediments deposited on a relatively stable, passive margin of the North American Plate. With separation and basement cooling, the margins of the plates begin to subside, creating sedimentary basins that accumulate sediments (Upchurch et al., 2019). Mesozoic and Cenozoic Era structural movement on the Florida Platform was entirely downward, and Florida's arches, or structural highs, were not formed by uplift, but as the result of subsiding more slowly than the flanking basins (Winston, 1991).

Consideration of the vertical components of the geodetic data from 2 stations in Florida and 1 station on Grand Bahamas, we see that they are both presently subsiding at rates similar to that determined for the Yucatán Platform (Figure III-7), ranging over -0.5 to -3 mm/year for Florida, and -1.3 for Grand Bahamas. However, uncertainties in vertical motion are ~10 times higher than those for horizontal motions. Further analysis beyond the scope of the present paper is

warranted in order to assess the coherence of these platform motions. In all cases, the broader tectonic histories of the plates on which each carbonate platform has developed is relevant, and that at least now at present, under high (and rising) modern sea levels all three carbonate platforms are subsiding, with flooded expansive shallow marine banks.

### III-5 CONCLUSIONS

- The geodetic stations with 5+ years record indicate vertical movement, on the order of 1 m /1000 years in the north and south Maya Block. The observed vertical motion is of significance in interpretations of sea level records from the Yucatán Peninsula, and of the hydrogeology, speleogenesis, paleoclimate records, and adaptation to climate change driven sea level rise.
- Observations of Maya coastal archeology, mangrove wetlands, and coastal ridges are consistent with the geodetic motions.
- The YB is tectonically rigid in the strict sense, without apparent deformation, yet the block is arguable in tilt/subsidence motions.
- Persistence of motion is not incompatible with the long term proposed subsidence back to Middle/Late Eocene. Rate of plate motion seems to be 3-orders of magnitude higher at present day.
- Additional instrumentation is required, notably in the NW of the platform, ideally offshore with the operation of the Alacranes Atoll station, to further assess the whole block/platform motion, to further understand geomorphological processes, and to address climate change related sea level rise impacts.

## **IV      Geochemical Characterization of Pleistocene-Holocene Carbonate Rocks from Northeastern Yucatán Peninsula, México**

### **ABSTRACT**

This study of young Pleistocene to Holocene carbonate rocks from the eastern Yucatán Peninsula (YP) provides substantive insight on the near-surface geochemistry of the carbonate platform. ICP-OES was used to quantify an array of elements, for nearly 400 rock samples, from along three ~350 km of transect, including outcrops, quarries, and vadose and phreatic caves. About 60% of the rock sampled are from the phreatic zone, collected by cave diving. Water-rock interactions through time are key to understand present chemo-stratigraphic setting, and geochemical evolution of shallow coastal environments, where the mixing zone plays a fundamental role.

Neither clear geographical distribution, nor depth distribution patterns are evident, likely due to the inherent patchiness of coastal shallow marine facies, and also because overlapping of geomorphological and diagenetic processes driven by sea level changes. Insight is gained on the recalcitrant origin *terra rossa* formed on karst, with examination of the residual elements leading to accumulation of pedogenetic Al, Fe and Si oxides in reddish clays in the soils, and sometimes lithified, as part of the landscape of the Yucatán Peninsula. An exploration of the bulk rock geochemistry in relation to modern ocean chemistry helps constrain diagenetic post-depositional processes such as leaching, dolomitization and pedogenic pathways.

## IV-1 INTRODUCTION

This study on the geochemistry of young carbonate rocks from the Yucatán Peninsula (YP) aims to provide substantive insight on the geochemical composition, distribution and its relation to the geological evolution of the platform. The focus of the research is to investigate the geochemical composition of young carbonate rocks aged Pleistocene to Holocene by ICP-OES methods and to explore on water-rock interactions within the aquifer, with potential downstream impacts on coastal water chemistry (Bobba et al., 2012; Price et al., 2006). This initial geochemistry atlas lays the foundation for further research on the geochemical evolution of shallow coastal environments and diagenetic processes taking place therein.

The Yucatán Peninsula is an ideal and unique natural laboratory to study water-rock interactions and understand the overall interactions and processes as well as the global scale impacts of elemental fluxes from these. Cave diving through innumerable flooded sinkholes, locally called cenotes, provides unprecedented access to ~1000 km (600+ miles) of flooded caves in the subterranean estuary zone within 10 km of the coastline. The marine water is shallow, and within reach of open circuit diving at 10–20 m depth in most sites.

Nearly 400 samples from different environments were analyzed, of which 60% are from the phreatic zone collected by cave diving, and the rest from vadose zone from quarries, dry caves and outcrops. A lithological description was recorded in order to create a structured dataset which includes depth profiles and distance transects, both parallel and perpendicular to coastline, to cover for geographical patterns.

The chemo-stratigraphic understanding begins with determination of the *bulk rock chemistry* of the various facies and how are these systematically different when modified by the

hydrogeology. Here I investigate the geologic sequestering of elements in the host rock in locations that have less water-rock interaction in the freely draining vadose zone with near-ambient atmosphere, and those in the most reactive phreatic zone depths of the carbonate aquifer.

Bulk rock multi-element composition was quantified by Inductively Coupled Plasma-Optical Emission Spectroscopy (ICP-OES) using a set of 30 elements and a total of 385 samples from 38 different sites along the northeastern Yucatán platform. Samples are from vadose zone and phreatic zone, ranging in elevation from -48 to +18 m with respect to sea level.

Initial experiments were conceived for a tectonically stable platform as the Yucatán Platform was understood to be (prior to this PhD research – see CHAPTER III on re-evaluation of tectonic stability), where sample profiles would be taken in the phreatic marine, mixing, and freshwater zone, and in the vadose zone at different depths. As thermodynamically equilibrium shifts under different conditions of pH, dissolved oxygen and salinity, it was expected to geochemically distinguish those environments examining the distribution of a number of elements.

The report begins with a targeted introduction covering points specifically relevant to the discussion and does not aim to be a broad overview of the peninsula geochemistry and hydrogeology at large. Following Section 2: Methods, the Section 3: Results & Bulk Rock Geochemistry Overview is a systematic walk-through of the geochemical results. Note that some plots and maps are presented in Section 3, but with targeted discussion occurring later. The integrative discussion sections include: Section 4 – Comparison with modern ocean chemistry; Section 5 – Geographical distribution – with a more focused view of the geographical plots from Section 3; Section 6 – Stratigraphic distribution with consideration of rock geochemistry in the vadose and phreatic zones, chemo-stratigraphy, implications of specific observations in quarries

and outcrops, and finally hydrogeochemical implications from sampling in cenotes and caves. Section 7 then addresses Diagenesis, with content on dolomitization, soil development with implications for Saharan aeolian transport and/or volcanic tephra, interpretation of SAF plots, and finally Fe:P ratios with implications for limiting nutrient elements to coastal oceans.

#### **IV-1.1 STUDY AREA**

The Yucatán Peninsula is the ~165,000 km<sup>2</sup> subaerial portion of a tropical carbonate platform deposited since Jurassic over the structural unit of the Maya Block, covering southeast Mexico, northern Guatemala, and Belize. The geology of the YP consists of limestones, dolomites and anhydrites that combined reach thicknesses of more than 1,500 m, down to the upper part of a granodioritic basement.

The limestone rock shelf with an area of ~300,000 km<sup>2</sup> consists of a submerged shelf and an emergent portion that are roughly the same size. Disconformities in the sediment layers indicate intermittent partial subaerial exposure and erosion of the platform surface, with sequentially younger ages of the carbonate sedimentary rocks towards the northern parts (Figure IV-2).

About 66 Ma a large meteorite hit the Earth causing a mass extinction (Artemieva & Morgan, 2017; Schulte et al., 2010). The general stratigraphy of the Yucatán platform extends offshore to the Caribbean down the borderland to the Yucatán Basin and to the west to the Campeche Bank (López-Ramos, 1975; Ward et al., 1995).

#### IV-1.2 GEOLOGICAL SETTING

Surface geology knowledge is of low detail, and the entire eastern part of the subaerial peninsula spanning the state of Quintana Roo has been described as the Carrillo Puerto Fm, undifferentiated Miocene-Holocene or undifferentiated Miocene-Pliocene (López-Ramos, 1973). Stratigraphically, a helpful approach by Ward *et al.* (1995) divides the coastal limestones into three different Pleistocene units consisting of various facies that accumulated in platform-margin reefs and on back-reef platforms during interglacial high stands of sea level. Each unit is capped by a zone of *calichification*, the product of subaerial occluding diagenesis during low stands of sea level and providing a reasonable horizon to identify parasequence units. Pleistocene reef limestones, lagoonal *packstone-wackestones*, strandline *grainstones* and *caliche* (calcretes) are exposed in quarries and low sea cliffs along the Caribbean coast of the Yucatán Peninsula from northeastern cape Catoche to Tulum (e.g. Ward, 1997; Ward *et al.*, 1995).

Tropical carbonate sediments and rocks are the products of the biogenic carbonate factory which occurs at high rates in shallow and warm waters. Due to the shallow setting and high productivity, carbonate sequences commonly display shallowing-upwards trends (Wright, 1994). As a consequence, such shallow water origin makes them susceptible to multiple stages of subaerial and subaquatic exposure by the Pleistocene sea level changes, allowing overprint of associated eogenetic karstification processes and meteoric diagenesis, such as the formation of calcrete/caliche horizons. Massive carbonate beds deposited during interglacial stages and high stands of sea level, while caliche zones developed during glacial stages when the Yucatán platform was subjected to prolonged periods of subaerial exposure (Figure IV-1). Regional Caribbean Sea-level studies show that the Yucatán Peninsula was influenced by a sea-level rise of ~2 m over the

last 3,000 years (Milne & Peros, 2013). There is evidence that this sea-level rise submerged certain parts of some ancient Maya coastal archaeological sites (McKillop, 2005).

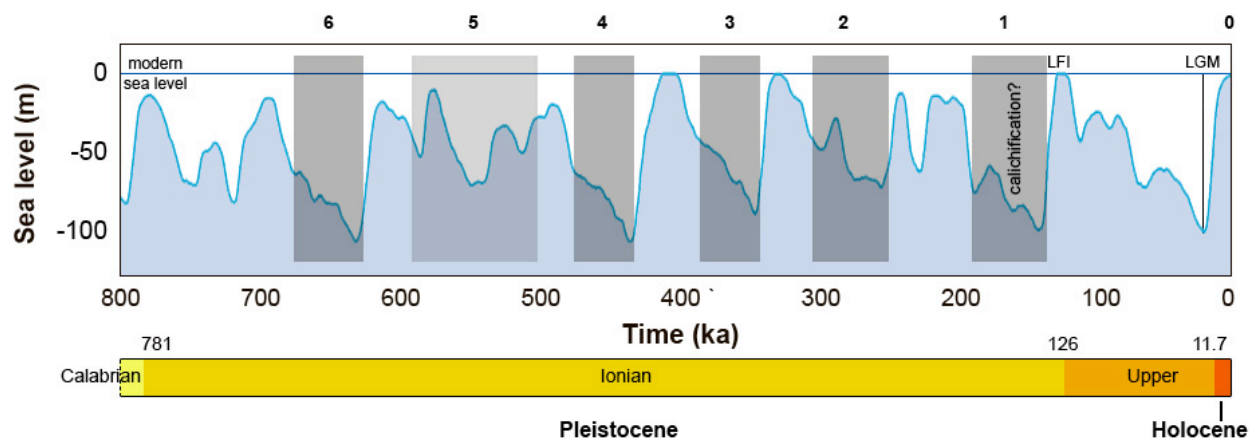


Figure IV-1 Eustatic global sea level variations over the last 800,000 yrs, for the Holocene and Upper Pleistocene. LGM - Last Glacial Maximum; LFI - Last Full Interglacial. Sea-level data from Siddall et al. (2007). Grey bands mark sea levels  $-50$  m or lower, and where the near-surface rocks in this study have likely been sub-aerially exposed assuming no vertical displacement of the platform.

In this setting of young carbonate geology, limestone is easily *karstified* with rainfall flowing through the porous rock and dissolving out extensive cave networks that efficiently drain water to large coastal springs (Beddows, 2004; QRSS, 2020; Smart et al., 2006). They comprise a large magnitude exchange of ocean-terrestrial water and are chemically reactive and biologically significant. The caves measure 10-100 m wide and transmit turbulent flows of  $1-10 \text{ m}^3 \text{ s}^{-1}$  of water (Beddows et al., 2007). The flows are density stratified with freshwater streams passing over intruding marine water, while complex water-sediment-rock interactions result in significant variations in the fluxes of terrestrial elements to the coastal waters. The reaction zone occurs where meteoric freshwater comes in contact with seawater, the *halocline*. As sea-level changes, the location of this reactive mixing zone moves vertically and influences the chemistry of freshwater

discharge. Large dissolution systems and cenotes are just beginning to be systematically mapped across the peninsula beyond the 10 km Caribbean coastal zone.

The Triassic to Holocene Yucatán limestone platform is located in the vicinity of the North American/Caribbean plate boundary and has been reshaped by a series of tectonic events over its long geologic history. The Chicxulub meteorite impact 66 Ma at the end of Cretaceous period fractured the existing sub-marine platform and modified the hydrogeological properties of the platform at the time, and with subsequent propagating influence through the 500 – 1000 m thick supra-deposited stratigraphy including with present-day surface expression (See CHAPTER II). The most notable regional-scale fracture zones with surface-expression are the *Ring of Cenotes* (Perry et al., 1995), the Sierrita de Ticul fault line, the Holbox fracture zone, the Rio Hondo block fault zone and the La Libertad fault zone as noted in Figure IV-2 (Bauer-Gottwein et al., 2011).

Five physiographic regions are presently recognized: the coastal zone, the northwestern coastal plain, the northeastern coastal plain, the central hill district and the eastern block fault district. All regions are characterized by a variable degree of fracturing.

Along the northeastern margin of the Yucatán Peninsula corresponding to the field area of this study (red box, Figure IV-2), is a narrow strip of Pleistocene limestones, including both marine and non-marine facies. The general stratigraphy of units consists of facies of platform margin reef or back-reef during interglacial high stands of sea level. Marine limestones include beach and near-shore *grainstone*, lagoonal *wackestone-packstone-grainstone*, and coral-reef limestone. These units are separated by *calichified* surfaces (subaerial calcretion), and no anhydrites are associated with these carbonates (Ward & Halley, 1985).

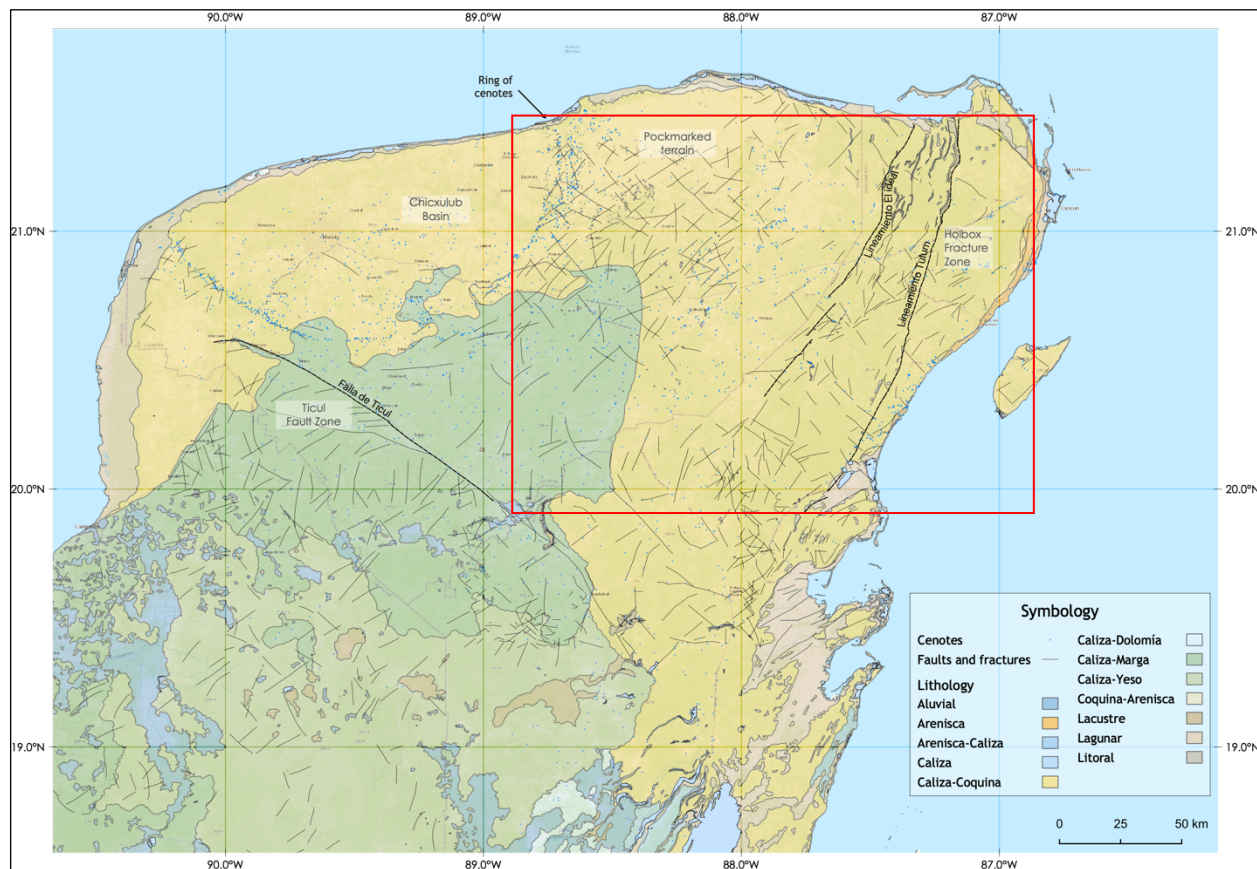


*Figure IV-2 Regional scale fracture features with surface expression are: Ring of Cenotes (Perry et al., 1995), the Sierrita de Ticul fault line, the Holbox fracture zone, the Rio Hondo block fault zone, and the La Libertad fault zone (south of figure extent). The five recognized physiographic regions with variable degrees of distributed fractures are: the coastal zone that spans 1-10 km of the peninsula perimeter (not marked), the northwestern coastal plain (NWCP) that broadly overlaps with the Chicxulub basin demarcated by the Ring of Cenotes, the northeastern coastal plain (NECP), the central hill district (CHD), and the eastern block fault district (EBFD).*

A hypothetical cross-section perpendicular to the coast showing the sequence of different Pleistocene units and caliche horizons is presented in Figure IV-3.

With the onset of the Holocene rise of sea level, the now consolidated eolian ridges were partly eroded and inundated. The islands of Contoy, Mujeres, and Cancun are mostly remnants of the Pleistocene eolianite ridges. Position and alignment of Isla Blanca suggest that it is underlain by a Pleistocene dune ridge. Coastal land area from Cancun northward has been built up by

progradation of beach and dune ridges and mangrove swamps during the Holocene high stand of sea level (Ward, 1997).

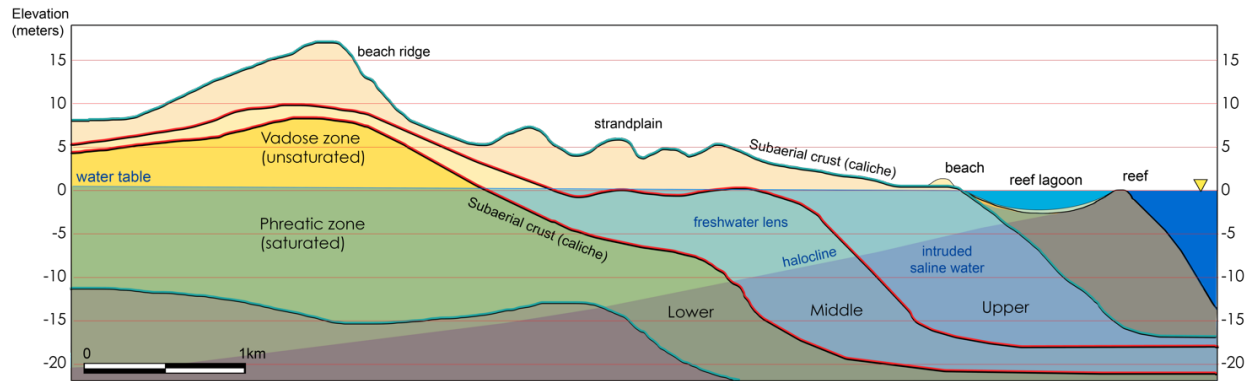


Figure IV-3 Hypothetical cross section perpendicular to northeastern coast of the Yucatán Peninsula, showing stratigraphic relationships of older Pleistocene units and caliche horizons. Modified from Ward & Halley (1985).

Table IV-1 Pleistocene and Holocene stratigraphic relationships of carbonates on islands and the main land coast of northeastern Yucatán. From Ward (1997).

		Oxygen Isotopic Stage	Eolian-ridge islands	Cozumel	Yucatán coast
Holocene	1		Blanca eolianite Cancun eolianite	Lagoon mud Beach deposits	Coral reef Lagoon mud Beach sediment Mangrove swamps
	2		Caliche crust	Caliche II	Caliche crust
	3				
	4				
Pleistocene	5	a	Mujeres eolianite	Eolianite	Tulum eolianite
		b			
		c	Contoy eolianite Puerto Viejo eolianite		
		d			
	e		Super-Caliche I facies	Strandline grainstones Coral reef – lagoon limestones	
	6			Caliche I	Caliche crust
	7 (?)			Sub-Caliche I facies	Shallow marine limestone and dolomite

#### IV-1.3 DENSITY STRATIFIED COASTAL KARST AQUIFER

The most iconic features of the peninsula's physiography are *cenotes*, or dissolution dolines/sinkholes, caverns and caves above and below the water table. Present explored extent suggests they are concentrated in the northern portion of the Peninsula even though that correspond with the zone targeted by explorers along the Riviera Maya section of the coastline from Playa del Carmen to near Tulum, and an apparent decrease towards the south of the peninsula although exceptional karst features are well known into Belize (e.g. Boundary Fault, Vaca Plateau, Yalbac Hills, Chiquibul System, and the well-known Blue Hole off-shore; Miller, 1983). The emergence of the carbonate sequence in the NNE sector of the Yucatán Peninsula began during the Neogene period and has been subject to intense processes of dissolution and erosion.

The Yucatán Peninsula near-surface young limestone diagenetically immature, retaining the majority of its primary ~25% porosity. It is characterized by high permeability including leading to an exceptionally low hydraulic gradient on the order of  $10^{-5}$ , or cm:km slopes (Beddows, 2004). Meteoric water infiltrates rapidly, with negligible overland flow, including to the complete absence of true surface rivers on the whole north Yucatán Peninsula to the foothills of the Maya Mountains near Belize. Meteoric water then accumulates in the subsurface forming a thin freshwater lens that floats as a distinct and defined volume on top of denser near-normal saline water mass embedded in the matrix of the rock and deeper conduits, whose origin is marine intrusion and tidal pumping. The contact between the two distinct fresh and marine waters bodies, forms a mixing zone or halocline which is in itself an important geological and hydrogeochemical component of the aquifer.

In karst landscapes, soluble bedrock such as limestone or dolomite is dissolved by water enriched with carbon dioxide. On the surface, karst denudation operates dissolving material under conditions open to the atmosphere and removed by the aqueous solution. Within the karst aquifer, material is removed from narrow fissures and bedding plane, in which water enriched by carbon dioxide circulates. The voids are enlarged over time, altering the permeability of the bedrock, and changing the flow patterns. Dissolution then proceeds either under open-system in contact with the atmosphere, such as in soil, epikarst, and vadose caves, or under closed-system conditions with solution completely filling the voids, as occurs in phreatic caves and other voids below the water-table. Closed system is decoupled from the atmosphere (Kaufmann, 2009).

Mixing corrosion is a result of the nonlinear relation between the calcium equilibrium concentration and the carbon dioxide pressure (Figure IV-4). The mixing of two solutions saturated with respect to calcite, but with different carbon dioxide concentrations, results in an undersaturated with respect to calcite (black dots). As a consequence, water flowing in the karst aquifer through the network of small fissures and cracks all hydrologically connected will mix everywhere and results in additional distributed corrosive power. The mixing corrosion, though much less effective than the normal corrosion, will also occur in small fissures deep into the phreatic zone.

The freshwater lens is the only source of fresh water in the Yucatán peninsula since prehistoric times, renewable only by seasonal rain. This aquifer is, due to its characteristics, intrinsically vulnerable to contamination (Escolero et al., 2002; Marín et al., 2016).

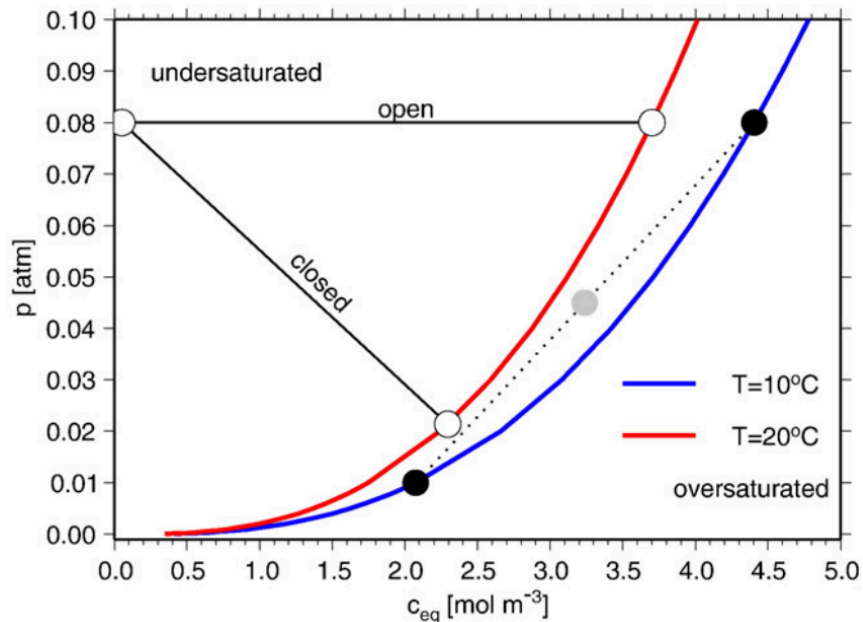


Figure IV-4 Calcium equilibrium concentration as a function of carbon dioxide pressures. Different pathways for solutions towards their equilibrium values are shown. In open systems, dissolution proceeds along horizontal (solid) lines, while in closed systems dissolution proceeds along sloping (solid) lines. The effect of mixing two saturated solutions equally (black circles), results in a new undersaturated solution (grey circle), which again can dissolve calcium. From Kaufmann (2009).

The groundwater system is made up of the aquifer, its subcomponents, and the biogeochemical processes that take place there. The subcomponents of the system are: **a)** the vadose zone, which is the freely draining rock from the earth's surface, down to the **b)** water table, through which the water passes, recharging and infiltrating the aquifer; **c)** the freshwater lens, which may also commonly have sub-stratifications within it, **d)** the halocline demarcating the base of the fresh water lens, and that may span anywhere from 10 cm to 20+ m thickness in transitioning from fresh (or near fresh) water to full marine salinity, and **e)** the saltwater layer, which is also sub-stratified. The set of these underground zones form the coastal karst aquifer of the Yucatán Peninsula (Figure IV-5).

The functioning of the aquifer depends on the set of hydrological, geological, chemical and biological processes that take place in the mother rock or matrix, the network of fractures and the network of underground conduits organized and of high permeability and hydraulic conductivity.

Meteoric recharge on coastal unconfined aquifers results in a freshwater lens (FWL) floating on top of higher density saline water zone (SWZ) intruding from the coastal margin. Different classical studies in coastal aquifers reviewed in Nunes et al. (2002) indicate that the level of the base of the FWL below sea level is related to the elevation of the water table above sea level by a proportionality ratio of 40:1, derived from the density difference between fresh and saline water, and known as the Ghyben-Herzberg relationship. Importantly though, this ratio also assumes a homogeneous and isotropic geological matrix, neither condition being met in young eogenetic carbonate. The classic Ghyben-Herzberg estimate of the depth of the freshwater-saltwater interface, together with the Dupuit approximation, is a useful tool for developing analytical solutions to many seawater intrusion problems. The limited application of the assumptions combined with the extreme karstification, leads to the ratio being half the calculated, at 20:1 for the Yucatán Peninsula (Beddows, 2004).

The origin of the cenotes is due to the geomorphological process called karstification, which consists in the combination of dissolution mechanisms of limestone rock, collapse and infill sedimentation including abiotic/biotic speleothems. The processes are governed by intrinsic and extrinsic factors, which act on different spatial-temporal scales, generating a wide range of forms and degrees of karstification. Intrinsic factors include lithology, degree of matrix porosity, and rock fracture. Extrinsic factors include climate, temperature, vegetation, the mix of fresh and salt water, and the duration of exposure to the process in question (Worthington, 2007).

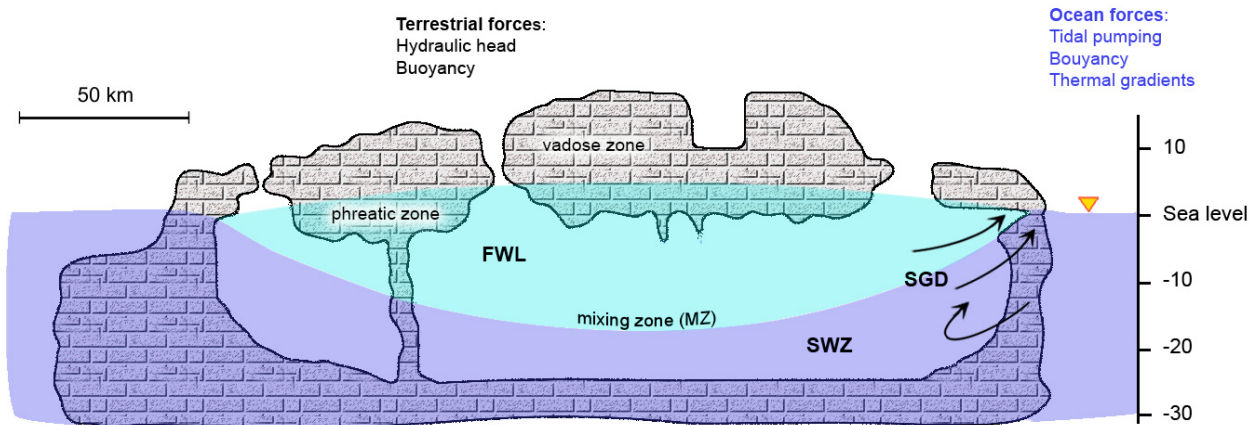


*Figure IV-5 Schematic conceptual diagram showing the 'freshwater lens' (FWL); saline water zone (SWZ); mixing zone (MZ), also called halocline; submarine groundwater discharge (SGD) and cave formations in a coastal density stratified carbonate aquifer. With sea level changes, the whole system including the intruding marine water, the mixing zone, and the freshwater lens, all move coherently, upward during sea level rise, and downward when sea level falls.*

Cave passages at or near the coast and within beach ridges consist of shallow anastomosing passages that crosscut the coast and/or the beach ridges. Analyses of cave data and maps indicate that cave system configuration and passage morphology are influenced by regional and local structures as well as stratigraphy (Kambesis, 2013). Passage morphologies are also influenced by local conditions such as ceiling collapse or speleothem development both which may result in stream diversion. Comparison and analyses of the underwater caves within the vadose-epiphreatic zone caves of the region indicated that they share the same characteristics with the exception of elevation and location with respect to the coast.

The vadose-epiphreatic zone caves occur at slightly higher elevations than the submerged caves and are absent in areas less than a kilometer from the coast. The very similar morphologies of both groups of caves indicate that speleogenesis of vadose-epiphreatic zone caves involves same mixing-zone corrosion processes as underwater caves.

Halocline deepens with inland, with greater distance to the coast, ranging from 5-6 m at the eastern coast of the Yucatán Peninsula, and reaching up to 40 m at 20 km inland (Beddows, 2004). Close to the eastern coastline, salinity just above the halocline is higher and the temperature difference between water layers is larger, whereas with the increase of distance from the coast salinity decreases above the halocline as it gets deeper, and the temperature difference of the two water masses tends to disappear. This suggests a hydrological continuum preserved by water circulation through the large underground conduits and cave passages in the area (Beddows et al., 2007).

## **IV-2 METHODS**

This chapter describes the different methodologies employed during this research. The set of protocols and instrumentation includes fieldwork, experimental, and data analysis stages.

### **IV-2.1 FIELDWORK**

Collection of samples was performed during multiple field campaigns spanning 2011-2016 to the Mexican Caribbean area. Planning for underwater sampling was made to avoid two consecutive days of immersions, for maintaining physical health purposes, thus intercalating “wet” cave diving activities with “dry” vadose zone geological profiles during field campaigns.

Established methodologies were conducted on each sampling site, including a description of the geological setting of the place, sketch of stratigraphic profiles (SedLogs), along with detailed lithological description and thickness of bedrock units, record of fossils, sedimentary structures, collection of rock samples as hand-size specimens from different strata and registration on the sketched sedimentary column. A general description is as follows.

### **Vadose zone sampling**

- Generally, quarries, dry caves, and roadway/urban outcrops.
- General geological setting.
- Sketch of sedimentary logs.
- Depth profile / through different identifiable units.

### **Phreatic zone sampling**

- Location of sampling sites on an exploration map prior to diving.
- Technical cave diving. Entrance through a cenote.
- Time-constrained.
- Depth profiles.
- Rock sampling below and above the halocline.



*Sketching a sedimentary column of medium—size rock wall at an abandoned quarry in the eastern Quintana Roo (2014).*

#### IV-2.1.1 Rock Sampling

Rock sampling consisted of separating hand-specimen size rocks with the help of a rock hammer and a chisel in the field and placing these in labelled bags for storage and transport. Rock samples were obtainable down to ~48 m water depth by cave diving. A total of 385 samples were collected in both *vadose* and *phreatic* environments. When possible, depth stratified sampling above and below the halocline was also conducted.

The study area geographically spans from -89.174, 19.571 to -86.931, 21.431 (WGS84). Sampling sites depth distribution ranges from -48 to +18 m in elevation.

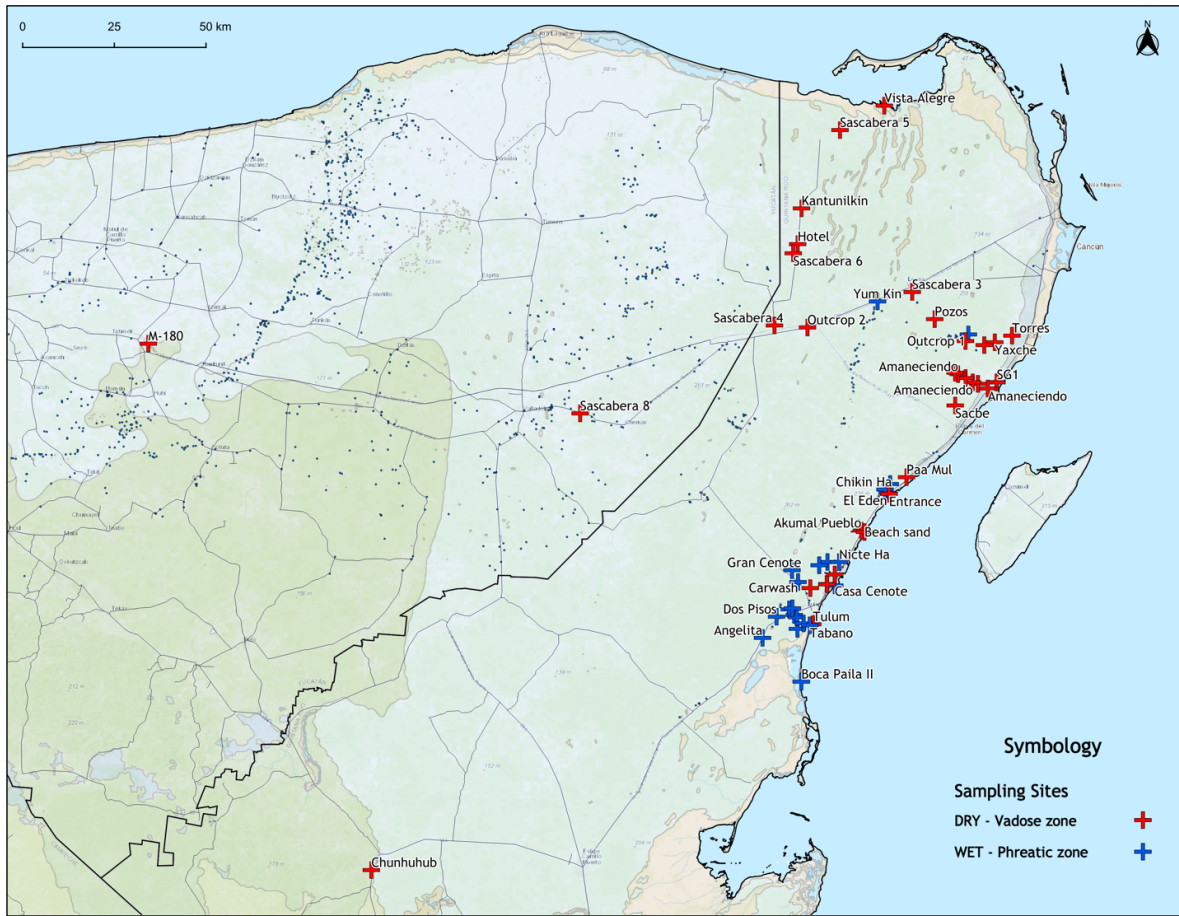


Figure IV-6 Location of sampling sites, where phreatic zone samples obtained by cave diving marked in blue; vadose zone samples are marked in red, for a total of 385 samples in 38 different sites.

## IV-2.2 ICP-OES GEOCHEMICAL ANALYZES

This section describes the conventional methods employed to accomplish multi-elemental geochemical quantification on rocks, from sample preparation protocols, standard solutions used, and analytical considerations of the method and instrumentation used.

ICP-OES is widely used for elemental analysis of most metals, sulfur and phosphorous in concentrations down to the ppb level (Todorov et al., 2014). ICP-OES offers a number of advantages over atomic absorption spectrometry: 1) a greater number of elements can be determined, 2) an array of elements can be analyzed essentially simultaneously, and 3) a wider dynamic range of concentration can be determined for each element.

A Varian-MPX model ICP Spectrometer at IMSERC at Northwestern University was used with axial view configuration, with a 180 slot autosampler. It can cover the spectral range from 175-785 nm. This means that elements with emission lines in the far UV, such as sulfur, phosphorous, and aluminum can be detected and determined.

*Table IV-2 ICP-OES wavelengths used and limits of detection (LOD) for selected elements under simultaneous multi-element conditions with axial view and a concentric nebulizer. Source: US EPA Method 200.7; Martin et al. (1994).*

<i>Element</i>	<i>Atomic #</i>	<i>λ (nm)</i>	<i>LOD (mg/L)</i>	<i>Element</i>	<i>Atomic #</i>	<i>λ (nm)</i>	<i>LOD (mg/L)</i>
<i>Mg</i>	12	279.553	0.5	<i>Ca</i>	20	393.366	0.5
		279.8	1.5	<i>Mn</i>	25	257.604	0.04
<i>Al</i>	13	308.215	1.2	<i>Fe</i>	26	238.204	0.3
<i>Si</i>	14	251.607	0.9			240.488	0.05
<i>P</i>	15	213.617	4			259.940	0.06
		214.912	2.9	<i>Sr</i>	38	421.534	0.5
		177.432	5	<i>Ba</i>	56	493.390	0.04
<i>S</i>	16	180.669	5				
		181.971	10				

### IV-2.2.1 Sample and standard preparation

A conventional laboratory oven was used for sample drying. All solutions and sample dilutions were prepared using ultrapure water (resistivity of 18.2 MΩ cm) obtained from the laboratory purification system. The sample masses were measured using an analytical with a resolution of 0.0001 g and a maximum load of 220 g, where 100 mg of powdered sample is weighted and dissolved in 2% grade A nitric acid. A subsequent set of 1:50 dilutions for all samples was prepared in 2% nitric acid to assure Ca and Mg concentrations in the whole set are between 0-40 mg L<sup>-1</sup> (ppm), within good range on the calibration curve. Conventional laboratory materials were cleaned by immersion in 10%<sub>v/v</sub> HNO<sub>3</sub> for 24 h.

Standard solutions (S<sub>n</sub>) for all elements determined by ICP-OES were prepared before its use by serial dilution of a 10 mg L<sup>-1</sup> solution (*Fluka, TraceCERT*). The calibration curves were prepared by serial dilution in 2%<sub>v/v</sub> HNO<sub>3</sub>, with element concentration ranging as shown in Table IV-3.

*Table IV-3 The three standard solutions concentration range (ppm) for selected elements used for calibration curve in ICP-OES analyses.*

<i>Element</i>	<i>Ag, Be, Bi, Cs, Cd, Co, Cr, Cu, Ga, In, Mn, Ni, Pb, Rb, Tl, V</i>	<i>Al, Ba, K, Li, Na, P, S, Sr</i>	<i>Ca Fe Mg Si</i>
<b>S<sub>0</sub> blank</b>	0	0	0
<b>S<sub>1</sub></b>	0.125	0.625	1.25
<b>S<sub>2</sub></b>	0.25	1.25	2.5
<b>S<sub>3</sub></b>	0.5	2.5	5
<b>S<sub>4</sub></b>	1	5	10
<b>S<sub>5</sub> high</b>	2	10	20

#### IV-2.2.2 Comparison between analytical runs

Due to the logistics of obtaining the samples, which involved field trips to the Mexican Caribbean in different years, and transportation of physical hand-sized rock samples, they were grouped in two separated batches for ICP-OES analyses. The first batch was analyzed employing a 10-element standard, and the second batch was analyzed employing a commercial 30-element standard. The second set of samples were analyzed for the 30 elements: silver (Ag), aluminum (Al), barium (Ba), beryllium (Be), bismuth (Bi), calcium (Ca), cadmium (Cd), cobalt (Co), chrome (Cr), cesium (Cs), copper (Cu), iron (Fe), gallium (Ga), indium (In), potassium (K), lithium (Li), magnesium (Mg), manganese (Mn), molybdenum (Mo), sodium (Na), nickel (Ni), phosphorous (P), lead (Pb), rubidium (Rb), sulfur (S), silicon (Si), strontium (Sr), thallium (Tl), vanadium (V), and zinc (Zn).

In order to validate results between the two separate runs, about 75 samples from the first batch were re-analyzed in the second batch. Accordingly, this analytical validation allows to compare with high certainty results from both analytical runs. Comparison of both runs is shown in Figure IV-7 from which analytical ranges can be inferred for each of the elements.

In general, analytical result values obtained are coherent and consistent; element concentrations are within expectable ranges for carbonate rocks with little siliciclastic inputs. Some elements were persistently under the analytical detection limit (LOD) of the ICP method and instrument used in most of the samples analyzed, as that is the case for Ag, Be, Bi, Cs, Ga, and Zn. If these elements are present in the rocks, their concentrations are below the LOD in most samples, and therefore are excluded from further considerations as otherwise noted.

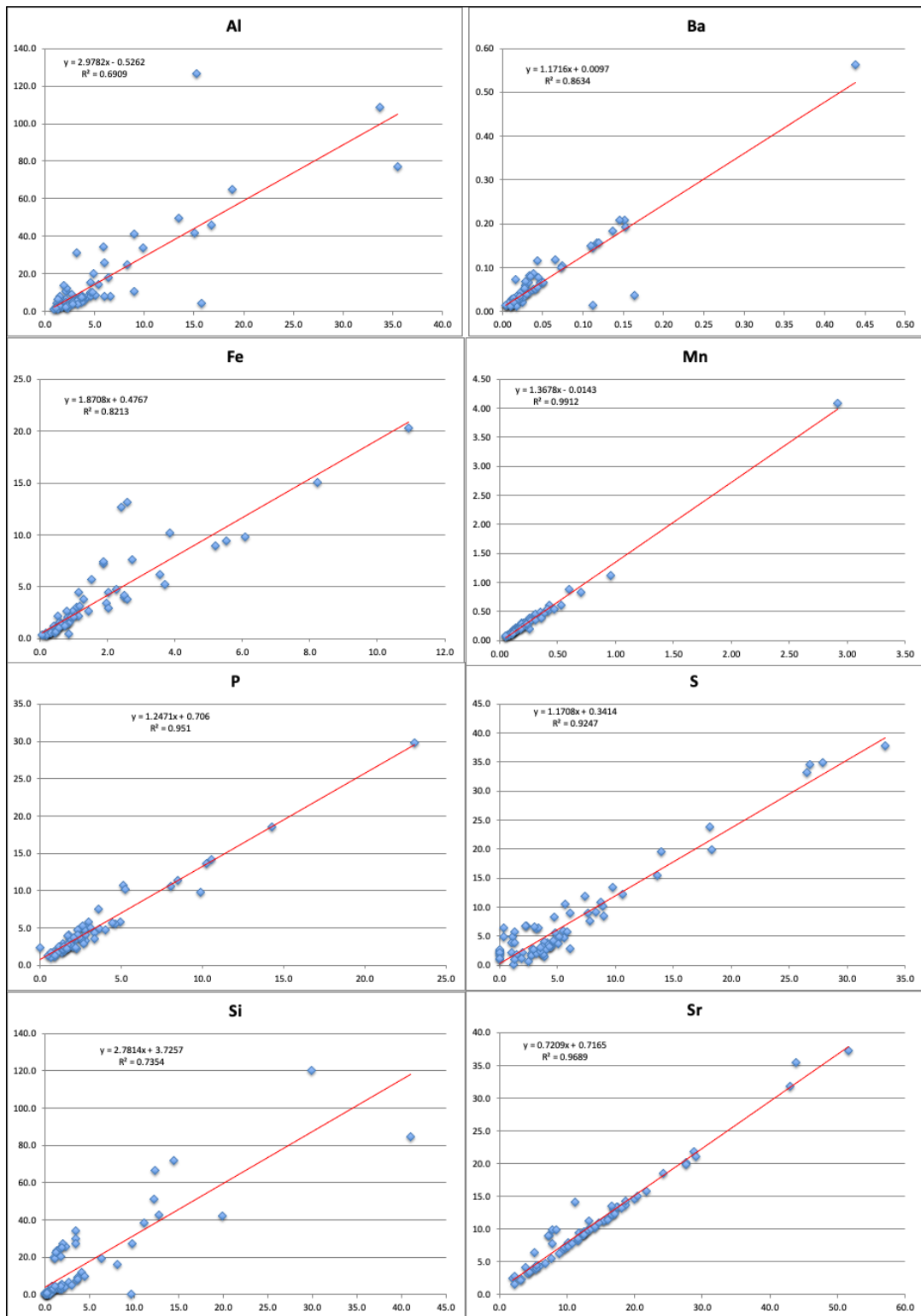


Figure IV-7 Comparison of results (mmol/kg) 8 selected elements (Al, Ba, Fe, Mn, P, S, Si, Sr) for the 75 samples that were run initially with 10 element standards in the first batch, and then repeat analyzed with the 30-element standard in two analytical runs.



### IV-3 RESULTS & BULK ROCK GEOCHEMISTRY OVERVIEW

This section presents the quantification of an array of elements for a considerable collection of rock samples. A total of 385 samples were analyzed, with 75 replications as described in the last section of this chapter. Thirty (30) elements were analyzed in the present study, each element chosen by multi-factor criteria according to its presumed abundance in the rocks, its importance to identifying diagenetic and pedogenic processes, its biogeochemical relevance, and to be suitable for quantification by ICP-OES methods. Some elements were included due to their presence in the 30-element standard even though LOD determinations were expected.

#### IV-3.1 BULK ROCK GEOCHEMISTRY

The *bulk rock* is here defined as the global average of the total of values of element concentration, regardless the sample origin, or depth. It is employed solely as a simple concept useful to rapidly explore element concentration ranges and relative distribution at a glance for the whole set of rock samples. No weighing has been applied to the calculated bulk rock values to account for differential number of surficial, vadose, and phreatic samples, nor distance from the coast or depth that broadly correlate with age and facies.

It is geochemically convenient to group elements relative to their contributions to rock composition, as *Major*, *Intermediate*, *Minor*, and *Trace* elements, the latter being those elements with most values at or below the detection limit (LOD) of the method employed in this research.

<b><i>Major elements</i></b>	Ca and Mg are in very high concentrations (>300 mmol kg <sup>-1</sup> ), and about two orders of magnitude above the other groups. Those were analyzed using a 1:50 dilution of dissolved sample solution.
<b><i>Intermediate elements</i></b>	Those elements between 0.3 – 300 mmol kg <sup>-1</sup> , in decreasing order of concentrations, are: Na, Al, Si, Sr, S, Fe, P, K, Li, and Mn.

<b>Minor elements</b>	Elements between the LOD and the value of 0.3 mmol kg <sup>-1</sup> , in decreasing concentration values, the third group is comprised of: Cr, Co, Ba, V, Cu, Ni, Pb, Cd, and Mo.
<b>Trace elements</b>	Elements that were generally below the limit of detection (LOD) of the ICP-OES method employed in this study.

Figure IV-9 shows slice diagrams contrasting results for major, intermediate, and minor elements. Mean, maximum, minimum, and standard deviation values for the whole set analyzed can be found in **Appendix B**. Each pie chart excludes the elements not explicitly plotted, such that Ca + Mg = 100, since there was great variation in the bulk average concentration of the intermediate and minor elements.

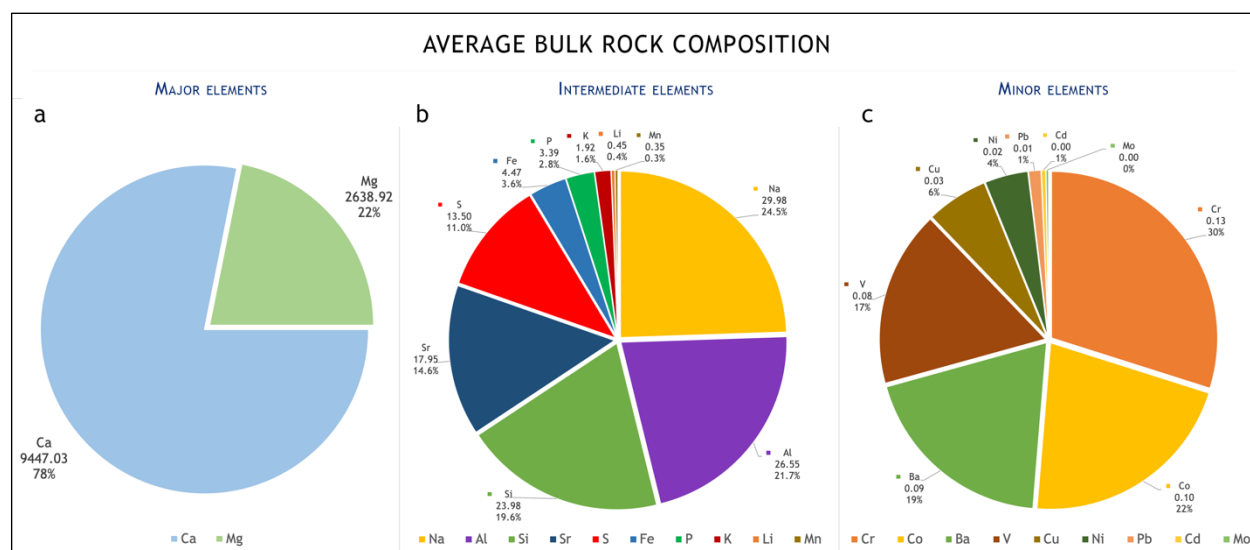


**Figure IV-9** Global average bulk rock composition ( $n=385$ ) for all elements considered in this study, grouped in a) Major elements (Ca, Mg); b) Intermediate elements (Al, Ba, Fe, Mn, P, S, Si, Sr); c) Minor elements (Ba, Cd, Co, Cr, Cu, Ni, Pb, V); and Trace elements (Ag, Be, Bi, Cs, Ga, In, Rb, Tl, Zn), those below detection limit, not shown. Each panel excludes elements of other panels so % is not over the total. For total percentages see Table IV-5. Label values in mmol kg<sup>-1</sup> of dry rock (upper) and mol % (lower).

Table IV-5 Global average bulk rock composition showing mean, minimum, maximum, and standard deviation values obtained by ICP-OES quantification in rock samples ( $n = 385$ ). Concentration values given in mmol per kg of dry rock ( $\text{mmol kg}^{-1}$ ).

	<i>Element</i>	<i>Mean mmol kg<sup>-1</sup></i>	<i>Min mmol kg<sup>-1</sup></i>	<i>Max mmol kg<sup>-1</sup></i>	<i>Std Dev (p)</i>	<i>mol %</i>
MAJOR	<i>Ca</i>	9447.03	5435.44	12984.34	992.36	86.5
	<i>Mg</i>	895.37	48.36	4703.95	903.50	13.5
INTERMEDIATE	<i>Na</i>	29.98	2.04	441.16	54.75	0.25
	<i>Al</i>	26.55	1.17	605.18	68.20	0.22
	<i>Si</i>	23.98	0.22	696.26	76.13	0.20
	<i>Sr</i>	17.95	1.39	93.17	20.82	0.15
	<i>S</i>	13.50	0.27	91.35	15.61	0.11
	<i>Fe</i>	4.13	0.22	103.90	10.33	0.04
	<i>P</i>	3.41	0.15	29.79	3.65	0.03
	<i>K</i>	1.92	0.17	32.59	4.06	0.02
	<i>Li</i>	0.45	0.28	4.87	0.42	$3.7 \times 10^{-3}$
	<i>Mn</i>	0.35	0.02	4.08	0.43	$2.9 \times 10^{-3}$
MINOR	<i>Cr</i>	0.13	0.00	0.77	0.10	$1.10 \times 10^{-3}$
	<i>Co</i>	0.10	0.00	0.96	0.15	$7.86 \times 10^{-4}$
	<i>Ba</i>	0.09	0.01	0.56	0.08	$7.12 \times 10^{-4}$
	<i>V</i>	0.08	0.01	2.02	0.17	$6.28 \times 10^{-4}$
	<i>Cu</i>	0.03	0.00	0.26	0.03	$2.22 \times 10^{-4}$
	<i>Ni</i>	0.02	0.04	0.27	0.05	$1.55 \times 10^{-4}$
	<i>Pb</i>	0.01	0.03	0.10	0.01	$4.46 \times 10^{-5}$
	<i>Cd</i>	0.00	0.01	0.20	0.02	$1.64 \times 10^{-5}$
	<i>Mo</i>	0.00	0.03	0.18	0.02	$9.92 \times 10^{-6}$
TRACE	<i>Ag</i>	N/A	N/A	N/A	N/A	N/A
	<i>Be</i>	N/A	N/A	0.065	N/A	N/A
	<i>Bi</i>	N/A	N/A	0.003	N/A	N/A
	<i>Cs</i>	N/A	N/A	N/A	N/A	N/A
	<i>Ga</i>	N/A	N/A	0.044	N/A	N/A
	<i>In</i>	N/A	N/A	0.025	N/A	N/A
	<i>Rb</i>	N/A	N/A	0.302	N/A	N/A
	<i>Tl</i>	N/A	N/A	0.005	N/A	N/A
	<i>Zn</i>	N/A	N/A	N/A	N/A	N/A

#### IV-3.1.1 Major elements: Ca and Mg

The *major elements*, Ca and Mg, comprise 99 weight % of the rock. Of that 99%, the bulk Ca accounts for 37.6% weight (96.14 mol %), which corresponds accordingly to the expected value of ~40 w % assuming an ideal pure calcium carbonate rock. Despite the Yucatán platform having negligible depositional allochthonous siliciclastic contributions, a variety of elements are expected as replacement, trace, and impurities, as discussed in the upcoming pages.

Mean calcium concentration in the rock, given in  $\text{mmol}_{\text{Ca}} \text{kg}^{-1}_{\text{rock}}$  and expressed as  $[\text{Ca}]_{\text{rock}}$ , is  $9447.03 \pm 992.36$  with a min-max range from 5,435.44 to 12,984.34  $\text{mmol kg}^{-1}$ . Magnesium (Mg) is unsurprisingly the second most abundant element. Diagenetic processes can lead to Mg enrichment of limestone by dolomitization and/or replacement of  $\text{Ca}^{2+}$  by  $\text{Mg}^{2+}$  ions in the crystal lattice.  $\text{Ba}^{2+}$  and  $\text{Sr}^{2+}$  also can replace Ca as they belong to the same periodic group and thus behave chemically similar. Distribution of this element across the whole set of samples is heterogeneous as the high standard deviation between samples ( $n = 385$ ) relative to mean accounts. Mean magnesium concentration in the rock  $[\text{Mg}]_{\text{rock}}$ , is  $895.37 \pm 903.50$  with a minimum concentration of 48.36 and a maximum of 4,703.95  $\text{mmol kg}^{-1}$ .

In addition to be the principal cation in carbonate limestone, Ca is also present as calcium sulfate, either as anhydrite ( $\text{CaSO}_4$ ), or its hydrated form, gypsum ( $\text{CaSO}_4 \cdot 2\text{H}_2\text{O}$ ). Thin to even massive units of these minerals have been reported in different cores from the UNAM drilling project (Urrutia Fucugauchi et al., 1996; Ward et al., 1995), disposed mainly over Ticul Fault and a transect from the inside— going eastern outside the Chicxulub crater. They are commonly presented as evaporites even when observed at depths of 200 – 2,000 m below the surface (López-Ramos, 1975; Perry et al., 2002; Urrutia-Fucugauchi et al., 2011; Ward et al., 1995).

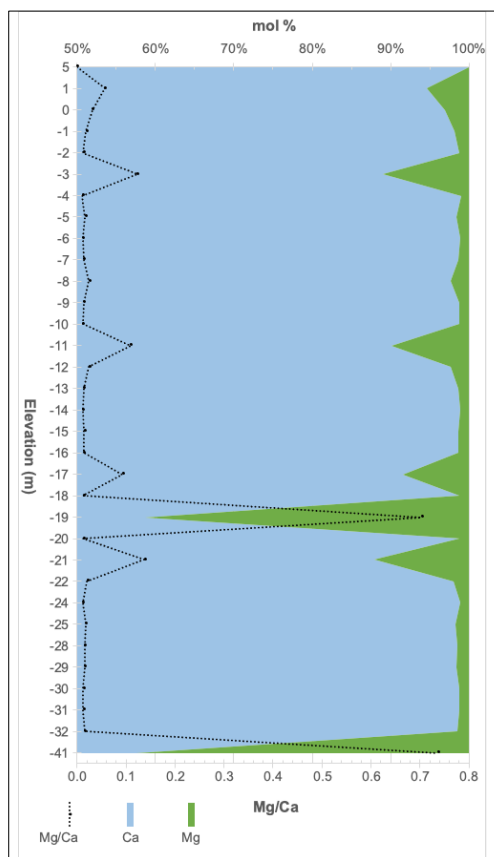


Figure IV-10 Depth-average representation of Ca and Mg concentration in mol %. Mg/Ca molar ratio is also shown. Note that the elevation bin sizes are not equally sized, based on the number of samples available for each bin. Distribution statistics for each elevation bin not shown.

Global average concentrations include all of the samples in a single packet. Depth-average means the MEAN value at a depth interval, for that element. This approach perhaps does not possess a physical or geological meaning, because it does not account for specific geological settings, but it does illustrate depth and concentration ranges. The standardized relative to sea level, is based on the water table being approximately at sea level due to the very low hydraulic gradient ranging from 7–10 mm/km through most of the northern part of the peninsula (Beddows, 2004; González-Herrera et al., 2002). The water table rises only a few centimeters even with kilometers distance inland, and for coastal sites it is essentially the same.

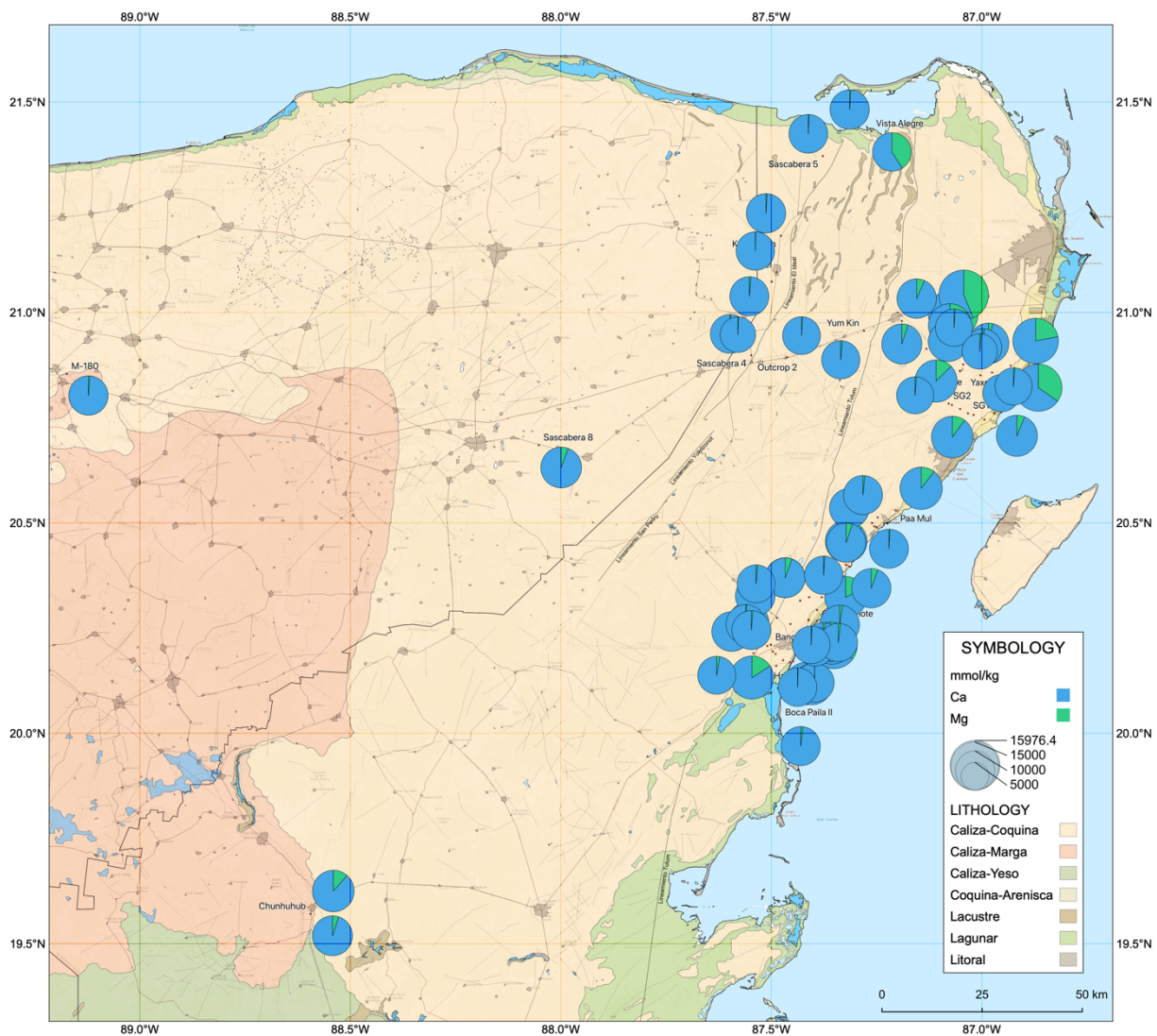


Figure IV-11 Regional distribution of Ca and Mg, excluding all other elements. Concentration values given in  $\text{mmol kg}^{-1}$ .

#### IV-3.1.2 Intermediate elements: Al, Ba, Be, Fe, K, Li, Na, P, S, Si, Sr

Elements whose concentrations are between  $0.3 - 300 \text{ mmol kg}^{-1}$ , are considered *intermediate elements*. In decreasing order of concentrations, are Na, Al, Si, Sr, S, Fe, P, K, Li, and Mn. Of these, the first 5 account for 90+% of the bulk intermediate elements. Subsequently, the Fe and P, are 4.5 and 3.4 % respectively.

***Alkali (Group 1) metals: Li, Na, K***

Alkali metals considered in this study include Li, Na, and K, most probably sourced from marine waters at time of deposition, and from ocean aerosols as post-depositional process. Although discussed in latter sections, Barium (Ba) was added to the plots in this section by means of comparison respecting their depth-profile behavior (Figure IV-12).

Potassium (K) is present on an average concentration of  $1.92 \pm 4.06 \text{ mmol kg}^{-1}$ , and ranges from 0.17 to 32.59  $\text{mmol kg}^{-1}$  in the dataset.

Average lithium (Li) content in the rocks is  $0.45 \pm 0.42 \text{ mmol kg}^{-1}$ , having a minimum of 0.28 and a maximum value of 4.87  $\text{mmol kg}^{-1}$ .

With respect to sodium (Na), it is present in some samples at very high concentrations reaching up to 440  $\text{mmol kg}^{-1}$ , thus covering a wide range, with an average value of  $29.98 \pm 54.75 \text{ mmol kg}^{-1}$  and a minimum of 2.04  $\text{mmol kg}^{-1}$ . Mineral halite (NaCl) has been reported on cores from the UNAM drilling project (Urrutia Fucugauchi et al., 1996) taken near the southern margin of the Chicxulub impact crater. The core contains anhydrite-gypsum, halite, and celestite, at depths shallow enough to interact with groundwater during the Cenozoic (and presently saturated with saline water). Its sources could be either from saline intrusion or from halite formation under evaporative regimes. Saline intrusion is very high in the whole area of the northern Yucatán peninsula. In many water samples from shallow groundwater, Perry et al. (2002) reported Na/Cl values of 1.17, same as seawater values.

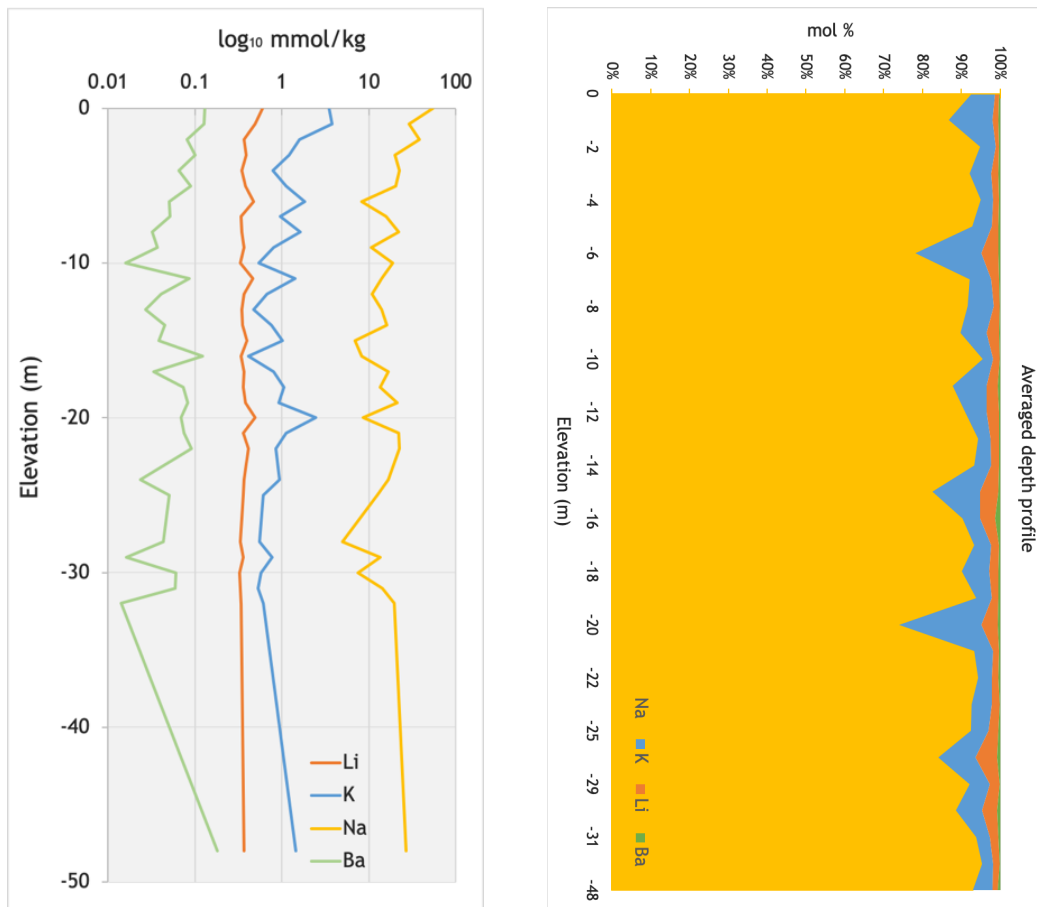


Figure IV-12 Depth-average concentration profiles for alkali and alkaline earth metals considered in this study (Ba, K, Li, Na), excluding all other elements. Concentration values given in  $\text{mmol kg}^{-1}$  and percentages are in mol %. Note the log scale on the left plot.

The bulk concentrations binned by elevation (depth) is relatively invariant for these alkali metals (Figure IV-12). In bulk, they show higher values near the coast. Some samples located inland around Kantunilkin Town present differences, in which K and Li relative proportions are higher than the coastal counterparts, where total concentrations seem to be higher. Coastal samples also show constant proportions with higher variations in relative abundance of these three elements advancing further inland.

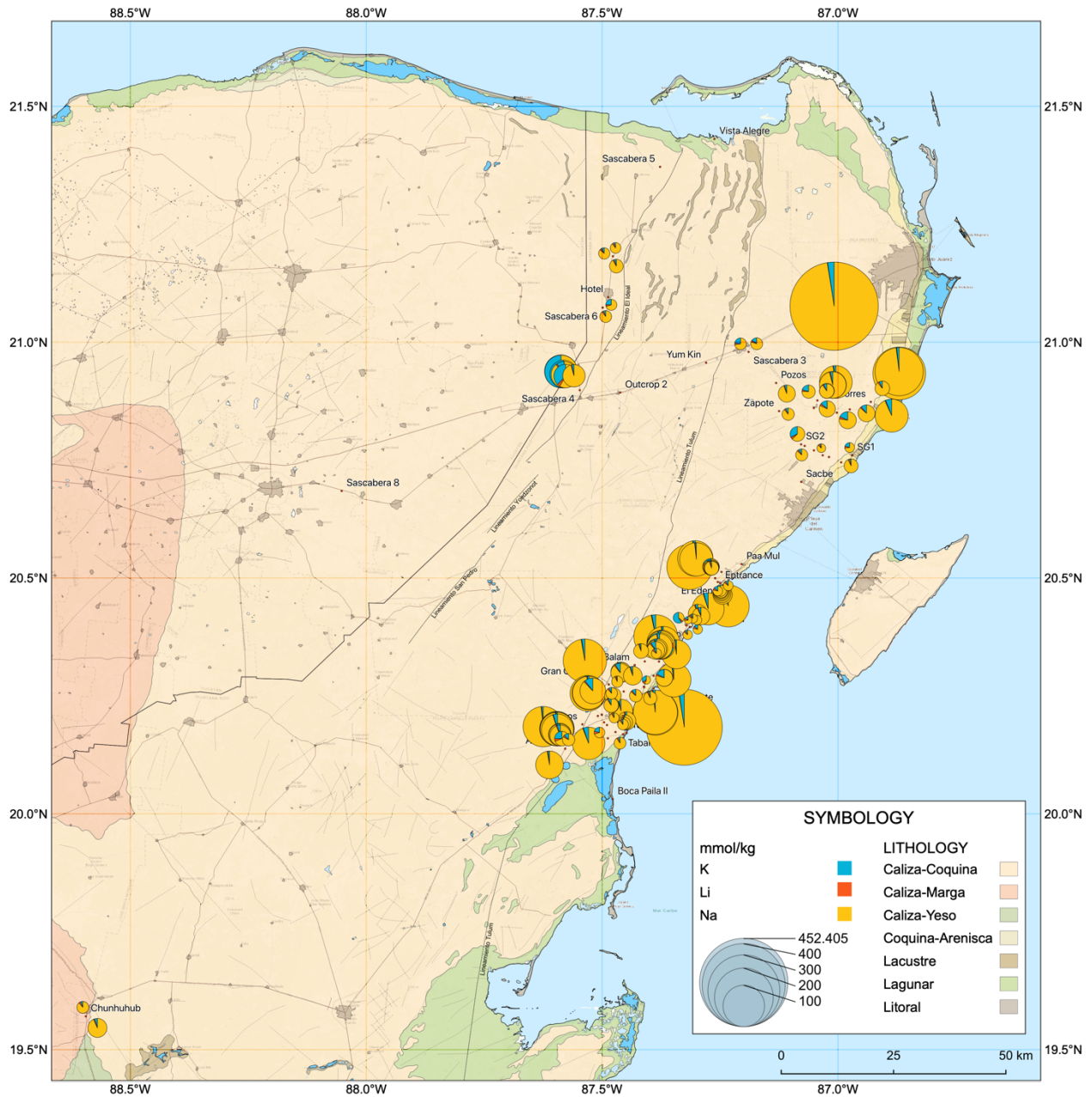


Figure IV-13 Geographic distribution of K, Li, Na, excluding all other elements. Concentration values given in  $\text{mmol kg}^{-1}$ .

***Alkaline earth (Group 2) metals: Ba, Be, Ca, Mg, Sr***

The alkaline earth (Group 2) metals are interesting because they share the same periodic group with Ca and Mg, and they are suitable replacement cation in carbonate minerals. Ca and Mg were described above.

Strontium (Sr) is commonly associated to carbonate rocks, as  $\text{Sr}^{2+}$  can easily replace  $\text{Ca}^{2+}$  cations in the crystal lattice. Bulk average calculations show  $[\text{Sr}]_{\text{rock}}$  equals  $17.95 \pm 20.82$  mmol  $\text{kg}^{-1}$ , with min=max of 1.39 and 93.17 mmol  $\text{kg}^{-1}$ . Pure strontium carbonate mineral, or strontianite ( $\text{SrCO}_3$ ), is far more insoluble than calcite ( $\text{CaCO}_3$ ) and magnesite ( $\text{MgCO}_3$ ). Sr is also environmentally common in coastal-marine locations in the form of the mineral celestite ( $\text{SrSO}_4$ ).

Barium (Ba) is also associated with carbonate rocks by replacement of  $\text{Ca}^{2+}$  cations. However, its concentration values are a fraction of those for strontium.  $[\text{Ba}]_{\text{rock}}$  ranges from 0.01 to 0.56 mmol  $\text{kg}^{-1}$ , with an average value of  $0.09 \pm 0.08$  mmol  $\text{kg}^{-1}$ .

Expectedly, most Beryllium (Be) values are below the LOD of the ICP-OES method employed for the whole batch of samples analyzed. Some samples gave positive results on the order of 0.05 mmol  $\text{kg}^{-1}$ . As most values were under LOD, this element was excluded from detailed analyses in further sections.

In bulk, these elements show a similar distribution than alkali metals, with higher concentrations in the rocks from the coastal zones and decreasing inland. However, their abundances are also relatively high in rocks from areas of known fractures (Holbox Fracture Zone), and massive phreatic caves (Tulum Area), both of which are preferential flow paths of groundwater transportation.

To quickly assess relative abundance of a 3-component system, ternary plots are used to represent geochemical data. These graphically depict the ratios of the three variables as positions in an equilateral triangle, and readily shows the relative abundance of elemental or mineral species.

A 3-component system, where relative contributions of Ba, Mg, and Sr for a large dataset ( $n = 290$ ) is shown in Figure IV-14a. Although there is one far outlier value for high relative abundance of Sr, most samples are expectably dominated by Mg when considering alkali group 2 metals and excluding calcium. Diagrams confirm that Mg, followed by Sr and then Ba is the most common replacement element for Ca, either within the crystal lattice of calcite or in form or in different mineralogical forms, in the northeastern Yucatán carbonate rocks.

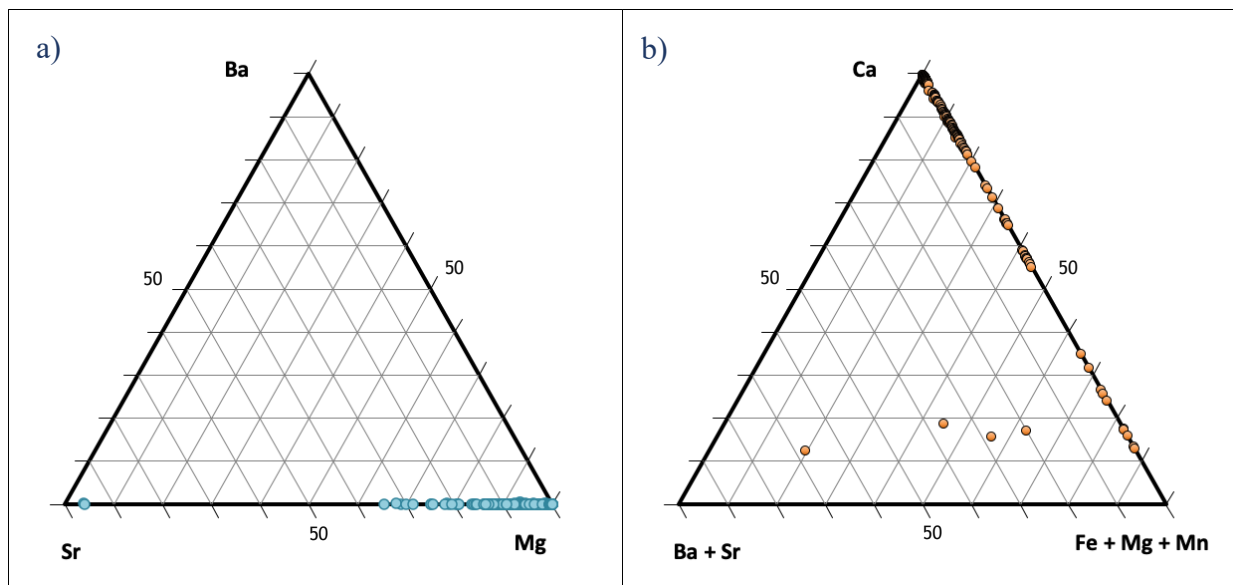


Figure IV-14 Ternary plot showing molar composition of rocks; normalized to mol % ( $n = 290$ ). Spreadsheet for creating tri-plots from Graham & Midgley (2000).

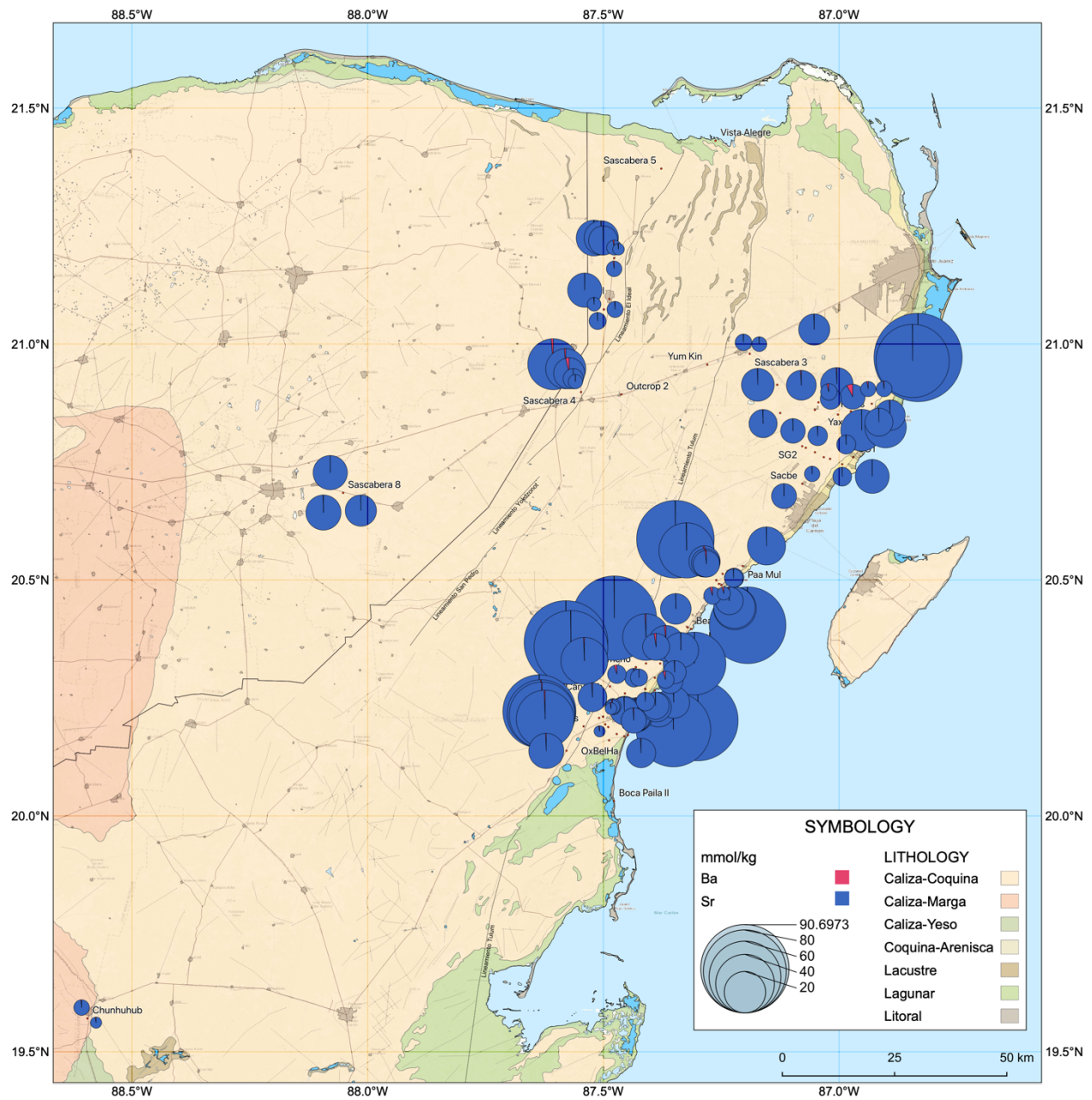


Figure IV-15 Geographic distribution of Ba and Sr excluding all other elements. Concentration values given in  $\text{mmol kg}^{-1}$ .

### IV-3.1.3 Metals forming carbonates and oxides: Fe and Mn

Minerals siderite ( $\text{FeCO}_3$ ) and rhodochrosite ( $\text{MnCO}_3$ ) are commonly associated with limestone in carbonate environments. Of particularly interest is the determination of its origins in

a depositional setting with no siliciclastic inputs as in the Yucatán platform. Hypothesis have been made (Bautista et al., 2011; Cabadas-Báez et al., 2010) about the provenance of these elements, which include: residual accumulation through time of components in the rock matrix since time of deposition; advective transport from the south through the Yucatán current onto the platform; tephra or volcanic ash origins; and eolian aerosol transport from Saharan dust into the Caribbean region (Doherty et al., 2008; Muhs & Budahn, 2009) and even into the Gulf of Mexico area (Chen et al., 2018; Lack et al., 2009).

Iron (Fe) has an average concentration  $[\text{Fe}]_{\text{rock}}$  of  $4.13 \pm 10.33 \text{ mmol kg}^{-1}$ , and ranges from a minimum value of 0.22 to a max value of 103.90  $\text{mmol kg}^{-1}$ . Manganese (Mn) concentration ranges from 0.02 to 4.08  $\text{mmol kg}^{-1}$ , with an average value of  $0.35 \pm 0.43 \text{ mmol kg}^{-1}$ .

In general, concentrations of Al, Fe, Mn, and Si are at least one order of magnitude smaller compared to those of the major elements.

Figure IV-14b depicts a multi-component system, where each one of the triangle corners represents either one or a conveniently grouped set of elements. Again, variability along the Ca-Mg axis shows the replacement behavior of Mg, in much greater abundance than the sum of Ba + Sr. Specially Sr is present in all samples, but only in a few contributes larger than the undifferentiated sum of Mg + Fe + Mn.

To get more detail on the Mg + Fe + Mn distribution, mol % ternary plots show the relative abundance of their most common carbonate mineral species as end members. Figure IV-16 presents the composition data under the grossly simplistic assumption that these elements exist only as carbonates the predominance of calcite and magnesite over other assumed carbonates.

The bulk system is dominated by calcite with variable Mg content. Bulk contributions from Al, Fe, Mn, and Si are negligible compared to Ca and Mg, but these remain fundamental elements in epikarst weathering processes, as discussed in Section IV-7.2. If there is dolomite mineral present, as discussed later, it would appear in the central region of the  $\text{CaCO}_3 - \text{MgCO}_3$  axis.

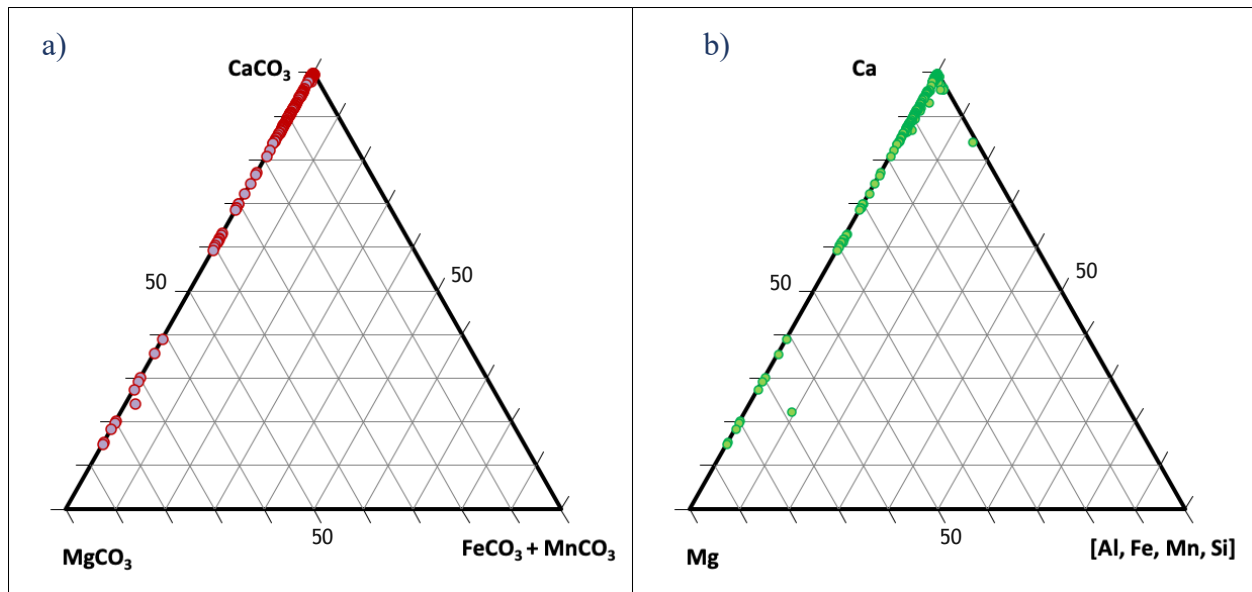


Figure IV-16 a) Mass  $\text{CaCO}_3 - \text{MgCO}_3 - (\text{Fe}+\text{Mn})\text{CO}_3$  ternary plot assuming all elements are present as their corresponding carbonate minerals; normalized mol % ( $n = 290$ ); b) Molar composition  $\text{Ca}-\text{Mg}-[\text{Al}+\text{Fe}+\text{Mn}+\text{Si}]$ , normalized mol %.

#### IV-3.1.4 Aluminosilicates: Al and Si

Al and Si are present naturally in soil-forming clays commonly as their oxides. Aluminosilicate minerals are composed of aluminum, silicon, and oxygen. They are a major component of kaolinite and other ubiquitous clay minerals,  $\text{Al}_2\text{Si}_2\text{O}_5(\text{OH})_4$ .

Aluminum ( $\text{Al } 26.55 \pm 68.20 \text{ mmol kg}^{-1}$ ) is the most abundant element present in the rocks that is not either alkali or alkaline earth, followed by Si ( $23.98 \pm 76.13$ ), then Fe ( $4.47 \pm 11.27$ ), and finally Mn ( $0.35 \pm 0.43$ ).

A further examination of the corresponding abundance of these elements in samples, shows Al and Si have highly correlated concentrations ( $r^2$  of 0.65, Figure IV-19) even when all samples with concentrations >LOD from the Peninsula are plotted together with no consideration of geological site character. The indicated 1:1 molar relationship as in some aluminosilicates, where the most common form would be the phyllosilicate *kaolinite*  $\text{Al}_2\text{Si}_2\text{O}_5(\text{OH})_4$ , or, written as aluminum silicate dihydrate  $\text{Al}_2\text{O}_3 \cdot 2\text{SiO}_2 \cdot 2\text{H}_2\text{O}$ . Geographical distribution of aluminum (Al), iron (Fe), manganese (Mn), and silicon (Si) also shows higher contributions of these four elements combined in rocks from the coastal zone, in general decreasing inland, although some samples far from the coast – and located near or very close to preferential groundwater flow paths, as the Holbox Fracture Zone, also show high values.

In general, Al and Fe increase proportionally on inland sample rocks, while Si general trend is to decrease landwards. To explore Mn low bulk distribution, it would be necessary to examine in more detail as in these figures is almost not perceptible. Some geochemical paths of Al, Fe, and Si are further discussed in Section IV-7.2 Residual Elements and Soils.

Exploring on the relationships in geochemical paths for Al and Si, Figure IV-18 shows their total concentrations to follow an approximately 1:1 molar ratio in the dataset ( $n = 290$ ).

Higher bulk abundance sequence from  $\text{Al} > \text{Fe} > \text{Si}$  is illustrated in Figure IV-19, showing the distribution of these three elements forcedly assumed as their oxides, in a diagram called SAF-plot (silicon-aluminum-iron), diagrams which are commonly employed in soil sciences and pedogenic transformation of rocks.

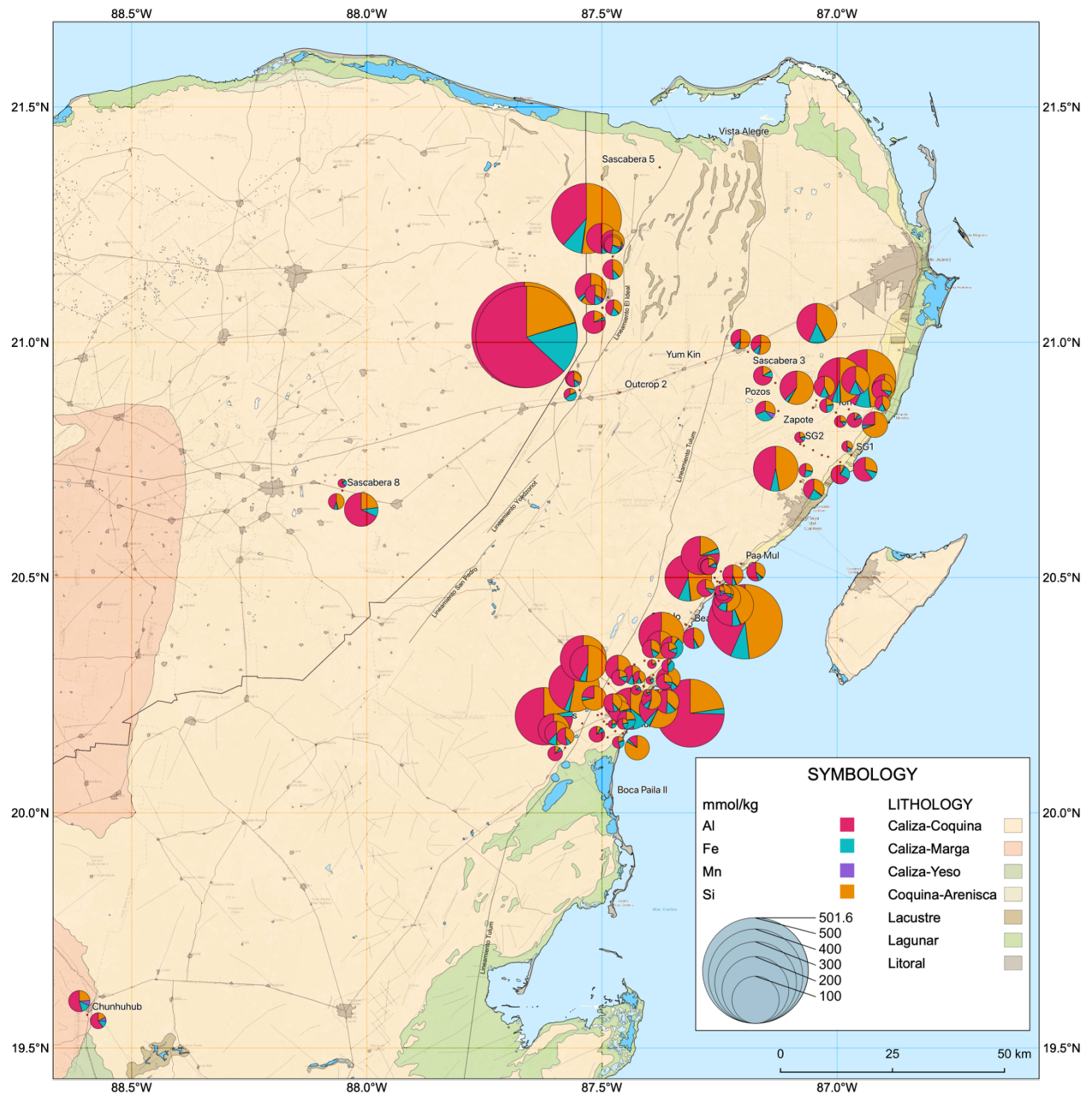


Figure IV-17 Geographic distribution of Al, Fe, Mn, and Si, excluding all other elements. Concentration values given in  $\text{mmol kg}^{-1}$ .

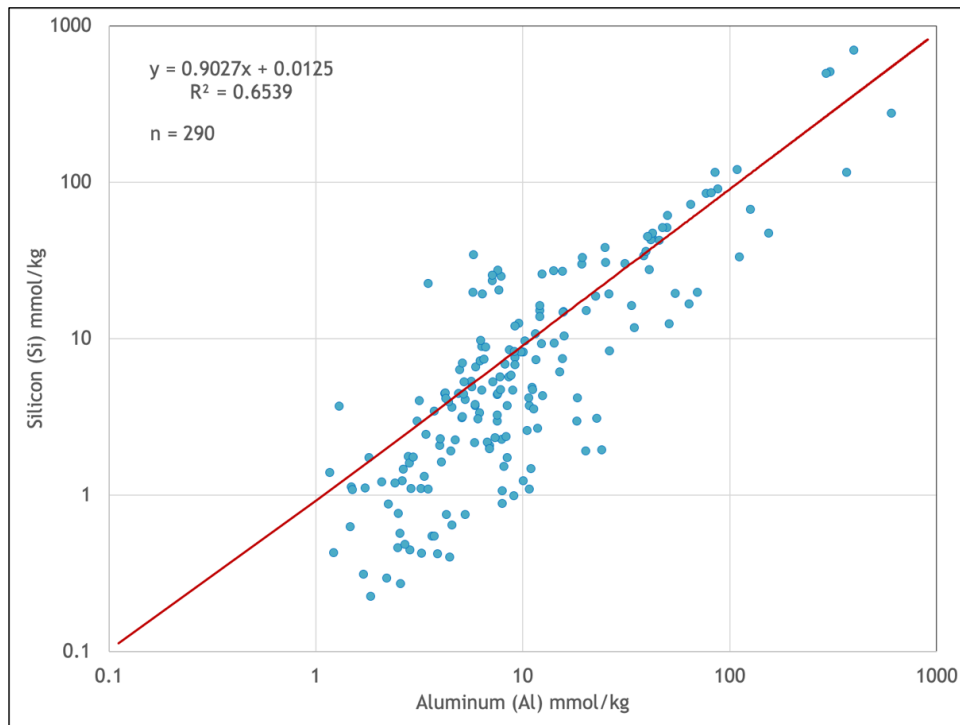
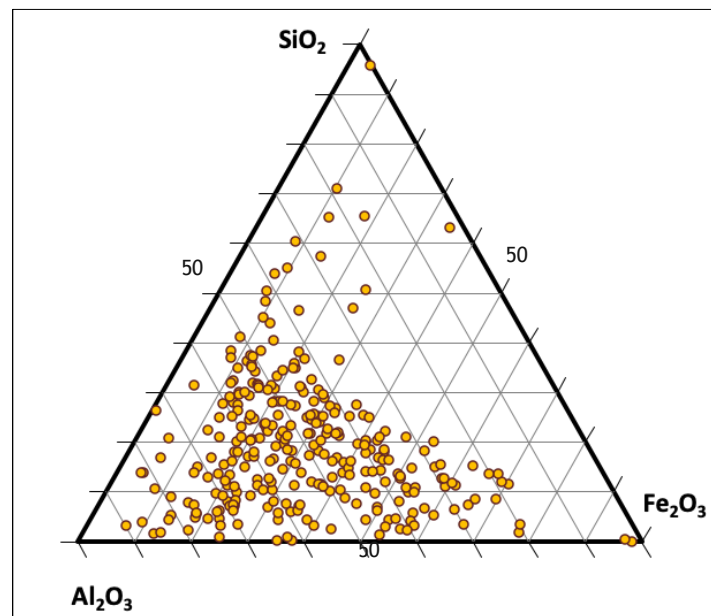


Figure IV-18 Total Aluminum (Al) and Silicon (Si) content ( $\text{mmol kg}^{-1}$ ) in 290 sample rocks from eastern coastal Quintana Roo, illustrating the chemical composition of bulk samples. Linear regression (red line) approximately represents 1:1 molar ratio for Al and Si. When forcing intercept to zero, regression equation is  $y = 0.9027x$  with  $R^2 = 0.6852$ .



*Figure IV-19* Mass  $\text{SiO}_2 - \text{Al}_2\text{O}_3 - \text{Fe}_2\text{O}_3$  (SAF) ternary plots illustrating the chemical composition of bulk samples. Calculations assuming Al, Fe, Si are all present as their oxide, normalized mol %;  $n = 290$ .

#### IV-3.1.5 Minor elements: Ba, Cd, Co, Cr, Cu, Mo, Ni, Pb, V

The group containing the *Minor elements* consists of the following, in decreasing order of concentration: Cr ( $0.13 \pm 0.10$ ), Co ( $0.10 \pm 0.15$ ), Ba ( $0.09 \pm 0.08$ ), V ( $0.08 \pm 0.17$ ), Cu ( $0.03 \pm 0.03$ ), Ni ( $0.02 \pm 0.05$ ), Pb ( $0.01 \pm 0.01$ ), Cd ( $0.002 \pm 0.015$ ), and Mo ( $0.001 \pm 0.21$ ). All values in mmol  $\text{kg}^{-1}$ .

All these elements are kept below 1 mmol per kg of rock in the whole dataset with significant variation in proportions along geographical and depth distributions. Chromium (Cr) and cobalt (Co) are in greater proportions, followed by vanadium (V), barium (Ba), nickel (Ni), copper (Cu), cadmium (Cd), lead (Pb) and molybdenum (Mo).

It is worth note that the higher cadmium (Cd) concentrations were found in rocks from different phreatic depths at Cenote Siete Bocas in Ruta de los Cenotes, reaching values of 0.06 mmol per kg of rock (mean  $0.002 \text{ mmol kg}^{-1}$ ), while other cenotes in the area don't show that behavior. Other Cd high concentration sites include Quarry 8 along the highway M180D, rock samples from the inner roads to extraction wells in Puerto Morelos, all of them surface rock samples.

Vanadium (V) also is present at high concentrations at variable depths in Cenote Siete Bocas, although its higher values are from rocks sampled in quarries and outcrops located nearby or along transited roads. Such is also the case for chromium (Cr), which higher concentrations are located in surface rock samples close to human activities, reaching out values of  $0.5 \text{ mmol kg}^{-1}$  (mean  $0.13 \text{ mmol kg}^{-1}$ ). Closer inspection of lead (Pb) show that its higher concentrations are

located either close to a transited road, or very close to sand beaches, and could be indicative of fuel emissions from vehicles and motorboats.

Despite the exceptional case of Cenote Siete Bocas, it can be shown that, in general, *Minor elements* such as Cd, Cr, V, Co, and Pb have higher concentrations at the surface rocks, which suggest a top deposition under anthropogenic influence.

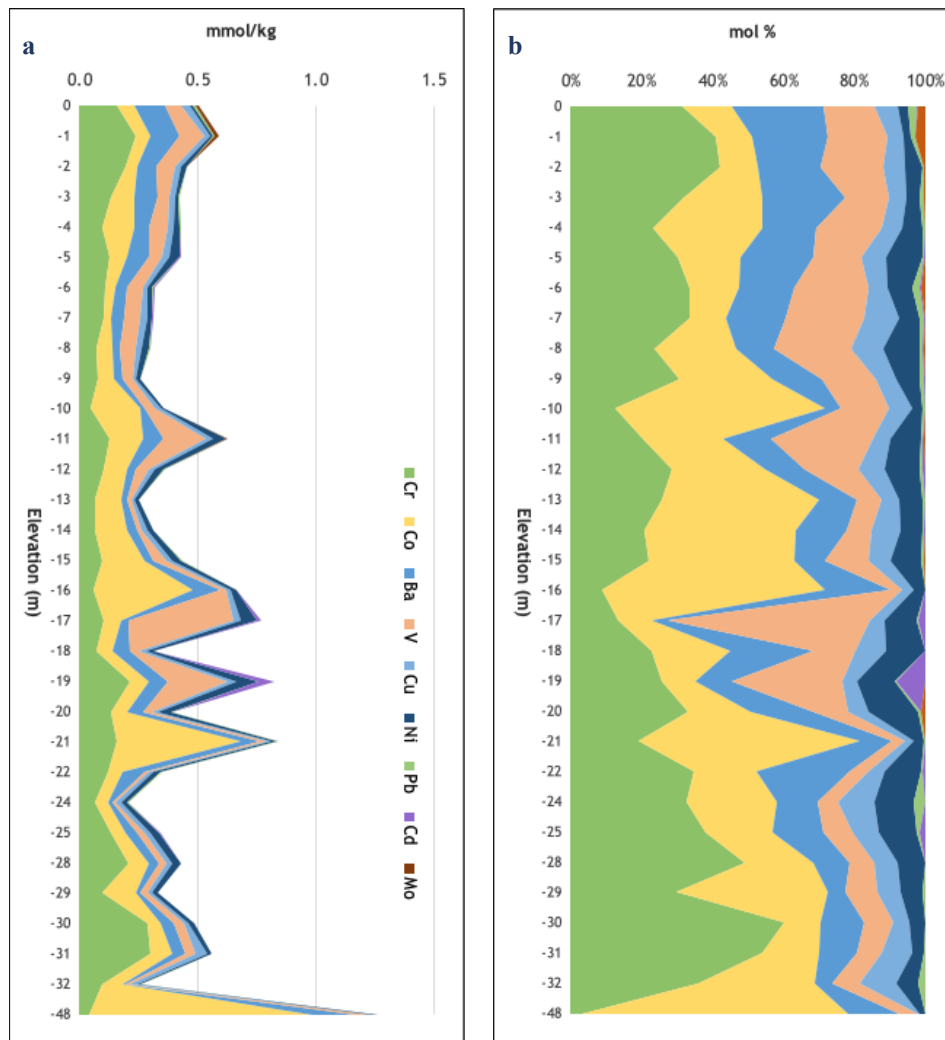


*Figure IV-20* Depth-average concentration values for Minor elements in decreasing order of concentration: Cr, Co, Ba, V, Cu, Ni, Pb, Cd, and Mo; **a)** values in  $\text{mmol kg}^{-1}$ ; **b)** normalized to 100 mol %. Note that the elevation bin sizes are not equally sized, based on the number of samples available for each bin. Distribution statistics for each elevation bin not shown.

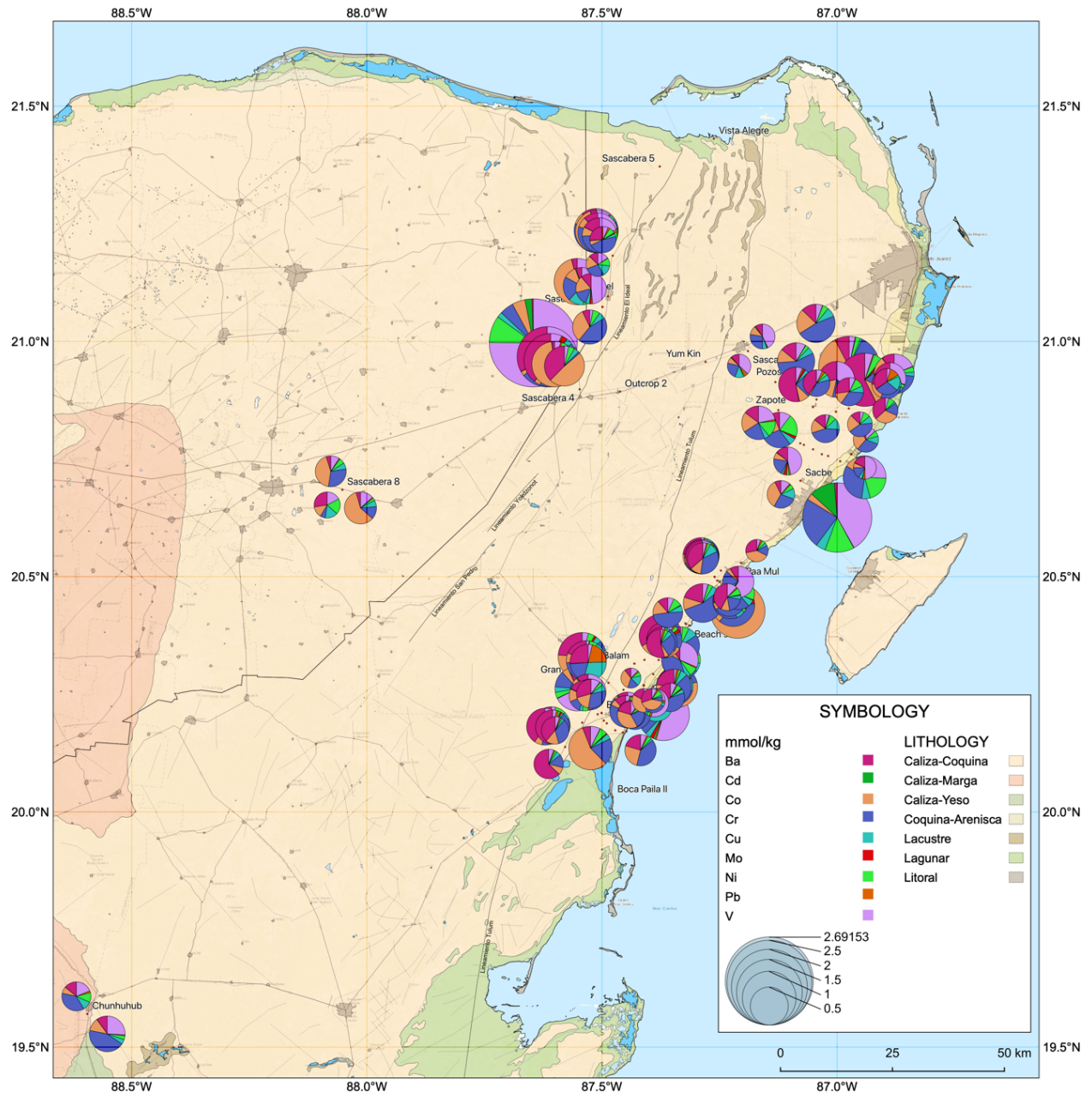


Figure IV-21 Geographic distribution of Ba, Cd, Co, Cr, Cu, Mo, Ni, Pb, and V, excluding all other elements. Concentration values given in  $\text{mmol kg}^{-1}$ .

#### **IV-3.1.6 Trace elements: Ag, Be, Bi, Cs, Ga, In, Rb, Tl, Zn**

Concentrations of elements Ag, Be, Bi, Cs, Ga, In, Rb, Tl, and Zn are below the LOD in the whole range of the analytical methods employed. Therefore, even that in some samples a positive signal was obtained, for general considerations these elements would be excluded from further considerations, unless otherwise specifically stated.

#### **IV-4 BULK GEOCHEMISTRY COMPARED TO MODERN OCEAN WATER**

Table IV-6 summarizes the mean/max/min of the bulk rock composition, aligned with the elemental global composition of modern marine water (Libes, 2009; Millero, 2013). Comparison of some element concentrations in rocks with that of modern seawater, show that proportions of many elements and the total composition of Yucatán rocks, cannot be explained by the solely fact of evaporating a certain amount of seawater. Many of them, at least in certain amounts, must have allochthonous transported provenance. Therefore, post-depositional processes must had happened, with a variety of differential mechanisms operating on specific elements to effectively change relative concentrations, in order to reflect actual rock composition.

Climate and eustatic sea level variations through the Pleistocene are first order controls on the nature and depth range of influence of the geochemical alterations from leaching, diagenesis, and pedogenetic processes. Combined, these geochemically alter the limestone from its depositional composition, into the rocks we observe today. These processes are without question overprinted, and spanning different timescales, leaving a fingerprint in the rock, that is inexorably hard to interpret.

If all elements are hypothetically considered syndepositional with limestone sedimentary accretion, then we would expect to reflect those from marine waters at the time, following Marcet's principle. As a first approach, a reflection is made on the composition of rock samples and modern ocean water.

The geography of the Yucatán Platform has been relatively similar to the today since at least the Cenozoic, situated between the Western Caribbean, and the Gulf of Mexico, and effectively flanked from the Western Atlantic by Cuba. With the Panama closure, ocean currents would have been much the same as today, with western Caribbean loop current passing through the basin, impinging on the Yucatán Peninsula and being deflected northward to pass through the Yucatán Straights between Cabo Catoche (Cancún) and the Island of Cuba. There are no major sources of terrigenous cratonic siliciclastic inputs on the Caribbean Yucatán flank. Other possible sources should be explored. Provenance of some elements contributing to the Yucatán peninsula rock composition, had been explored by many authors, in general for the Caribbean area and the Gulf of Mexico. Hypothesis include volcanic detritus and ash (Bautista et al., 2011; Cabadas-Báez et al., 2010; Solleiro-Rebolledo et al., 2011), and eolian dust transportation of Saharan dust (Chen et al., 2018; Doherty et al., 2008; Lack et al., 2009; Muhs & Budahn, 2009).

To test the hypothesis that all intermediate and trace elements are syndepositional with calcite during limestone sedimentary accretion of the platform, the aqueous product solubility and precipitation of the common mineral compounds associated with carbonates containing some selected elements is considered. The baseline concentrations in ocean waters (Table IV-6 right columns), and a log-log solubility diagram and an evaporation line are generated (Figure IV-22), taking into account the most abundant cations and anions and their solubility product constants

(K<sub>sp</sub>). The simplification made here is that the interest relies only in a final full-evaporation scheme, despite the differential precipitation of different compounds with different solubility involving the same element. Constant ambient temperature and pressure (NTP; 20 °C, 1 atm) are assumed, and pH is allowed to vary. This approach neglects any chemical transformation of mineral rocks, as is assessing for the total concentration of the element [X]<sub>T</sub>, regardless of kinetics, bio-mediation, mineralogical partitions, or metal-ligand complexation reversible reactions, diagenetic processes, and assuming total precipitation due to evaporation. Also, this approach only compares soluble salts, not particulate matter. In general terms, complete evaporation of 1 L of seawater would produce ~35 g of salt compounds, dominated by NaCl.

Under this oversimplified scheme, the ranked Table 4.4 shows that elements like Co, Cr, V, Fe, Ni, and Mn are in “excess” with respect to the amount of seawater evaporated and constrained by Ca concentration value, that suggest accumulation processes. In contrast, elements as Na, K, S, Cu, Mg, Sr, and Pb, are below the expected concentration and consequently treated as “scarce”, and it could be interpreted as those elements were leached from the rock since time of deposition. Elements as Si, P, S are biologically relevant (excluding other micro-nutrient-elements as Fe and Cu, treated separately), so they would have complex mobilities through local biochemical pathways.

As far at the present stage of this research there haven't been performed detailed mineralogical and or speciation analyzes of elements, an oversimplified approach is presented on the bulk rock concentrations found in this work, and modern seawater composition.

Assuming a fixed quantity and the amount of calcium in the rock is considered “fixed” through time since deposition, a normalized index was created with the Ca value to “1”. This is

taking the volume of seawater needed to completely evaporate to give the amount of average Ca concentration in the bulk rock. Calculations show that in order to get the average measured Ca concentration in 1 kg of bulk rock, that would take roughly 946.5 L of modern seawater to evaporate (Table IV-6). This, for instance, could be a reasonable and feasible amount (a cubic meter of water per kilogram of rock), but if we move on to examine elements with the lowest concentrations in Yucatán rocks, then that number becomes larger at several orders of magnitude.

Sodium (Na) was first used as a constrained element and is shown for comparison (third column right to left). Na is present in the form of NaCl, a very soluble compound that we can assume is leached in far greater extent than any Ca from surface and subsurface rock samples.

Aluminum (Al) is a test element that we know its general trend is to accumulate in kaolinite at the surface. However, it is located in a relative position very close to Ca, and under this model would be of ambiguous interpretation.

The great deviations calculated in rock composition from modern ocean waters, mostly are due to differential solubility of mineral compounds (e.g., differences in Ca and Na, because differences in their capacity to be leached away from the rock matrix, inherently to differences in solubility of their common mineral forms, CaCO<sub>3</sub> (calcite) and NaCl (halite).

Another complementary explanation could be that changes in ocean chemistry through Cenozoic and / or local exceptions to Marcet's principle would be sufficient to explain for that, but despite that further detailed calculations hadn't been yet done, this seems highly improbable.

Accounting for the observations presented in this section, it's reasonable to support hypotheses of allochthonous input for at least certain elements, such as Al, Cd, Cr, Co, Fe, Mn,

Pb, Si and V, whose concentration values in ocean waters cannot explain the ranges observed in sample rocks from different environments in the Yucatán Peninsula.

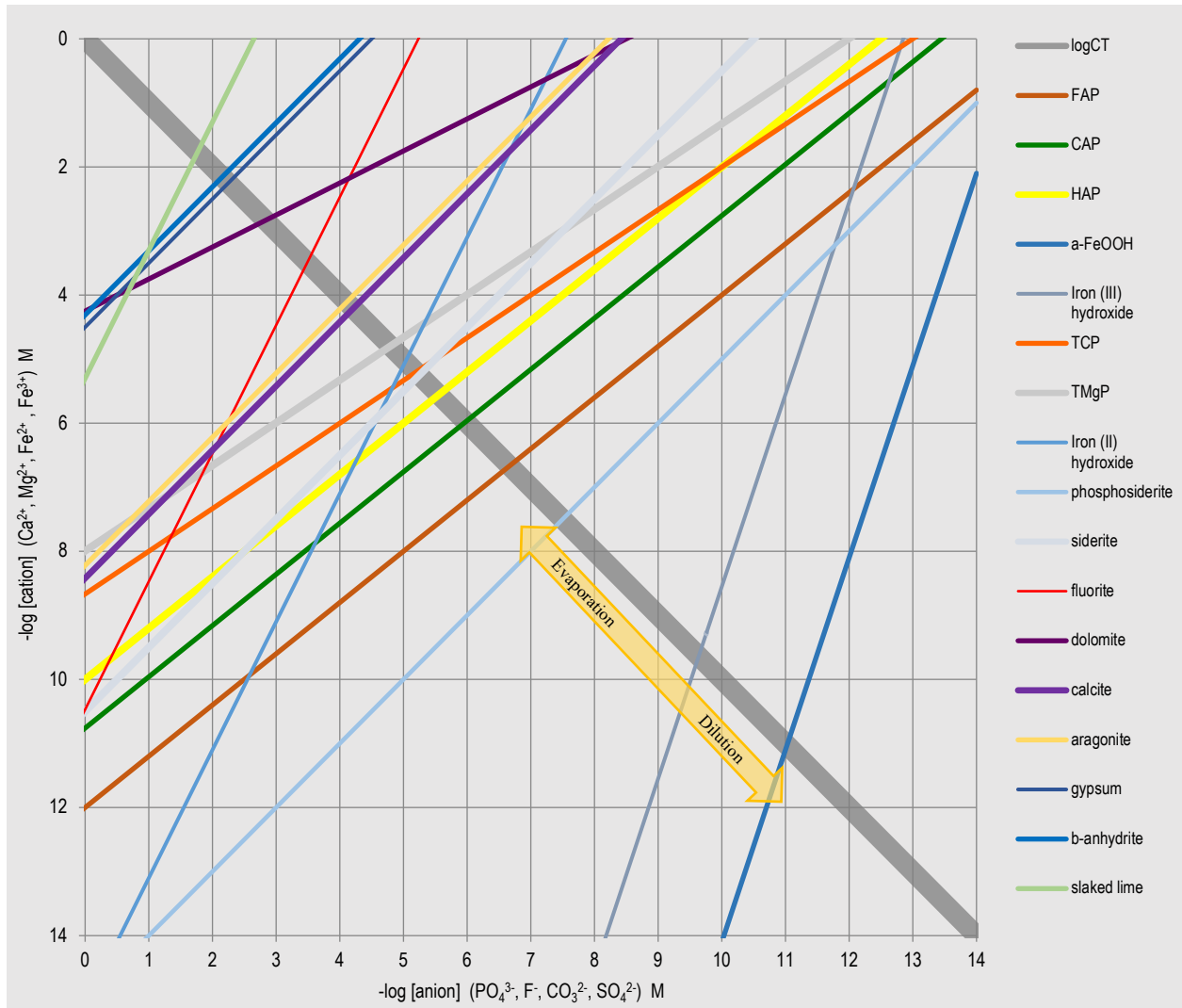


Figure IV-22 *log-log solubility diagram and generated evaporation line, taking into account the most abundant cations and anions and their solubility product constants ( $K_{sp}$ ) at 20 °C and 1 atm.*

Table IV-6 Concentration of studied elements in young carbonate rocks,  $n = 290$  (this work); and in modern mean seawater, data from Libes (2009) and Millero (2013).

CARBONATE ROCKS (MMOL/KG <sub>ROCK</sub> )						MEAN SEAWATER	
	<i>Element</i>	<i>Mean</i>	<i>Min</i>	<i>Max</i>	<i>ppm (mg/kg<sub>rock</sub>)</i>	<i>ppm (mg/L<sub>sw</sub>)</i>	<i>mmol/L<sub>sw</sub></i>
MAJOR	<i>Ca</i>	9500.64	5435.44	14074.27	378621.656	400	10.05
	<i>Mg</i>	895.37	48.36	4703.95	64139.218	1272	52.35
INTERMEDIATE	<i>Na</i>	29.98	2.04	441.16	689.337	10556	459.17
	<i>Al</i>	26.55	1.17	605.18	716.359	1.9	0.07
	<i>Si</i>	23.98	0.22	696.26	673.450	4	0.142
	<i>Sr</i>	17.95	1.39	93.17	1572.698	13	0.148
	<i>S</i>	13.50	0.00	91.35	432.968	884	27.63
	<i>Fe</i>	4.13	0.22	103.90	249.368	0.02	$3.6 \times 10^{-4}$
	<i>P</i>	3.41	0.15	29.79	104.983	0.114	$3.52 \times 10^{-3}$
	<i>K</i>	1.92	0.17	32.59	75.145	380	9.72
	<i>Li</i>	0.45	0.28	4.87	3.136	0.1	0.015
	<i>Mn</i>	0.35	0.02	4.08	19.163	0.01	$1.8 \times 10^{-4}$
MINOR	<i>Cr</i>	0.13	0.00	0.77	6.964	0.0004	-
	<i>Co</i>	0.10	0.00	0.96	5.659	0.0001	$1.7 \times 10^{-6}$
	<i>Ba</i>	0.09	0.01	0.56	11.941	0.05	$3.7 \times 10^{-4}$
	<i>V</i>	0.08	0.01	2.02	3.903	0.0003	$5.9 \times 10^{-6}$
	<i>Cu</i>	0.03	0.00	0.26	1.719	0.09	$1.4 \times 10^{-3}$
	<i>Ni</i>	0.02	0.04	0.27	1.110	0.0005	$8.5 \times 10^{-6}$
	<i>Pb</i>	0.01	0.03	0.10	1.130	0.005	$2.4 \times 10^{-5}$
	<i>Cd</i>	0.00	0.01	0.20	0.225	-	-
	<i>Mo</i>	0.00	0.03	0.18	0.116	0.002	$2.1 \times 10^{-5}$
TRACE	<i>Ag</i>	N/A	N/A	N/A	N/A	0.0003	$2.8 \times 10^{-6}$
	<i>Be</i>	N/A	N/A	0.065	0.000586	-	-
	<i>Bi</i>	N/A	N/A	0.003	0.000627	0.0002	-
	<i>Cs</i>	N/A	N/A	N/A	N/A	0.002	$1.5 \times 10^{-5}$
	<i>Ga</i>	N/A	N/A	0.044	0.003068	0.0005	$7.2 \times 10^{-6}$
	<i>In</i>	N/A	N/A	0.025	0.002870	-	-
	<i>Rb</i>	N/A	N/A	0.302	0.025811	0.2	$2.4 \times 10^{-3}$
	<i>Tl</i>	N/A	N/A	0.005	0.001022	-	-
	<i>Zn</i>	N/A	N/A	N/A	N/A	0.014	$2.1 \times 10^{-4}$

Table IV-7 Aqueous solubility values at 20 ° C and 1 atm for common compounds, containing some selected elements studied in this work. Data from Libes (2009) and Millero (2013).

Species	Solubility (s)		-log (s)
Ca <sub>5</sub> (PO <sub>4</sub> ) <sub>3</sub> F	1.00x10 <sup>-15</sup>	M	15.00
Ca <sub>5</sub> (PO <sub>4</sub> ) <sub>3</sub> Cl	3.55 x10 <sup>-14</sup>	M	13.45
Ca <sub>5</sub> (PO <sub>4</sub> ) <sub>3</sub> OH	3.16 x10 <sup>-13</sup>	M	12.50
α-FeOOH + H <sub>2</sub> O	9.44 x10 <sup>-12</sup>	M	11.03
Fe(OH) <sub>3</sub>	2.30 x10 <sup>-10</sup>	M	9.64
FeS	8.95 x10 <sup>-10</sup>	M	9.05
Ca <sub>3</sub> (PO <sub>4</sub> ) <sub>2</sub>	3.16 x10 <sup>-07</sup>	M	6.50
Mg <sub>3</sub> (PO <sub>4</sub> ) <sub>2</sub>	1.01 x10 <sup>-06</sup>	M	6.00
Fe(OH) <sub>2</sub>	1.68 x10 <sup>-04</sup>	M	3.78
FePO <sub>4</sub> · 2H <sub>2</sub> O	1.78 x10 <sup>-04</sup>	M	3.75
FeCO <sub>3</sub>	2.37 x10 <sup>-03</sup>	M	2.63
CaF <sub>2</sub>	2.41 x10 <sup>-03</sup>	M	2.62
CaMg(CO <sub>3</sub> ) <sub>2</sub>	7.50 x10 <sup>-03</sup>	M	2.13
CaCO <sub>3</sub>	7.85 x10 <sup>-03</sup>	M	2.11
CaCO <sub>3</sub>	8.81 x10 <sup>-03</sup>	M	2.06
Ca(OH) <sub>2</sub>	4.73 x10 <sup>-02</sup>	M	1.33
MgCO <sub>3</sub>	5.10 x10 <sup>-02</sup>	M	1.29
CaSO <sub>4</sub> · 2H <sub>2</sub> O	7.50 x10 <sup>-02</sup>	M	1.13
CaSO <sub>4</sub>	8.37 x10 <sup>-02</sup>	M	1.08

Table IV-8 Aqueous product solubility constants for common mineral compounds associated with carbonates containing some selected elements studied.

Species	Solubility equation	Solubility constant	-log K <sub>sp</sub>
FAP	Ca <sub>5</sub> (PO <sub>4</sub> ) <sub>3</sub> F ↔ 5Ca <sup>2+</sup> + 3PO <sub>4</sub> <sup>3-</sup> + F <sup>-</sup>	K <sub>sp</sub> = 1.00E-60	pK <sub>sp</sub> = 60.00
CAP	Ca <sub>5</sub> (PO <sub>4</sub> ) <sub>3</sub> Cl ↔ 5Ca <sup>2+</sup> + 3PO <sub>4</sub> <sup>3-</sup> + Cl <sup>-</sup>	K <sub>sp</sub> = 1.58E-54	pK <sub>sp</sub> = 53.80
HAP	Ca <sub>5</sub> (PO <sub>4</sub> ) <sub>3</sub> OH ↔ 5Ca <sup>2+</sup> + 3PO <sub>4</sub> <sup>3-</sup> + OH <sup>-</sup>	K <sub>sp</sub> = 1.00E-50	pK <sub>sp</sub> = 50.00
goethite	α-FeOOH + H <sub>2</sub> O ↔ Fe <sup>3+</sup> + 3OH <sup>-</sup>	K <sub>sp</sub> = 7.94E-45	pK <sub>sp</sub> = 44.10
Iron (III) hydroxide	Fe(OH) <sub>3</sub> ↔ Fe <sup>3+</sup> + 3OH <sup>-</sup>	K <sub>sp</sub> = 2.82E-39	pK <sub>sp</sub> = 38.55
TCP	Ca <sub>3</sub> (PO <sub>4</sub> ) <sub>2</sub> ↔ 3Ca <sup>2+</sup> + 2PO <sub>4</sub> <sup>3-</sup>	K <sub>sp</sub> = 1.00E-26	pK <sub>sp</sub> = 26.00
TMgP	Mg <sub>3</sub> (PO <sub>4</sub> ) <sub>2</sub> ↔ 3Mg <sup>2+</sup> + 2PO <sub>4</sub> <sup>3-</sup>	K <sub>sp</sub> = 1.05E-24	pK <sub>sp</sub> = 23.98
Iron (II) sulfide	FeS ↔ Fe <sup>2+</sup> + S <sup>2-</sup>	K <sub>sp</sub> = 8.00E-19	pK <sub>sp</sub> = 18.10
pyrite	FeS <sub>2</sub> ↔ Fe <sup>2+</sup> + 2S <sup>1-</sup>	K <sub>sp</sub> = 3.98E-17	pK <sub>sp</sub> = 16.40
greigite	Fe <sub>3</sub> S <sub>4</sub> ↔ Fe <sup>2+</sup> + 2Fe <sup>3+</sup> + 4S <sup>2-</sup>	K <sub>sp</sub> = 3.98E-05	pK <sub>sp</sub> = 4.40
pyrrhothite	Fe <sub>1-x</sub> S ↔ (1-x)Fe <sup>2+</sup> + 2S <sup>2-</sup>	K <sub>sp</sub> = 7.94E-06	pK <sub>sp</sub> = 5.10
Iron (II) hydroxide	Fe(OH) <sub>2</sub> ↔ Fe <sup>2+</sup> + 2OH <sup>-</sup>	K <sub>sp</sub> = 7.94E-16	pK <sub>sp</sub> = 15.10
phosphosiderite	FePO <sub>4</sub> · 2H <sub>2</sub> O ↔ Fe <sup>2+</sup> + PO <sub>4</sub> <sup>3-</sup> + 2H <sub>2</sub> O	K <sub>sp</sub> = 1.00E-15	pK <sub>sp</sub> = 15.00
siderite	FeCO <sub>3</sub> ↔ Fe <sup>2+</sup> + CO <sub>3</sub> <sup>2-</sup>	K <sub>sp</sub> = 3.16E-11	pK <sub>sp</sub> = 10.50
fluorite	CaF <sub>2</sub> ↔ Ca <sup>2+</sup> + 2F <sup>-</sup>	K <sub>sp</sub> = 3.39E-11	pK <sub>sp</sub> = 10.47
dolomite	CaMg(CO <sub>3</sub> ) <sub>2</sub> ↔ Ca <sup>2+</sup> + Mg <sup>2+</sup> + 2CO <sub>3</sub> <sup>2-</sup>	K <sub>sp</sub> = 3.16E-09	pK <sub>sp</sub> = 8.50
calcite	CaCO <sub>3</sub> ↔ Ca <sup>2+</sup> + CO <sub>3</sub> <sup>2-</sup>	K <sub>sp</sub> = 3.80E-09	pK <sub>sp</sub> = 8.42
aragonite	CaCO <sub>3</sub> ↔ Ca <sup>2+</sup> + CO <sub>3</sub> <sup>2-</sup>	K <sub>sp</sub> = 6.03E-09	pK <sub>sp</sub> = 8.22
slaked lime	Ca(OH) <sub>2</sub> ↔ Ca <sup>2+</sup> + 2OH <sup>-</sup>	K <sub>sp</sub> = 5.01E-06	pK <sub>sp</sub> = 5.30
magnesite	MgCO <sub>3</sub> ↔ Mg <sup>2+</sup> + CO <sub>3</sub> <sup>2-</sup>	K <sub>sp</sub> = 6.76E-06	pK <sub>sp</sub> = 5.17
gypsum	CaSO <sub>4</sub> · 2H <sub>2</sub> O ↔ Ca <sup>2+</sup> + SO <sub>4</sub> <sup>2-</sup> + 2H <sub>2</sub> O	K <sub>sp</sub> = 3.16E-05	pK <sub>sp</sub> = 4.50
β-anhydrite	CaSO <sub>4</sub> ↔ Ca <sup>2+</sup> + SO <sub>4</sub> <sup>2+</sup>	K <sub>sp</sub> = 4.90E-05	pK <sub>sp</sub> = 4.31

Table IV-9 Concentration of studied elements in young carbonate rocks,  $n = 290$  (this work); and in modern mean seawater, data from Libes (2009) and Millero (2013). On the right side, calculations on apparent accumulation/leaching as explained in text. Table is ordered top down for elements most in excess or accumulated and descending to scarcity or leached.

Element	Yucatán carbonate rocks (this work)				Mean seawater		Calculations			Relative effect*	
	Mean	Min	Max	ppm (mg/kg <sub>rock</sub> )	ppm (mg/L <sub>sw</sub> )	mmol/L <sub>sw</sub>	Liters of seawater needed to achieve concentrations found in 1 kg of rock	Na	Ca		
Co	0.10	0.00	0.96	5.659	0.0001	$1.7 \times 10^{-6}$	56590	866578	59.785	↑ Excess or Accumulation	
Cr	0.13	0.00	0.77	6.964	0.0004		17410	266604	18.393		
V	0.08	0.01	2.02	3.903	0.0003	$5.9 \times 10^{-6}$	13010	199226	13.745		
Fe	4.13	0.22	103.9	249.368	0.02	$3.6 \times 10^{-4}$	12468	190932	13.172		
Ni	0.02	0.04	0.27	1.11	0.0005	$8.5 \times 10^{-6}$	2220	33995	2.345		
Mn	0.35	0.02	4.08	19.163	0.01	$1.8 \times 10^{-4}$	1916	29345	2.024		
Ca	9500.64	5435.44	14074.27	378621.656	400	10.05	946.5	14494	1		
P	3.41	0.15	29.79	104.983	0.114	$3.52 \times 10^{-3}$	920.9	14102	0.972		↓ Scarcity or Leaching
Al	26.55	1.17	605.18	716.359	1.9	0.07	377.0	5773	0.398		
Ba	0.09	0.01	0.56	11.941	0.05	$3.7 \times 10^{-4}$	238.8	3657	0.252		
Pb	0.01	0.03	0.1	1.13	0.005	$2.4 \times 10^{-5}$	226.0	3460	0.239		
Si	23.98	0.22	696.26	673.45	4	0.142	168.4	2578	0.178		
Sr	17.95	1.39	93.17	1572.698	13	0.148	121.0	1852	0.128		
Mo	0.00	0.03	0.18	0.116	0.002	$2.1 \times 10^{-5}$	58.0	888.2	0.061		
Mg	895.37	48.36	4703.95	64139.218	1272	52.35	50.4	772.2	0.053		
Li	0.45	0.28	4.87	3.136	0.1	0.015	31.36	480.2	0.033		
Cu	0.03	0.00	0.26	1.719	0.09	$1.4 \times 10^{-3}$	19.10	292.5	0.020		
Ga	N/A	N/A	0.044	0.003068	0.0005	$7.2 \times 10^{-6}$	6.14	94	0.007		
Bi	N/A	N/A	0.003	0.000627	0.0002		3.14	48	0.003		
S	13.5	0.00	91.35	432.968	884	27.63	0.49	7.50	0.0005		
K	1.92	0.17	32.59	75.145	380	9.72	0.20	3.03	0.0002		
Rb	N/A	N/A	0.302	0.025811	0.2	$2.4 \times 10^{-3}$	0.13	1.98	0.0001		
Na	29.98	2.04	441.16	689.337	10556	459.17	0.07	1	0.0001		

#### IV-5 GEOGRAPHICAL DISTRIBUTION

Selected sites were sampled at different depths to track characteristic facies features and account for any local chemo-stratigraphic pattern. The initial goals were to refine the stratigraphy of the Carrillo Puerto Formation and obtain some details of the Pleistocene caliche horizons on the northeastern coast of the Peninsula (Ward & Halley, 1985).

Field mapping was undertaken to correlate strata between different sites using standard sedimentary-stratigraphy field mapping methods to document geological sections in different areas and identify exposures of the same strata close to the coast (even though underwater), and further inland. Trying to establish sedimentary or geochemical correlation proved to be complex, in part due to lack of literature information and data, the very patchy nature of facies distribution in coastal-marine facies that varies over spatial scales of 10-100 m, and the overprint of post-depositional diagenetic processes. Lithological units are not described in the detail necessary to correlate chemo-stratigraphically with the findings of this research.

Section correlation proved impossible with the available outcrops and quarries, pointing to the need for a coring campaign which was beyond the scope of the current thesis efforts. Despite this explained situation, sedimentary columns were sketched, described, and sampled in any differentiate unit was identified. This report substantially expands the carbonate sedimentology and stratigraphy data for the region.

Sampling was distributed, both geographically and with depth. Two transects each span ~50 km, running N-S perpendicular to the northern coast, and east-west perpendicular to the Caribbean coast, shown as A and B respectively in Figure IV-23. This is designed to capture variations related with distance to the coast.

A third transect C runs parallel to the Caribbean coast at a relatively “fixed” distance and always <10 km, to achieve for latitudinal variations and those due to local geology.

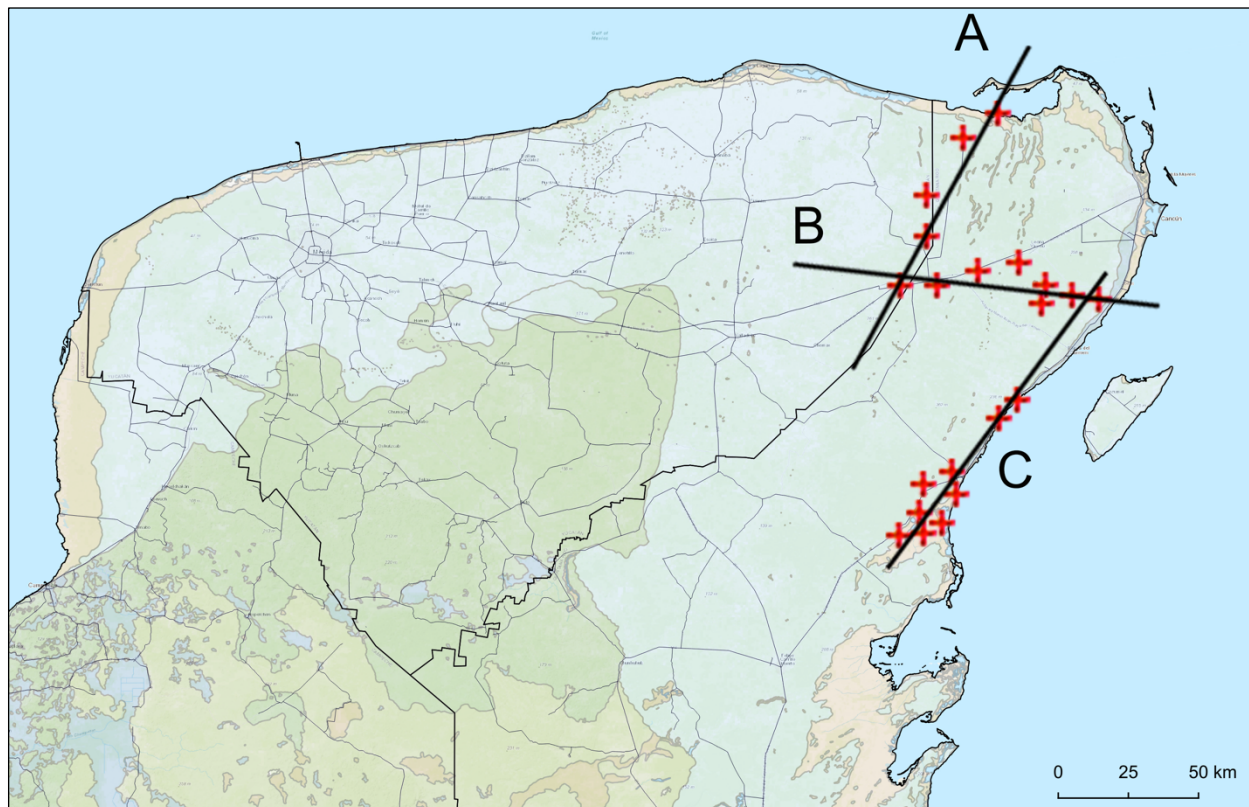


*Figure IV-23 Geographically distributed transects, two perpendicular (A and B) to the north and Caribbean coast, respectively; and one running parallel (C) to the Caribbean coast. This configuration was intended to capture hypothesized patterns explained in text.*

**Transect A** – Starting in Vista Alegre, an archaeological coastal site in Laguna Conil, close to the town of Holbox. Road outcrops from Chiquilá and via Kantunilkin, Quintana Roo; n = 21.

**Transect B** – Labeled as SG. Three sections: Yaxché, Ruta de los Cenotes, path to Amaneciendo.

**Transect C** – Along the eastern coast of the Yucatán Peninsula from Puerto Morelos to south Tulum.

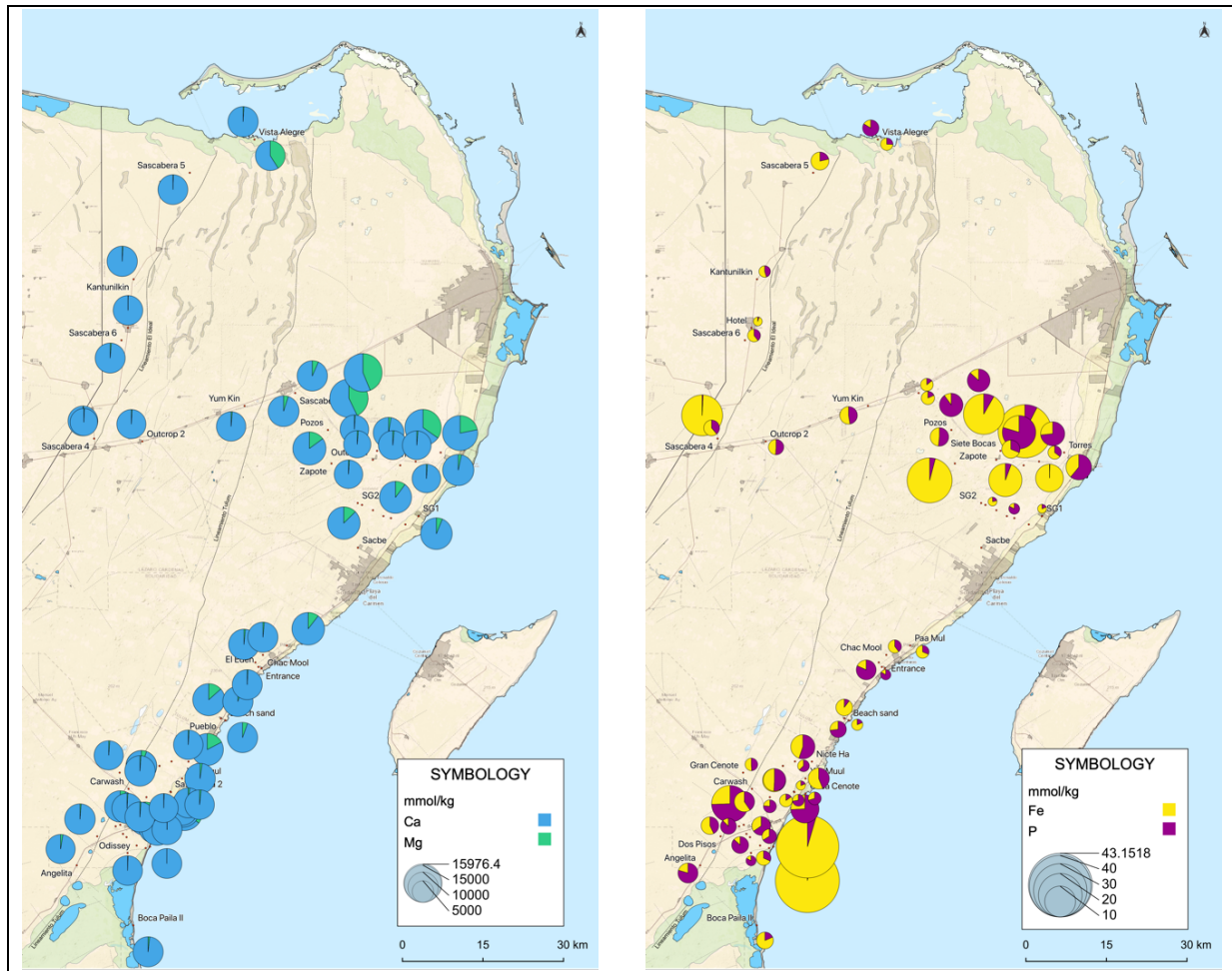


Figure IV-24 Distribution of a) Ca, Mg and b) Fe, P contribution to rock composition along the three transects A, B and C. Values given in  $\text{mmol kg}^{-1}$ .

The elemental distribution in  $\text{mmol kg}^{-1}$  of in the surface rocks along the Transects A, B, and C are shown in Figure IV-24a for Ca and Mg, and then Figure IV-24b for Fe and P.

The sites with higher Mg in the surface rocks occur at the north coast (Vista Alegre), near coast on Transect B (north of Puerto Morelos), and then some scattered surface rock samples near Tulum (Transect C) and  $\sim 25$  km inland on Transect B. It is possible that there may be greater prevalence of Mg in the surface rocks in the very late Pleistocene / Holocene coastal margin.

Alternatively, it may be that higher Mg was determined due to the near coast surface rocks having sea spray environmental Mg, although the not notably high Na in the corresponding samples refutes sea spray as a source of the Mg. In all cases, for surface rocks, there is definitive surface rock distribution evident in the current sample set.

A clearer pattern of near coast (~5 km or less) higher P relative to Fe is observed (Figure IV-24b). The inland surface samples of Transects A and B are higher in F compared to the dominance of P in the near coast sites of all three transects. Few scattered samples (n=4) have overall abundance of P+Fe reaching 20-30 mmol kg<sup>-1</sup> in no obvious pattern, but overall the great majority of distributed samples have low overall concentrations of P+Fe reaching only ~10 mmol kg<sup>-1</sup> of rock, which will be discussed further below in relation to these elements being limiting nutrients in marine ecosystems.

Figure IV-25 shows the distribution of the intermediate elements of Al, Fe, Mn, Si, and the minor elements of Ba, Cd, Co, Cr, Cu, Mo, Ni, Pb, V, in surface rocks along the three transects in mmol kg<sup>-1</sup>. Where symbols are not plotted, it is due to either the one or more elements being below LOD, or analysis not being run as the rocks were analyzed exclusively in the first batch with the 10-element standard suite. Five samples had very high concentrations of the Intermediate elements reaching 100-120 mmol kg<sup>-1</sup> of rock, with no obvious geographical pattern as 2 samples are from 2 inland sites and 2 are from coastal sites.

There are no overall patterns emerging over the three Transects for the intermediate and minor elements in this graphical presentation, nor in other attempts to group, plot, or layout in transects with distance or geography. The lack of pattern particularly in the Transect A and B lines that should progressively increase in age with distance inland is less significant than the

geochemical reflection of the inherent patchiness of the coastal-marine facies captured in distributed surface samples, or patchiness in diagenesis, or simply the size of the sample set needs to be multiplied.

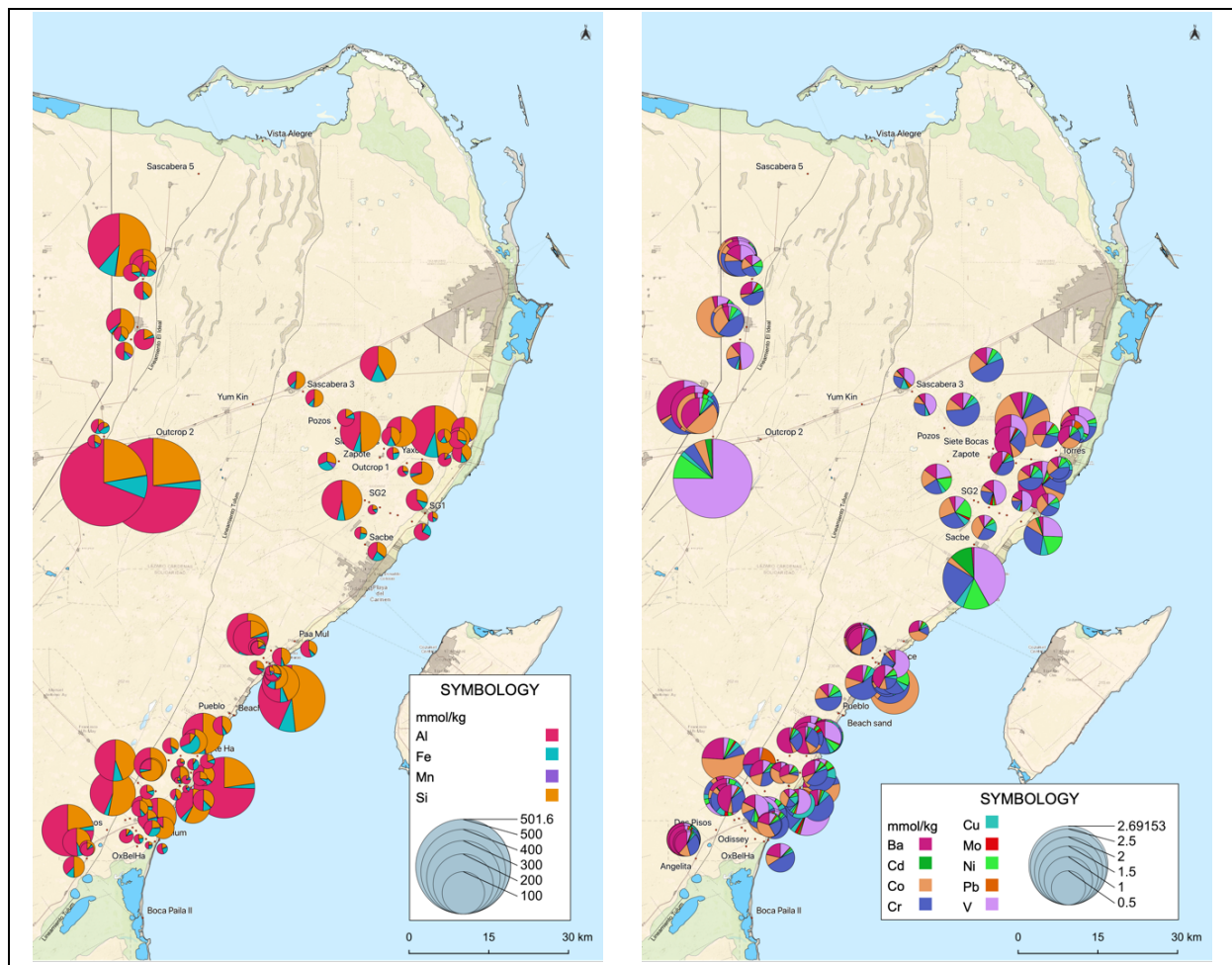


Figure IV-25 Distribution of Intermediate (Al, Fe, Mn, Si) and Minor (Ba, Cd, Co, Cr, Cu, Mo, Ni, Pb, V) elements on rock composition along transects A, B and C. Values given in  $\text{mmol kg}^{-1}$ .

## IV-6 STRATIGRAPHIC DISTRIBUTION

Massive carbonate beds deposited during interglacial stages and high stands of sea level, while caliche zones developed during glacial stages when the Yucatán platform was subjected to prolonged periods of subaerial exposure, exacerbating weathering.

### IV-6.1 VADOSE / PHREATIC ZONE DISTRIBUTION

Sea level changes and their effect on the rocks, is one of the biggest challenges this research faced, as these cycles of changing conditions overprinted diagenetic processes perhaps many times. With falling sea level, the deeper rock was, in effect, taken from the marine phreatic environment, through the mixing zone / halocline with high dissolution rates that have been measured to range over  $5 - 10 \text{ g m}^{-2} \text{ yr}^{-1}$  using direct mass loss on dissolution tablets (Smith, 2004), then into the freshwater phreatic zone, and finally drained placing it into the vadose zone. When sea level rose, the limestone was returned through the phreatic zones.

A simple way to sample vadose rocks is from wall rock inside a dry cave. Location of caves within the vadose zone does not define their genesis, their origin is likely the same as that of underwater caves. A cave formed underwater at a high stand of sea level and then subaerially exposed as sea level falls. Caves currently within the vadose zone have been documented with the greatest concentration in the area between Akumal and Puerto Aventuras localities, and extending from the coast and up to 7 km inland (Kambesis & Coke, 2013). Over 350 km of “dry” passages have been surveyed in the region, despite dry cave exploration only having started less than 15 years ago in earnest.

Similar to the lack of clear spatial trend in the surface rock transects, the dataset is likely not large enough to find a clear trend yet also in the depth profiles, and definitely is presently inadequate for correlations.

However, there are marked differences in vadose (“dry”) and phreatic (“aquatic”) samples (Figure IV-26 and Table IV-11). The vadose zone “dry” samples from outcrops, quarries, and some caves, present consistently higher average concentrations of Al, Fe, K, Na, S, Si, and Sr, while phreatic aquatic samples obtained by cave diving have consistently higher Ca, and P concentrations than their terrestrial counterparts. Aluminum and silicon show, in general, a coupled behavior through the rock column.

One of the problems arises because many rocks on the vadose zone now, were submerged in the phreatic zone for a large amount of time. This leads to overprints on the geochemical signals on the rocks and makes further analyzes on water-rock interactions a very complex task at this time, with this dataset. In bulk, until further detailed calculations, this oversimplified fractionation scheme is related to the relative mobility of the elements and their compounds through differential leaching and pedogenetic processes. And for some elements, also their bioavailability through their biogeochemical cycles once deposited on the rocks.

Whereas these considerations are for the bulk rock, detailed observations can be made on the vertical elemental patterns in specific places, by examining depth profile plots. The next section examines the geochemical profiles for a set of samples obtained from the vadose zone (outcrops, quarries and dry caves) and phreatic zone (underwater caves and cenotes).

Table IV-10 Principal distinctions between vadose and phreatic zone rock samples. This table employs less data than previous one

	<i>Most abundant elements</i>	<i>Observations</i>	<i>Interpretation</i>
<b>VADOSE ZONE</b>	Al, Fe, K, Mn, Na, S, Si	Enriched in most elements. Al, Fe, and S decreasing consistently with depth.	Low mobility in general due to kinetic controls on pedogenetic processes, solubility, and bioavailability. Retention in soils and vegetation roots.
<b>PHREATIC ZONE</b>	Ca, Mg, P, Sr	Enriched Mg, Sr  Deficiency of Al, Fe, Si	Most probably sourced from intruded marine water. Due to differential leaching in the reactive mixing zone and/or low mobility from surface oxides in soils. Some are trapped in reddish paleosol horizons. P - Likely more cation-substitution of Ca <sup>2+</sup>

Table IV-11 Comparison of average concentration values for the most abundant elements in the vadose and the phreatic zone. Values in mmol kg<sup>-1</sup>. Phreatic zone is underrepresented due to cave diving limitations.

	<i>Ca</i>	<i>Mg</i>	<i>Al</i>	<i>Ba</i>	<i>Co</i>	<i>Cr</i>	<i>Cu</i>	<i>Fe</i>	<i>K</i>	<i>Li</i>	<i>Mn</i>	<i>Mo</i>	<i>Na</i>	<i>P</i>	<i>Pb</i>	<i>S</i>	<i>Si</i>	<i>Sr</i>	<i>V</i>
ALL ZONES																			
<b>MEAN</b>	9500	2833	26.5	0.1	0.1	0.1	0.0	4.5	1.9	0.5	0.3	0.0	30.0	3.4	0.0	13.5	24.0	17.9	0.1
<b>MIN</b>	5435	48	1.2	0.0	0.0	0.0	0.0	0.2	0.2	0.3	0.0	0.0	2.0	0.1	0.0	0.0	0.2	1.4	0.0
<b>MAX</b>	14074	4704	605.2	0.6	1.0	0.8	0.3	103.9	32.6	4.9	4.1	0.2	441.2	29.8	0.1	91.3	696.3	93.2	2.0
<b>STDEV</b>	992	7319	68.2	0.1	0.1	0.1	0.0	11.3	4.1	0.4	0.4	0.0	54.8	3.6	0.0	15.6	76.1	20.8	0.2
VADOSE ZONE																			
<b>MEAN</b>	9391	1149	38.9	0.1	0.1	0.2	0.0	6.2	2.9	0.5	0.4	0.0	42.6	2.7	0.0	20.8	37.6	24.0	0.1
<b>MIN</b>	6312	80	1.3	0.0	0.0	0.0	0.0	0.2	0.2	0.3	0.0	0.0	2.0	0.1	0.0	0.0	0.3	1.4	0.0
<b>MAX</b>	14074	4704	605.2	0.6	0.5	0.8	0.3	103.9	32.6	4.9	1.7	0.2	441.2	11.8	0.1	91.3	696.3	93.2	0.5
<b>STDEV</b>	1104	9830	92.2	0.1	0.1	0.1	0.0	15.5	5.6	0.6	0.4	0.0	74.5	2.7	0.0	18.6	105.5	27.1	0.1
PHREATIC ZONE																			
<b>MEAN</b>	9606	1560	14.6	0.1	0.1	0.1	0.0	2.8	1.0	0.4	0.3	0.0	17.7	4.1	0.0	6.5	10.8	12.1	0.1
<b>MIN</b>	5435	48	1.2	0.0	0.0	0.0	0.0	0.2	0.2	0.3	0.1	0.0	3.9	0.6	0.0	0.0	0.2	2.4	0.0
<b>MAX</b>	12984	3639	154.8	0.3	1.0	0.4	0.1	19.9	7.1	1.0	4.1	0.0	71.0	29.8	0.0	34.9	114.8	53.8	2.0
<b>STDEV</b>	857	2027	25.1	0.1	0.2	0.1	0.0	3.3	1.0	0.1	0.4	0.0	15.0	4.2	0.0	6.8	16.8	8.6	0.2

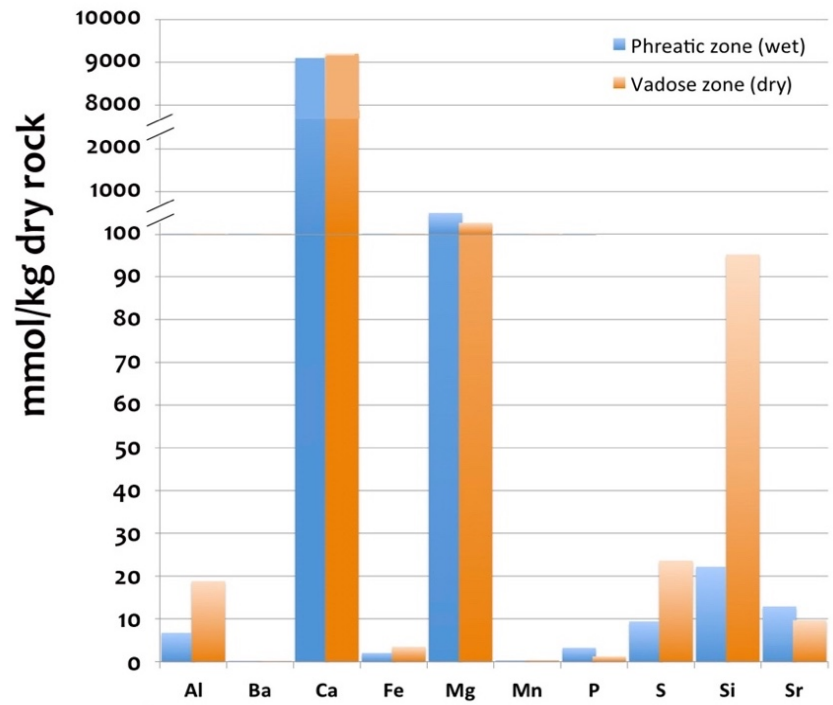


Figure IV-26 Bulk rock composition. Average concentration values distribution for the most abundant elements in the vadose and the phreatic zone. Values in  $\text{mmol kg}^{-1}$ . Phreatic zone is underrepresented due to cave diving limitations.

With the broad assumption that Al, Fe, Si are present as their oxides, the ternary plot shows the broad distribution for vadose rocks sampled in quarries, outcrops, and dry caves (Figure IV-27a) and in flooded caves and cenotes (Figure IV-27b). Surface rock samples are plotted as grey circles in the background. The distributions are overlapping for surface, vadose, and phreatic. In all cases, the representation is sparse in the  $\text{SiO}_2$  zone despite some outliers, and weighted to the  $\text{Al}_2\text{O}_3$  for the vadose, and to the  $\text{Fe}_2\text{O}_3$  for the phreatic samples. It is surprising that there are as many samples weighted to  $\text{SiO}_2$  given the absence of siliciclastic sources for the massively bedded carbonate Yucatán Peninsula with no local cratonic source.

For the vadose zone, the slight bias to  $Al_2O_3$  may in part reflect an accumulation of Al clays in the near surface drier vadose, with some being in the rock pore spaces analyzed. Also, the progressive dissolution and surface lowering tied to the indicated vertical tectonic block motion (See preceding Chapter) would result in progressive accumulation and enrichment of low solubility mineral including clays in the patchy and limited soil development, with some working into rock pores.

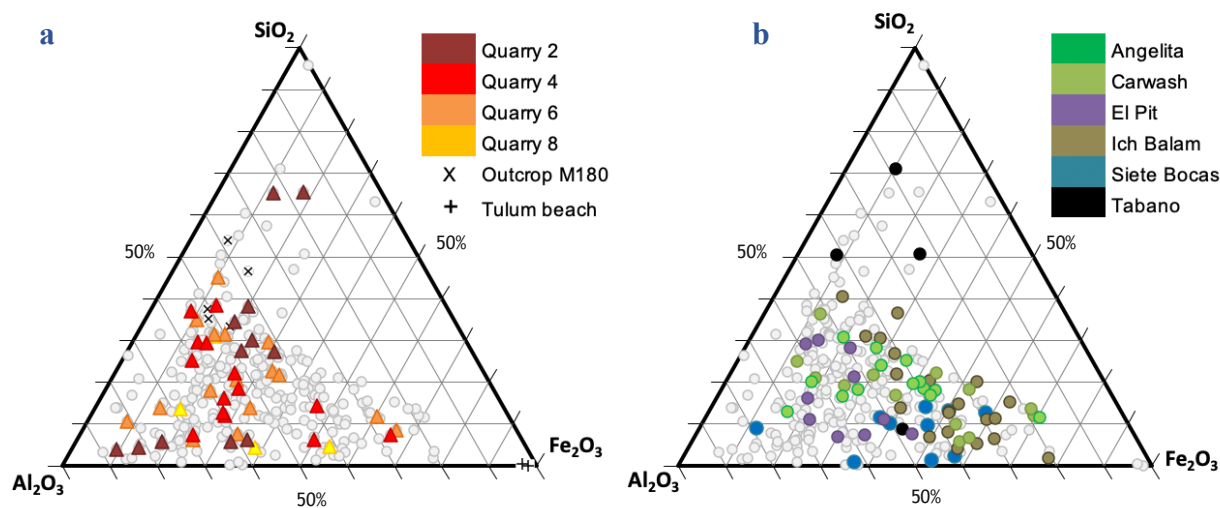


Figure IV-27 Mass  $SiO_2 - Al_2O_3 - Fe_2O_3$  (SAF) ternary plots illustrating the chemical composition of rocks in: **a)** Vadose zone, sampled in outcrops, quarries and dry caves; and **b)** Phreatic zone, sampled in underwater caves and cenotes. Data is in normalized weight %. Calculations assuming all Al, Fe, Si are present as their oxides.

## IV-6.2 CHEMOSTRATIGRAPHY

Surface geology and sedimentary logs are used to correlate to geochemical data, as different lithostratigraphic units would have different geochemical signals. In order to interpret the data, it is needed to know the facies presentation of the rocks and to think about the processes the rock would have been through. Perhaps the rock is reflecting its original depositional facies.

Maybe the sample has been diagenetically altered, or at the least weathered on exposure. Samples for geochemical analysis were taken from behind the weathered outcrop face, and furthermore hand samples were cut so as to extract, crush, and analyze the interior un-weathered rock. The types of facies expected to be found varies from a range of depositional environments from shallow marine, reef and lagoonal facies deposited during the Pleistocene, including lagoonal *wackestone*, beach-ridge *grainstone*, back-reef *calcarenite* and barrier-reef *rudstone*.

Natural wall outcrops are extremely scarce on the northeastern part of the Peninsula where local topographic relief is usually limited to gentle slope 1-3 m depressions. Vertical walled cenotes offer an option, but the surfaces are highly weathered, and geological sampling would break the ecological covering and leave a visual scare. Quarries are the best place to find suitable stratigraphic sections and sketch sedimentary logs. Quarries are locally called *sascabera*, after those which have been used to mine the *sascab* which is the friable and powdery weathered carbonate that develops below a caliche caprock. It was excavated by hand by the Maya and is preferentially used today as a building and paving material. Samples in *sascaberas* were taken once units determined. Sedimentary records of one large outcrop and three quarries are reported using SedLog Software (Figure IV-28, Figure IV-30, Figure IV-32, and Figure IV-34). Sedimentary structures found include obvious horizontal planar bedding of variable thickness, but no other bedforms are detected yet. Burrows, root marks, soil entrainments and cavities are common. Also found are articulated bivalves, not-imbricated gastropods and coral fossils often apparently in growth position.

All of the quarries examined include a relatively thin 0.25-0.50 cm crust of apparently modern capping calcrete, locally called caliche, was found indicating a subaerial exposure horizon.

Correlations have not been possible, and the available sections are laid out in the common Figure IV-37. More sites and stratigraphic sections are needed in order to continue to attempt a regional correlation, especially given the paucity of all such data on the Carrillo Puerto Formation in any published literature, and in order to establish an adequate correlation between sites through the different transects studied.

#### **IV-6.2.1 Outcrops and quarries**

##### ***Outcrops***

Outcrop 2, 3, and 4 are part of a transect going inland from Puerto Morelos through Ruta de los Cenotes, passing Leona Vicario up to Cristobal Colón, Quintana Roo along the M-180 Highway.

##### ***Outcrop 1***

Located west of Akumal Pueblo, this small quarry has eroded and rounded walls and seems to not have seen extraction activities for a while. Samples labeled as AKS01. Total samples: 5. SedLog available in Figure IV-28.

##### ***Outcrop 2***

Close to Cristóbal Colón, Quintana Roo. Total samples: 2. Labeled as RUT.

##### ***Outcrop 3***

Medium sized outcrop on roadside to Puerto Morelos. Labeled as PMS. Total samples: 3.

##### ***Outcrop 4***

Outcrop on side of the highway M-180 heading to Merida. Total samples: 5.

## ***Quarries***

### *Quarry 1*

A quarry located in the Tulum area on the right side of the road to Cobá. Samples from two large gastropod fossil shell specimens collected over what it looks like a transgressive lag or ravinement surface, a subaqueous erosional surface resulting from nearshore marine and shoreline erosion associated with a sea-level rise. It is crowded with large clasts and large pieces of hand-sized broken shells. Total samples: 2.

### *Quarry 2*

Medium sized quarry apparently active at the time of sampling, very close to the city of Tulum. Labeled as Sascabera 2. Total samples: 11. SedLog available in Figure IV-30.

### *Quarry 3*

Located close to Leona Vicario, Quintana Roo. Small quarry site with half of the terrain now used as garbage dump. Labeled as Sascabera 3. Total samples: 3.

### *Quarry 4*

Located near the town of Solferino Quintana Roo, at a distance of 55 km from the eastern coast and 60 km from the northern coast. It has very large exposed walls, one of the best sites for a more complete sedimentary log sketch. Labeled as Sascabera 4. Total number of samples: 14. SedLog available in Figure IV-32.

### *Quarry 6*

A massive quarry located close to the town of Kantunilkin Quintana Roo, at a distance of 43 km from the north coast. Labeled as *Sascabera 6* (SAS06). A very large wall where 6 units were identified. Because the size, it was also possible to subsample two units (Unit 2 & 6).

*Quarry 8*

*Sascabera* on the way to Valladolid Yucatán, labeled as SAS08, located 96 km inland. Total samples: 4.

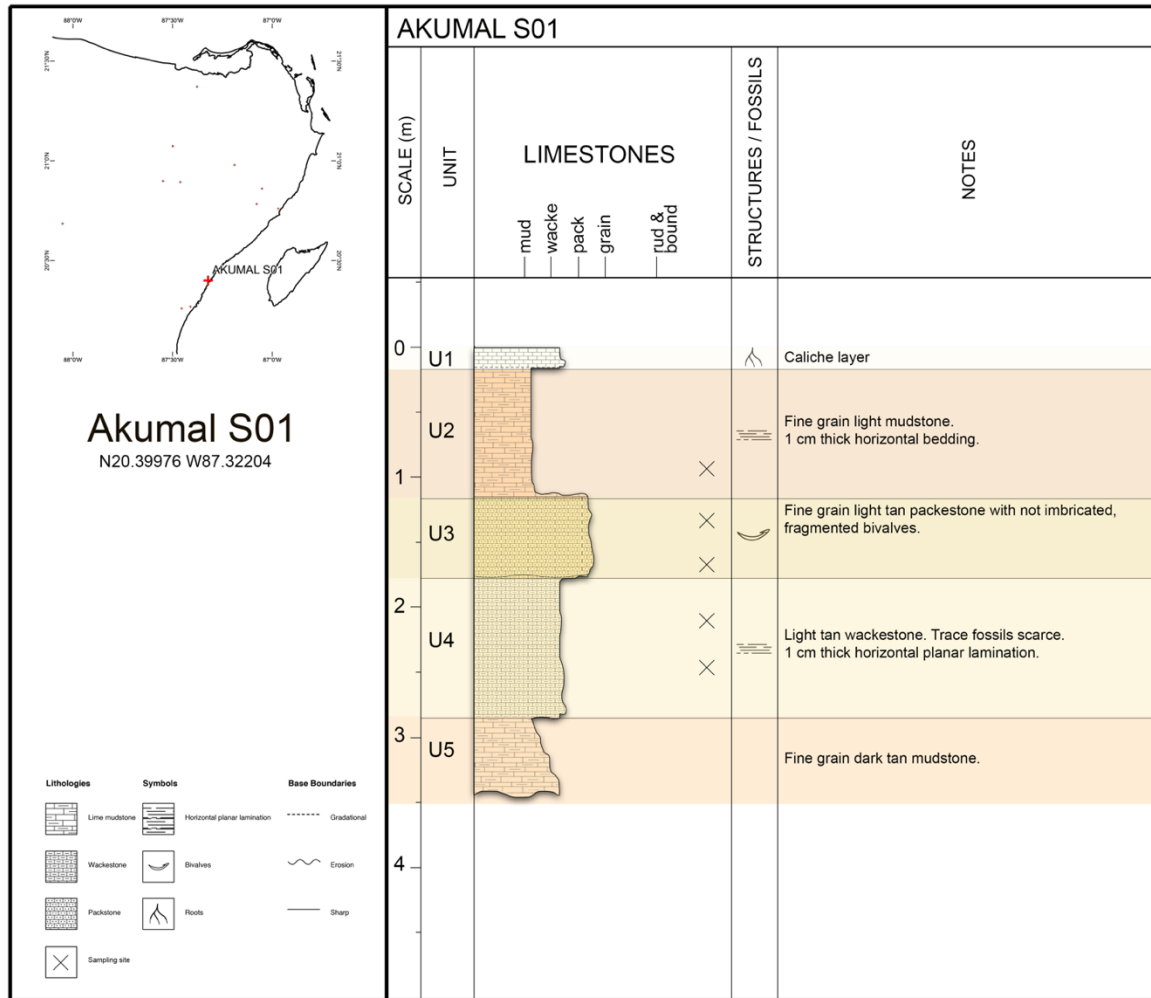


Figure IV-28 Sedimentary record for an outcrop located west to Akumal Pueblo, approximately 1 km inland; SedLog software was used to generate the sedimentary records. A simple lithological description at the right.

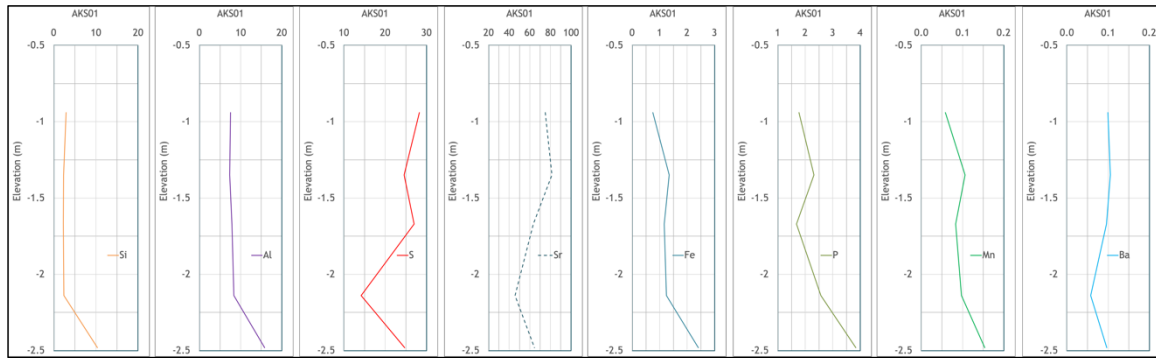


Figure IV-29 Geochemical profiles for selected elements in Outcrop 1 located in Akumal Pueblo, Quintana Roo, Mexico.

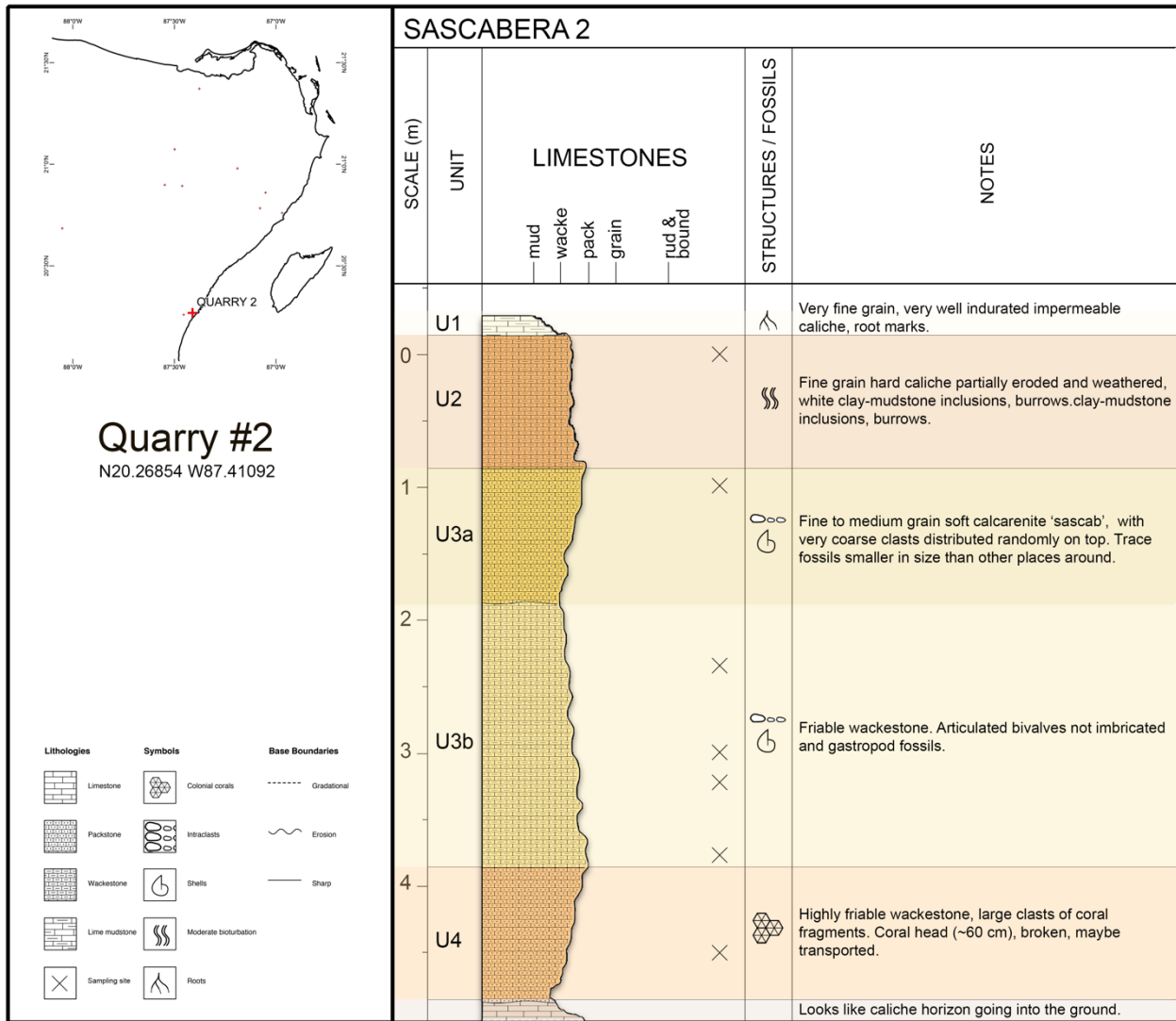


Figure IV-30 Sedimentary record for Quarry 2 near Tulum, located 2 km inland; SedLog software was used to generate the sedimentary records. Sampling depths are marked with a black cross and a simple lithological description is shown at the right.

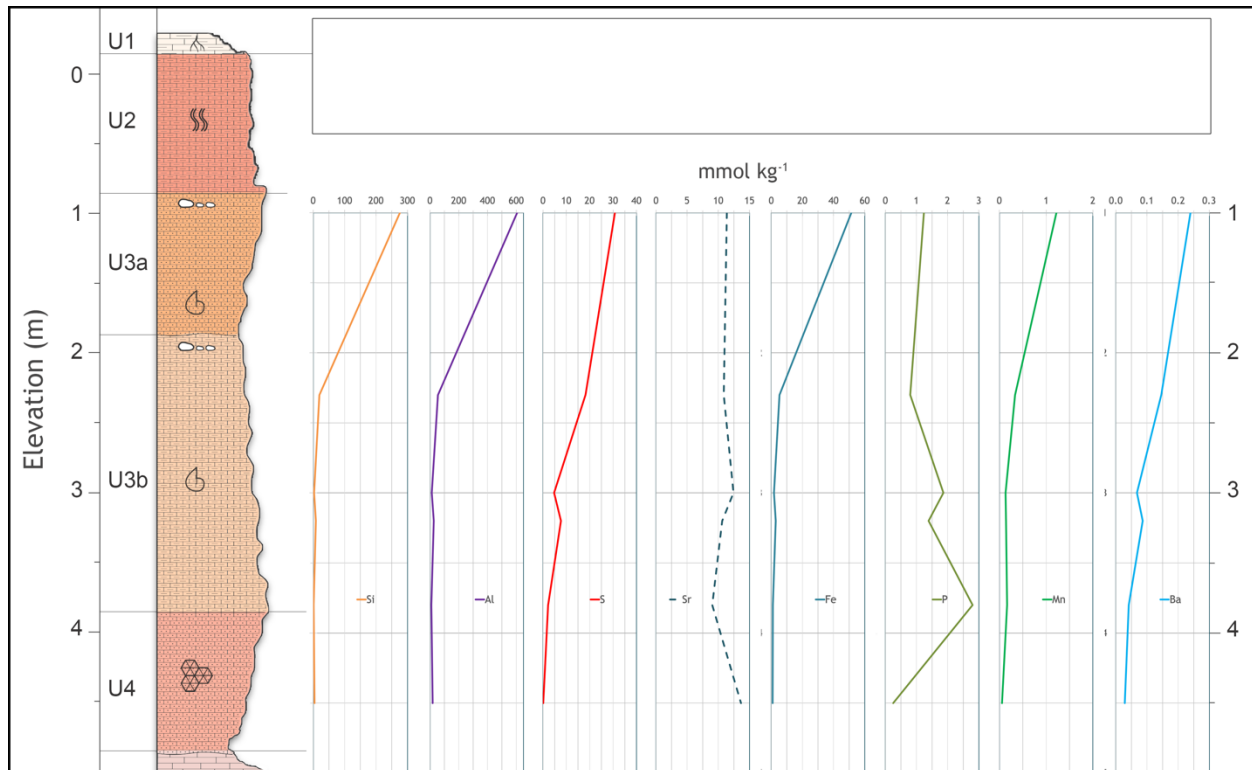


Figure IV-31 Depth profile concentrations—in decreasing concentration order—of Si, Al, S, Sr, Fe, P, Mn, and Ba for Quarry 2 near Tulum, located 2 km inland. Concentration values in mmol kg<sup>-1</sup>. SedLog software was used to generate the sedimentary records.

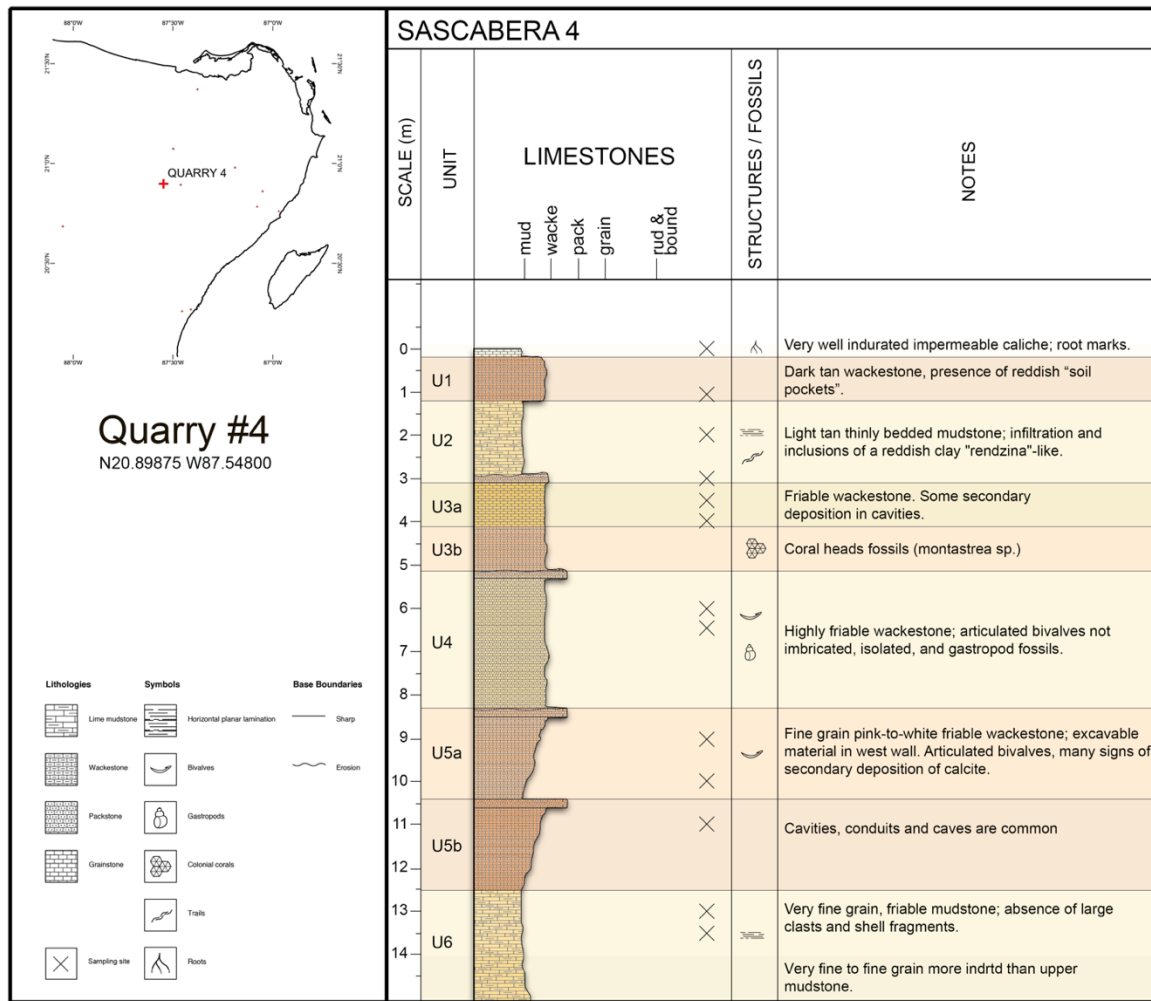


Figure IV-32 Sedimentary record for Quarry 4 located 55 km inland; SedLog software was used to generate the plots. A digital image of the site is shown to the left and a simple lithological description at the right. Rock samples also shown.

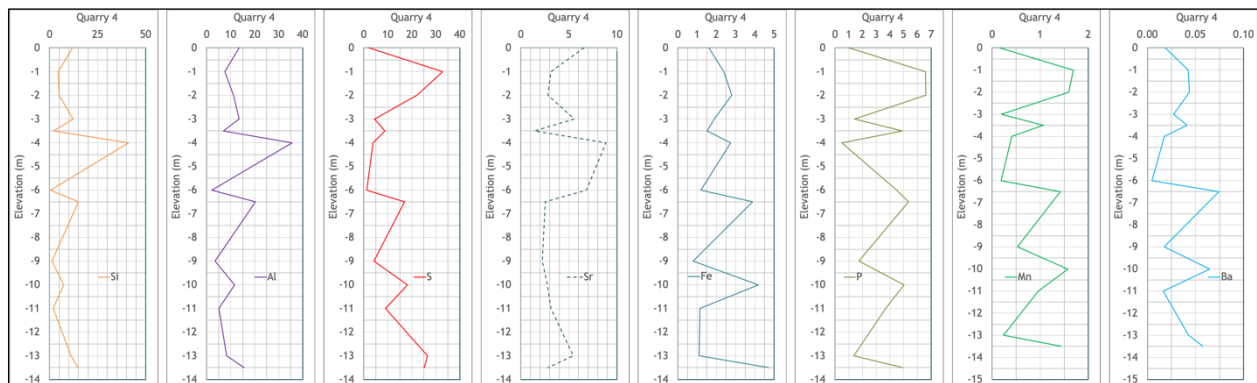


Figure IV-33 Geochemical profiles for selected elements in Quarry 4, located 55 km inland.

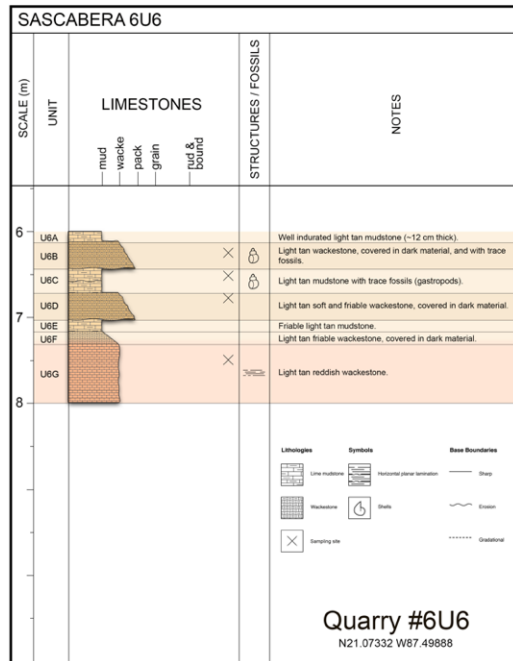
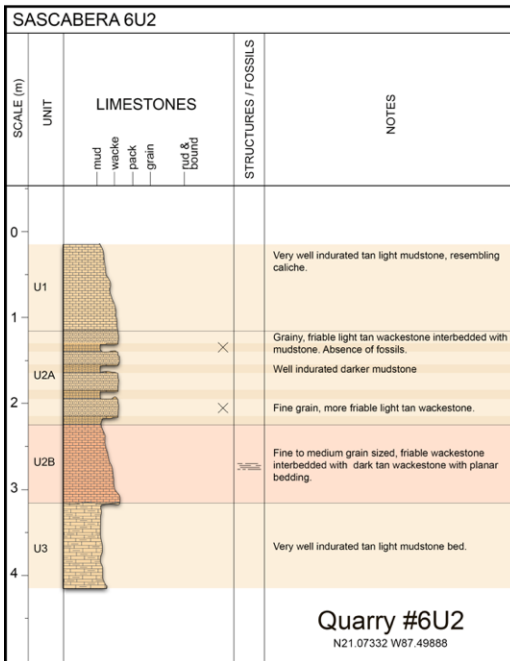
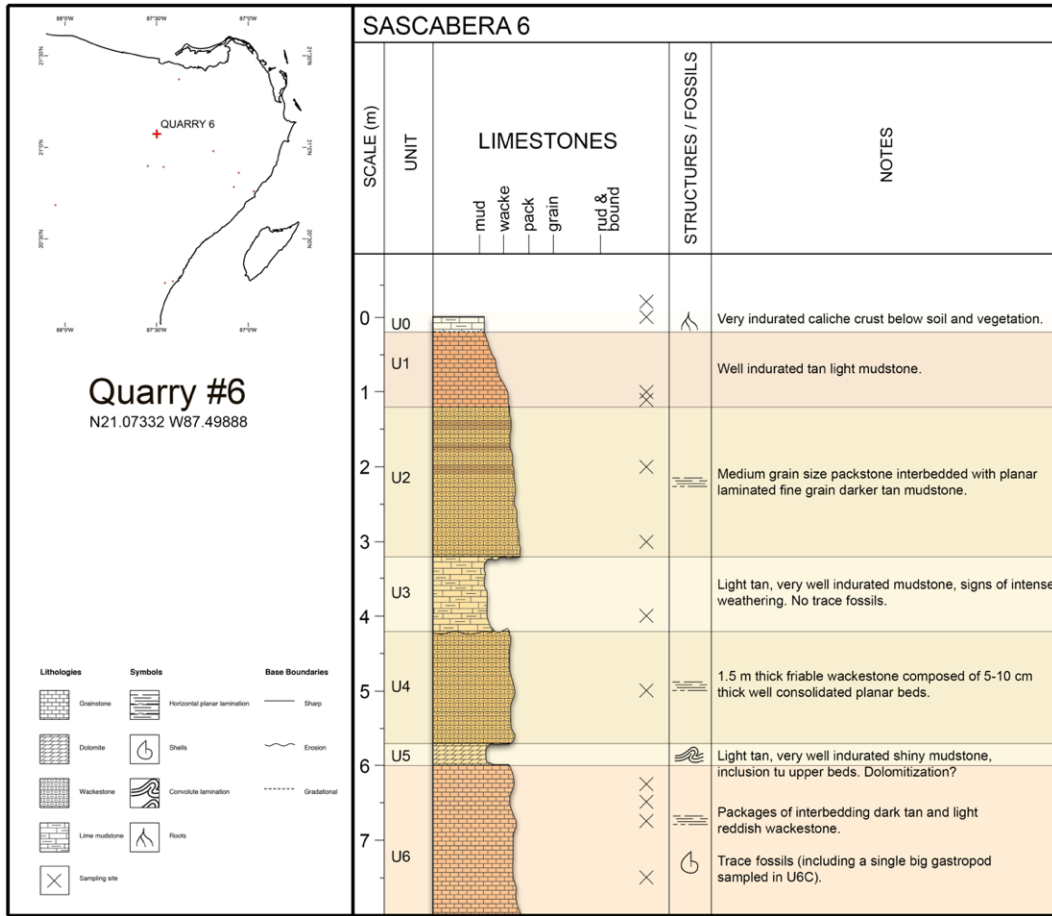


Figure IV-34 Sedimentary record for Quarry 6 located 43 km inland; SedLog software was used to generate the plots. A simple lithological description shown at right. Size of the wall allowed subsampling on Unit 2 and Unit 6.

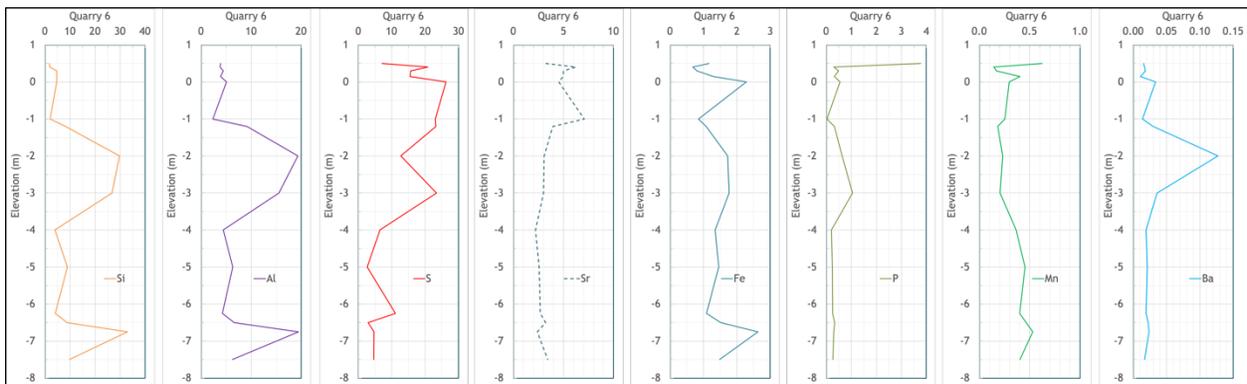


Figure IV-35 Geochemical profiles for selected elements in Quarry 6, located 43 km inland from the north coast.

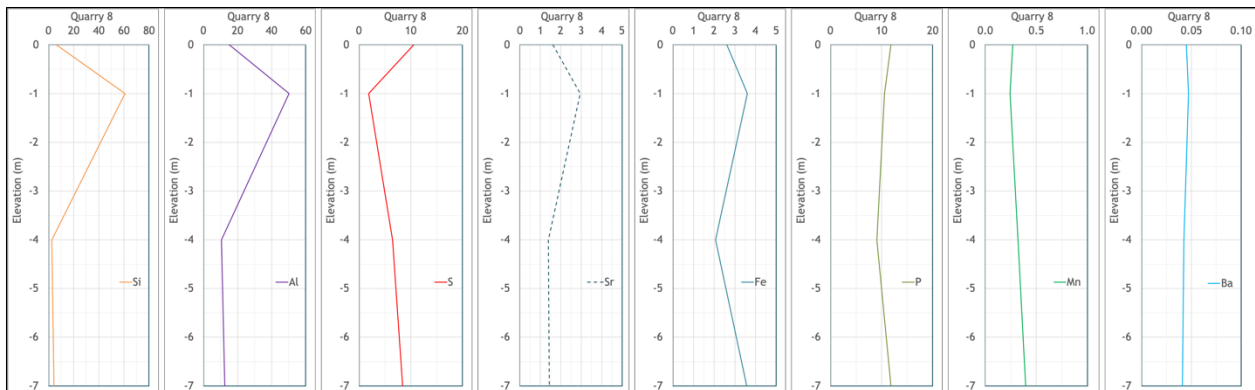


Figure IV-36 Geochemical profiles for selected elements in Quarry 8.

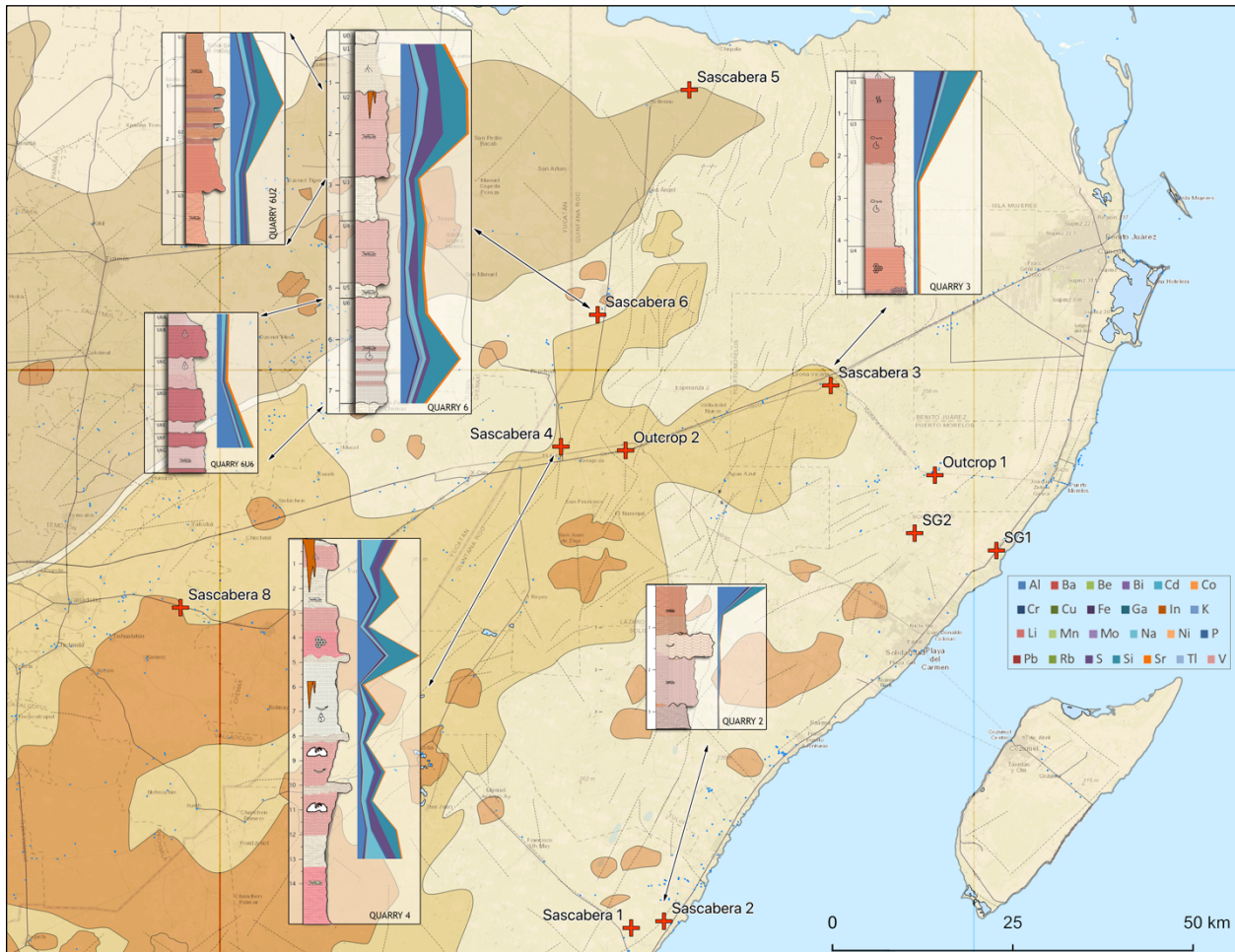


Figure IV-37 Location of outcrops and quarries from which SedLog profiles were sketched. Associated geochemical profiles are also shown. Detailed individual profiles are found in previous figures.

#### IV-6.2.2 Phreatic caves and cenotes

This section presents the chemo-stratigraphic profiles of wall-rock of different caves and cenotes located along the eastern coast of the peninsula. The area with phreatic samples includes inland of Puerto Morelos in an area called the Ruta de Cenotes, mid-section of the coastline south of Playa del Carmen, and then Sistema Sac Aktun north of Tulum, and finally south of Tulum with Ox Bel Ha (Table IV-12, and Figure IV-39 and Figure IV-40). One hundred and sixty (160) wall rock samples were obtained from 21 phreatic caves and cenotes. There are significant variations

in the concentration of some elements with depth, but any clear relationship with the relative position of the mixing zone (i.e., halocline) has not yet been found.

### ***Puerto Morelos Area***

#### *Cenote Siete Bocas*

Cenote Siete Bocas (“seven mouths”) is located on the touristic Ruta de los Cenotes that runs inland from Puerto Morelos. It is an area with numerous pit cenotes, but as yet no sub-horizontal flooded caves have been found. It is a large dome with a number of collapsed entrances and a deep shaft to at least the max plumbed depth of 82 m. Number of samples: 12.

#### *Cenote Zapote*

Located in the Kin Ha area, heading northwest along Ruta de los Cenotes. Also known as Hell Bells. Renowned for the presence of biogenic folia speleothems in the upper boundary of the present halocline level (Stinnesbeck et al., 2018), that are now also document in a number of adjacent cenotes although not as massively developed (Figure IV-38). Total samples: 4.

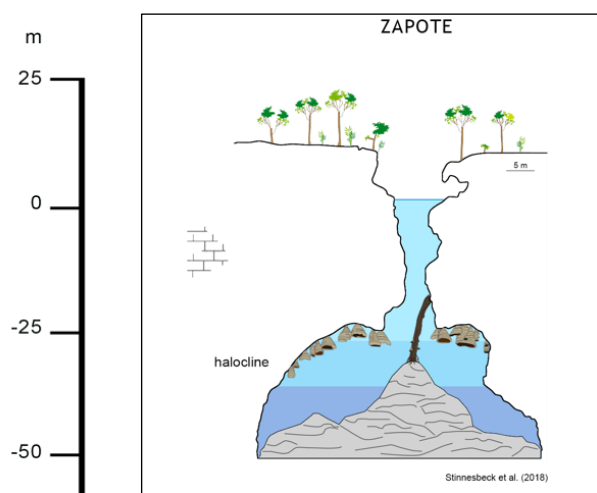


*Figure IV-38* Cross section of Cenote Zapote (Hell Bells) modified from Stinnesbeck et al. (2018). Position of the halocline is shown. Elevation in meters relative to water table.

Table IV-12 Summary table of phreatic cenote and cave sites sampled, grouped from north to south along the Caribbean coast, Quintana Roo.

<i>Cenote</i>	<i>Distance to coast (km)</i>	<i>Max depth (m)</i>	<i>Top of the halocline (m)</i>	<i># Rock samples</i>
<b>PUERTO MORELOS INLAND</b>				
<i>Cenote Siete Bocas</i>	14.9	82	28	12
<i>Cenote Zapote</i>	20.5	54	39	4
<b>SISTEMA PONDEROSA – MID CARIBBEAN COAST</b>				
<i>Cenote El Edén</i>	1.5	16	12	11
<i>Cenote Chikin Ha</i>	2.3	16	11	8
<i>Cenote Chac Mool</i>	2.5	18	12	8
<b>SISTEMA SAC AKTUN – TULUM AND NORTH</b>				
<i>Casa Cenote (Manatí)</i>	0.5	9	7.5	7
<i>Cenote Nichte Ha</i>	2.7	19	13	5
<i>Cenote El Pit</i>	5.6	127	16	10
<i>Cenote Ich Balam</i>	6.5	29	18	21
<i>Cenote Phenomeno</i>	6.5	28	19	9
<i>Cenote Aktun Ha (Carwash)</i>	8.4	26	21	13
<i>Gran Cenote</i>	11.8	39	24	6
<b>SISTEMA OX BEL HA – SOUTH</b>				
<i>Cenote Ox Bel Ha</i>	0.3	16	12	2
<i>Cenote Tábano</i>	0.8	16	11	4
<i>Cenote Odyssey</i>	3.1	18	13	5
<i>Cenote Escondido (Mayan Blue)</i>	5.6	21	17	6
<i>Cenote Muknal (Jailhouse)</i>	6.5	20	14	6
<i>Cenote Cristal</i>	7.4	22	18	4
<i>Cenote Dos Pisos</i>	9.8	28	22	2
<i>Cenote Bang</i>	10.2	24	18	5
<i>Cenote Angelita</i>	11.7	57.5	27	12

### ***Sistema Ponderosa and Chac Mool***

Around the area of Puerto Aventuras, Sistema Ponderosa, Sistema Chac Mool and Sistema Minotauro discharge fresh groundwater to the Caribbean coast. Roof collapses had formed many cenotes in the area.

### ***Sistema Sac Aktun – North of Tulum***

Sistema Sac Aktun is the most extensive underwater cave system known on Earth with ~370 km of explored phreatic cave (QRSS, 2020), as well as forming part of one of the most extensive and significant eogenetic karst aquifers in the world. The development of Sistema Sac Aktun, and adjacent caves systems along the Caribbean coast, is controlled by the coastal hydrologic regime, driven by glacio-eustasy, and modified by stratigraphic and structural controls (Kambesis & Coke, 2013). Similar to most of the coastal conduit systems along the Caribbean Yucatán coast, the near coast sub-horizontal conduits are particularly low tunnels that form mazes paralleling the coast and rudimentary conduits broken by fracture-controlled rooms (Kambesis & Coke, 2016). The near coast conduits are interpreted to be younger and notably structurally controlled. Further inland, the shallow phreatic to ~ 20 m water depth commonly include drowned speleothems, and sections of air-filled upper-level passages indicate speleogenesis above modern sea level. Sac Aktun passage depths range typically to 20 m, although the two deep underground breakdown pits of the El Pit and the Blue Abyss (not sampled) extend to 110 m below sea level.

### ***Casa Cenote (Manati)***

Brackish to marine rocky walled collapsed conduit now an open roofed channel, locally called *caleta*, extending a few hundred meters from the coastline. The conduit ceiling remains intact at the coast, with an underground passage under the beach, which discharges to a shallow coastal

blue hole. Sampling undertaken in the initial 100's of m of phreatic conduit, at the inland headland of the open channel. Number of samples: 7.

#### *Cenote Aktun Ha*

Also known as Cenote Carwash, located northwest of Tulum. Total samples: 13.

#### *Gran Cenote*

Located north of Tulum on the road to Cobá. Number of samples: 6.

#### *Cenote El Pit*

Pit cenote, with connection to shallow sub-horizontal passages of the vast Sistema Sac Aktun. El Pit sinkhole is open to the surface, and extends deeper than 110 m below sea level, although only the upper ~40 meters are reachable using standard open-circuit cave diving techniques. Submerged in this cenote between 35 and 45 m depth, are Late Pleistocene human remains from ~11,200 years ago. They are among the earliest human remains discovered in the American continent.

#### *Cenote Ich Balam*

An entrance to the *Aktun Hu* section of Sistema Sac Aktun, where there is a place known as *Hoyo Negro*, where the remains of *Naia*, one of the oldest skeletons in the American continent, were found.

### ***Sistema Ox Bel Ha – Tulum Area & South***

Sistema Ox Bel Ha is presently the second longest underwater cave systems in Quintana Roo and the world, at ~285 km of mapped phreatic passages, conduit roof collapses have created 140 cenotes.

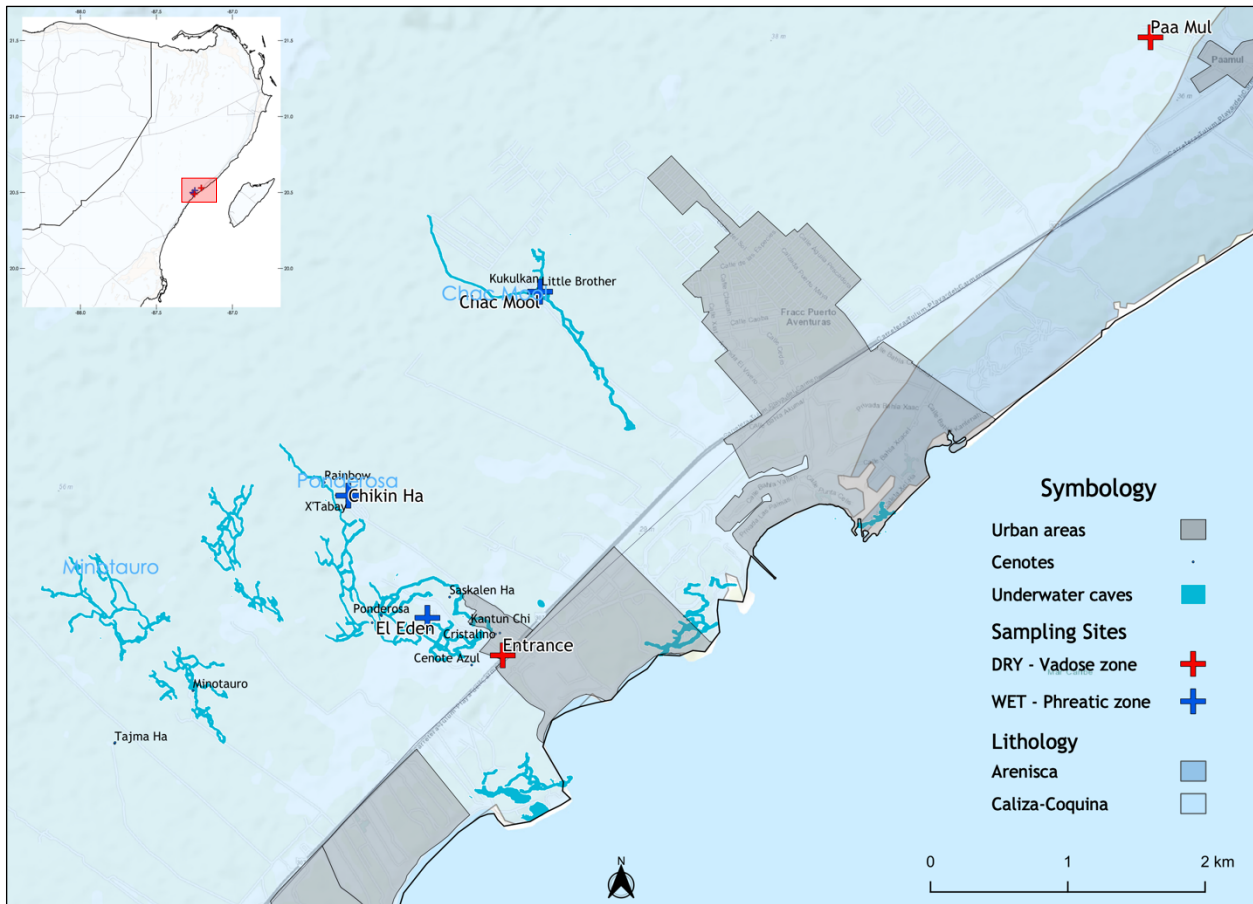


Figure IV-39 Location of cenotes around the area of Puerto Aventuras. Sistema Ponderosa, Chac Mool and Minotauro discharge fresh groundwater to the Caribbean coast. Lithology from Servicio Geológico Mexicano; underwater caves from Atlas Nacional de Riesgos (Mexican National Risk Atlas, CENAPRED, 2018; data from QRSS, 2020).

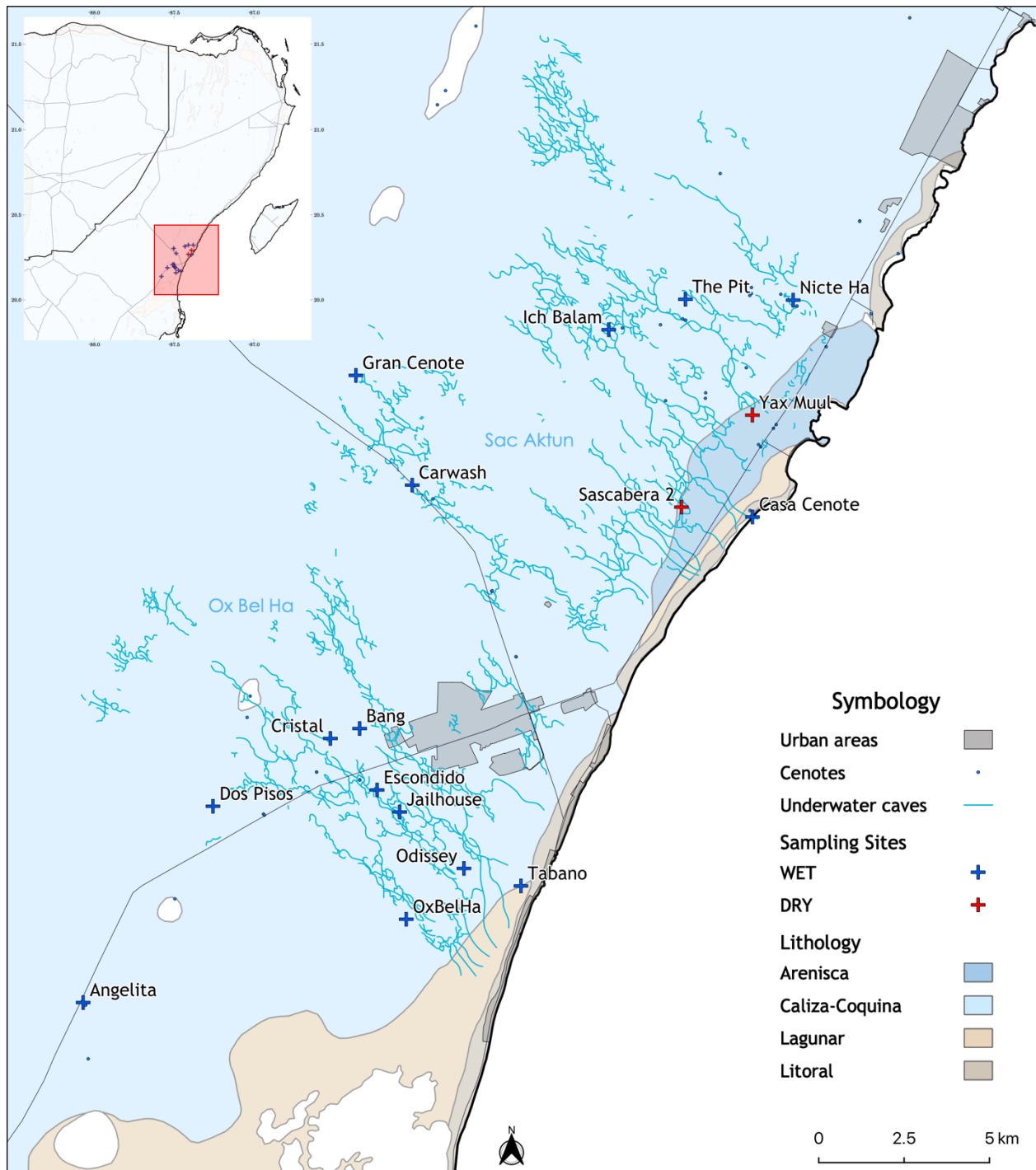


Figure IV-40 Location of cenotes around the area of the largest underwater cave systems of planet Earth around Tulum. Sac Aktun and Ox Bel Ha discharge fresh groundwater to the Caribbean coast. Lithology from Servicio Geológico Mexicano (2018), Underwater caves from Atlas Nacional de Riesgos (CENAPRED, 2020), although displacement of 7+ km has been detected.

Three remarkable Late Pleistocene human remains have been found: the skeleton of an 18-20-year-old woman, *Eve of Naharon*, dated to 13,454±117 calBP was found 368 m from the Jailhouse cenote; a 44- 50-year-old woman, *Mujer de Las Palmas* dated to 8,937±203 calBP was found ~2 km from the Jailhouse cenote; and a 40-50-year-old man, the *Muknal Grandfather*, dated to 9,600 calBP. Ox Bel Ha was likely used as an important site for ritual burial (González et al., 2014; S. R. Stinnesbeck et al., 2018).

### *Cenote Angelita*

Cenote Angelita is a pit cenote (e.g., vertical shaft) located southwest Tulum. It has a maximum depth of 57.5 m and a very noticeable hydrogen sulfide (H<sub>2</sub>S) cloud just below the halocline. It has a large debris pile with dead trees on top. Number of samples: 14.

Some similar trends and features in the geochemistry of the wall rock of different cenotes in the area around northeastern coast of the Yucatán peninsula are observed. Sulfur in general decreasing in concentration with depth. Al, Si covary, and follow the same pattern at different sites, as their geochemistry is related, maybe in the form of aluminosilicates, as a residual product of calcite dissolution, silicate weathering and pedogenetic processes.

The hydrochemistry within and below the halocline is distinct. The is frequently warmer at 27-28 °C at sites close to the coast, hypoxic, higher ion strength because elevated salinity, and under reducing conditions (Beddows, 2004). The complex oxides are unlikely to survive the reducing conditions below the halocline, at least for the more exposed rocks, the ones being sampled on the exposed cave walls. The few data available below the halocline seems to point out in that direction.

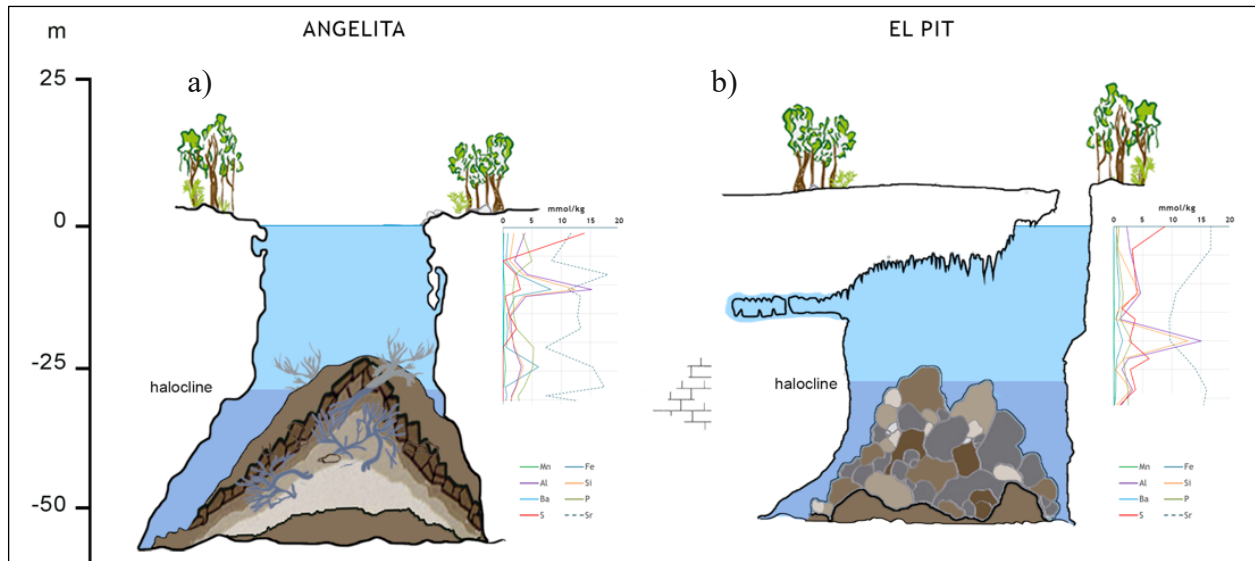


Figure IV-41 Location, cross sections, and geochemical (Al, Ba, Fe, Mn, P, S, Si, Sr) depth profiles of two pit-cenotes: a) Angelita, b) El Pit. Cross sections modified from Octavio del Río. Elevation in meters relative to water table.

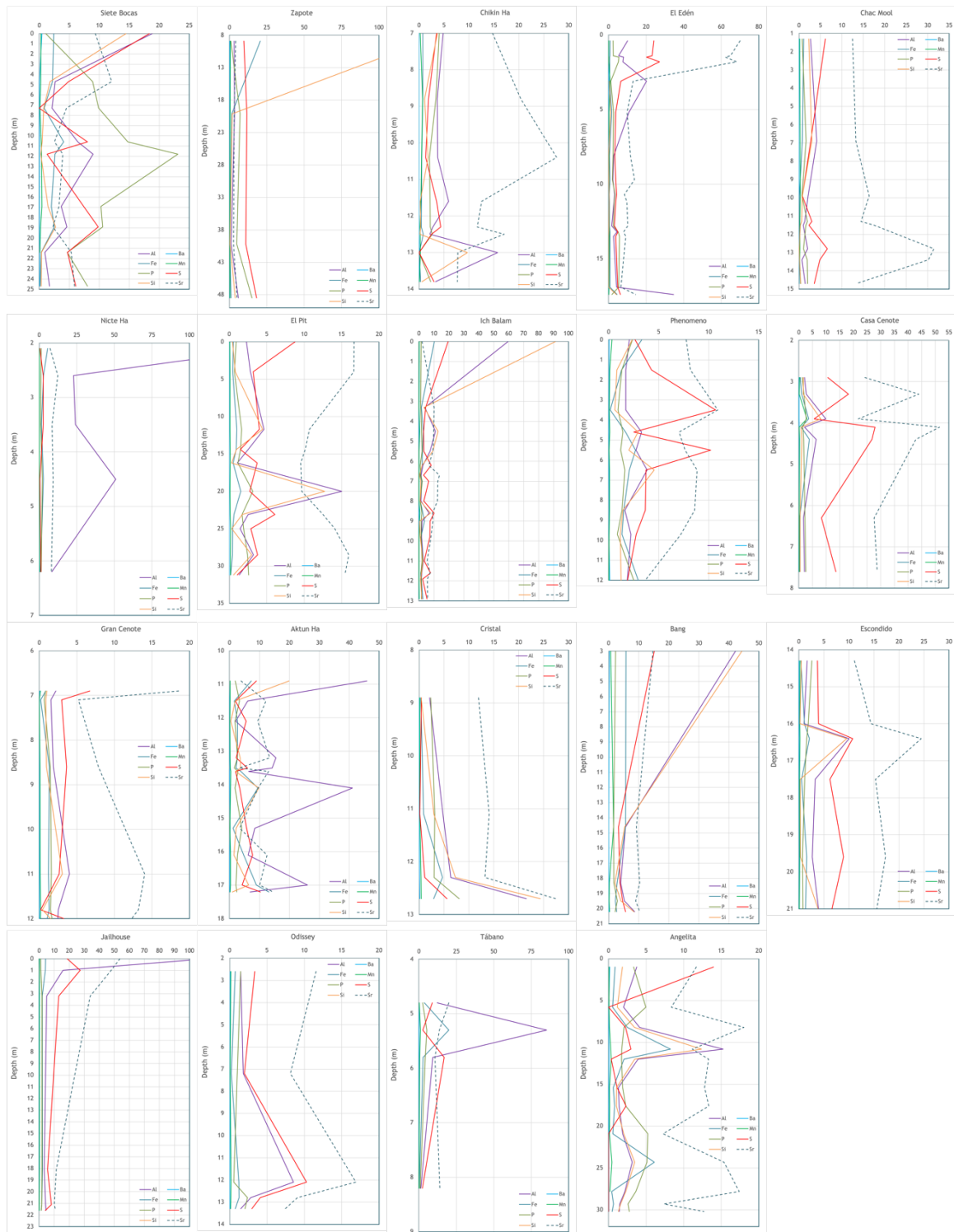


Figure IV-42 Depth geochemical profiles of selected of the intermediate concentration elements (Al, Ba, Fe, Mn, P, S, Si, Sr) in rock samples from 19 cenotes located in the eastern Caribbean coastal Yucatán Peninsula, from the Puerto Morelos area, Sistema Ponderosa, Sistema Sac Aktun and Sistema Ox Bel Ha. Depth relative to water table. All values in  $\text{mmol kg}^{-1}$ .

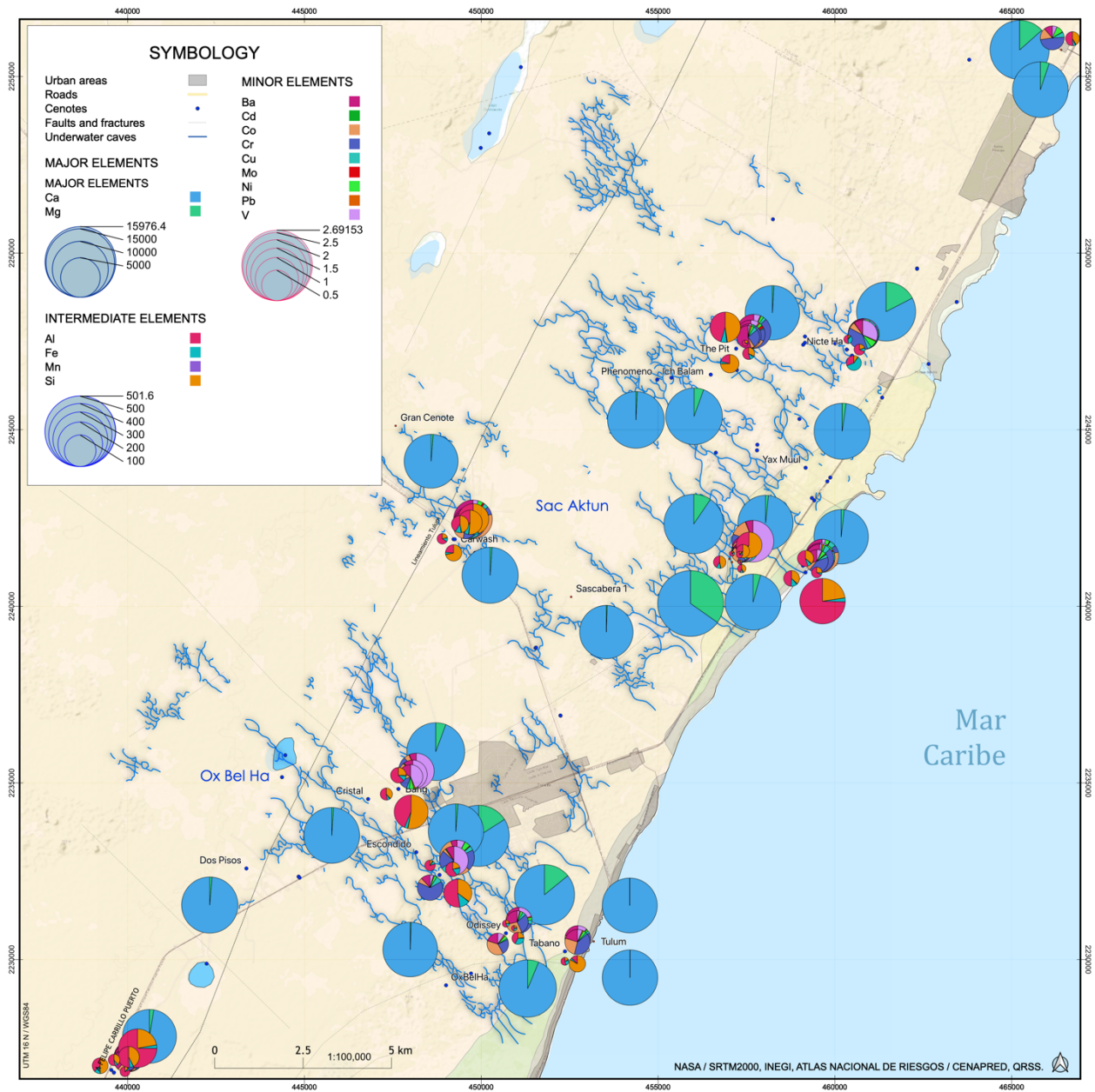


Figure IV-43 Overall distribution of Major (Ca, Mg), Intermediate (Al, Fe, K, Li, Mn, Na, P, S, Si, Sr), and Minor (Ba, Cd, Co, Cr, Cu, Mo, Ni, Pb, V) elements in rock samples distributed along the extensive underwater cave systems around Tulum, eastern coastal Quintana Roo. All values in  $\text{mmol kg}^{-1}$ .

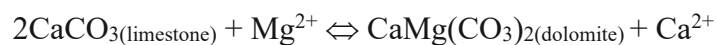
## IV-7 DIAGENETIC PROCESSES

Diagenesis is any physical and chemical process that affects a sedimentary earth material after initial deposition, during or after lithification, exclusive of weathering and metamorphism. The study of diagenesis in rocks is used to understand the geologic history they have undergone and the nature and type of fluids that have circulated through them. Two important post-depositional processes affecting the Yucatán Peninsula carbonate rocks are considered now. One is the process of dolomite formation (Section IV-7.1), dolomitization. The second explores on the pedogenetic transformation of rock to soils, and the geochemical paths of a number of residual elements (Section IV-7.2).

The origin of dolomite both as mineral and as a rock remains subject to controversy because some of the chemical and/or hydrological conditions of dolomite formation are poorly understood, and because petrographic and geochemical data commonly permit more than one genetic interpretation. Considerations in this section does not attempt to fully characterize dolomite composition, but to provide some basic accounting to explore on the mechanism followed by diagenetic processes in shallow phreatic areas and their relative distribution within the carbonate platform and its relationship with fluids circulation. This section and discussion are based only on Ca and Mg mol-to-mol ratios.

### IV-7.1 DOLOMITIZATION

Most dolomites,  $\text{CaMg}(\text{CO}_3)_2$  are considered secondary, formed by replacement of original limestone ( $\text{CaCO}_3$ ), and dolomitization is commonly described by the stoichiometric equation:



As indicated by this expression, dolomitization requires substantial mass transport of magnesium, and because of the density contrast between calcite and dolomite, such mole-for-mole replacement has been linked to an approximately 13% porosity increase (Whitaker & Xiao, 2010). Upon burial, a range of processes may result in preferential preservation of porosity in dolomitized carbonates (Machel, 2004).

Despite the abundance of dolomite in the global rock record and dolomite supersaturation of modern seawater, dolomites are rare and occur sparsely in modern carbonate sediments (Land, 1985; Ward & Halley, 1985; Whitaker & Xiao, 2010; W. B. White, 2002). Patchy dolomitization of middle Pleistocene limestone along the northeastern margin of the Yucatán Peninsula probably took place where discharging fresh groundwater mixed with marine intruded groundwater in the halocline reaction zone, following the paragenetic sequence of (Ward & Halley, 1985).

The sequence of cements from 1) calcian dolomite to 2) zoned high-calcium dolomite/dolomite and calcite/dolomite to 3) calcite reflects a general change in pore-water composition to progressively lower Mg:Ca ratios. This suggests progressive freshening of ground water as sea level falls. However, the pre-dolomitization freshwater diagenesis of the Yucatecan limestone would have required a short-term sea-level drop of at least 12 m during the 200-ka interglacial period. The simplest explanation is that dolomitization in Yucatán occurred during the latest Pleistocene interglacial period.

Little or no aragonite remains in dolomitized portions of Yucatecan cores (Ward et al. 1995). This suggests surface dolomitization occurred after or during the later stages of aragonite dissolution, in contrast to the deep early burial dolomitization processes that could explain dolomitization at depth, with different mechanisms of formation (See CHAPTER I). The first

mechanism implies a time scale of  $10^5$  years, while the latter, according to reactive transport models for hydrothermal circulation in carbonate platforms, would take several  $10^6$  years (Whitaker & Xiao, 2010). Both of them have fluid flow and water masses circulation within the rock matrix as a primordial component in order to occur.

The hypothesis that dolomitization takes place in the mixing zone between fresh and ocean-derived ground water has been a popular explanation for many dolomites not associated with supratidal and evaporite deposits (Back et al., 1979; Hanshaw et al., 1971; Ward & Halley, 1985). In previous works on the Yucatán Peninsula, dolomites are predominantly calcian, from  $\text{Ca}_{57}\text{Mg}_{43}$  to  $\text{Ca}_{62}\text{Mg}_{38}$ , but also with the more-calcian-rich phases partly dissolved. The  $\delta^{18}\text{O}$  compositions of Yucatán dolomite and of modern groundwater suggest dolomite precipitation from groundwater ranging from 75% seawater to nearly all sea water (Stoessell et al., 1989; Ward & Halley, 1985). Isotopic analyses together with position of dolomite in the cementation sequence suggest the most stable dolomite (least calcian) precipitated from mixed ground water with large proportions of seawater, and the less-stable dolomite (more-calcian) precipitated from fresher ground water.

Distribution of dolomite occurs in some of the rock samples a few meters below the water table. At least minor amounts of stoichiometrically ratios similar to those in dolomite are present in 12 of samples taken between Cancun and Tulum. The most extensive dolomitization is in the vuggy reef limestone presumably of mid-Pleistocene age, which may relate to the higher permeability associated with the reef facies, allowing for higher flux rates and exposure to the Mg in near-normal marine waters actively circulating in the 1-10 m below the halocline (Beddows et al., 2007). In the most-dolomitic zones, the rock is about 50% dolomite and 50% low-Mg calcite.

Deep exploration wells drilled across the peninsula by *Petróleos Mexicanos* (Pemex) penetrated about 1300–3500 m of stratified Neogene, Paleogene, Cretaceous, and Jurassic sedimentary rocks, show hundreds of meters thick beds of dolomite both below and up the Chicxulub impact breccia unit. Cores show an overall setting of sedimentary rocks consisting ~35%–40% dolomite, 25%–30% limestone, 25%–30% anhydrite, and 3%–4% sandstone and shale (Ward et al., 1995). These deeper dolomite deposits are most readily explained by coupled dolomitization followed by anhydritization from the platform circulation of near-normal marine water driven by geothermal gradients, all while the whole platform remained persistently submarine at ~ 200 m water depth through to at least 10 Ma (See Chapter II).

In contrast, the uppermost 10's meters of young limestones of the coastal northeastern Yucatán Peninsula do not include laterally extensive or thick beds of dolomite. Distribution of dolomite occurs patchy and erratic in rock samples from the surface and shallow subsurface with no indication of extensive massive dolomitization. This limestone accumulated during the last interglacial high stand of sea level. Dolomitization was preceded by freshwater diagenesis, including precipitation of calcite cement and partial dissolution of aragonitic components. Distribution of dolomite apparently was at least in part controlled by distribution of larger cavities, particularly coral molds.

This latter implies that shallow dolomitization takes place in the conduits of greatest groundwater flow (Ward & Halley, 1985). It is possible to distinguish between two depth-distributed diagenetic settings for dolomite formation as shown in Table IV-13.

Table IV-13 Comparison of two different dolomitization mechanisms operating as function of depth and their specific requirements.

<i>Process</i>	<i>Mechanism</i>	<i>Product</i>	<i>Timescale</i>
Dolomitization at shallow	Paragenetic sequences (Ward & Halley, 1985).	Patchy, erratic, in the shallow mixing zone of coastal environments. Requires both freshwater and saline flows.	10 <sup>5</sup> years, hundreds of thousands.
Dolomitization at depth	Early burial dolomitization + anhydritization by geothermal convection (Al-Helal et al., 2012; Land, 1985; Lugo-Hubp et al., 1992; Whitaker & Xiao, 2010).	Deeply buried, massive thick bedrock, requires an established geothermal (Kohout) convection in the carbonate platform.	10 <sup>7</sup> years, tenths of millions for a complete process.

#### IV-7.1.1 Mg:Ca ratio

Determining the Mg:Ca ratio would help to elucidate the diagenetic history of rock minerals in relation to fresh and marine water flux through the platform. This could be helpful in order to both identify mineral species, and to infer the sequence of major diagenetic events.

aragonite/calcite → low-Mg calcite → Mg calcite → dolomite

A Mg:Ca ratio equal to or greater than unity is required for dolomite to precipitate in shallow phreatic water. Mg is *supplied* by saline waters, but precipitation is *permitted* only by dilution with fresh waters (Back et al., 1979; Folk & Land, 1975; Hanshaw et al., 1971).

The *paragenetic sequences* described by Ward & Halley (1985), that is, the chronological order of crystallization of minerals in a rock, imply that diagenetic dolomitization processes in the coastal shallow subsurface of the northeastern Yucatán platform, would involve that this process takes place where freshwater and saline water masses coexist, at the mixing zone in the shallow phreatic zone. Dolomitization mechanism requires both a constant pumping supply of seawater

Mg ions, and further dilution with freshwater to allow precipitation of dolomite when a certain range of Mg:Ca ratios are achieved.

Unequivocal dolomite identification in this study is not intended, although some constraints could be obtained with additional analysis such as Raman Spectroscopy or directly assess and map mineralogy in hand samples, it is not possible to achieve employing only molar stoichiometry assessments. This is due to the fact that mixtures of different carbonate species can yield similar stoichiometric values. Furthermore, geochemical analyses were performed on samples from bulk rock by means of crushing approximately cubic cm sub-samples that most of the times was not mineralogically or petrographically differentiated prior to crushing. As stated by Machel (2004), complete dolomite genesis characterization should involve a combination of methodologies, partly because some of the chemical and/or hydrological conditions of dolomite formation are not fully understood, and mainly because petrographic and geochemical data alone, commonly permit more than one genetic interpretation. The correct characterization of dolomite distribution or to constrain its diagenetic environment, samples should be petrographically and crystallographic analyzed, in combination with interpretation of  $^{18}\text{O}$  and  $^{13}\text{C}$  stable isotopes,  $^{86}\text{Sr}/^{87}\text{Sr}$  isotopes, trace elements, and fluid inclusion parameters, which under favorable circumstances can contribute to determine the direction of fluid flow at the time of dolomitization.

The overall distribution of dolomite is patchy and erratic, and assuming it is dolomite the main contributor to the mineralogy of some selected samples. is presumably calcian according to mol-to-mol ratios and texture assessment. ICP-OES analysis of bulk-rock samples indicates an average cation composition of  $\text{Ca}_{0.89}\text{Mg}_{0.11}$ . For the vadose zone, average Mg:Ca ratio is  $0.120 \pm 0.057$  ranging from 0.034 to 0.256. The phreatic zone average Mg:Ca ratio is slightly higher, at

$0.156 \pm 0.054$  ranging from 0.069 to 0.364. As an exercise similar to that in previous sections, stoichiometry shows a composition in the bulk samples ranging from  $\text{Ca}_{0.13}\text{Mg}_{0.87}$  to  $\text{Ca}_{0.99}\text{Mg}_{0.01}$ .

*Table IV-14 Cation composition of carbonate rocks from the shallow subsurface on the northeastern coast of the Yucatán Peninsula. Data from Ward & Halley (1985).*

Mineral source	Stoichiometric ratio	Mg:Ca ratio
<b>Dolomite</b>	$\text{Ca}_{58}\text{Mg}_{42}$	0.72
<b>Limpid crystals</b>	$\text{Ca}_{57}\text{Mg}_{43}$	0.75
<b>Zoned crystals</b>	$\text{Ca}_{57-59}\text{Mg}_{43-41}$	0.69 – 0.75
	$\text{Ca}_{62}\text{Mg}_{38}$	0.61
<b>Low-Mg Calcite</b>	$\text{Ca}_{99-97}\text{Mg}_{1-3}$	0.01 – 0.03
<b>Mg Calcite</b>	$\text{Ca}_{96-93}\text{Mg}_{4-7}$	0.04 – 0.08

There are 9 suspect samples with high amounts of Mg reaching 40,000+ mmol kg<sup>-1</sup>, that are reserved for further investigation and traceability, which were taken out from considerations and calculations in this section. The 9 samples are from the surface in Quarry 2 and Quarry 6.

Notably the samples with the higher and maximum Mg values and Mg:Ca ratios are distributed along or near the coast, in general decreasing inland. This includes samples on the north coast, and then also along the Caribbean coast. The exception to this observation would be the samples described above, located 60 km inland near the town of Kantunilkin, that show very high Mg:Ca ratios, however that site is far enough south that the Chicxulub impact breccia is shallow or even emergent at the surface (Perry et al., 2009), and the high Mg:Ca samples may represent redeposition of much older/deeper platform dolomite.

In this context, a high sea level is related to a high Mg:Ca ratio. When sea level declines, the meteoric freshwater lens can develop, sinking into the subsurface rocks of the platform. Dolomitization, therefore, must have taken place during or nearly after a high stand of sea level.

When sea level falls, freshwater lens forms and fresh groundwater is circulated through the rock matrix. Perhaps pulses of marine water circulating actively through the caves under current conditions, such as those identified by Beddows et al. (2007), which operate for parts of the year depending on the local sea level, could be responsible for dolomitization in the mixing zone in the shallow coastal parts of the aquifer. That would suggest that a higher marine-pumped flux of Mg would result in higher dolomitization. The patchy distribution might account for this process to happen at least in some determined areas.

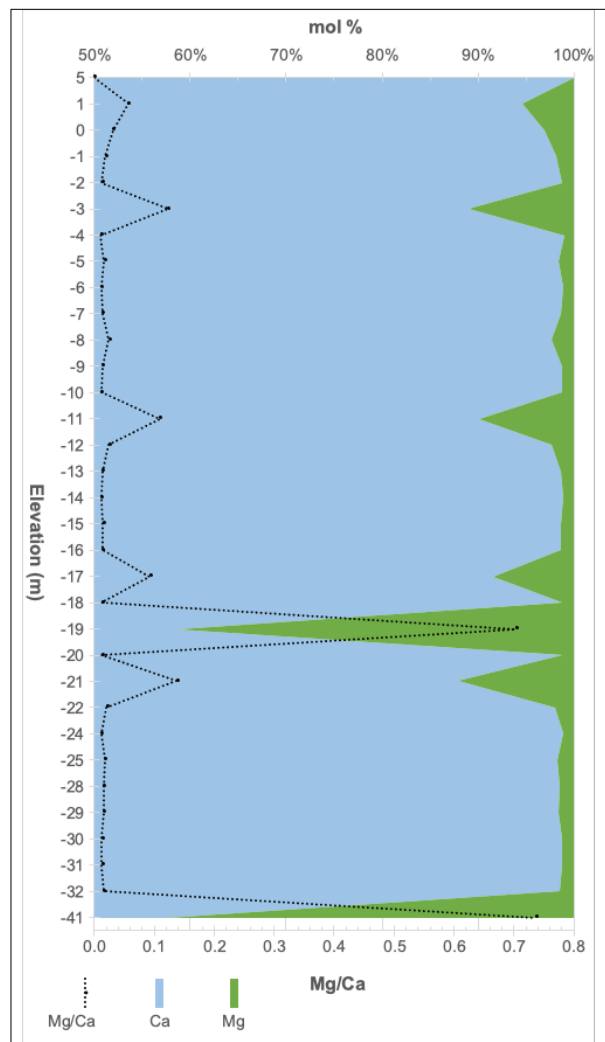


Figure IV-44 Bulk distribution of Ca, Mg and Mg:Ca ratio by depth average (n = 290).

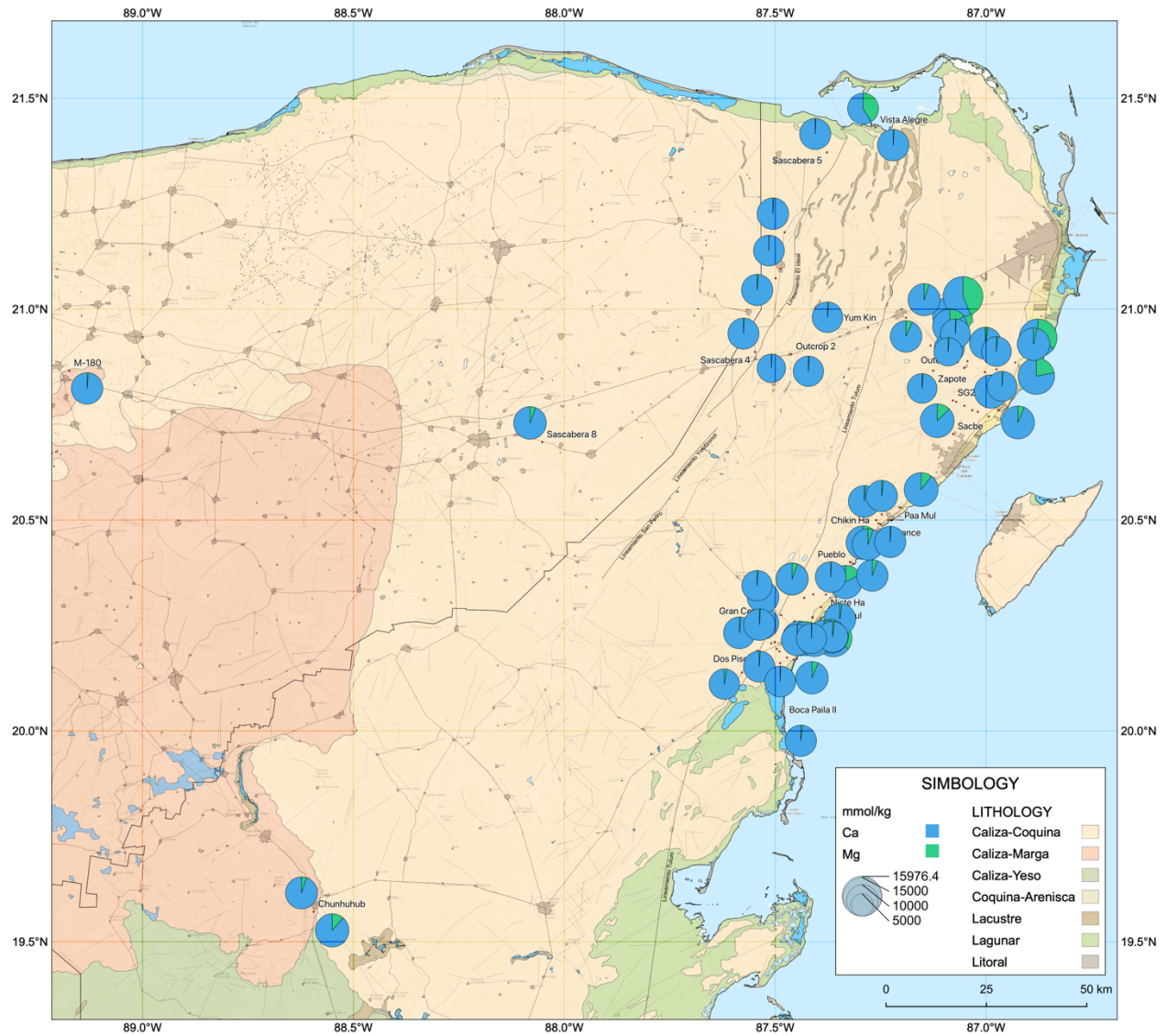


Figure IV-45 Regional distribution of Ca and Mg composition on rock samples.

#### IV-7.2 RESIDUAL ELEMENTS AND SOILS

The quantification and distribution of some metal and non-metal elements in the rocks can be useful for pedogenetic analyses on formation, development and distribution of soil studies in the tropical karstic landscapes, such as the Yucatán Peninsula.

Silicate soils develop on limestone and dolomite rocks and they can form thick, reddish clay soils, associated with karst carbonates, called *terra rossa* in Mediterranean settings (Durn, 2003; Yaalon, 1997), where the reddish color of is the result of the preferential formation of hematite over goethite (Schwertmann, 1993). The Yucatán landscape presents a high pedodiversity despite the patchy soil development overall, including thin rendzinas as well as thick red soils (Bautista et al., 2011; Cabadas-Báez et al., 2010; Sedov et al., 2008), called locally *haylu'um*. In the international system for classification of soils (WRB, Chesworth et al., 2008; these soils are classified as Cambic Leptosols, Cambisols, Luvisols, Nitisols and Haplic Vertisols (IUSS Working Group WRB, 2014).

For many soils developed on limestones it has been difficult to identify carbonate that formed in the soil versus carbonate mechanically inherited from the rock. Carbonate formed in the soil has been termed “pedogenic” or “authigenic” (Monger, 2002). Carbonate mechanically inherited directly from the limestone has been termed “lithogenic” or “geogenic” (Doner & Lynn, 1989). Criteria for distinguishing pedogenic from lithogenic carbonates involve both field and laboratory analyses.

There has been a debate over decades about whether clay constituents associated with *terra rossa* formation are of autochthonous or allochthonous origin and several hypotheses (Table

IV-15) have been proposed to explain its formation, which can be grouped in three variants: a) accumulation of insoluble residues (Moresi & Mongelli, 1988) ; b) detrital allochthonous materials (Durn et al., 1999; Muhs & Budahn, 2009; Yaalon, 1997); and c) residual dissolution with allochthonous contributions from either mud marine sediments, tephra, volcanic ash, eolian dust, or a combinations of those (Merino & Banerjee, 2008). This latter hypothesis of the replacement of limestone by authigenic clay along a reaction front explains the association between *terra rossa* and karst morphology. Since the clay is authigenic, its major elements—Al, Si, and Fe—must come to the front as aqueous ions, probably result from dissolution of dust at the surface (Merino & Banerjee, 2008). There is evidence of Saharan dust reaching the Caribbean region (Doherty et al., 2008; Muhs & Budahn, 2009).

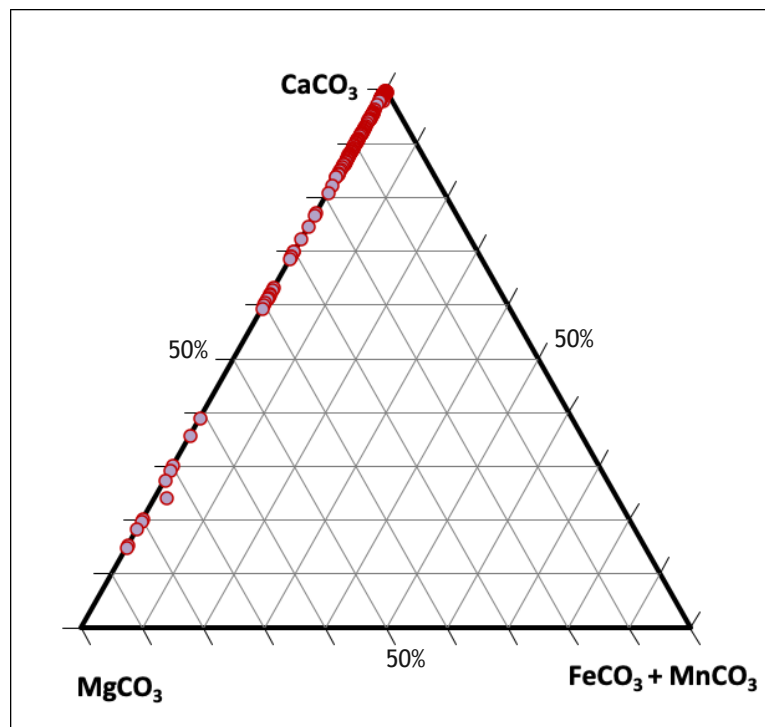


Figure IV-46 *Calcite – Magnesite – Siderite ternary plot illustrating chemical composition of bulk samples; normalized to mol % (n = 290). Spreadsheet for creating tri-plots from Graham & Midgley (2000).*

Cabadas-Báez et al. (2010) calculated based on a 150 cm-diameter soil pocket and found that to produce 2.22 tons of soil (formed from lime-free residue), it would be necessary to dissolve 2405.41 tons of calcarenite, occupying a volume of 1260.03 m<sup>3</sup>, that is 700 times larger than the volume of the pocket. They refuted the hypothesis as improbable, that such volume of carbonate rock was dissolved above the pocket. Duch (1988) calculated that generating an acre of soil 1 m depth, would require the total weathering of 625,000 m<sup>3</sup> carbonate rock. Although here such profound weathering is also low improbable, these authors favor the weathering hypothesis.

Table IV-15 *Pedogenetic hypotheses on terra rossa formation.*

<i>Hypothesis</i>	<i>Input</i>	<i>Mechanism</i>	<i>Weakness</i>	<i>References</i>
<b>Insoluble residual origin</b>	Autochthonous	Insoluble residuum left by dissolution of limestone.	Limestones contain little or no clay or other insoluble minerals. Very large amount of limestone would have to be dissolved to yield a significant thickness of <i>terra rossa</i> .	(Moresi & Mongelli, 1988)
<b>Detrital origin</b>	Allochthonous	Accumulation of alluvial mud, volcanic ash, Accumulation of eolian dust.	Does not account for the worldwide association of <i>terra rossa</i> with karst carbonate rocks.	(Durn et al., 1999; Green et al., 2011; Mee et al., 2004; Muhs & Budahn, 2009; Yaalon, 1997)
<b>Residual dissolution with replacement</b>	Allochthonous	Limestone replacement with authigenic clay along a narrow reaction front.	Hard to prove experimentally narrow reaction front. May be tested with this sample and dataset in future research extension.	(Cabadas-Báez et al., 2010; Merino et al., 2006; Merino & Banerjee, 2008)

The soils in the area are poorer in silicon and enriched in iron and aluminum, than any of the potential source sediments. Thus the proportions of Fe, Al and Si, can hardly be attributed just to the sediment mixing; the most probable explanation is desilicification, due to weathering and

leaching processes, in agreement with other studies (Cabadas-Báez et al., 2010; Moresi & Mongelli, 1988). In addition, litter and organic matter decomposition may be faster in red soils due to the catalytic activity of the Al, Fe, and Mn oxides (Oades, 1989).

Although this work does not include soils characterization or formal pedogenetic, nor mineralogical analyzes, it does introduce geochemical data from the parent rocks, as an attempt to evaluate with some evidence to favor one of the hypotheses (Table IV-15), or to point out to a polygenetic mechanism in the formation of soils in limestone and provide some guidance on the provenance of parent material either of autochthonous or allochthonous origin.

Considerable accumulation of pedogenic iron oxides is a common residual weathering product. The other one is clay, which comprises the most part of the fine material in the fills. Among the potential source materials, only lime-free residue of calcarenite contains a high clay amount. However, it has been shown that lime-free residue, makes a minor contribution to the soil parent material (Cabadas-Báez et al., 2010). Then, the high clay content should be at least, partly a result of the mineral transformations within the soil system (Solleiro-Rebolledo et al., 2011).

Aluminum (Al), iron (Fe), manganese (Mn), and silicon (Si) all show covariations in mol abundance in the rock samples through depth into the rock column. This indicates that their geochemical paths are intrinsically related and/or associated. Figure IV-47 illustrates this coupled behavior. The plot shows average bulk values for all samples in this study, in that depth increments with elevation plotted with respect to sea level. This very broad aggregation of data is illustrative and in no way accounts for physiographical or hydrogeological characteristics of the site or sample. Also, it does not have an even distribution, with substantially fewer samples available for the deeper depths due to cave diving technical restrictions.

In more practical terms, desilification of the materials can be indirectly assessed comparing Al, Fe, Si relative concentrations, as in an incomplete phase of the process the silicon content would be still higher, than that of iron and aluminum.

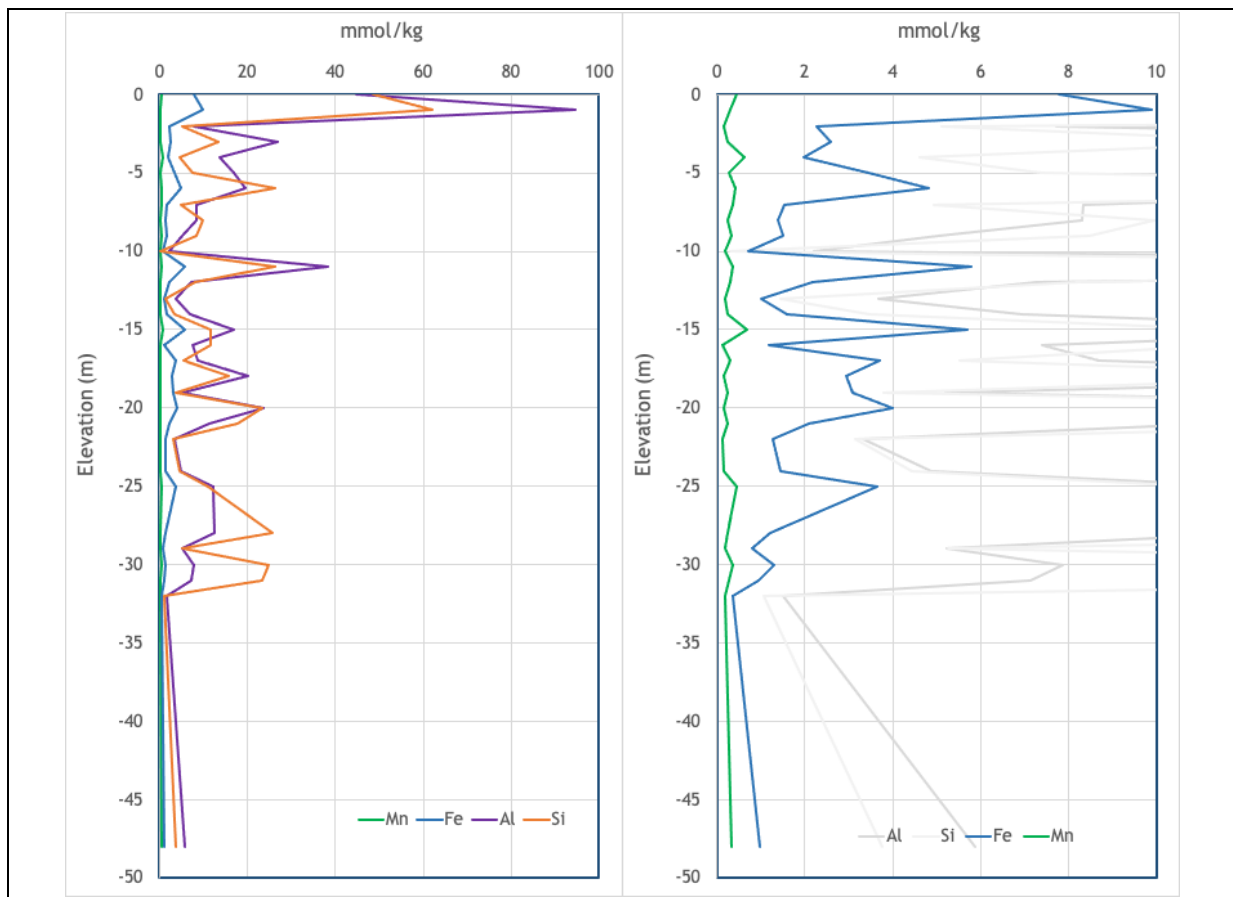


Figure IV-47 Elevation plots showing Al, Fe, Si, and Mn average concentration in the rock column. Same plot on the right with different scale to observe less abundant Mn. Units are in mmol of element per kilogram of dry rock ( $\text{mmol kg}^{-1}$ ).

An interesting rock fragment was sampled at Quarry 2 (Figure IV-49). The reddish material resembles an intruded fluid advancing in a reaction front replacing calcite similar as those related to pedogenetic mechanisms discussed earlier. The irregular shape of boundaries between white and reddish material also suggests rather than a syndepositional event, but a post-depositional diagenetic process which involves a fluid elemental transport mechanism. The white limestone includes good condition gastropod fossils that are crosscut at the boundary with the red clay. The reddish-clay material is notably enriched in Al, Fe and Si and is now very well-indurated.

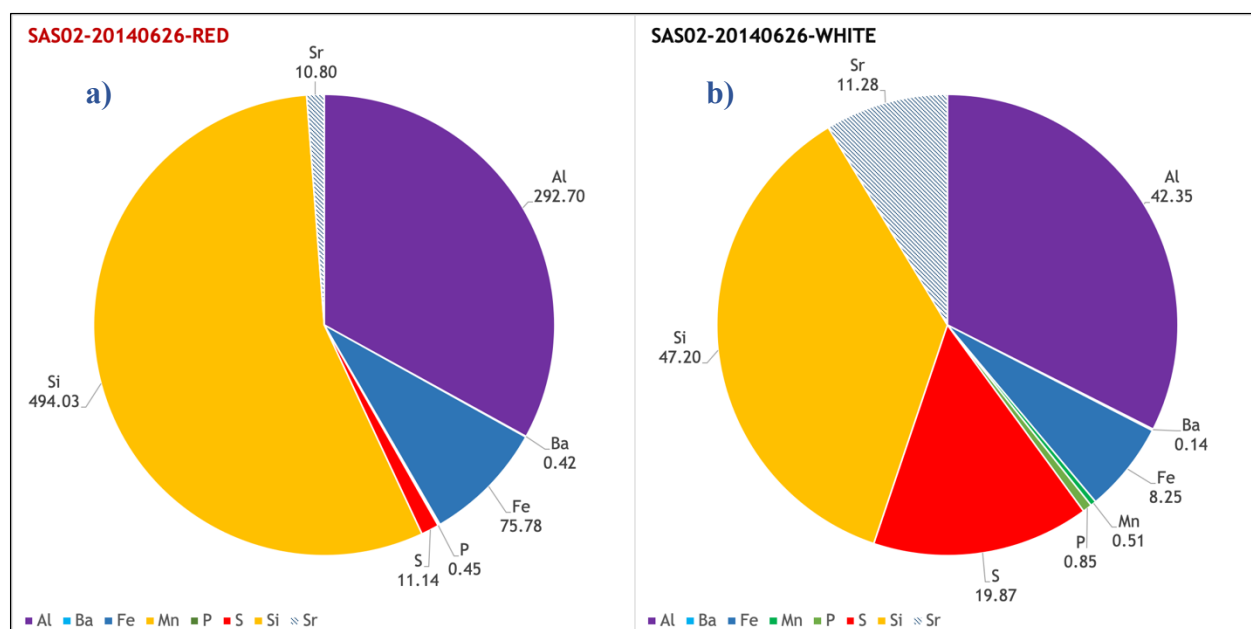


Figure IV-48 Average bulk rock composition for two sections of the rock shown in Figure IV-49 a) very well indurated reddish clay; b) a white very fine-grained limestone with gastropods crosscut at the contact with the red infill clay. Values by elements are mmol kg<sup>-1</sup> concentrations. The Ca and Mg are not plotted, and these are the intermediate and minor elements.

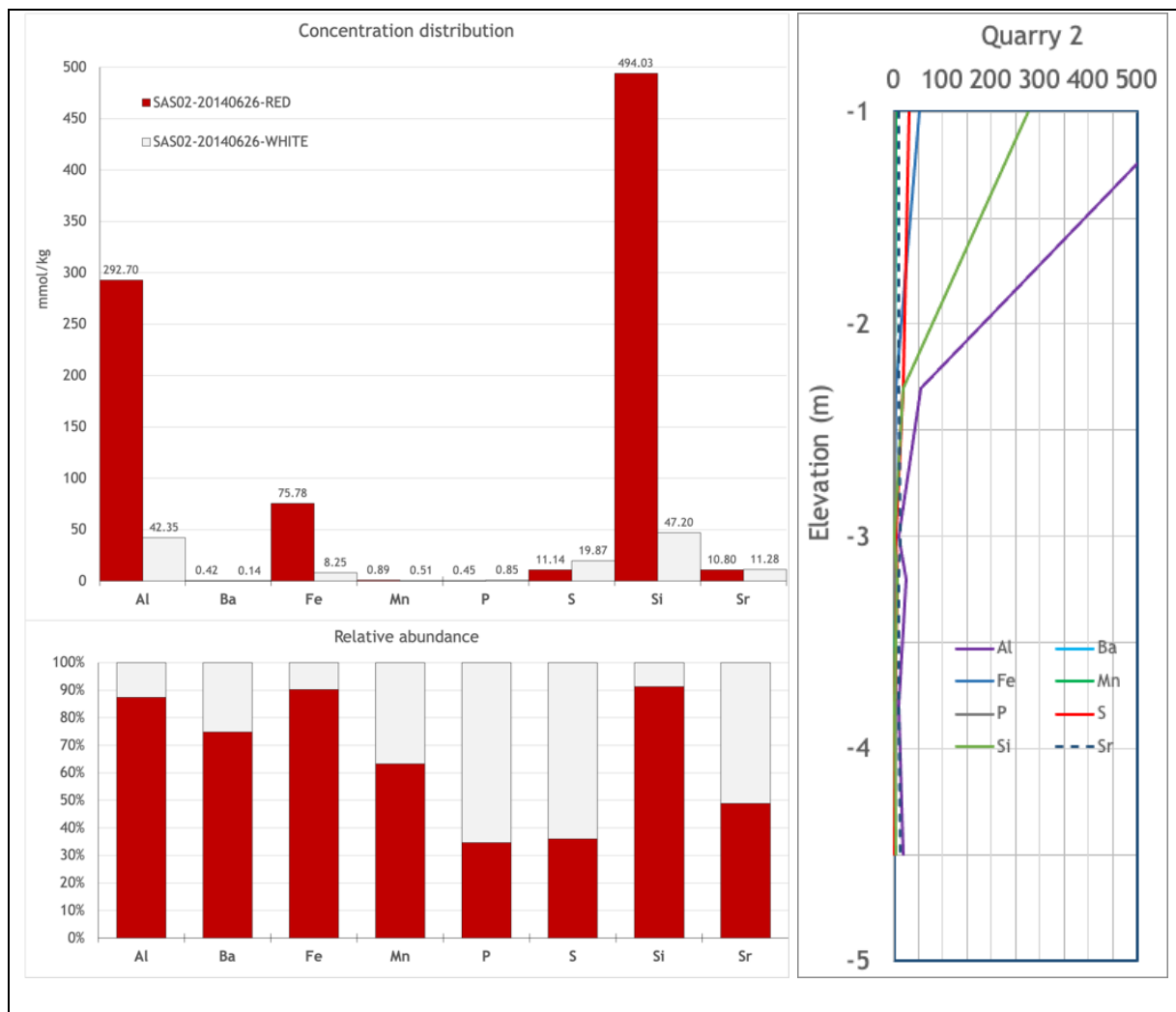
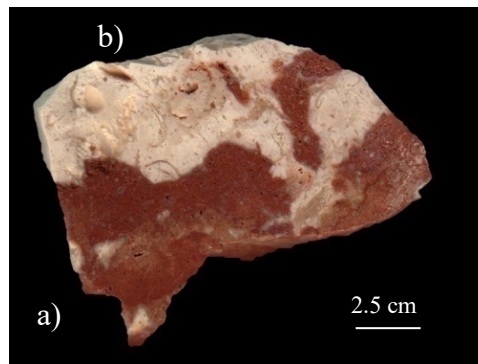


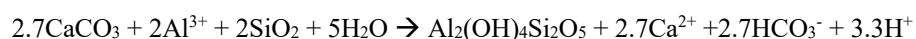
Figure IV-49 Geochemical assessment of the contrasting and intercalated and cross cutting white fossil bearing limestone and red infill indurated sediment. Concentration of Al, Ba, Fe, Mn, P, S, Si and Sr in the two sections of the rock shown above, from Quarry 2. Rock sample shows secondary calcite deposition in both phases, and abundant bivalve fossils into the white matrix; a) and b) at left panel correspond to Figure IV-48.

#### IV-7.2.1 SAF Plots

A SAF plot is a ternary diagram showing chemical composition and reaction paths for a system of the three components SiO<sub>2</sub>-Al<sub>2</sub>O<sub>3</sub>-Fe<sub>2</sub>O<sub>3</sub>. Calculations were made assuming all Al, Fe, Si are present as their oxides (Al<sub>2</sub>O<sub>3</sub>, Fe<sub>2</sub>O<sub>3</sub>, SiO<sub>2</sub>), as an identification of these specific compounds was not performed. The SAF ternary plots aid here in addressing the question of whether minerals found in red clays are insoluble residuals from the parent carbonate rock, or they are of allochthonous input, such as from aeolian dust, oceanic aerosols, or other. Many hypothesis have been made about the provenance of Al, Fe and Si in the carbonate rocks of the Yucatán Peninsula (Bautista et al., 2002, 2011; Cabadas-Báez et al., 2010; Solleiro-Rebolledo et al., 2011), which include: residual accumulation through time of components in the rock matrix since time of deposition; advective transport from the south through the Yucatán current onto the platform; tephra or volcanic ash origins (Durn et al., 1999; Merino et al., 2006); and eolian transport from Saharan dust (Doherty et al., 2008; Muhs & Budahn, 2009).

Under this scheme, silicate weathering processes coupled with carbonate dissolution lead to release of acidic H<sup>+</sup>, which in turn, promotes further dissolution of limestone, and conducting to the accumulation of pedogenetic Fe and Al oxides in reddish clays and soils in the limestone landscapes of the Yucatán Peninsula.

Accordingly, pedogenetic replacement of calcite by kaolinite clay releases an acidic H<sup>+</sup>, which in turn, contributes to further dissolution of limestone:



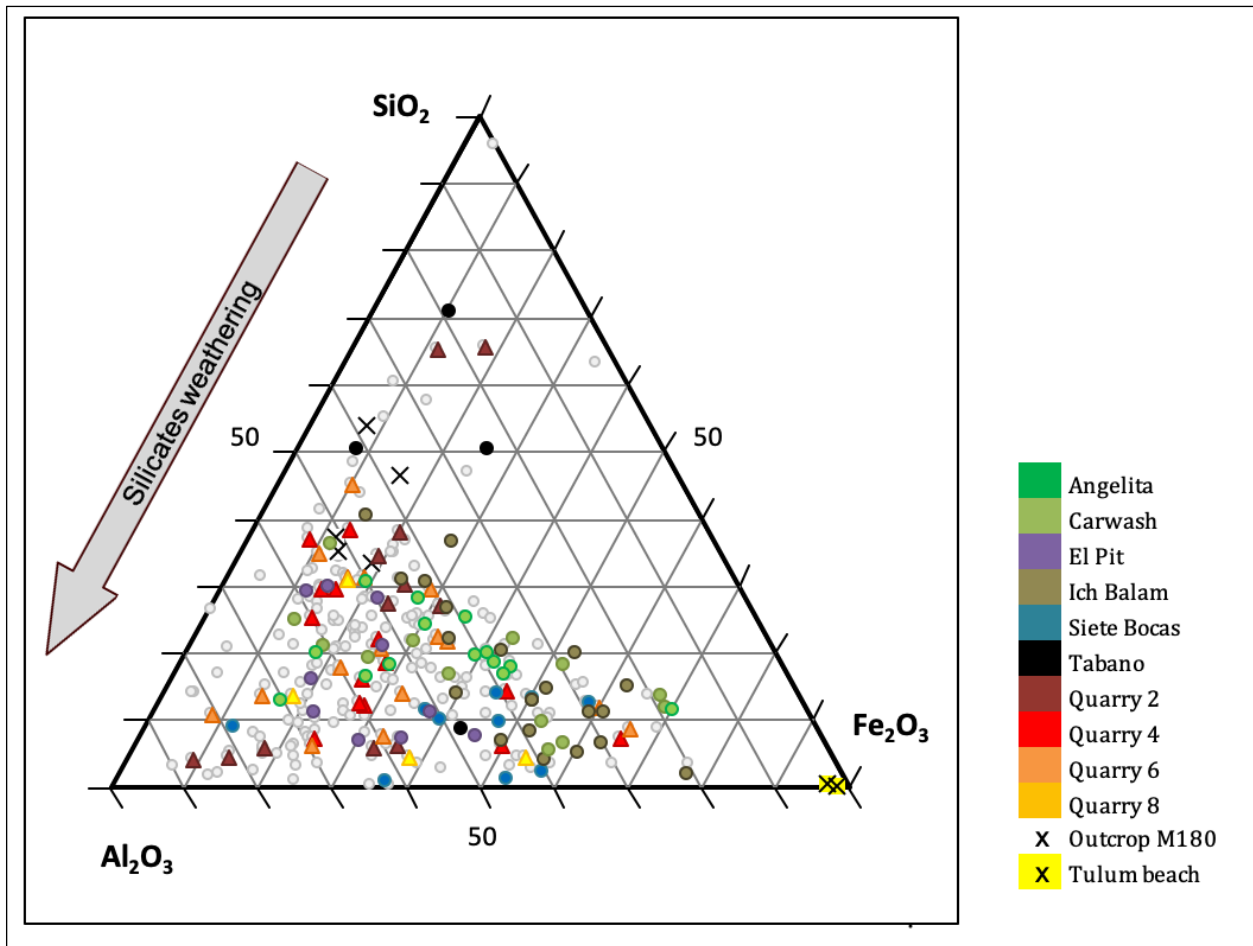


Figure IV-50 Mass  $\text{SiO}_2 - \text{Al}_2\text{O}_3 - \text{Fe}_2\text{O}_3$  (SAF) ternary plots illustrating the chemical composition of rocks and different degrees of alteration experienced; recalculated to 100% w. Calculations assuming all Al, Fe, Si are present as their oxides. All surface rock samples are plotted as small grey circles and sets of samples taken in depth sequences from select quarries and phreatic caves plotted in colors according to the legend.

As silicate weathering advances through time, its coupled nature with carbonate dissolution leads to release of acidic  $\text{H}^+$ , which in turn, promotes further dissolution of limestone as Al-Fe-Si-rich fluid intrudes and replaces the calcite matrix, leading to accumulation of pedogenetic Al, Fe and Si oxides in the reddish clays found in soils horizons across the peninsula, as well as accumulation in the so-called shallow soil-pockets.

Table IV-16 Chemical formulas and stoichiometric coefficients of limestone components and naturally occurring Al, Fe, Mn, Si minerals common in carbonate settings.

<i>Mineral</i>	<i>Chemical formula</i>
<i>Calcite</i>	$\text{CaCO}_3$
<i>Low-Mg calcite</i>	
<i>High-Mg calcite</i>	$\text{Ca}_x\text{Mg}_y(\text{CO}_3)_2$
<i>Calcian dolomite (Ca-rich)</i>	
<i>Dolomite (stoichiometric, ordered)</i>	$\text{CaMg}(\text{CO}_3)_2$
<i>Naturally occurring dolomite</i>	$\text{Ca}_{1.16}\text{Mg}_{0.84}(\text{CO}_3)_2$ — $\text{Ca}_{0.96}\text{Mg}_{1.04}(\text{CO}_3)_2$
<i>High-Mg dolomite</i>	
<i>Magnesite</i>	$\text{MgCO}_3$
<i>Ankerite</i>	$\text{CaFe}^{2+}(\text{CO}_3)_2$
<i>Siderite</i>	$\text{FeCO}_3$
<i>Rhodochrosite</i>	$\text{MnCO}_3$
<i>Kaolinite</i>	$\text{Al}_2(\text{OH})_4\text{Si}_2\text{O}_5$
<i>Illite</i>	$(\text{K},\text{H}_3\text{O})(\text{Al},\text{Mg},\text{Fe})_2(\text{Si},\text{Al})_4\text{O}_{10}[(\text{OH})_2,(\text{H}_2\text{O})]$

In general, there is no alignment of the rock samples analyzed in this work with Saharan dust, nor El Chichon, even further out with granite. Apparently, these results suggest that any of those sources can explain the amount of Al, Fe, and Si determined here.

Since the clay is authigenic, its major elements —Al, Si, and Fe— must come to the front as aqueous ions, probably result from dissolution of dust (or any other source) at the surface (Merino & Banerjee, 2008), as there exist some evidence of Saharan dust reaching the Caribbean (Doherty et al., 2008; Muhs & Budahn, 2009); or maybe due to differential leaching of interbedded marlstone horizons, locally called *margas*, which are thin beds of argillaceous limestone containing variable small amounts of clays and silt, whose dissolution and transport would produce accumulation of the less soluble materials at the surface.

Those elements forming insoluble oxidized compounds, including Al, Fe, Mn and Si, can follow different paths down through the bedrock layers, carried in small amounts of water fluid across surficial fractures, or down into a dissolution channel or cavity eventually forming soil pockets. The authigenic clay-rich fluid is corrosive by nature to limestone, and also advances in narrow reaction fronts (e.g. Merino & Banerjee, 2008) at microscopic level by replacing calcite.

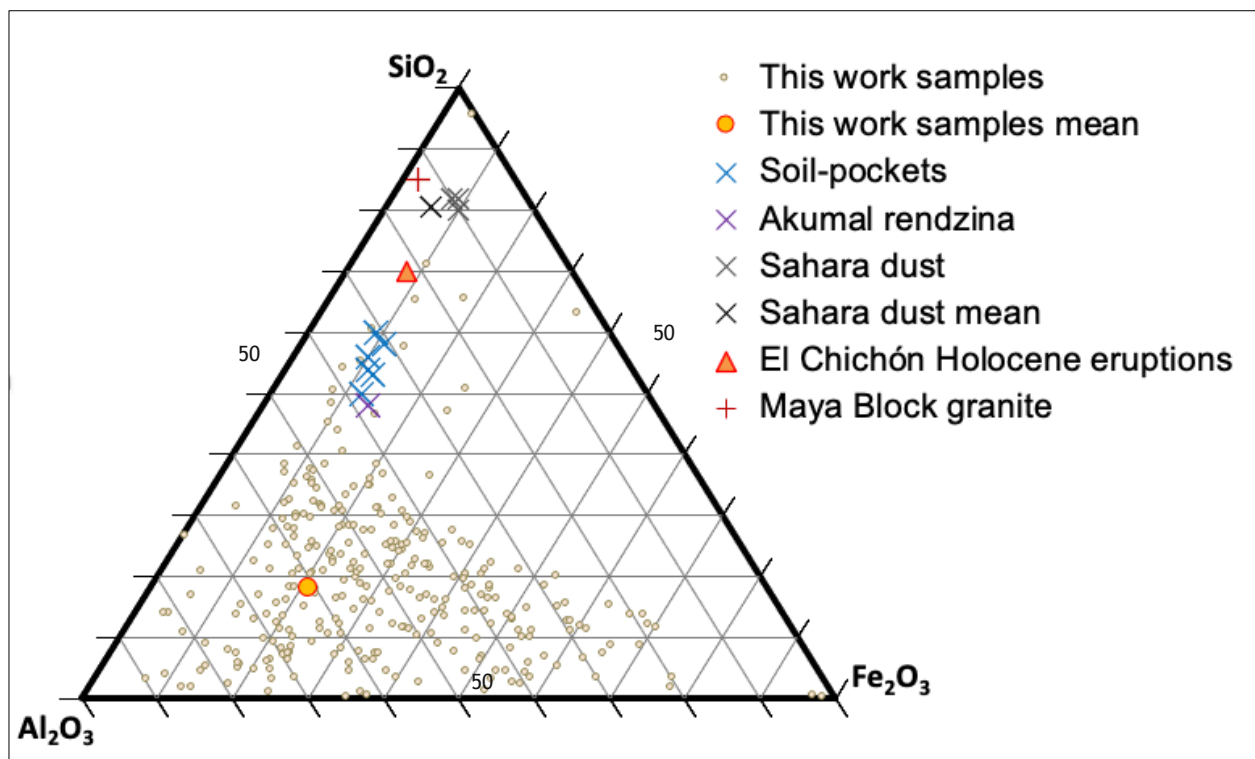


Figure IV-51 Mass  $\text{SiO}_2 - \text{Al}_2\text{O}_3 - \text{Fe}_2\text{O}_3$  (SAF) ternary plots showing the range and mean ( $n = 290$ ) reported in this work; values reported for soil-pockets infilled with pedosediments, Akumal rendzina, and Maya Block granite (Cabadas-Báez et al., 2010); Saharan dust (Castillo et al., 2008); and El Chichón Holocene eruptions (B. J. Andrews et al., 2008); normalized weight %. Calculations assuming all Al, Fe, and Si are present as their oxide in bulk samples.

#### IV-7.2.2 Assessment of Saharan dust input

The Saharan desert is the world's largest producer of aeolian dust with 26 - 62 Mt yr<sup>-1</sup> (Petit et al., 2005; Yaalon, 1997) transported westward over the Atlantic, including reaching the Caribbean Sea. The annual cycle in Saharan dust transport has a clear summer maximum 10 times greater than winter. The annual mean concentration in dry air reaching Barbados for peak years with highest recorded concentrations is ~15 µg m<sup>-3</sup> ranging from ~ 4 – 18 µg m<sup>-3</sup> (Prospero & Nees, 1986). The quantity of dust and the length of the summer “dust season” in the Caribbean have been increasing over time since the 1980s and flattened into the 1990s (Doherty et al., 2008).

Published field data on area weighted deposition on the Peninsula is not available in the indexed literature. van der Does et al. (2020) provide robust direct measurement of dust deposition over a transect of moored stations across the Atlantic, with average annual 2.8 mg m<sup>-2</sup> day<sup>-1</sup> at their M4 station located at 50°W, directly east of Barbados. We crudely estimate of deposition on the Yucatán Peninsula, 4,000 km further along the trans-Atlantic and Caribbean, as 1 mg m<sup>-2</sup> day<sup>-1</sup>, which is conservatively less than a standard Tylenol pill per meter squared per year. Given the exceptional pipping of soil into the epikarst vadose zone on the peninsula, and that some fraction of the dust is soluble, it is hard to conceive how dust mass flux of <500 mg m<sup>-2</sup> yr<sup>-1</sup> contribute significantly to Terra Rossa soil mass.

Table IV-17 shows mean major element analyses expressed as wt% oxides determined in this work in rocks from the Yucatán Peninsula and in samples of eolian dust in Western Sahara (Moreno et al., 2006). There is no concordance in composition of oxide compounds between the

carbonate rocks of the Peninsula and the eolian Saharan dust, although detailed analyses are beyond the scope of this work.

*Table IV-17 Major (wt% oxides) element analyses determined by means of ICP–OES in rocks from the Yucatán Peninsula (this work) and in Western Saharan dust (Moreno et al., 2006). Assuming all elements are present as their oxides.*

<i>Compound</i>	<i>Yucatán carbonate rocks</i>	<i>Western Saharan dust</i>
	<i>wt% oxides</i>	<i>wt% oxides</i>
SiO <sub>2</sub>	0.2	56.8
TiO <sub>2</sub>	*	1.0
Al <sub>2</sub> O <sub>3</sub>	0.8	5.1
Fe <sub>2</sub> O <sub>3</sub>	2.0	4.2
MnO	0.005	0.1
MgO	17	1.9
CaO	79	12.2
Na <sub>2</sub> O	0.6	0.8
K <sub>2</sub> O	.03	1.4
P <sub>2</sub> O <sub>5</sub>	0.4	0.5
SO <sub>3</sub>	0.2	0.1

\* Titanium (Ti) not measured in this work.

### IV-7.2.3 Fe:P ratio

Iron and phosphorus are two key limiting nutrients that regulate the primary production in aquatic environments. Increasing nutrient concentrations can degrade water quality. Interaction of  $\text{PO}_4^{3-}$  with carbonate rocks would determine the concentration of  $\text{PO}_4^{3-}$  in the water column, therefore its bioavailability. Low concentrations might be indicative of P-limitation.

The carbonate sands (calcite and aragonite), which often dominate tropical lagoons, have been found to be a major sink for phosphorus (Lapointe et al., 1999). Phosphate readily adsorbs onto these sediments, which contributes to phosphorus limitation in many tropical seagrass systems. Therefore, calcium carbonate minerals may exert significant control on phosphate chemistry in coastal carbonate waters, for example, the retention of phosphate by carbonate affects the growth of primary producers. The retention of P in carbonate sediments is considered to be the main reason that primary production often appears to be P limited in tropical and subtropical coastal waters (Fourqurean et al., 1992). The adsorption and release of phosphate onto rocks has been studied as a chemical equilibrium between dissolved *o*-phosphate and iron- and calcium-bound phosphate, whereas organic phosphate seems to play a minor role (Golterman, 1997).

The concentrations of Fe and P are typically low in open ocean. Average total P concentration is 0.6  $\mu\text{M}$  in the Caribbean Sea and 1.09  $\mu\text{M}$  in Mexican coastal waters (Hernández-Terrones et al., 2011). Corresponding values for Fe in open ocean are as low as 2.0 nM, while in coastal waters its concentration may be greatly increased when upwelling brings the iron-enriched benthic boundary layer to the surface. The shallow unconsolidated sediments of the Mexican Caribbean coast have extremely low iron concentrations; with an average of 43  $\text{mg kg}^{-1}$  (dry weight) of total Fe and < 10  $\mu\text{M}$  in pore waters (Duarte et al., 1995).

### *Iron (Fe)*

The average Fe concentration in the bulk rock is  $4.13 \pm 10.33$  mmol kg<sup>-1</sup> (230.64 mg kg<sup>-1</sup>), ranging from 0.22 to 103.90 mmol kg<sup>-1</sup>. However, these results include several weathered and perturbed samples from different environments. In Florida Fe concentration in sediments (Fe<sub>s</sub>) span from 5 to 66 mmol kg<sup>-1</sup> with a strong gradient of decreasing concentration away from mainland. In Bermuda sands, Fe<sub>s</sub> concentrations range from 1 to 5 mmol kg<sup>-1</sup> presenting the same off-shore gradient behavior (Fourqurean et al., 1992; Price et al., 2006).

### *Phosphorous (P)*

The average phosphorus concentration in the rock is  $3.41 \pm 3.65$  mmol kg<sup>-1</sup> of dry rock (105.52 mg kg<sup>-1</sup>), ranging from 0.15 – 29.79 mmol kg<sup>-1</sup>. These values are in the same order of magnitude than those total phosphorus values in sediments (TP<sub>s</sub>) reported in south Florida,  $2 < TP_s < 10$  mmol kg<sup>-1</sup> (Chambers et al., 2001) and in Bermuda carbonate sands averaging TP<sub>s</sub> = 3 mmol kg<sup>-1</sup> (Jensen et al., 1998). However, detailed spatial analyses of the results are yet to be done.

On average, Fe:P molar ratio results in  $3.88 \pm 17.71$  (6.99 in weight). It ranges from very low values around 0.03 to 169.56 as maximum value. Comparing with other hydrological systems, as in lakes, generally the Fe concentration is considerably high, and the maximum adsorption capacity correlates with total iron. Thus, the Fe:P ratio may provide a measure of free sorption sites for orthophosphate ions (Jensen et al., 1992). In shallow coastal carbonate sediments, Fe<sub>s</sub> concentrations are generally very low (Duarte et al., 1995) and the interaction of P binding with the solid-phase carbonate matrix becomes predominant (Jensen et al., 2009).

In bulk, as illustrated in Figure IV-52, mol % show a general predominance of sulfur (S) over iron (Fe) and (P). This might be explained by the high sulfate content reported in the rocks of the area (Perry et al., 2002), mainly in the form of gypsum ( $\text{CaSO}_4$ ), also sulfate constitutes a major anion in ocean waters. In this work there is no distinction between organic and inorganic sulfur, discussions here are based in total concentration in the rocks.

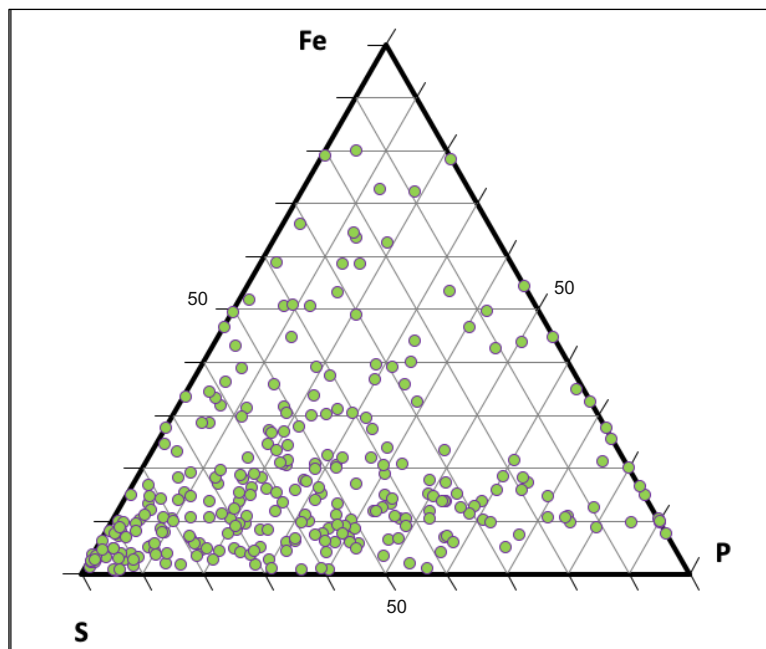


Figure IV-52 Ternary plot showing distribution of three biologically relevant elements present in the young carbonate rocks of the Yucatán Peninsula: Fe, P, and S; normalized mol % (n=290).

As it is the case for aluminum (Al) and silicon (Si) discussed earlier, iron (Fe) also presents the highest values in surface samples from outcrops quarries tenths of km inland, as part of the residual elements with similar geochemical paths in pedogenic processes. Phosphorous is more abundant near the coast, or more specifically, close to urban areas along the eastern coast.

The relative high values of Fe and P (i.e., as compared to Florida) suggest that, if massive weathering that is favored by some authors as the process giving the red clays, also would lead to massive discharge of P into coastal waters, while most iron being retained and accumulated within the surface red clay horizons, ranging in thickness from 0.30 m up to 4.15 m observed in some places far inland. If there has been 10-100's of m of carbonates dissolved off the surface, that could only have happened since the <10 Ma sea level maximum.

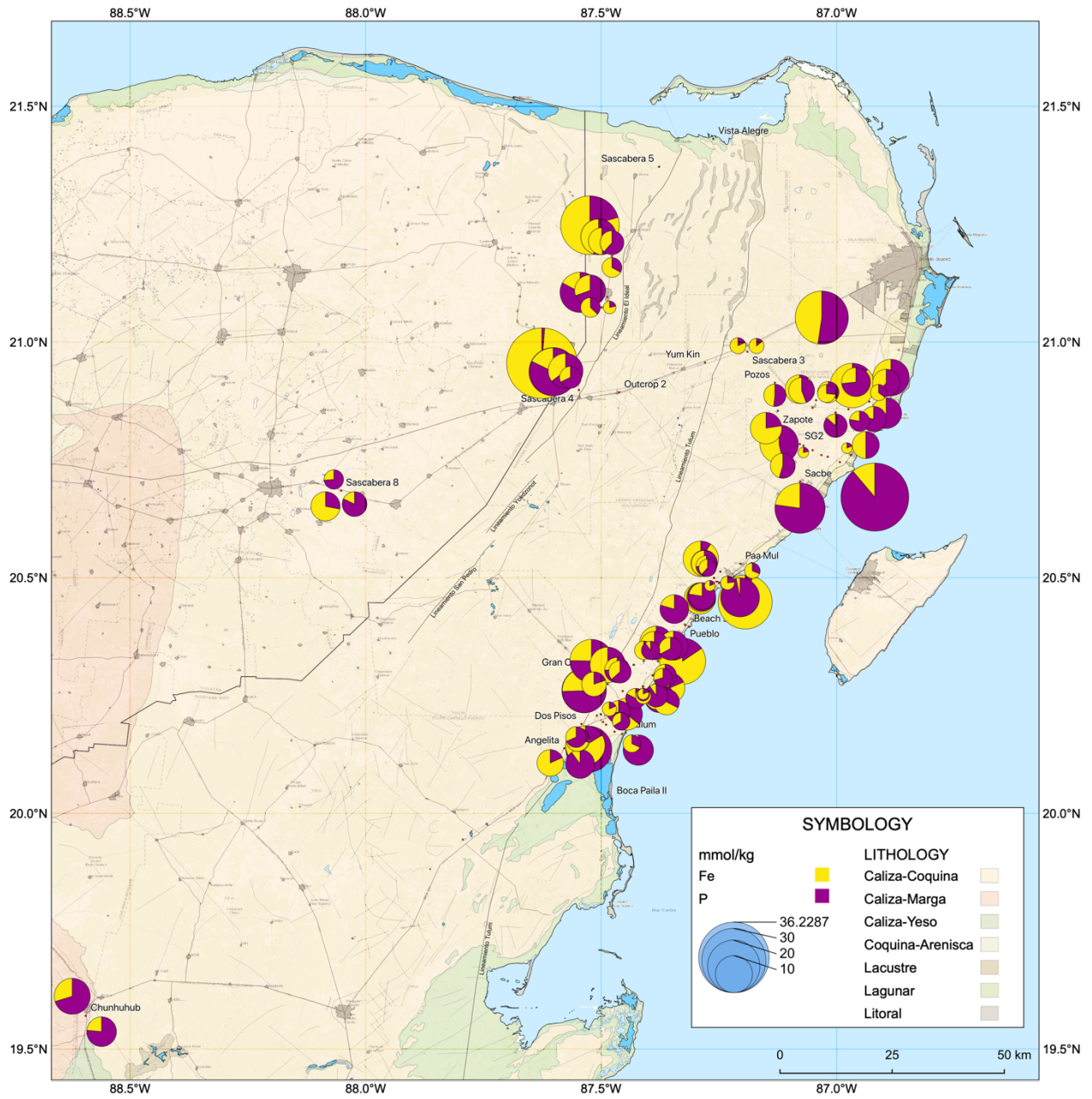


Figure IV-53 Regional distribution of iron (Fe) and phosphorous (P) relative composition on rock samples ( $\text{mmol kg}^{-1}$ ).

#### IV-7.2.4 Assessing anthropic inputs in surface rocks

Some low-concentration Minor Elements are used to track anthropic inputs into surficial rocks. Table IV-18 shows cadmium (Cd), chromium (Cr), copper (Cu), lead (Pb), and vanadium (V) concentrations in three different locality types of beach sand, vadose and phreatic zones.

*Table IV-18 Mean concentrations of some Minor Elements: cadmium (Cd), chromium (Cr), copper (Cu), lead (Pb), and vanadium (V) sampled in vadose and phreatic rocks, and from sand at a public beach. All values in  $\text{mmol kg}^{-1}_{\text{rock}}$ .*

<i>Sites</i>	<i>Cd</i>	<i>Cr</i>	<i>Cu</i>	<i>Pb</i>	<i>V</i>
Akumal beach sand	0.0005	0.0789	0.1066	0.0406	0.0167
Vadose samples	0.0010	0.1657	0.0199	0.0064	0.0924
Phreatic samples	0.0000	0.1092	0.0223	0.0015	0.0338
Total Average	0.0003	0.1319	0.0260	0.0058	0.0581

Consideration of the geographical distribution of samples with higher bulk concentrations of these selected elements does not show a pattern for samples more likely influenced by anthropogenic contamination. Sample from proximate ~10 – 100 m to highways, roads and in the sands of an actively public beach with abundant motorboat traffic are comparable to those collected in Quarries 2, 4, 6, and 8; in surface sample rocks from *Ruta de los Cenotes*, and Akumal beach sand. With the exception of Cu, all selected elements show higher concentrations in vadose samples than phreatic samples, which likely related to leaching and not contamination. Pb concentration is notably higher in beach sand samples such as in Akumal Bay, due probably to the often-extreme use of this bay by motorboats, open-water scuba diving that commonly uses uncoated lead weights, and fishing tackle use.

## IV-8 CONCLUSIONS

### General

- This work presents the quantification of an array of elements for a considerable collection of rock samples. A total of 385 samples were analyzed, with 75 replications
- Use of analytical geochemistry to help understand geomorphological processes and evolution of the different strata on the limestone bedrocks of the YP.
- It provides insight on the geochemical composition of carbonate rocks, their overall distribution and its relation to some selected elements geochemical paths and fate.
- Changes in water-rock interactions through time are key to understand present chemo-stratigraphic settings, as it results evident the importance of fluid circulation in the understanding of the geochemical evolution of the carbonate platform.
- It's difficult to establish a pattern or correlation at this stage of the research of chemo-facies related to sea level changes due to its patchy and overlapping distribution.
- For some specific geomorphological settings is possible to correlate geochemical distribution with geological sedimentary history, especially in older rocks with diagenetic or pedogenic products.
- Assumptions made in this work rely on the apparent homogenous depositional environment and in the nearly horizontal, undisturbed sedimentary beds in the Yucatán Peninsula, as well under the assumption of tectonic stability throughout the geological history of the platform.

## Methods

- Bulk analytical result values obtained are coherent and consistent.
- Elemental concentrations are within expectable ranges for carbonate rocks with little siliciclastic inputs.
- Some elements prevailed below the analytical detection limit (LOD) of the ICP methodologies and instrumentation employed (Ag, Be, Bi, Cs, Ga, and Zn).

## Results & Discussion

- As silicate weathering advances through time, its coupled nature with carbonate dissolution led to release of acidic  $H^+$ , which in turn, promotes further dissolution of limestone as Al-Fe-Si-rich fluid intrudes and replaces the calcite matrix, leading to accumulation of pedogenetic Al, Fe and Si oxides in reddish clays in the soils of the limestone landscapes of the Yucatán Peninsula.

## Further Work

- Further fieldwork should be planned based on these primary results, targeting for new samples located below the halocline in selected sites and in new different sites along the working transects established.
- This organized dataset would be the basis to perform more detailed examination of the geochemical paths taken by different elements, their fate, and their relationships among other elements commonly intertwined with carbonate rocks.

## V References

- Abreu, V. S., & Anderson, J. B. (1998). Glacial eustasy during the Cenozoic: sequence stratigraphic implications. *AAPG Bulletin*, 82(7), 1385–1400. <https://doi.org/10.1306/1d9bca89-172d-11d7-8645000102c1865d>
- Aguilar-Duarte, Y., Bautista, F., Mendoza, M. E., Frausto, O., & Ilh, T. J. (2016). Density of karst depressions in Yucatán state, Mexico. *Journal of Cave and Karst Studies*, 78(2), 51–60. <https://doi.org/10.4311/2015ES0124>
- Al-Helal, A. B., Whitaker, F. F., & Xiao, Y. (2012). Reactive transport modeling of brine reflux: dolomitization, anhydrite precipitation, and porosity evolution. *Journal of Sedimentary Research*, 82(3), 196–215. <https://doi.org/10.2110/jsr.2012.14>
- Alvarez, L. W., Alvarez, W., Asaro, F., & Michel, H. V. (1980). Extraterrestrial cause for the Cretaceous-Tertiary extinction. *Science*, 208(4448), 1095–1108. <https://doi.org/10.1126/science.208.4448.1095>
- Ames, D. E., Kjarsgaard, I. M., Pope, K. O., Dressler, B. O., & Pilkington, M. (2004). Secondary alteration of the impactite and mineralization in the basal Tertiary sequence, Yaxcopoil-1, Chicxulub impact crater, Mexico. *Meteoritics and Planetary Science*, 39(7), 1145–1167. <https://doi.org/10.1111/j.1945-5100.2004.tb01134.x>
- Andrews, A. P., & Corletta, R. (1995). A Brief History of Underwater Archaeology in the Maya Area. *Ancient Mesoamerica*, 6(24), 101–117. <https://doi.org/10.1017/S0956536100002121>
- Andrews, B. J., Gardner, J. E., & Housh, T. B. (2008). Repeated recharge, assimilation, and hybridization in magmas erupted from El Chichón as recorded by plagioclase and amphibole phenocrysts. *Journal of Volcanology and Geothermal Research*, 175(4), 415–426. <https://doi.org/10.1016/j.jvolgeores.2008.02.017>
- Arp, G., Kolepka, C., Simon, K., Karius, V., Nolte, N., & Hansen, B. T. (2013). New evidence for persistent impact-generated hydrothermal activity in the Miocene Ries impact structure, Germany. *Meteoritics and Planetary Science*, 48(12), 2491–2516. <https://doi.org/10.1111/maps.12235>

- Artemieva, N., & Morgan, J. V. (2017). Quantifying the Release of Climate-Active Gases by Large Meteorite Impacts with a Case Study of Chicxulub. *Geophysical Research Letters*, *44*(20), 10,180-10,188. <https://doi.org/10.1002/2017GL074879>
- Babel, M., & Schreiber, B. C. (2014). Geochemistry of Evaporites and Evolution of Seawater. In *Treatise on Geochemistry: Second Edition* (Vol. 9). Elsevier. <https://doi.org/10.1016/B978-0-08-095975-7.00718-X>
- Back, W., Hanshaw, B. B., Pyle, T. E., Plummer, L. N., & Weidie, A. E. (1979). Geochemical significance of groundwater discharge and carbonate solution to the formation of Caleta Xel Ha, Quintana Roo, Mexico. *Water Resources Research*, *15*(6), 1521–1535. <https://doi.org/10.1029/WR015i006p01521>
- Bahtijarević, A., & Faivre, S. (2016). Quantitative comparative geomorphological analysis of fluvial and karst relief of Florida. *Environmental Earth Sciences*, *75*(5), 1–20. <https://doi.org/10.1007/s12665-016-5397-8>
- Bardeen, C. G., Garcia, R. R., Toon, O. B., & Conley, A. J. (2017). On transient climate change at the Cretaceous–Paleogene boundary due to atmospheric soot injections. *Proceedings of the National Academy of Sciences of the United States of America*, *114*(36), E7415–E7424. <https://doi.org/10.1073/pnas.1708980114>
- Bauer-Gottwein, P., Gondwe, B. R. N., Charvet, G., Marín, L. E., Rebolledo-Vieyra, M., & Merediz-Alonso, G. (2011). Review: The Yucatán Peninsula karst aquifer, Mexico. *Hydrogeology Journal*, *19*(3), 507–524. <https://doi.org/10.1007/s10040-010-0699-5>
- Bautista, F., Jiménez-Osornio, J., Navarro, J. A., & Manu, A. (2002). Micro-Relief and Soil Color as Diagnostic Properties in Karstic Leptosols. *Terra*, 1–11.
- Bautista, F., Palacio-Aponte, G., Quintana, P., & Zinck, J. A. (2011). Spatial distribution and development of soils in tropical karst areas from the Peninsula of Yucatan, Mexico. *Geomorphology*, *135*(3–4), 308–321. <https://doi.org/10.1016/j.geomorph.2011.02.014>
- Bayari, C. S., Pekkan, E., & Ozyurt, N. N. (2009). Obruks, as giant collapse dolines caused by hypogenic karstification in central Anatolia, Turkey: Analysis of likely formation processes. *Hydrogeology Journal*, *17*(2), 327–345. <https://doi.org/10.1007/s10040-008-0351-9>

- Beddows, P. A. (2004). *Groundwater Hydrology of a Coastal Conduit Carbonate Aquifer: Caribbean Coast of the Yucatán Peninsula, México*. PhD Thesis. University of Bristol. 332 pp.
- Beddows, P. A., Glover, J. B., Rissolo, D., Carter, A. M., Jaijel, R., Smith, D. M., & Goodman-Tchernov, B. N. (2016). The Proyecto Costa Escondida: Recent interdisciplinary research in search of freshwater along the North Coast of Quintana Roo, Mexico. *Wiley Interdisciplinary Reviews: Water*, 3(5), 749–761. <https://doi.org/10.1002/wat2.1161>
- Beddows, P. A., Smart, P. L., Whitaker, F. F., & Smith, S. L. (2007). Decoupled fresh-saline groundwater circulation of a coastal carbonate aquifer: Spatial patterns of temperature and specific electrical conductivity. *Journal of Hydrology*, 346(1–2), 18–32. <https://doi.org/10.1016/j.jhydrol.2007.08.013>
- Berner, R. A. (2003). The long-term carbon cycle, fossil fuels and atmospheric composition. *Nature*, 426(November), 323–326. <https://doi.org/10.1038/nature02131>
- Bird, D. E., Burke, K., Hall, S. A., & Casey, J. F. (2005). Gulf of Mexico tectonic history: Hotspot tracks, crustal boundaries, and early salt distribution. *AAPG Bulletin*, 89(3), 311–328. <https://doi.org/10.1306/10280404026>
- Blanchon, P. (2010). Reef demise and back-stepping during the last interglacial, northeast Yucatan. *Coral Reefs*, 29(2), 481–498. <https://doi.org/10.1007/s00338-010-0599-0>
- Blanchon, P., Eisenhauer, A., Fietzke, J., & Liebetrau, V. (2009). Rapid sea-level rise and reef back-stepping at the close of the last interglacial highstand. *Nature*, 458(7240), 881–884. <https://doi.org/10.1038/nature07933>
- Bobba, A. G., Chambers, P. A., & Wrona, F. J. (2012). Submarine groundwater discharge (SGWD): An unseen yet potentially important coastal phenomenon in Canada. *Natural Hazards*, 60(3), 991–1012. <https://doi.org/10.1007/s11069-011-9884-7>
- Brett, R. (1992). The Cretaceous-Tertiary extinction: A lethal mechanism involving anhydrite target rocks. *Geochimica et Cosmochimica Acta*, 56(9), 3603–3606. [https://doi.org/10.1016/0016-7037\(92\)90406-9](https://doi.org/10.1016/0016-7037(92)90406-9)

- Brugger, J., Feulner, G., & Petri, S. (2017). Baby, it's cold outside: Climate model simulations of the effects of the asteroid impact at the end of the Cretaceous. *Geophysical Research Letters*, *44*(1), 419–427. <https://doi.org/10.1002/2016GL072241>
- Cabadas-Báez, H. V., Solleiro-Rebolledo, E., Sedov, S., Pi-Puig, T., & Gama-Castro, J. (2010). Pedosediments of karstic sinkholes in the eolianites of NE Yucatán: A record of Late Quaternary soil development, geomorphic processes and landscape stability. *Geomorphology*, *122*(3–4), 323–337. <https://doi.org/10.1016/j.geomorph.2010.03.002>
- Camargo-Zanoguera, A., & Suárez, G. (1994). Evidencia sísmica del cráter de impacto de Chicxulub. *Bol. Asoc. Mex. Geofis. Expl.*, *34*, 1–28.
- Case, J. E., & Holcombe, T. L. (1980). Geologic-tectonic map of the Caribbean region. In *IMAP* (USGS Numbe). <https://doi.org/10.3133/i1100>
- Castillo, S., Moreno, T., Querol, X., Alastuey, A., Cuevas, E., Herrmann, L., Mounkaila, M., & Gibbons, W. (2008). Trace element variation in size-fractionated African desert dusts. *Journal of Arid Environments*, *72*(6), 1034–1045. <https://doi.org/10.1016/j.jaridenv.2007.12.007>
- Chambers, R. M., Fourqurean, J. W., Macko, S. A., & Hoppenot, R. (2001). Biogeochemical effects of iron availability on primary producers in a shallow marine carbonate environment. *Limnology and Oceanography*, *46*(6), 1278–1286. <https://doi.org/10.4319/lo.2001.46.6.1278>
- Chen, S. P., Lu, C. H., McQueen, J., & Lee, P. (2018). Application of satellite observations in conjunction with aerosol reanalysis to characterize long-range transport of African and Asian dust on air quality in the contiguous U.S. *Atmospheric Environment*, *187*(May), 174–195. <https://doi.org/10.1016/j.atmosenv.2018.05.038>
- Chesworth, W., Camps Arbestain, M., Macías, F., Spaargaren, O., Spaargaren, O., Mualem, Y., Morel-Seytoux, H. J., Horwath, W. R., Almendros, G., Chesworth, W., Grossl, P. R., Sparks, D. L., Spaargaren, O., Fairbridge, R. W., Singer, A., Eswaran, H., & Micheli, E. (2008). *Classification of Soils: World Reference Base (WRB) for soil resources BT - Encyclopedia of Soil Science* (W. Chesworth (ed.); pp. 120–122). Springer Netherlands. [https://doi.org/10.1007/978-1-4020-3995-9\\_104](https://doi.org/10.1007/978-1-4020-3995-9_104)

- Christeson, G. L., Collins, G. S., Morgan, J. V., Gulick, S. P. S., Barton, P. J., & Warner, M. R. (2009). Mantle deformation beneath the Chicxulub impact crater. *Earth and Planetary Science Letters*, 284(1–2), 249–257. <https://doi.org/10.1016/j.epsl.2009.04.033>
- Christeson, G. L., Nakamura, Y., Buffler, R. T., Morgan, J. V., & Warner, M. R. (2001). Deep crustal structure of the Chicxulub impact crater. *Journal of Geophysical Research: Solid Earth*, 106(B10), 21751–21769. <https://doi.org/10.1029/2001jb000337>
- Collins, G. S., Morgan, J. V., Barton, P. J., Christeson, G. L., Gulick, S. P. S., Urrutia-Fucugauchi, J., Warner, M. R., & Wünnemann, K. (2008). Dynamic modeling suggests terrace zone asymmetry in the Chicxulub crater is caused by target heterogeneity. *Earth and Planetary Science Letters*, 270(3–4), 221–230. <https://doi.org/10.1016/j.epsl.2008.03.032>
- Connors, M., Hildebrand, A. R., Pilkington, M., Ortiz-Aleman, C., Chavez, R. E., Urrutia-Fucugauchi, J., Graniel-Castro, E., Camara-Zi, A., Vasquez, J., & Halpenny, J. F. (1996). Yucatán karst features and the size of Chicxulub crater. *Geophysical Journal International*, 127(3). <https://doi.org/10.1111/j.1365-246X.1996.tb04066.x>
- Dahlin, B. H., Andrews, A. P., Beach, T., Bezanilla, C., Farrell, P., Luzzadder-Beach, S., & McCormick, V. (1998). Punta Canbalam in context: a peripatetic coastal site in northwest Campeche, Mexico. *Ancient Mesoamerica*, 9(1), 1–15. <https://doi.org/10.1017/s0956536100001814>
- De Waele, J., Gutiérrez, F., Parise, M., & Plan, L. (2011). Geomorphology and natural hazards in karst areas: A review. *Geomorphology*, 134(1–2), 1–8. <https://doi.org/10.1016/j.geomorph.2011.08.001>
- Dillon, W. P., & Vedder, J. G. (1973). Structure and development of the continental margin of british honduras. *Bulletin of the Geological Society of America*, 84(8), 2713–2732. [https://doi.org/10.1130/0016-7606\(1973\)84<2713:SADOTC>2.0.CO;2](https://doi.org/10.1130/0016-7606(1973)84<2713:SADOTC>2.0.CO;2)
- Djidi, K., Bakalowicz, M., & Benali, A. M. (2008). Mixed, classical and hydrothermal karstification in a carbonate aquifer. Hydrogeological consequences. The case of the Saida aquifer system, Algeria. *Comptes Rendus - Geoscience*, 340(7), 462–473. <https://doi.org/10.1016/j.crte.2008.04.002>

- Doherty, O. M., Riemer, N., & Hameed, S. (2008). Saharan mineral dust transport into the Caribbean: Observed atmospheric controls and trends. *Journal of Geophysical Research Atmospheres*, *113*(7), 1–10. <https://doi.org/10.1029/2007JD009171>
- Doner, H. E., & Lynn, W. C. (1989). Carbonate, Halide, Sulfate, and Sulfide. In J. B. Dixon & S. B. Weed (Eds.), *Minerals in Soil Environments* (2nd ed., Vol. 1, Issue 1, pp. 280–330). Soil Science Society of America.
- Donnelly, T. W., Home, G. S., Finch, R. C., & López-Ramos, E. (2015). Northern Central America; The Maya and Chortis blockse. *The Caribbean Region*, 37–76. <https://doi.org/10.1130/dnag-gna-h.37>
- Dressler, B. O., Sharpton, V. L., Morgan, J. V., Buffler, R., Moran, D., Smit, J., Stäffler, D., & Urrutia, J. (2003). Investigating a 65-Ma-Old smoking gun: Deep drilling of the chicxulub impact structure. *Eos*, *84*(14). <https://doi.org/10.1029/2003EO140001>
- Duarte, C. M., Merino-Ibarra, M., & Gallegos, M. E. (1995). Evidence of iron deficiency in seagrasses growing above carbonate sediments. *Limnology and Oceanography*, *40*(6), 1153–1158. <https://doi.org/10.4319/lo.1995.40.6.1153>
- Duch, G. J. (1988). *La conformación territorial del estado de Yucatán: los componentes del medio físico*. Centro Regional de la Península de Yucatán. Universidad Autónoma de Chapingo.
- Durn, G. (2003). Terra Rossa in the Mediterranean region: Parent materials, composition and origin. *Geologia Croatica*, *56*(1), 83–100. <https://doi.org/10.4154/GC.2003.06>
- Durn, G., Ottner, F., & Slovenec, D. (1999). Mineralogical and geochemical indicators of the polygenetic nature of terra rossa in Istria, Croatia. *Geoderma*, *91*(1–2), 125–150. [https://doi.org/10.1016/S0016-7061\(98\)00130-X](https://doi.org/10.1016/S0016-7061(98)00130-X)
- Dürr, H. H., Meybeck, M., & Dürr, S. H. (2005). Lithologic composition of the Earth's continental surfaces derived from a new digital map emphasizing riverine material transfer. *Global Biogeochemical Cycles*, *19*(4), 1–23. <https://doi.org/10.1029/2005GB002515>
- Ellison, J. C., & Stoddart, D. R. (1991). Mangrove ecosystem collapse during predicted sea-level rise: Holocene analogues and implications. *Journal of Coastal Research*, *7*(1), 151–165. <https://doi.org/10.2307/4297812>

- Eppelbaum, L., Kutasov, I., & Pilchin, A. (2014). Thermal Properties of formations. In *Applied Geothermics*. <https://doi.org/10.1007/978-3-642-34023-9>
- Escobar-Sanchez, J. E., & Urrutia-Fucugauchi, J. (2010). Chicxulub crater post-impact hydrothermal activity - evidence from Paleocene carbonates in the Santa Elena Borehole. *Geofisica Internacional*, *49*(2), 97–106.
- Escolero, O. A., Marín, L. E., Steinich, B., Pacheco-Ávila, J., Cabrera S., A., & Alcocer, J. (2002). Development of a protection strategy of karst limestone aquifers: The Merida Yucatan, Mexico case study. *Water Resources Management*, *16*(5), 351–367. <https://doi.org/10.1023/A:1021967909293>
- Espinosa-Cardena, J. M., Campos-Enriquez, J. O., & Unsworth, M. (2016). Heat flow pattern at the Chicxulub impact crater, northern Yucatan, Mexico. *Journal of Volcanology and Geothermal Research*, *311*, 135–149. <https://doi.org/10.1016/j.jvolgeores.2015.12.013>
- Fairbanks, R. G. (1989). A 17,000-year glacio-eustatic sea level record: Influence of glacial melting rates on the Younger Dryas event and deep-ocean circulation. *Nature*, *342*(6250), 637–642. <https://doi.org/10.1038/342637a0>
- Folk, R. L., & Land, L. S. (1975). Mg/Ca Ratio and Salinity: Two Controls over Crystallization of Dolomite. *AAPG Bulletin*, *59*(1), 60–68. <https://doi.org/10.1306/83d921f4-16c7-11d7-8645000102c1865d>
- Ford, D. C., & Williams, P. (2007). Karst Hydrogeology and Geomorphology. In *Karst Hydrogeology and Geomorphology* (Rev. ed.). John Wiley & Sons, Ltd. <https://doi.org/10.1002/9781118684986>
- Forti, P., Galdenzi, S., & Sarbu, S. M. (2002). The hypogenic caves: A powerful tool for the study of seeps and their environmental effects. *Continental Shelf Research*, *22*(16), 2373–2386. [https://doi.org/10.1016/S0278-4343\(02\)00062-6](https://doi.org/10.1016/S0278-4343(02)00062-6)
- Fourqurean, J. W., Zieman, J. C., & Powell, G. V. N. (1992). Phosphorus limitation of primary production in Florida Bay: Evidence from C:N:P ratios of the dominant seagrass *Thalassia testudinum*. *Limnology and Oceanography*, *37*(1), 162–171. <https://doi.org/10.4319/lo.1992.37.1.0162>

- Gary, M. O., & Sharp, J. M. (2006). Volcanogenic karstification of Sistema Zacatón, Mexico. *Special Paper of the Geological Society of America*, 404, 79–89. [https://doi.org/10.1130/2006.2404\(08\)](https://doi.org/10.1130/2006.2404(08))
- Glover, J. B., Rissolo, D., & Mathews, J. P. (2011). The Hidden World of the Maritime Maya: Lost Landscapes Along the North Coast of Quintana Roo, Mexico. In B. Ford (Ed.), *The Archaeology of Maritime Landscapes. When the Land Meets the Sea* (ACUA and S, pp. 195–216). Springer New York. [https://doi.org/10.1007/978-1-4419-8210-0\\_11](https://doi.org/10.1007/978-1-4419-8210-0_11)
- Gmitro, D. A. (1987). *The Interaction of Water with Carbonate Rocks in Yucatan, Mexico*. Northern Illinois University, DeKalb.
- Goldscheider, N., Mádl-Szonyi, J., Eross, A., & Schill, E. (2010). Aperçu: les ressources en eau thermale des aquifères carbonatés. *Hydrogeology Journal*, 18(6), 1303–1318. <https://doi.org/10.1007/s10040-010-0611-3>
- Golterman, H. L. (1997). The distribution of phosphate over iron-bound and calcium-bound phosphate in stratified sediments. *Hydrobiologia*, 364 I(1), 75–81. <https://doi.org/10.1023/A:1003159924052>
- Gondwe, B. R. N., Lerer, S., Stisen, S., Marín, L. E., Rebolledo-Vieyra, M., Merediz-Alonso, G., & Bauer-Gottwein, P. (2010). Hydrogeology of the south-eastern Yucatan Peninsula: New insights from water level measurements, geochemistry, geophysics and remote sensing. *Journal of Hydrology*, 389(1–2), 1–17. <https://doi.org/10.1016/j.jhydrol.2010.04.044>
- González-Herrera, R., Sánchez-y-Pinto, I., & Gamboa-Vargas, J. (2002). Groundwater-flow modeling in the Yucatan karstic aquifer, Mexico. *Hydrogeology Journal*, 10(5), 539–552. <https://doi.org/10.1007/s10040-002-0216-6>
- González, A. H., Terrazas, A., Stinnesbeck, W., Benavente, M. E., Avilés, J., Rojas, C., Padilla, J. M., Velásquez, A., Acevez, E., & Frey, E. (2014). The first human settlers on the Yucatan Peninsula: Evidence from drowned caves in the State of Quintana Roo (South Mexico). *Paleoamerican Odyssey*, 323–337.

- Graham, D. J., & Midgley, N. G. (2000). Graphical representation of particle shape using triangular diagrams: An excel spreadsheet method. *Earth Surface Processes and Landforms*, 25(13), 1473–1477. [https://doi.org/10.1002/1096-9837\(200012\)25:13<1473::AID-ESP158>3.0.CO;2-C](https://doi.org/10.1002/1096-9837(200012)25:13<1473::AID-ESP158>3.0.CO;2-C)
- Green, T. R., Taniguchi, M., Kooi, H., Gurdak, J. J., Allen, D. M., Hiscock, K. M., Treidel, H., & Aureli, A. (2011). Beneath the surface of global change: Impacts of climate change on groundwater. *Journal of Hydrology*, 405(3–4), 532–560. <https://doi.org/10.1016/j.jhydrol.2011.05.002>
- Guerrero, J., Gutiérrez, F., Bonachea, J., & Lucha, P. (2008). A sinkhole susceptibility zonation based on paleokarst analysis along a stretch of the Madrid-Barcelona high-speed railway built over gypsum- and salt-bearing evaporites (NE Spain). *Engineering Geology*, 102(1–2), 62–73. <https://doi.org/10.1016/j.enggeo.2008.07.010>
- Gulick, S. P. S., Barton, P. J., Christeson, G. L., Morgan, J. V., McDonald, M., Mendoza-Cervantes, K., Pearson, Z. F., Surendra, A., Urrutia-Fucugauchi, J., Vermeesch, P. M., & Warner, M. R. (2008). Importance of pre-impact crustal structure for the asymmetry of the Chicxulub impact crater. *Nature Geoscience*, 1(2), 121–125. <https://doi.org/10.1038/ngeo103>
- Gulick, S. P. S., Christeson, G. L., Barton, P. J., Grieve, R. A. F., Morgan, J. V., & Urrutia-Fucugauchi, J. (2013). Geophysical characterization of the Chicxulub impact crater. *Reviews of Geophysics*, 51(1), 31–52. <https://doi.org/10.1002/rog.20007>
- Gulick, S. P. S., Morgan, J. V., Mellett, C. L., Lofi, J., Chenot, E., Christeson, G. L., Claeys, P., Cockell, C. S., Coolen, M. J. L., Ferrière, L., Gebhardt, C., Goto, K., Jones, H., Kring, D. A., Lowery, C. M., Ocampo-Torres, R., Perez-Cruz, L., Pickersgill, A. E., Poelchau, M., ... Bralower, T. J. (2017). Chicxulub: drilling the K-Pg impact crater. Expedition 364 Scientific Prospectus. In *International Ocean Discovery Program* (p. 38). International Ocean Discovery Program. <https://doi.org/10.14379/iodp.sp.364.2016>
- Gulley, J. D., Martin, J. B., & Moore, P. J. (2014). Vadose CO<sub>2</sub> gas drives dissolution at water tables in eogenetic karst aquifers more than mixing dissolution. *Earth Surface Processes and Landforms*, 39(13), 1833–1846. <https://doi.org/10.1002/esp.3571>

- Gulley, J. D., Martin, J. B., Moore, P. J., & Murphy, J. (2013). Formation of phreatic caves in an eogenetic karst aquifer by CO<sub>2</sub> enrichment at lower water tables and subsequent flooding by sea level rise. *Earth Surface Processes and Landforms*, 38(11), 1210–1224. <https://doi.org/10.1002/esp.3358>
- Gupta, S. C., Ahrens, T. J., & Yang, W. (2001). Shock-Induced vaporization of anhydrite and global cooling from the K/T impact. *Earth and Planetary Science Letters*, 188(3–4), 399–412. [https://doi.org/10.1016/S0012-821X\(01\)00327-2](https://doi.org/10.1016/S0012-821X(01)00327-2)
- Hagerty, J. J., & Newsom, H. E. (2003). Hydrothermal alteration at the Lonar Lake impact structure, India: Implications for impact cratering on Mars. *Meteoritics and Planetary Science*, 38(3), 365–381. <https://doi.org/10.1111/j.1945-5100.2003.tb00272.x>
- Hanshaw, B. B., Back, W., & Deike, R. G. (1971). A geochemical hypothesis for dolomitization by Ground Water. *Economic Geology*, 66(5), 710–724. <https://doi.org/10.2113/gsecongeo.66.5.710>
- Haq, B. U., Hardenbol, J., & Vail, P. R. (1988). Mesozoic and Cenozoic chronostratigraphy and cycles of sea-level change. In C. K. Wilgus, B. S. Hastings, C. G. Kendall, C. A. Ross, & J. C. Van Wagoner (Eds.), *Sea-level changes: an integrated approach* (SEPM Spec. Issue 42, pp. 71–108). Society of Economic Paleontologists and Mineralogists. <https://doi.org/10.2110/pec.88.01.0071>
- Hearty, P. J., & Kindler, P. (1995). Sea-level highstand chronology from stable carbonate platforms (Bermuda and the Bahamas). *Journal of Coastal Research*, 11(3), 675–689.
- Hearty, P. J., & Neumann, A. C. (2001). Rapid sea level and climate change at the close of the Last Interglaciatiion (MIS 5e): Evidence from the Bahama Islands. *Quaternary Science Reviews*, 20(18), 1881–1895. [https://doi.org/10.1016/S0277-3791\(01\)00021-X](https://doi.org/10.1016/S0277-3791(01)00021-X)
- Herman, J. S. (2019). *Chapter 133 - Water chemistry in caves* (W. B. White, D. C. Culver, & T. B. T.-E. of C. (Third E. Pipan (eds.); pp. 1136–1143). Academic Press. <https://doi.org/https://doi.org/10.1016/B978-0-12-814124-3.00133-3>

- Hernández-Terrones, L. M., Rebolledo-Vieyra, M., Merino-Ibarra, M., Soto, M., Le-Cossec, A., & Monroy-Ríos, E. (2011). Groundwater pollution in a karstic region (NE Yucatan): Baseline nutrient content and flux to coastal ecosystems. *Water, Air, and Soil Pollution*, *218*(1–4), 517–528. <https://doi.org/10.1007/s11270-010-0664-x>
- Hildebrand, A. R., Jacobsen, S. B., Penfield, G. T., Kring, D. A., Pilkington, M., Antonio, C. Z., & Boynton, W. V. (1991). Chicxulub crater: a possible Cretaceous/Tertiary boundary impact crater on the Yucatan Peninsula, Mexico. *Geology*, *19*(9), 867–871. [https://doi.org/10.1130/0091-7613\(1991\)019<0867:CCAPCT>2.3.CO;2](https://doi.org/10.1130/0091-7613(1991)019<0867:CCAPCT>2.3.CO;2)
- Hildebrand, A. R., Pilkington, M., Connors, M., Ortiz-Aleman, C., & Chavez, R. E. (1995). Size and structure of the Chicxulub crater revealed by horizontal gravity gradients and cenotes. *Nature*, *376*(6539), 415–417. <https://doi.org/10.1038/376415a0>
- Hildebrand, A. R., Pilkington, M., Ortiz-Aleman, C., Chavez, R. E., Urrutia-Fucugauchi, J., Connors, M., Graniel-Castro, E., Camara-Zi, A., Halpenny, J. F., & Niehaus, D. (1998). Mapping Chicxulub crater structure with gravity and seismic reflection data. *Geological Society Special Publication*, *140*, 155–176. <https://doi.org/10.1144/GSL.SP.1998.140.01.12>
- Hill, C. A. (1990). Sulfuric acid speleogenesis of Carlsbad Cavern and its relationship to hydrocarbons, Delaware Basin, New Mexico and Texas. *American Association of Petroleum Geologists Bulletin*, *74*(11), 1685–1694. <https://doi.org/10.1306/0c9b2565-1710-11d7-8645000102c1865d>
- Hughes, J. D., Vacher, H. L., & Sanford, W. E. (2007). Three-dimensional flow in the Florida platform: Theoretical analysis of Kohout convection at its type locality. *Geology*, *35*(7), 663–666. <https://doi.org/10.1130/G23374A.1>
- IUSS Working Group WRB. (2014). World Reference Base for Soil Resources 2014: International soil classification systems for naming soils and creating legends for soil maps (Update 2015). In *World Soil Resources Reports No. 106*. <http://www.fao.org/soils-portal/soil-survey/soil-classification/world-reference-base/en/>

- Jaijel, R., Glover, J. B., Rissolo, D., Beddows, P. A., Smith, D. M., Ben-Avraham, Z., & Goodman-Tchernov, B. N. (2018). Coastal reconstruction of Vista Alegre, an ancient maritime Maya settlement. *Palaeogeography, Palaeoclimatology, Palaeoecology*, 497(Estudios de Cultura Maya 11 1978), 25–36. <https://doi.org/10.1016/j.palaeo.2018.02.003>
- Jaijel, R., Kanari, M., Glover, J. B., Rissolo, D., Beddows, P. A., Ben-Avraham, Z., & Goodman-Tchernov, B. N. (2018). Shallow geophysical exploration at the ancient maritime Maya site of Vista Alegre, Yucatan Mexico. *Journal of Archaeological Science: Reports*, 19(Estuar. Coast. Shelf Sci. 63 2005), 52–63. <https://doi.org/10.1016/j.jasrep.2018.02.018>
- Jensen, H. S., Kristensen, P., Jeppesen, E., & Skytthe, A. (1992). Iron:phosphorus ratio in surface sediment as an indicator of phosphate release from aerobic sediments in shallow lakes. *Hydrobiologia*, 235–236(1), 731–743. <https://doi.org/10.1007/BF00026261>
- Jensen, H. S., McGlathery, K. J., Marino, R., & Howarth, R. W. (1998). Forms and availability of sediment phosphorus in carbonate sand of Bermuda seagrass beds. *Limnology and Oceanography*, 43(5), 799–410. <https://doi.org/10.4319/lo.1998.43.5.0799>
- Jensen, H. S., Nielsen, O. I., Koch, M. S., & De Vicente, I. (2009). Phosphorus release with carbonate dissolution coupled to sulfide oxidation in Florida Bay seagrass sediments. *Limnology and Oceanography*, 54(5), 1753–1764. <https://doi.org/10.4319/lo.2009.54.5.1753>
- Jones, G. (1994). Global warming, sea level change and the impact on estuaries. *Marine Pollution Bulletin*, 28(1), 7–14. [https://doi.org/10.1016/0025-326X\(94\)90179-1](https://doi.org/10.1016/0025-326X(94)90179-1)
- Kaiho, K., Oshima, N., Adachi, K., Adachi, Y., Mizukami, T., Fujibayashi, M., & Saito, R. (2016). Global climate change driven by soot at the K-Pg boundary as the cause of the mass extinction. *Scientific Reports*, 6(1), 28427. <https://doi.org/10.1038/srep28427>
- Kambesis, P. N. (2013). The Geologic Controls on the Development of Caves within the Phreatic, Epiphreatic, and Vadose Zones on the Northeast Coast of Quintana Roo, Mexico. In *Cave Research Foundation Annual Report 2012–13*.
- Kambesis, P. N., & Coke, J. G. (2013). Overview of the controls on eogenetic cave and Karst development in Quintana Roo, Mexico. In M. J. Lacey (Ed.), *Coastal Karst Landforms* (Vol. 5, pp. 347–373). Springer. [https://doi.org/10.1007/978-94-007-5016-6\\_16](https://doi.org/10.1007/978-94-007-5016-6_16)

- Kambesis, P. N., & Coke, J. G. (2016). The sac actun system, Quintana Roo, Mexico. *Boletín Geológico y Minero*, *127*(1), 177–192.
- Kaufmann, G. (2009). Modelling karst geomorphology on different time scales. *Geomorphology*, *106*(1–2), 62–77. <https://doi.org/10.1016/j.geomorph.2008.09.016>
- Kendall, A. C., & Walters, K. L. (1978). The age of metasomatic anhydrite in Mississippian reservoir carbonates, southeastern Saskatchewan. *Can J Earth Sci*, *15*(3), 424–430. <https://doi.org/10.1139/e78-046>
- Kenkmann, T., Wittmann, A., & Scherler, D. (2004). Structure and impact indicators of the Cretaceous sequence of the ICDP drill core Yaxcopoil-1, Chicxulub impact crater, Mexico. *Meteoritics and Planetary Science*, *39*(7), 1069–1088. <https://doi.org/10.1111/j.1945-5100.2004.tb01129.x>
- Keppie, D. F., & Keppie, J. D. (2014). The Yucatan, a Laurentian or Gondwanan fragment? Geophysical and palinspastic constraints. *International Journal of Earth Sciences*, *103*(5), 1501–1512. <https://doi.org/10.1007/s00531-013-0953-x>
- Khan, N. S., Ashe, E., Horton, B. P., Dutton, A., Kopp, R. E., Brocard, G., Engelhart, S. E., Hill, D. F., Peltier, W. R., Vane, C. H., & Scatena, F. N. (2017). Drivers of Holocene sea-level change in the Caribbean. *Quaternary Science Reviews*, *155*(Geology 38 2010), 13–36. <https://doi.org/10.1016/j.quascirev.2016.08.032>
- Kinsland, G. L., Hurtado, M., & Pope, K. O. (2000). Detection of groundwater conduits in limestones with gravity surveys: Data from the area of the Chicxulub Impact Crater, Yucatan Peninsula, Mexico. *Geophysical Research Letters*, *27*(8), 1223–1226. <https://doi.org/10.1029/1999GL008404>
- Klimchouk, A. B. (2009). Morphogenesis of hypogenic caves. *Geomorphology*, *106*(1–2), 100–117. <https://doi.org/10.1016/j.geomorph.2008.09.013>

- Klimchouk, A. B., & Ford, D. C. (2009). Hypogene Speleogenesis and Karst Hydrogeology of Artesian Basins. In A. B. Klimchouk & D. C. Ford (Eds.), *Hypogene Speleogenesis and Karst Hydrogeology of Artesian Basins* (p. 280). Ukrainian Institute of Speleology and Karstology. [http://www.institute.speleoukraine.net/libpdf/Klimchouk\\_Ford\\_2009\\_HypoConf\\_Title-Contents.pdf](http://www.institute.speleoukraine.net/libpdf/Klimchouk_Ford_2009_HypoConf_Title-Contents.pdf)
- Kohout, F. A. (1960). Cyclic flow of salt water in the Biscayne aquifer of southeastern Florida. *Journal of Geophysical Research*, 65(7), 2133–2141. <https://doi.org/10.1029/jz065i007p02133>
- Kohout, F. A. (1965). A Hypothesis Concerning Cyclic Flow of Salt Water Related To Geothermal Heating in the Floridan Aquifer. *Transactions of the New York Academy of Sciences*, 28(2 Series II), 249–271. <https://doi.org/10.1111/j.2164-0947.1965.tb02879.x>
- Kring, D. A. (1995). The dimensions of the Chicxulub impact crater and impact melt sheet. *Journal of Geophysical Research*, 100(E8), 979–986. <https://doi.org/10.1029/95je01768>
- Kring, D. A. (2007). The Chicxulub impact event and its environmental consequences at the Cretaceous-Tertiary boundary. *Palaeogeography, Palaeoclimatology, Palaeoecology*, 255(1–2), 4–21. <https://doi.org/10.1016/j.palaeo.2007.02.037>
- Kring, D. A., & Durda, D. D. (2002). Trajectories and distribution of material ejected from the Chicxulub impact crater: Implications for postimpact wildfires. *Journal of Geophysical Research E: Planets*, 107(8). <https://doi.org/10.1029/2001je001532>
- Kring, D. A., Horz, F., Zürcher, L., & Urrutia-Fucugauchi, J. (2004). Impact lithologies and their emplacement in the Chicxulub impact crater: Initial results from the Chicxulub Scientific Drilling Project, Yaxcopoil, Mexico. *Meteoritics and Planetary Science*, 39(6), 879–897. <https://doi.org/10.1111/j.1945-5100.2004.tb00936.x>
- Kump, L. R., Brantley, S. L., & Arthur, M. A. (2000). Chemical weathering, atmospheric CO<sub>2</sub>, and Climate. *Annual Review of Earth and Planetary Sciences*, 28, 611–667. <https://doi.org/10.1146/annurev.earth.28.1.611>

- Lack, D. A., Quinn, P. K., Massoli, P., Bates, T. S., Coffman, D., Covert, D. S., Sierau, B., Tucker, S., Baynard, T., Lovejoy, E., Murphy, D. M., & Ravishankara, A. R. (2009). Relative humidity dependence of light absorption by mineral dust after long-range atmospheric transport from the Sahara. *Geophysical Research Letters*, *36*(24), 1–5. <https://doi.org/10.1029/2009GL041002>
- Lambeck, K., & Chappell, J. (2001). Sea level change through the last glacial cycle. *Science*, *292*(5517), 679–686. <https://doi.org/10.1126/science.1059549>
- Land, L. S. (1985). The origin of massive dolomite. *Journal of Geological Education*, *33*(2), 112–125. <https://doi.org/10.5408/0022-1368-33.2.112>
- Lapointe, B. E., O'Connell, J. D., Garrett, G. S., Julie, O., & Garrett, G. S. (1999). Nutrient couplings between on-site sewage disposal systems, groundwaters, and nearshore surface waters of the Florida Keys. *Biogeochemistry*, *10*(3), 289–307. <https://doi.org/10.1007/BF00003149>
- Leal-Bautista, R. M., Lenczewski, M., Morgan, C., Gahala, A., & McLain, J. E. (2013). Assessing Fecal Contamination in Groundwater from the Tulum Region, Quintana Roo, Mexico. *Journal of Environmental Protection*, *04*(11), 1272–1279. <https://doi.org/10.4236/jep.2013.411148>
- Lefticariu, M., Perry, E. C., Ward, W. C., & Lefticariu, L. (2006). Post-Chicxulub depositional and diagenetic history of the northwestern Yucatan Peninsula, Mexico. *Sedimentary Geology*, *183*(1–2), 51–69. <https://doi.org/10.1016/j.sedgeo.2005.09.008>
- Lesser, J. M., & Weidie, A. E. (1988). Regional geology of Yucatan Peninsula. In *The hydrogeology of North America* (pp. 237–241).
- Libes, S. M. (2009). *Introduction to Marine Biogeochemistry* (Academic Press (ed.); 2nd Editio). Elsevier.
- López-Ramos, E. (1973). Estudio geológico de la Península de Yucatán. *Bol. Asoc. Mexicana Geol. Petrol.*, *25*(1–3), 25–76.
- López-Ramos, E. (1975). Geological Summary of the Yucatan Peninsula. In A. E. M. Nairn (Ed.), *The Gulf of Mexico and the Caribbean* (pp. 257–282). Plenum Press. [https://doi.org/10.1007/978-1-4684-8535-6\\_7](https://doi.org/10.1007/978-1-4684-8535-6_7)

- Lugo-Hubp, J., Aceves-Quesada, J. F., & Espinasa-Pereña, R. (1992). Rasgos geomorfológicos mayores de la Península de Yucatán. ... *de Ciencias Geológicas*, 20 VN-r(4), 259–270. <https://doi.org/10.2142/biophys.20.259>
- Machel, H. G. (2004). Concepts and models of dolomitization: A critical reappraisal. *Geological Society Special Publication*, 235(1), 7–63. <https://doi.org/10.1144/GSL.SP.2004.235.01.02>
- Marín, L. E., & Alcocer, J. (2002). The Chicxulub impact crater and the regional hydrogeology of Northwest Yucatan. *Karst Waters Institute Special Publication*, 7(7), 146–150. [https://www.academia.edu/23393791/The\\_Chicxulub\\_Impact\\_Crater\\_and\\_the\\_Regional\\_Hydrogeology\\_of\\_Northwest\\_Yucatan](https://www.academia.edu/23393791/The_Chicxulub_Impact_Crater_and_the_Regional_Hydrogeology_of_Northwest_Yucatan)
- Marín, L. E., Perry, E. C., Essaid, H. I., & Steinich, B. (2016). Hydrogeological investigations and numerical simulation of groundwater flow in the karstic aquifer of northwestern Yucatan, Mexico. *Coastal Aquifer Management-Monitoring, Modeling, and Case Studies*, 257–277.
- Marín, L. E., Steinich, B., Pacheco, J., & Escolero, O. A. (2000). Hydrogeology of a contaminated sole-source karst aquifer, Mérida, Yucatán, Mexico. *Geofísica Internacional*, 39(4), 359–365. <https://doi.org/10.22201/igeof.00167169p.2000.39.4.246>
- Marriner, N., Morhange, C., Doumet-Serhal, C., & Carbonel, P. (2006). Geoscience rediscovers Phoenicia's buried harbors. *Geology*, 34(1), 1–4. <https://doi.org/10.1130/G21875.1>
- Martin, J. B. (2017). Carbonate minerals in the global carbon cycle. *Chemical Geology*, 449, 58–72. <https://doi.org/10.1016/j.chemgeo.2016.11.029>
- Martin, T. D., Brockhoff, C. A., Creed, J. T., & Long, S. E. (1994). METHOD 200.7 - Determination of elements and trace elements in water and wastes by Inductively Coupled Plasma-Atomic Emission Spectrometry. In *Methods for Determining Metals in Environmental Samples: Vol. EPA 200.7-*.
- Martini, M., & Ortega-Gutiérrez, F. (2018). Tectono-stratigraphic evolution of eastern Mexico during the break-up of Pangea: A review. *Earth-Science Reviews*, 183, 38–55. <https://doi.org/10.1016/j.earscirev.2016.06.013>

- Maruoka, T., & Koeberl, C. (2003). Acid-neutralizing scenario after the Cretaceous-Tertiary impact event. *Geology*, *31*(6), 489–492. [https://doi.org/10.1130/0091-7613\(2003\)031<0489:ASATCI>2.0.CO;2](https://doi.org/10.1130/0091-7613(2003)031<0489:ASATCI>2.0.CO;2)
- Mayr, S. I., Burkhardt, H., Popov, Y., & Wittmann, A. (2008). Estimation of hydraulic permeability considering the micro morphology of rocks of the borehole YAXCOPOIL-1 (Impact crater Chicxulub, Mexico). *International Journal of Earth Sciences*, *97*(2), 385–399. <https://doi.org/10.1007/s00531-007-0227-6>
- McKillop, H. (2005). Finds in Belize document Late Classic Maya salt making and canoe transport. *Proceedings of the National Academy of Sciences of the United States of America*, *102*(15), 5630–5634. <https://doi.org/10.1073/pnas.0408486102>
- Mee, A. C., Bestland, E. A., & Spooner, N. A. (2004). Age and origin of Terra Rossa soils in the Coonawarra area of South Australia. *Geomorphology*, *58*(1–4), 1–25. [https://doi.org/10.1016/S0169-555X\(03\)00183-1](https://doi.org/10.1016/S0169-555X(03)00183-1)
- Merino, E., & Banerjee, A. (2008). Terra rossa genesis, implications for karst, and eolian dust: A geodynamic thread. *Journal of Geology*, *116*(1), 62–75. <https://doi.org/10.1086/524675>
- Merino, E., Banerjee, A., & Dworkin, S. (2006). Dust, terra rossa, replacement, and karst: Serendipitous geodynamics in the critical zone. *Geochimica et Cosmochimica Acta*, *70*(18), A416. <https://doi.org/10.1016/j.gca.2006.06.837>
- Meybeck, M. (1987). Global chemical weathering of surficial rocks estimated from river dissolved loads. *American Journal of Science*, *287*(5), 401–428. <https://doi.org/10.2475/ajs.287.5.401>
- Meyerhoff, A. A., & Hatten, C. W. (1973). Bahamas Salient of North America: Tectonic Framework, Stratigraphy, and Petroleum Potential. *AAPG Bulletin*, *57*(10), 2148. <https://doi.org/10.1306/83D912A4-16C7-11D7-8645000102C1865D>
- Miller, T. (1983). Hydrology and hydrochemistry of the Caves Branch karst, Belize. *Journal of Hydrology*, *61*(1–3), 83–88. [https://doi.org/10.1016/0022-1694\(83\)90236-6](https://doi.org/10.1016/0022-1694(83)90236-6)
- Millero, F. J. (2013). Chemical oceanography. In *CRC Press* (Fourth Ed.). Taylor & Francis Group, LLC. [https://doi.org/10.1016/S0422-9894\(08\)70141-7](https://doi.org/10.1016/S0422-9894(08)70141-7)

- Milliman, J. D. (1993). Production and accumulation of calcium carbonate in the ocean: Budget of a nonsteady state. *Global Biogeochemical Cycles*, 7(4), 927–957. <https://doi.org/10.1029/93GB02524>
- Milne, G. A., & Peros, M. (2013). Data-model comparison of Holocene sea-level change in the circum-Caribbean region. *Global and Planetary Change*, 107, 119–131. <https://doi.org/10.1016/j.gloplacha.2013.04.014>
- Minor, R., & Grant, W. C. (1996). Earthquake-Induced Subsidence and Burial of Late Holocene Archaeological Sites, Northern Oregon Coast. *American Antiquity*, 61(4), 772–781. <https://doi.org/10.2307/282017>
- Monger, C. H. (2002). Pedogenic carbonate: links between biotic and abiotic CaCO<sub>3</sub>. *Proceedings of the 17th World Congress of Soil Science*, 20(897), 1–9. <http://citeseerx.ist.psu.edu/viewdoc/download?doi=10.1.1.5.1987&rep=rep1&type=pdf>
- Moreno, T., Querol, X., Castillo, S., Alastuey, A., Cuevas, E., Herrmann, L., Mounkaila, M., Elvira, J., & Gibbons, W. (2006). Geochemical variations in aeolian mineral particles from the Sahara-Sahel Dust Corridor. *Chemosphere*, 65(2), 261–270. <https://doi.org/10.1016/j.chemosphere.2006.02.052>
- Moresi, M., & Mongelli, G. (1988). The relation between the terra rossa and the carbonate-free residue of the underlying limestones and dolostones in Apulia, Italy. *Clay Minerals*, 23(4), 439–446. <https://doi.org/10.1180/claymin.1988.023.4.10>
- Morgan, J. V., Artemieva, N., & Goldin, T. J. (2013). Revisiting wildfires at the K-Pg boundary. *Journal of Geophysical Research: Biogeosciences*, 118(4), 1508–1520. <https://doi.org/10.1002/2013JG002428>
- Morgan, J. V., Gulick, S., Mellett, C. L., Green, S. L., & Scientists, the E. 364. (2017). Chicxulub: Drilling the K-Pg Impact Crater. Expedition 364 of the mission-specific drilling platform from and to Progresso, Mexico. In *Proceedings of the International Ocean Discovery Program* (Vol. 364, p. 12). International Ocean Discovery Program. <http://publications.iodp.org/proceedings/364/364title.html>

- Morgan, J. V., Lana, C., Kearsley, A., Coles, B., Belcher, C., Montanari, S., Díaz-Martínez, E., Barbosa, A., & Neumann, V. (2006). Analyses of shocked quartz at the global K-P boundary indicate an origin from a single, high-angle, oblique impact at Chicxulub. *Earth and Planetary Science Letters*, 251(3–4), 264–279. <https://doi.org/10.1016/j.epsl.2006.09.009>
- Morgan, J. V., Warner, M., Brittan, J., Buffler, R., Camargo-Zanoguera, A., Christeson, G., Denton, P., Hildebrand, A., Hobbs, R., Macintyre, H., Mackenzie, G., Maguire, P., Marin, L., Nakamura, Y., Pilkington, M., Sharpton, V., Snyder, D., Suarez, G., & Trejo, A. (1997). Size and morphology of the Chicxulub impact crater. *Nature*, 390(6659), 472–476. <https://doi.org/10.1038/37291>
- Moseley, G. E., Richards, D. A., Smart, P. L., Standish, C. D., Hoffmann, D. L., ten Hove, H., & Vinn, O. (2015). Early–middle Holocene relative sea-level oscillation events recorded in a submerged speleothem from the Yucatán Peninsula, Mexico. *Holocene*, 25(9), 1511–1521. <https://doi.org/10.1177/0959683615585832>
- Moseley, G. E., Smart, P. L., Richards, D. A., & Hoffmann, D. L. (2013). Speleothem constraints on marine isotope stage (MIS) 5 relative sea levels, Yucatan Peninsula, Mexico. *Journal of Quaternary Science*, 28(3), 293–300. <https://doi.org/10.1002/jqs.2613>
- Muhs, D. R., & Budahn, J. R. (2009). Geochemical evidence for African dust and volcanic ash inputs to terra rossa soils on carbonate reef terraces, northern Jamaica, West Indies. *Quaternary International*, 196(1–2), 13–35. <https://doi.org/10.1016/j.quaint.2007.10.026>
- Mylroie, J. R., & Mylroie, J. E. (2007). Development of the carbonate island karst model. *Journal of Cave and Karst Studies*, 69(1), 59–75.
- NASA/JPL. (2000). *Shaded and colored SRTM elevation model of the Yucatan Peninsula, Mexico. Original Data: Shuttle Radar Topography Mission*. SRTM Mexico Images. Original Data: Shuttle Radar Topography Mission (Feb 2000) Jet Propulsion Laboratory, NASA. <http://www2.jpl.nasa.gov/srtm/mexico.htm>
- Naumov, M. V. (2005). Principal features of impact-generated hydrothermal circulation systems: Mineralogical and geochemical evidence. *Geofluids*, 5(3), 165–184. <https://doi.org/10.1111/j.1468-8123.2005.00092.x>

- Nelson, M. J., Newsom, H. E., Spilde, M. N., & Salge, T. (2012). Petrographic investigation of melt and matrix relationships in Chicxulub crater Yaxcopoil-1 brecciated melt rock and melt rock-bearing suevite (846-885m, units 4 and 5). *Geochimica et Cosmochimica Acta*, *86*, 1–20. <https://doi.org/10.1016/j.gca.2012.02.022>
- Null, K. A., Knee, K. L., Crook, E. D., de Sieyes, N. R., Rebolledo-Vieyra, M., Hernández-Terrones, L. M., & Paytan, A. (2014). Composition and fluxes of submarine groundwater along the Caribbean coast of the Yucatan Peninsula. *Continental Shelf Research*, *77*, 38–50. <https://doi.org/10.1016/j.csr.2014.01.011>
- Nunes, L. M., Carvalho Dill, A., Ribeiro, L., & Vieira, J. (2002). Mixed analytical and numerical modelling of an oceanic peninsula. *Acta Universitatis Carolinae, Geologica*, *46*(2–3), 204–207.
- Oades, J. M. (1989). An Introduction to Organic Matter in Mineral Soils. In J. B. Dixon & S. B. Weed (Eds.), *Minerals in Soil Environments*. (2nd ed., Issue 1, pp. 89–159). Soil Science Society of America. <https://doi.org/10.2136/sssabookser1.2ed.c3>
- Ohno, S., Kadono, T., Kurosawa, K., Hamura, T., Sakaiya, T., Shigemori, K., Hironaka, Y., Sano, T., Watari, T., Otani, K., Matsui, T., & Sugita, S. (2014). Production of sulphate-rich vapour during the Chicxulub impact and implications for ocean acidification. *Nature Geoscience*, *7*(4), 279–282. <https://doi.org/10.1038/ngeo2095>
- Ortí, F., Rosell, L., Playà, E., & Salvany, J. M. (2012). Meganodular anhydritization: A new mechanism of gypsum to anhydrite conversion (Palaeogene-Neogene, Ebro Basin, North-east Spain). *Sedimentology*, *59*(4), 1257–1277. <https://doi.org/10.1111/j.1365-3091.2011.01305.x>
- Osinski, G. R. (2005). Hydrothermal activity associated with the Ries impact event, Germany. *Geofluids*, *5*(3), 202–220. <https://doi.org/10.1111/j.1468-8123.2005.00119.x>
- Osinski, G. R., Tornabene, L. L., Banerjee, N. R., Cockell, C. S., Flemming, R., Izawa, M. R. M., McCutcheon, J., Parnell, J., Preston, L. J., Pickersgill, A. E., Pontefract, A., Sapers, H. M., & Southam, G. (2013). Impact-generated hydrothermal systems on Earth and Mars. *Icarus*, *224*(2), 347–363. <https://doi.org/10.1016/j.icarus.2012.08.030>

- Palmer, A. N. (2011). Distinction between epigenic and hypogenic maze caves. *Geomorphology*, 134(1–2), 9–22. <https://doi.org/10.1016/j.geomorph.2011.03.014>
- Parnell, J., Taylor, C. W., Thackrey, S., Osinski, G. R., & Lee, P. (2010). Permeability data for impact breccias imply focussed hydrothermal fluid flow. *Journal of Geochemical Exploration*, 106(1–3), 171–175. <https://doi.org/10.1016/j.gexplo.2009.12.002>
- Penfield, G. T., & Camargo-Zanoguera, A. (1981). Definition of a major igneous zone in the central Yucatán platform with aeromagnetics and gravity. *Technical Program, Abstracts and Biographies (Society of Exploration Geophysicists 51st Annual International Meeting.)*, 37.
- Penfield, G. T., & Camargo-Zanoguera, A. (1991). Interpretation of Geophysical Cross Sections on the North Flank of the Chicxulub. *Abstracts of the Lunar and Planetary Science Conference*, 22, 1051. <http://adsabs.harvard.edu/full/1991LPI...22.1051P>
- Pérez-Ceballos, R., Pacheco-Ávila, J., Euán-Ávila, J. I., & Hernández-Arana, H. (2012). Regionalization based on water chemistry and physicochemical traits in the ring of Cenotes, Yucatan, Mexico. *Journal of Cave and Karst Studies*, 74(1), 90–102. <https://doi.org/10.4311/2011es0222>
- Perry, E. C., Marín, L. E., McClain, J., & Velazquez-Oliman, G. (1995). Ring of Cenotes (sinkholes), northwest Yucatan, Mexico: its hydrogeologic characteristics and possible association with the Chicxulub impact crater. *Geology*, 23(1), 17–20. [https://doi.org/10.1130/0091-7613\(1995\)023<0017:ROCSNY>2.3.CO;2](https://doi.org/10.1130/0091-7613(1995)023<0017:ROCSNY>2.3.CO;2)
- Perry, E. C., Paytan, A., Pedersen, B., & Velazquez-Oliman, G. (2009). Groundwater geochemistry of the Yucatan Peninsula, Mexico: Constraints on stratigraphy and hydrogeology. *Journal of Hydrology*, 367(1–2), 27–40. <https://doi.org/10.1016/j.jhydrol.2008.12.026>
- Perry, E. C., Velazquez-Oliman, G., & Marín, L. E. (2002). The hydrogeochemistry of the karst aquifer system of the northern Yucatan peninsula, Mexico. *International Geology Review*, 44(3), 191–221. <https://doi.org/10.2747/0020-6814.44.3.191>

- Petit, R. H., Legrand, M., Jankowiak, I., Molinié, J., Asselin de Beauville, C., Marion, G., & Mansot, J. L. (2005). Transport of Saharan dust over the Caribbean Islands: Study of an event. *Journal of Geophysical Research D: Atmospheres*, 110(18), 1–19. <https://doi.org/10.1029/2004JD004748>
- Pierazzo, E., Hahmann, A. N., & Sloan, L. C. (2003). Chicxulub and Climate: Radiative Perturbations of Impact-Produced S-Bearing Gases. *Astrobiology*, 3(1), 99–118. <https://doi.org/10.1089/153110703321632453>
- Pierazzo, E., Kring, D. A., & Jay Melosh, H. (1998). Hydrocode simulation of the Chicxulub impact event and the production of climatically active gases. *Journal of Geophysical Research E: Planets*, 103(E12), 28607–28625. <https://doi.org/10.1029/98JE02496>
- Pilkington, M., & Grieve, R. A. F. (1992). The Geophysical Signature of Terrestrial Impact Craters. *The American Geophysical Union*, 92, 161–181.
- Pope, K. O., Ocampo, A. C., & Duller, C. E. (1991). Mexican site for K/T impact crater? *Nature*, 351(6322), 105. <https://doi.org/10.1038/351105a0>
- Pope, K. O., Ocampo, A. C., & Duller, C. E. (1993). Surficial geology of the Chicxulub impact crater, Yucatan, Mexico. *Earth, Moon, and Planets*, 63(2), 93–104. <https://doi.org/10.1007/BF00575099>
- Pope, K. O., Ocampo, A. C., Kinsland, G. L., & Smith, R. (1996). Surface expression of the Chicxulub crater. *Geology*, 24(6), 527–530. [https://doi.org/10.1130/0091-7613\(1996\)024<0527:SEOTCC>2.3.CO;2](https://doi.org/10.1130/0091-7613(1996)024<0527:SEOTCC>2.3.CO;2)
- Potter, E. K., & Lambeck, K. (2004). Reconciliation of sea-level observations in the Western North Atlantic during the last glacial cycle. *Earth and Planetary Science Letters*, 217(1–2), 171–181. [https://doi.org/10.1016/S0012-821X\(03\)00587-9](https://doi.org/10.1016/S0012-821X(03)00587-9)
- Price, R. M., Swart, P. K., & Fourqurean, J. W. (2006). Coastal groundwater discharge - An additional source of phosphorus for the oligotrophic wetlands of the Everglades. *Hydrobiologia*, 569(1), 23–36. <https://doi.org/10.1007/s10750-006-0120-5>

- Prospero, J. M., & Nees, R. T. (1986). Impact of the North African drought and El Niño on mineral dust in the Barbados trade winds. *Nature*, 320(6064), 735–738. <https://doi.org/10.1038/320735a0>
- QRSS. (2020). *List of Long Underwater Caves in Quintana Roo Mexico*. Quintana Roo Speleological Survey. <https://caves.org/project/qrss/qrlong.htm>
- Rathje, W. (1973). Ancient Maya commercial systems: A research design for the island of Cozumel, Mexico. *World Archaeology*, 5(2), 221–231. <https://doi.org/10.1080/00438243.1973.9979569>
- Rebolledo-Vieyra, M., Urrutia-Fucugauchi, J., Marín, L. E., Trejo-García, A., Sharpton, V. L., & Soler-Arechalde, A. M. (2000). UNAM Scientific shallow-drilling program of the Chicxulub impact crater. *International Geology Review*, 42(10), 928–940. <https://doi.org/10.1080/00206810009465118>
- Robertson, D. S., Lewis, W. M., Sheehan, P. M., & Toon, O. B. (2013). K-Pg extinction: Reevaluation of the heat-fire hypothesis. *Journal of Geophysical Research: Biogeosciences*, 118(1), 329–336. <https://doi.org/10.1002/jgrg.20018>
- Rosencrantz, E. (1990). Structure and tectonics of the Yucatan Basin, caribbean Sea, as determined from seismic reflection studies. *Tectonics*, 9(5), 1037–1059. <https://doi.org/10.1029/TC009i005p01037>
- Šafanda, J., Wilhelm, H., Heidinger, P., & Čermák, V. (2009). Interpretation and mathematical modeling of temporal changes of temperature observed in borehole Yaxcopoil-1 within the Chicxulub impact structure, Mexico. *Journal of Hydrology*, 372(1–4), 9–16. <https://doi.org/10.1016/j.jhydrol.2009.03.023>
- Sanford, W. E. (2005). A simulation of the hydrothermal response to the Chesapeake Bay bolide impact. *Geofluids*, 5(3), 185–201. <https://doi.org/10.1111/j.1468-8123.2005.00110.x>
- Sanford, W. E., Whitaker, F. F., Smart, P. L., & Jones, G. (1998). Numerical analysis of seawater circulation in carbonate platforms: I. Geothermal convection. *American Journal of Science*, 298(10), 801–828. <https://doi.org/10.2475/ajs.298.10.801>

- Schreiber, B. C., & El Tabakh, M. (2000). Deposition and early alteration of evaporites. *Sedimentology*, 47(SUPPL. 1), 215–238. <https://doi.org/10.1046/j.1365-3091.2000.00002.x>
- Schulte, P., Alegret, L., Arenillas, I., Arz, J. A., Barton, P. J., Bown, P. R., Bralower, T. J., Christeson, G. L., Claeys, P., Cockell, C. S., Collins, G. S., Deutsch, A., Goldin, T. J., Goto, K., Grajales-Nishimura, J. M., Grieve, R. A. F., Gulick, S. P. S., Johnson, K. R., Kiessling, W., ... Willumsen, P. S. (2010). The Chicxulub Asteroid Impact and Mass Extinction at the Cretaceous-Paleogene Boundary. *Science*, 327(5970), 1214–1218. <https://doi.org/10.1126/science.1177265>
- Schuraytz, B. C., Sharpton, V. L., & Marin, L. E. (1994). Petrology of impact-melt rocks at the Chicxulub multiring basin, Yucatan, Mexico. *Geology*, 22(10), 868–872. [https://doi.org/10.1130/0091-7613\(1994\)022<0868:POIMRA>2.3.CO;2](https://doi.org/10.1130/0091-7613(1994)022<0868:POIMRA>2.3.CO;2)
- Schwenzer, S. P., & Kring, D. A. (2013). Alteration minerals in impact-generated hydrothermal systems - Exploring host rock variability. *Icarus*, 226(1), 487–496. <https://doi.org/10.1016/j.icarus.2013.06.003>
- Schwertmann, U. (1993). Relations between iron oxides, soil color, and soil formation. *Soil Color. Proc. Symposium, San Antonio, 1990*, 31, 51–69. <https://doi.org/10.2136/sssaspecpub31.c4>
- Sedov, S., Solleiro-Rebolledo, E., Fedick, S. L., Pi-Puig, T., Vallejo-Gómez, E., & Flores-Delgado, M. D. L. (2008). Micromorphology of a soil catena in yucatán: Pedogenesis and geomorphological processes in a tropical karst landscape. In S. Kapur, A. Mermut, & G. Stoops (Eds.), *New Trends in Soil Micromorphology* (pp. 19–37). Springer. [https://doi.org/10.1007/978-3-540-79134-8\\_3](https://doi.org/10.1007/978-3-540-79134-8_3)
- Sendra, A., Garay, P., Ortuño, V. M., Gilgado, J. D., Teruel, S., & Reboleira, A. S. P. S. (2014). Hypogenic versus epigenic subterranean ecosystem: Lessons from eastern Iberian Peninsula. *International Journal of Speleology*, 43(3), 253–264. <https://doi.org/10.5038/1827-806X.43.3.2>

- Sharpton, V. L., Marín, L. E., Carney, J. L., Lee, S., Ryder, G., Schuraytz, B. C., Sikora, P., & Spudis, P. D. (1996). A model of the Chicxulub impact basin based on evaluation of geophysical data, well logs, and drill core samples. *Special Paper of the Geological Society of America*, 307, 55–74. <https://doi.org/10.1130/0-8137-2307-8.55>
- Shaub, F. J. (1983). Origin of the Catoche Tongue. In A. W. Bally (Ed.), *Seismic Expression of Structural Styles- A Picture and Work Atlas* (Vol. 15, pp. 2.2.3-129). American Association of Petroleum Geologists.
- Shen, A. H., Ahrens, T. J., & O'Keefe, J. D. (2003). Shock wave induced vaporization of porous solids. *Journal of Applied Physics*, 93(9), 5167–5174. <https://doi.org/10.1063/1.1563035>
- Siddall, M., Chappell, J., & Potter, E. K. (2007). Eustatic sea level during past interglacials. *Developments in Quaternary Science*, 7(C), 75–92. [https://doi.org/10.1016/S1571-0866\(07\)80032-7](https://doi.org/10.1016/S1571-0866(07)80032-7)
- Smart, P. L., Beddows, P. A., Coke, J. G., Doerr, S., Smith, S. L., & Whitaker, F. F. (2006). Cave development on the caribbean coast of the Yucatan Peninsula, Quintana Roo, Mexico. In *Special Paper of the Geological Society of America* (Vol. 404, pp. 105–128). Geological Society of America. [https://doi.org/10.1130/2006.2404\(10\)](https://doi.org/10.1130/2006.2404(10))
- Smith, S. L. (2004). *The Geochemistry and Geomicrobiology of a Salinity-Stratified Coastal Carbonate Aquifer: Yucatan Peninsula, Mexico*. University of Bristol.
- Socki, R. A., Perry, E. C., & Romanek, C. S. (2002). Stable isotope systematics of two cenotes from the northern Yucatan Peninsula, Mexico. *Limnology and Oceanography*, 47(6), 1808–1818. <https://doi.org/10.4319/lo.2002.47.6.1808>
- Solleiro-Rebolledo, E., Cabadas-Báez, H. V., Pi, P. T., González, A., Fedick, S. L., Chmilar, J. A., & Leonard, D. (2011). Genesis of hydromorphic Calcisols in wetlands of the northeast Yucatan Peninsula, Mexico. *Geomorphology*, 135(3–4), 322–331. <https://doi.org/10.1016/j.geomorph.2011.02.009>

- Southworth, C. S. (1984). Structural and Hydrogeologic Applications of Remote Sensing Data, Eastern Yucatan Peninsula, Mexico. In B. F. Barry (Ed.), *Sinkholes: Their Geology, Engineering and Environmental Impact, Proceedings of the First Multidisciplinary Conference on Sinkholes*. (pp. 59–64). A. A. Balkema. <https://pubs.er.usgs.gov/publication/70013703>
- Spaw, R. H. (1977). *Late Pleistocene stratigraphy and geologic development of Cozumel Island, Quintana Roo, Mexico* [Rice University]. <https://scholarship.rice.edu/handle/1911/104042>
- Spötl, C., Desch, A., Dublyansky, Y., Plan, L., & Mangini, A. (2016). Hypogene speleogenesis in dolomite host rock by CO<sub>2</sub>-rich fluids, Kozak Cave (southern Austria). *Geomorphology*, 255(Geomorphology2292015), 39–48. <https://doi.org/10.1016/j.geomorph.2015.12.001>
- Sprynskyy, M., Lebedynets, M., & Sadurski, A. (2009). Gypsum karst intensification as a consequence of sulphur mining activity (Jaziv field, Western Ukraine). *Environmental Geology*, 57(1), 173–181. <https://doi.org/10.1007/s00254-008-1292-2>
- Steiner, M. B. (2005). Pangean reconstruction of the Yucatan Block: Its Permian, Triassic, and Jurassic geologic and tectonic history. *Special Paper of the Geological Society of America*, 393, 457–480. <https://doi.org/10.1130/0-8137-2393-0.457>
- Steinich, B., Velazquez-Oliman, G., Marín, L. E., & Perry, E. C. (1996). Determination of the ground water divide in the karst aquifer of Yucatán, Mexico, combining geochemical and hydrogeological data. *Geofísica Internacional*, 35(2), 153–159.
- Stinnesbeck, S. R., Stinnesbeck, W., Mata, A. T., Olguín, J. A., Sanvicente, M. B., Zell, P., Frey, E., Lindauer, S., Sandoval, C. R., Morlet, A. V., Nuñez, E. A., & González, A. G. (2018). The Muknal cave near Tulum, Mexico: An early-Holocene funeral site on the Yucatán Peninsula. *Holocene*, 28(12), 1992–2005. <https://doi.org/10.1177/0959683618798124>

- Stinnesbeck, W., Frey, E., Zell, P., Avilés Olguín, J., Hering, F., Frank, N., Arps, J., Geenen, A., Gescher, J., Isenbeck-Schröter, M., Ritter, S., Stinnesbeck, S. R., Aceves Núñez, E., Fito Dahne, V., González, A. H., & Deininger, M. (2018). Hells Bells – unique speleothems from the Yucatán Peninsula, Mexico, generated under highly specific subaquatic conditions. *Palaeogeography, Palaeoclimatology, Palaeoecology*, *489*, 209–229. <https://doi.org/10.1016/j.palaeo.2017.10.012>
- Stinnesbeck, W., Keller, G., Adatte, T., Harting, M., Stüben, D., Istrate, G., & Kramar, U. (2004). Yaxcopoil-1 and the Chicxulub impact. *International Journal of Earth Sciences*, *93*(6), 1042–1065. <https://doi.org/10.1007/s00531-004-0431-6>
- Stoessell, R. K., Ward, W. C., Ford, B. H., & Schuffert, J. D. (1989). Water chemistry and CaCO<sub>3</sub> dissolution in the saline part of an open-flow mixing zone, coastal Yucatan Peninsula, Mexico. *Geological Society of America Bulletin*, *101*(2), 159–169. [https://doi.org/10.1130/0016-7606\(1989\)101<0159:WCACDI>2.3.CO;2](https://doi.org/10.1130/0016-7606(1989)101<0159:WCACDI>2.3.CO;2)
- Sullivan, P. (2002). Tulum. Umbral entre dos mundos. *Arqueología Mexicana*, *1*(54), 56–59. <https://raices.com.mx/tienda/revistas-los-mayas-del-norte-de-quintana-roo-AM054>
- Szabo, B. J., Ward, W. C., Weidie, A. E., & Brady, M. J. (1978). Age and magnitude of the late Pleistocene sea-level rise on the eastern Yucatan Peninsula. *Geology*, *6*(12), 713–715. [https://doi.org/10.1130/0091-7613\(1978\)6<713:AAMOTL>2.0.CO;2](https://doi.org/10.1130/0091-7613(1978)6<713:AAMOTL>2.0.CO;2)
- Thomas, C. (2011). *Cuevas de Yucatán. Vol 1. La región de Valladolid*. Ed. Xibalba.
- Tisato, N., Sauro, F., Bernasconi, S. M., Bruijn, R. H. C., & De Waele, J. (2012). Hypogenic contribution to speleogenesis in a predominant epigenic karst system: A case study from the Venetian Alps, Italy. *Geomorphology*, *151–152*, 156–163. <https://doi.org/10.1016/j.geomorph.2012.01.025>
- Todorov, T. I., Wolf, R. E., & Adams, M. (2014). Multi-Elemental Analysis of Aqueous Geological Samples by Inductively Coupled Plasma-Optical Emission Spectrometry. *USGS Open-File Report 2014–1067*, 21. <https://doi.org/http://dx.doi.org/10.3133/ofr20141067>

- Tuchscherer, M. G., Reimold, W. U., Gibson, R. L., De Bruin, D., & Späth, A. (2006). Major and trace element compositions of melt particles and associated phases from the Yaxcopoil-1 drill core, Chicxulub impact structure, Mexico. *Meteoritics and Planetary Science*, *41*(9), 1361–1379. <https://doi.org/10.1111/j.1945-5100.2006.tb00527.x>
- Tulaczyk, S. M., Perry, E. C., Duller, C. E., & Villasuso, M. (1993). Influence of the Holbox fracture zone on the karst geomorphology and hydrogeology of northern Quintana Roo, Yucatan Peninsula, Mexico. *Applied Karst Geology. Proc. 4th Conference on Sinkholes and the Engineering and Environmental Impacts of Karst, Panama City, 1993*, 181–188. [https://doi.org/10.1016/0148-9062\(94\)92835-5](https://doi.org/10.1016/0148-9062(94)92835-5)
- Twenhofel, W. H. (1950). *Principles of Sedimentation* (2nd ed.). McGraw-Hill Book Company.
- UNAVCO. (2018). *UNAVCO Community (2018) PBO/COCONet/TLALOCnet GPS Network Datasets (DAI v2)*. PBO/COCONet/TLALOCnet GPS Network Datasets. <https://www.unavco.org/data/gps-gnss/data-access-methods/dai2/app/dai2.html>
- Upchurch, S., Scott, T. M., Alfieri, M. C., Fratesi, B., & Dobecki, T. L. (2019). *The Karst Systems of Florida: Understanding Karst in a Geologically Young Terrain*. Springer. <https://doi.org/10.1007/978-3-319-69635-5>
- Urrutia-Fucugauchi, J., Camargo-Zanoguera, A., Pérez-Cruz, L., & Pérez-Cruz, G. (2011). The Chicxulub multi-ring impact crater, Yucatan carbonate platform, Gulf of Mexico. *Geofisica Internacional*, *50*(1), 99–127.
- Urrutia-Fucugauchi, J., Chavez-Aguirre, J. M., Pérez-Cruz, L., & De la Rosa, J. L. (2008). Impact ejecta and carbonate sequence in the eastern sector of the Chicxulub crater. *Comptes Rendus - Geoscience*, *340*(12), 801–810. <https://doi.org/10.1016/j.crte.2008.09.001>
- Urrutia Fucugauchi, J., Marín, L. E., & García, A. T. (1996). Initial results of the UNAM scientific drilling program on the Chicxulub impact structure: Rock magnetic properties of UNAM-7 Tekax borehole. *Geofisica Internacional*, *35*(2), 125–133. <https://doi.org/10.22201/igeof.00167169p.1996.35.2.854>

- Vacher, H. L., & Mylroie, J. E. (2002). Eogenetic karst from the perspective of an equivalent porous medium. *Carbonates and Evaporites*, 17(2), 182–196. <https://doi.org/10.1007/BF03176484>
- Van Camp, M., & Vauterin, P. (2005). Tsoft: Graphical and interactive software for the analysis of time series and Earth tides. *Computers and Geosciences*, 31(5), 631–640. <https://doi.org/10.1016/j.cageo.2004.11.015>
- van der Does, M., Brummer, G. J. A., van Crimpen, F. C. J., Korte, L. F., Mahowald, N. M., Merkel, U., Yu, H., Zuidema, P., & Stuut, J. B. W. (2020). Tropical Rains Controlling Deposition of Saharan Dust Across the North Atlantic Ocean. *Geophysical Research Letters*, 47(5), 1–10. <https://doi.org/10.1029/2019GL086867>
- Velasco-Villareal, M., Urrutia-Fucugauchi, J., Rebolledo-Vieyra, M., & Perez-Cruz, L. (2011). Paleomagnetism of impact breccias from the Chicxulub crater – Implications for ejecta emplacement and hydrothermal processes. *Physics of the Earth and Planetary Interiors*, 186(3–4), 154171. <https://doi.org/10.1016/j.pepi.2011.04.003>
- Wahr, J. (1995). Earth Tides. In T. J. Ahrens (Ed.), *Global Earth Physics. A Handbook of Physical Constants* (pp. 40–46). American Geophysical Union. <https://doi.org/10.1029/rf001p0040>
- Waltham, A. C. (2008). Sinkhole hazard case histories in karst terrains. *Quarterly Journal of Engineering Geology and Hydrogeology*, 41(3), 291–300. <https://doi.org/10.1144/1470-9236/07-211>
- Waltham, A. C., Bell, F., & Culshaw, M. (2005). *Sinkholes and Subsidence Karst and Cavernous Rocks in Engineering and Construction* (T. Waltham, F. Bell, & M. Culshaw (eds.)). Springer.
- Ward, W. C. (1997). Geology of Coastal Islands, Northeastern Yucatan Peninsula. In H. L. Vacher & T. Quinn (Eds.), *Geology and Hydrogeology of Carbonate Islands. Developments in Sedimentology* (Vol. 54, pp. 275–298). Elsevier Science B.V. [https://doi.org/10.1016/S0070-4571\(04\)80029-3](https://doi.org/10.1016/S0070-4571(04)80029-3)

- Ward, W. C., & Halley, R. B. (1985). Dolomitization in a mixing zone of near-seawater composition, Late Pleistocene, northeastern Yucatan Peninsula. *Journal of Sedimentary Petrology*, 55(3), 407–420. <https://doi.org/10.1306/212F86E8-2B24-11D7-8648000102C1865D>
- Ward, W. C., Keller, G., Stinnesbeck, W., & Adatte, T. (1995). Yucatan subsurface stratigraphy: implications and constraints for the Chicxulub impact. *Geology*, 23(10), 873–876. [https://doi.org/10.1130/0091-7613\(1995\)023<0873:YNSSIA>2.3.CO;2](https://doi.org/10.1130/0091-7613(1995)023<0873:YNSSIA>2.3.CO;2)
- Warren, J. K. (2016). Evaporites A Geological Compendium Second Edition. In *Evaporites A Geological Compendium* (2nd ed.). Springer International Publishing. <https://doi.org/10.1007/978-3-319-13512-0>
- Weidie, A. E. (1985). Geology of the Yucatan Platform. Part 1. In W. C. Ward, A. E. Weidie, & W. Back (Eds.), *Geology and hydrogeology of the Yucatan and quaternary geology of northeastern Yucatan Peninsula* (pp. 1–19). New Orleans Geological Society.
- Whitaker, F. F., & Smart, P. L. (2007). Geochemistry of meteoric diagenesis in carbonate islands of the northern Bahamas: 1. Evidence from field studies. *Hydrological Processes*, 21(7), 949–966. <https://doi.org/10.1002/hyp.6532>
- Whitaker, F. F., & Xiao, Y. (2010). Reactive transport modeling of early burial dolomitization of carbonate platforms by geothermal convection. *AAPG Bulletin*, 94(6), 889–917. <https://doi.org/10.1306/12090909075>
- White, A. F. (2003). Natural Weathering Rates of Silicate Minerals. In J. I. Drever (Ed.), *Treatise on Geochemistry* (2nd ed., Vols. 5–9, pp. 133–168). Elsevier. <https://doi.org/10.1016/B0-08-043751-6/05076-3>
- White, W. B. (2002). Karst hydrology: Recent developments and open questions. *Engineering Geology*, 65(2–3), 85–105. [https://doi.org/10.1016/S0013-7952\(01\)00116-8](https://doi.org/10.1016/S0013-7952(01)00116-8)
- Wigley, T. M. L., & Plummer, L. N. (1976). Mixing of carbonate waters. *Geochimica et Cosmochimica Acta*, 40(9), 989–995. [https://doi.org/10.1016/0016-7037\(76\)90041-7](https://doi.org/10.1016/0016-7037(76)90041-7)

- Wilson, A. M., Sanford, W. E., Whitaker, F. F., & Smart, P. L. (2001). Spatial patterns of diagenesis during geothermal circulation in carbonate platforms. *American Journal of Science*, 301(8), 727–752. <https://doi.org/10.2475/ajs.301.8.727>
- Winston, G. O. (1991). *Atlas of structural evolution and facies development on the Florida-Bahama Platform – Triassic through Paleocene*.
- Wittmann, A., Kenkmann, T., Schmitt, R. T., Hecht, L., & Stöffler, D. (2004). Impact-related dike breccia lithologies in the ICDP drill core Yaxcopoil-1, Chicxulub impact structure, Mexico. *Meteoritics & Planetary Science*, 39(6), 931–954. <https://doi.org/10.1111/j.1945-5100.2004.tb00938.x>
- Wolbach, W. S., Lewis, R. S., & Anders, E. (1985). Cretaceous extinctions: Evidence for wildfires and search for meteoritic material. *Science*, 230(4722), 167–170. <https://doi.org/10.1126/science.230.4722.167>
- Worthington, S. R. H. (2007). Groundwater residence times in unconfined carbonate aquifers. *Journal of Cave and Karst Studies*, 69(1), 94–102.
- Worthington, S. R. H., Ford, D. C., & Beddows, P. A. (2000). Porosity and permeability enhancement in unconfined carbonate aquifers as a result of solution. In A. B. Klimchouk, D. C. Ford, A. N. Palmer, & W. Dreybrodt (Eds.), *Speleogenesis evolution of karst aquifers* (pp. 463–472). Cave Books.
- Wright, V. P. (1994). Paleosols in shallow marine carbonate sequences. *Earth Science Reviews*, 35(4), 367–395. [https://doi.org/10.1016/0012-8252\(94\)90002-7](https://doi.org/10.1016/0012-8252(94)90002-7)
- Wright, V. P., & Burchette, T. P. (1996). Shallow-water carbonate environments. In H. G. Reading (Ed.), *Sedimentary Environments: Processes, Facies and Stratigraphy* (pp. 325–394). Blackwell Publishing.
- Yaalon, D. H. (1997). Soils in the Mediterranean region: What makes them different? *Catena*, 28(3–4), 157–169. [https://doi.org/10.1016/S0341-8162\(96\)00035-5](https://doi.org/10.1016/S0341-8162(96)00035-5)
- Yang, W., & Ahrens, T. J. (1998). Shock vaporization of anhydrite and global effects of the K/T bolide. *Earth and Planetary Science Letters*, 156(3–4), 125–140. [https://doi.org/10.1016/s0012-821x\(98\)00006-5](https://doi.org/10.1016/s0012-821x(98)00006-5)

- Young, M. B., Gonnee, M. E., Fong, D. A., Moore, W. S., Herrera-Silveira, J. A., & Paytan, A. (2008). Characterizing sources of groundwater to a tropical coastal lagoon in a karstic area using radium isotopes and water chemistry. *Marine Chemistry*, *109*(3–4), 377–394. <https://doi.org/10.1016/j.marchem.2007.07.010>
- Zúñiga, F. R., Reyes, M. A., & Valdés, C. (2000). A general overview of the catalog of recent seismicity compiled by the Mexican Seismological Survey. *Geofísica Internacional*, *39*(2), 161–170. <https://doi.org/10.22201/igeof.00167169p.2000.39.2.273>
- Zürcher, L., & Kring, D. A. (2004). Hydrothermal alteration in the core of the Yaxcopoil-1 borehole, Chicxulub impact structure, Mexico. *Meteoritics and Planetary Science*, *39*(7), 1199–1221. <https://doi.org/10.1111/j.1945-5100.2004.tb01137.x>

## VI Appendix A

Geodetic data for the 40 GPS/GNNS stations considered in this study within the greater Caribbean area. Location, data temporal range and calculation of velocities are shown (Table VI-1) Displacements in mm yr<sup>-1</sup>. Data from UNAVCO (2018).

### UNAVCO DATASETS USED

#### [Caribbean Hurricane Prediction GPS Network - CNC0-Cancun P.S.](#)

Braun, John, 2007, Caribbean Hurricane Prediction GPS Network - CNC0-Cancun P.S., UNAVCO, GPS/GNSS Observations Dataset, <https://doi.org/10.7283/T5F18WV6>

#### [COCONet GPS Network - BARA-Barahona P.S.](#)

Bonetti, Luis, Holsteinson, Alexander T., 2012, COCONet GPS Network - BARA-Barahona P.S., UNAVCO, GPS/GNSS Observations Dataset, <https://doi.org/10.7283/T54J0CDH>

#### [COCONet GPS Network - CHIS-CHIS\\_IGN\\_GT\\_2009 P.S.](#)

UNAVCO Community, 2014, COCONet GPS Network - CHIS-CHIS\_IGN\_GT\_2009 P.S., UNAVCO, GPS/GNSS Observations Dataset, <https://doi.org/10.7283/T5QZ2876>

#### [COCONet GPS Network - CN00-BarbudaWBHCR2012 P.S.](#)

UNAVCO Community, 2012, COCONet GPS Network - CN00-BarbudaWBHCR2012 P.S., UNAVCO, GPS/GNSS Observations Dataset, <https://doi.org/10.7283/T5FN14GQ>

#### [COCONet GPS Network - CN05-CN05\\_PuntacanaDR P.S.](#)

UNAVCO Community, 2014, COCONet GPS Network - CN05-CN05\_PuntacanaDR P.S., UNAVCO, GPS/GNSS Observations Dataset, <https://doi.org/10.7283/T5VQ30ZH>

#### [COCONet GPS Network - CN11-Pedro\\_Cay\\_CR2011 P.S.](#)

UNAVCO Community, 2012, COCONet GPS Network - CN11-Pedro\_Cay\_CR2011 P.S., UNAVCO, GPS/GNSS Observations Dataset, <https://doi.org/10.7283/T5GM85K3>

#### [COCONet GPS Network - CN13-Sansalvadorbaham P.S.](#)

UNAVCO Community, 2014, COCONet GPS Network - CN13-Sansalvadorbaham P.S., UNAVCO, GPS/GNSS Observations Dataset, <https://doi.org/10.7283/T5QZ288N>

[COCONet GPS Network - CN15-GrandBahamCR2011 P.S.](#)

UNAVCO Community, 2011, COCONet GPS Network - CN15-GrandBahamCR2011 P.S., UNAVCO, GPS/GNSS Observations Dataset, <https://doi.org/10.7283/T5M906X3>

[COCONet GPS Network - CN19-ArubaNethARU2013 P.S.](#)

UNAVCO Community, 2013, COCONet GPS Network - CN19-ArubaNethARU2013 P.S., UNAVCO, GPS/GNSS Observations Dataset, <https://doi.org/10.7283/T5HD7SZB>

[COCONet GPS Network - CN23-BelmopanBZCR2012 P.S.](#)

UNAVCO Community, 2012, COCONet GPS Network - CN23-BelmopanBZCR2012 P.S., UNAVCO, GPS/GNSS Observations Dataset, <https://doi.org/10.7283/T5Q23XJH>

[COCONet GPS Network - CN24-FelipeCarMEX2012 P.S.](#)

UNAVCO Community, 2013, COCONet GPS Network - CN24-FelipeCarMEX2012 P.S., UNAVCO, GPS/GNSS Observations Dataset, <https://doi.org/10.7283/T5CN726Z>

[COCONet GPS Network - CN26-ArrecifeAMEX2016 P.S.](#)

UNAVCO Community, 2016, COCONet GPS Network - CN26-ArrecifeAMEX2016 P.S., UNAVCO, GPS/GNSS Observations Dataset, <https://doi.org/10.7283/W1SE-3691>

[COCONet GPS Network - CN40-CuracaoMetCR2011 P.S.](#)

UNAVCO Community, 2011, COCONet GPS Network - CN40-CuracaoMetCR2011 P.S., UNAVCO, GPS/GNSS Observations Dataset, <https://doi.org/10.7283/T5BV7DWT>

[COCONet GPS Network - LCSB-L\\_CAYMAN\\_CYM2014 P.S.](#)

Watts, Anthony, 2014, COCONet GPS Network - LCSB-L\_CAYMAN\_CYM2014 P.S., UNAVCO, GPS/GNSS Observations Dataset, <https://doi.org/10.7283/T537770Q>

[COCONet GPS Network - NARA-NARA\\_IGN\\_GT\\_2009 P.S.](#)

UNAVCO Community, 2014, COCONet GPS Network - NARA-NARA\_IGN\_GT\_2009 P.S., UNAVCO, GPS/GNSS Observations Dataset, <https://doi.org/10.7283/T5FF3QM7>

[COCONet GPS Network - Station CN00 and 45 Others](#)

UNAVCO Community, 2008, COCONet GPS Network - Station CN00 and 45 Others, UNAVCO, GPS/GNSS Observations (Aggregation of Multiple Datasets), <https://doi.org/10.7283/T5WM1BRG>

[COCONet GPS Network - TAXI-TAXI\\_IGN\\_GT\\_2008 P.S.](#)

UNAVCO Community, 2014, COCONet GPS Network - TAXI-TAXI\_IGN\_GT\_2008 P.S., UNAVCO, GPS/GNSS Observations Dataset, <https://doi.org/10.7283/T5K64GBZ>

[COCONet GPS Network - TEG2-Tegucigalpa P.S.](#)

UNAVCO Community, 2012, COCONet GPS Network - TEG2-Tegucigalpa P.S., UNAVCO, GPS/GNSS Observations Dataset, <https://doi.org/10.7283/YASD-J912>

[COCONet GPS Network - TAXI-TAXI\\_IGN\\_GT\\_2008 P.S.](#)

UNAVCO Community, 2014, COCONet GPS Network - TAXI-TAXI\_IGN\_GT\_2008 P.S., UNAVCO, GPS/GNSS Observations Dataset, <https://doi.org/10.7283/T5K64GBZ>

[COCONet GPS Network - TGMX-PtoMor\\_TG\\_MX2015 P.S.](#)

UNAVCO Community, 2015, COCONet GPS Network - TGMX-PtoMor\_TG\_MX2015 P.S., UNAVCO, GPS/GNSS Observations Dataset, <https://doi.org/10.7283/T5154FB7>

[COCONet GPS Network - TGPM-Bocas\\_TG\\_PAN2015 P.S.](#)

UNAVCO Community, 2015, COCONet GPS Network - TGPM-Bocas\_TG\_PAN2015 P.S., UNAVCO, GPS/GNSS Observations Dataset, <https://doi.org/10.7283/T5X065B1>

[COCONet GPS Network - UNPM-Puerto\\_Morelos\\_MX\\_2007 P.S.](#)

UNAVCO Community, 2012, COCONet GPS Network - UNPM-Puerto\_Morelos\_MX\_2007 P.S., UNAVCO, GPS/GNSS Observations Dataset, <https://doi.org/10.7283/J1GD-5S40>

[COCONet Partner GPS Network - Stations BARA, LVEG, SPED, SROD](#)

Bonetti, Luis, Holsteinson, Alexander T., 2012, COCONet Partner GPS Network - Stations BARA, LVEG, SPED, SROD, UNAVCO, GPS/GNSS Observations (Aggregation of Multiple Datasets), <https://doi.org/10.7283/T51C1V7S>

[SCIGN-PBO Nucleus GPS Network - KBRC-Kimball Ranch P.S.](#)

UNAVCO Community, 2005, SCIGN-PBO Nucleus GPS Network - KBRC-Kimball Ranch P.S., UNAVCO, GPS/GNSS Observations Dataset, <https://doi.org/10.7283/TCCJ-4H51>

[TLALOCNet GPS Network - TNGF\\_Geofisica-UNAM\\_Mexico\\_City\\_TNET\\_mx2015 P.S.](#)

Cabral-Cano, Enrique, Salazar-Tlaczani, Luis, 2016, TLALOCNet GPS Network - TNGF\_Geofisica-UNAM\_Mexico\_City\_TNET\_mx2015 P.S., UNAVCO, GPS/GNSS Observations Dataset, <https://doi.org/10.7283/T53X851M>

Table VI-1 Geodetic data for the 40 GPS/GNNS stations considered in this study within the greater Caribbean area. Location, data temporal range and calculation of velocities are shown. Displacements in mm yr<sup>-1</sup>. Data from UNAVCO (2018).

STATION				Location		Date Range		y			x			z			Estimated Velocity (mm yr <sup>-1</sup> )		
ID	4chID	interval	name	lat	lon	start date	end date	Delta days	Delta yrs	Delta North (mm)	Delta East (mm)	Delta Vertical (mm)	Vx	Vy	Vz				
1	ABMF	30.0 sec	Aeroport du Raizet -LES ABYMES - Mitio France	16.2623	-61.5275	25-Dec-2009	29-Jan-2020	3687	10.1	152.64	111.72	8.11	11.07	15.13	0.80				
2	ACPI	15.0 sec	ACPI	9.3714	-79.9499	24-Oct-2008	19-Jan-2020	4104	11.2	127.63	188.78	-7.39	16.81	11.37	-0.66				
3	ANG1	30.0 sec	Angleton 1	29.3015	-95.4851	03-Apr-2003	15-Nov-2007	1687	4.6	-36.95	-64.27	12.82	-13.93	-8.00	2.78				
4	BARA	15.0 sec	Barahona	18.2086	-71.0980	01-Jan-2011	27-Jan-2020	3313	9.1	82.49	81.17	10.93	8.95	9.10	1.21				
5	BDOS	30.0 sec	Barbados	13.0880	-59.6091	11-Jun-2004	16-Jun-2014	3657	10.0	152.50	142.62	-5.49	14.25	15.24	-0.55				
6	CCV3	30.0 sec	Cape Canaveral 3	28.4602	-80.5452	07-Aug-1998	24-Jan-2007	3092	8.5	22.28	-104.92	-25.07	-12.40	2.63	-2.96				
7	CHIS	30.0 sec	CHIS_IGN_GT_2009	15.8123	-90.2914	27-Mar-2012	04-Dec-2015	1347	3.7	-3.37	-24.78	-2.96	-6.73	-0.91	-0.80				
8	CN11	30.0 sec	PedroCay_JAM2011	17.0212	-77.7841	21-Sep-2011	07-May-2019	2785	7.6	51.85	61.53	2.48	8.07	6.81	0.33				
9	CN15	15.0 sec	GrandBah_BHS2011	26.5567	-78.6931	23-Jun-2011	01-Sep-2019	2992	8.2	29.92	-91.56	-11.37	-11.18	3.66	-1.39				
10	CN16	15.0 sec	Camaguey_CUB2014	21.4223	-77.8498	21-May-2014	19-May-2019	1824	5.0	20.98	-41.22	-2.19	-8.26	4.20	-0.44				
11	CN23	15.0 sec	Belmopan_BLZ2012	17.2606	-88.7788	25-Jul-2012	20-Jun-2018	2156	5.9	1.72	-43.34	13.80	-7.35	0.29	2.34				
12	CN24	15.0 sec	Felipe_Carrillo_MX_2012	19.5756	-88.0539	31-Oct-2013	03-Sep-2018	1768	4.8	6.01	-38.01	-1.41	-7.86	1.24	-0.29				
13	CN25	15.0 sec	Comitan_MX_2012	16.2321	-92.1353	13-Feb-2014	19-Jan-2020	2166	5.9	7.58	-29.89	13.65	-5.04	1.28	2.30				
14	CN26	15.0 sec	ArrecifeAMEX2016	22.3830	-89.6824	05-Dec-2016	01-Mar-2018	451	1.2	2.16	-10.49	8.28	-8.50	1.75	6.71				
15	CN38	15.0 sec	Cerrejon_COL2012	12.2218	-71.9880	31-Aug-2012	17-Aug-2016	1447	4.0	52.38	42.40	18.38	10.71	13.23	4.64				
16	CN40	15.0 sec	Curacao_CUW2011	12.1800	-68.9580	22-Jul-2011	29-Jan-2020	3113	8.5	104.29	91.83	3.11	10.78	12.24	0.37				
17	CNC0	15.0 sec	Cancun_MX_2007	21.1744	-86.8208	05-Jun-2007	23-Oct-2019	4523	12.4	9.50	-112.62	-20.81	-9.10	0.77	-1.68				
18	ELEN	30.0 sec	Santa Elena	16.9161	-89.8676	08-Dec-2001	16-Feb-2016	5183	14.2	8.81	-115.58	3.11	-8.15	0.62	0.22				
19	GCEA	30.0 sec	GC_Elgin_Ave2011	19.2930	-81.3780	08-Jul-2014	29-Jan-2020	2031	5.6	6.50	-47.93	-7.51	-8.63	1.17	-1.35				
20	GUAT	30.0 sec	Guatemala	14.5904	-90.5202	28-Jul-2000	03-Nov-2019	7037	19.3	41.52	74.59	-26.74	3.87	2.16	-1.39				
21	KVTX	15.0 sec	KingsvilleTX2006	27.5459	-97.8929	21-Mar-2007	02-Feb-2020	4701	12.9	-32.44	-154.66	-48.89	-12.02	-2.52	-3.80				

STATION			Location		Date Range		y			x		z	Estimated Velocity (mm yr <sup>-1</sup> )		
ID	4chID	interval	name	lat	lon	start date	end date	Delta days	Delta yrs	Delta North (mm)	Delta East (mm)	Delta Vertical (mm)	Vx	Vy	Vz
22	LMCN	30.0 sec	Louisiana University Marine Consortium	29.2550	-90.6613	24-Apr-2003	02-Feb-2020	6128	16.8	-14.09	-173.42	-122.56	-10.34	-0.84	-7.31
23	LMMF	30.0 sec	Aeroport -Meteo Fra.	14.5948	-60.9962	27-Dec-2009	29-Jan-2020	3685	10.1	155.88	130.08	-11.06	12.90	15.46	-1.10
24	MANA	30.0 sec	Managua_NIC2012	12.1491	-86.2486	13-May-2000	29-Jan-2020	7200	19.7	138.96	125.28	-48.96	6.36	7.05	-2.49
25	MCDI	30.0 sec	Mac Dill 1	27.8498	-82.5323	03-May-2001	21-Feb-2007	2120	5.8	8.93	-61.47	-2.98	-10.60	1.54	-0.51
26	NARA	30.0 sec	NARA_IGN_GT_2009	17.2268	-90.8100	27-Mar-2012	16-Feb-2016	1421	3.9	-2.42	-30.27	-19.04	-7.79	-0.62	-4.90
27	OXUM	15.0 sec	Puerto_Angel-UMAR_TNET_MX_2001	15.6623	-96.4990	22-Feb-2013	03-Feb-2020	2537	6.9	87.53	-71.04	-21.06	-10.23	12.61	-3.03
28	P780	15.0 sec	Cerrillos_PR2008	18.075	-66.5791	28-May-2008	29-Jan-2020	4263	11.7	159.44	103.59	-1.71	8.88	13.67	-0.15
29	ROA0	15.0 sec	RoatanAP_HND2007	16.3181	-86.5266	11-May-2007	29-Oct-2018	4189	11.5	126.93	268.93	-13.82	23.47	11.07	-1.21
30	SG05	30.0 sec	Florida Inst of Tech.	28.0652	-80.6228	05-Feb-2002	14-Feb-2016	5122	14.0	43.55	-155.23	-7.68	-11.08	3.11	-0.55
31	TEG2	30.0 sec	Tegucigalpa	14.0901	-87.2056	28-Apr-2011	16-Mar-2018	2514	6.9	36.96	54.30	41.48	7.89	5.37	6.03
32	TGMX	15.0 sec	Puerto_Morelos-TG_MX_2015	20.8681	-86.8669	18-Feb-2015	29-Jan-2020	1806	4.9	42.96	-41.70	1.26	-8.44	8.69	0.26
33	TNBA	15.0 sec	Bahia_Angeles_TNET_MX_2014	28.9719	-113.5473	29-Nov-2014	03-Feb-2020	1892	5.2	104.25	-224.01	-4.54	-43.28	20.14	-0.88
34	TNHM	15.0 sec	Hermosillo_TNET_MX_2014	29.0813	-110.9703	17-Jul-2014	03-Feb-2020	2027	5.5	-39.53	-61.22	-6.49	-11.04	-7.13	-1.17
35	TNMQ	15.0 sec	Marquelia_TNET_MX_2015	16.7104	-98.6116	26-Nov-2015	03-Feb-2020	1530	4.2	14.08	-29.99	20.96	-7.16	3.36	5.01
36	TNMR	15.0 sec	Maruata_TNET_MX_2014	18.2885	-103.3455	11-Sep-2014	02-Oct-2018	1482	4.1	23.12	-4.59	-22.67	-1.13	5.70	-5.59
37	TNPJ	15.0 sec	Pijijiapan_TNET_MX_2014	15.7046	-93.2189	19-Nov-2014	02-Oct-2018	1413	3.9	-13.42	-66.41	-62.03	-17.18	-3.47	-16.05
38	UNPM	15.0 sec	Puerto_Morelos_MX_2007	20.8685	-86.86817	08-Aug-2007	29-Jan-2020	4557	12.5	11.85	-111.19	-22.33	-8.92	0.95	-1.79
39	UXAL	15.0 sec	Jalapa_TNET_MX_2005	19.5164	-96.9248	15-Sep-2005	02-Feb-2020	5253	14.4	-39.40	-106.64	-2.63	-7.42	-2.74	-0.18
40	VRAI	15.0 sec	Veragua_CRI2012	9.9249	-83.1906	20-Oct-2012	22-Jan-2020	2650	7.3	81.62	117.13	-43.99	16.16	11.26	-6.07

## **VII Appendix B**

### **ROCK COMPOSITION TABLES**

Rock composition tables showing mean, minimum, maximum, and standard deviation values obtained by ICP-OES quantification of 22 selected elements in 185 samples grouped in three areas: beach sand vadose zone and phreatic zone (Table VII-1); and information on the geography, characteristics of sites, coordinates, and weight (mg) used in the multi-elemental quantification by ICP-OES geochemical analyzes for a selection of 185 samples (Table VII-2).

Table VII-1 Average bulk rock composition showing mean, minimum, maximum, and standard deviation values obtained by ICP-OES quantification in rock samples ( $n = 185$ ) grouped in three areas: beach sand vadose zone and phreatic zone. Concentration values for 22 elements given in mmol per kg of dry rock ( $\text{mmol kg}^{-1}_{\text{rock}}$ ). Depth means meters above ground for vadose sample rocks, and meters below water table for phreatic zone sample rocks.

ID	LOCATION	DEPTH (m)	Al	Ba	Be	Cd	Co	Cr	Cu	Fe	K	Li	Mn	Mo	Na	Ni	P	Pb	Rb	S	Si	Sr	Tl	V		
<b>AKUMAL BEACH SAND</b>																										
SAK01-20140316	Akumal	0.000	12.119	0.168	0.000	0.001	0.000	0.094	0.255	3.884	3.196	0.447	0.257	0.000	107.307	0.001	8.850	0.083	0.000	53.086	15.021	63.015	0.001	0.020		
SAK02-20140316	Akumal	0.000	12.106	0.119	0.000	0.001	0.000	0.090	0.137	3.363	2.613	0.441	0.249	0.000	106.066	0.000	10.241	0.096	0.000	51.031	13.822	63.185	0.000	0.016		
SAK03-20140316	Akumal	0.000	5.923	0.084	0.000	0.000	0.001	0.080	0.137	2.155	1.878	0.422	0.174	0.000	110.993	0.000	6.206	0.056	0.000	50.661	6.549	59.877	0.001	0.015		
SAK04-20140316	Akumal	0.000	6.241	0.089	0.000	0.001	0.002	0.064	0.101	2.436	1.990	0.418	0.160	0.000	116.805	0.001	5.671	0.048	0.000	47.447	7.156	60.746	0.000	0.014		
SAK05-20140316	Akumal	0.000	5.114	0.096	0.000	0.000	0.000	0.071	0.138	3.553	2.085	0.422	0.148	0.000	119.016	0.001	5.121	0.029	0.000	54.517	6.931	65.670	0.000	0.013		
SAK06-20140316	Akumal	0.000	6.496	0.084	0.000	0.001	0.000	0.069	0.172	1.753	2.080	0.427	0.158	0.000	114.765	0.000	4.529	0.030	0.000	51.494	7.387	64.685	0.000	0.017		
SAK07-20140316	Akumal	0.000	4.224	0.081	0.000	0.001	0.000	0.069	0.042	1.621	2.238	0.440	0.132	0.000	132.048	0.005	4.456	0.029	0.000	55.808	4.490	62.296	0.000	0.010		
SAK08-20140316	Akumal	0.000	3.158	0.072	0.000	0.001	0.000	0.082	0.036	0.635	8.085	0.401	0.134	0.000	325.790	0.005	4.718	0.012	0.000	75.336	3.998	49.303	0.000	0.029		
SAK09-20140316	Akumal	0.000	1.294	0.080	0.000	0.000	0.000	0.086	0.026	0.574	10.909	0.434	0.142	0.000	410.610	0.006	5.206	0.014	0.000	91.348	3.693	62.153	0.000	0.017		
SAK10-20140316	Akumal	0.000	3.737	0.079	0.000	0.000	0.000	0.085	0.021	0.723	10.778	0.467	0.158	0.000	441.160	0.015	4.700	0.009	0.000	89.336	3.431	60.078	0.001	0.014		
		<b>Beach Sand Mean</b>	<b>6.041</b>	<b>0.095</b>	<b>0.000</b>	<b>0.001</b>	<b>0.000</b>	<b>0.079</b>	<b>0.107</b>	<b>2.070</b>	<b>4.585</b>	<b>0.432</b>	<b>0.171</b>	<b>0.000</b>	<b>198.456</b>	<b>0.003</b>	<b>5.970</b>	<b>0.041</b>	<b>0.000</b>	<b>62.007</b>	<b>7.248</b>	<b>61.101</b>	<b>0.000</b>	<b>0.017</b>		
		<b>Beach Sand Min</b>	<b>1.294</b>	<b>0.072</b>	<b>0.000</b>	<b>0.000</b>	<b>0.000</b>	<b>0.064</b>	<b>0.021</b>	<b>0.574</b>	<b>1.878</b>	<b>0.401</b>	<b>0.132</b>	<b>0.000</b>	<b>106.066</b>	<b>0.000</b>	<b>4.456</b>	<b>0.009</b>	<b>0.000</b>	<b>47.447</b>	<b>3.431</b>	<b>49.303</b>	<b>0.000</b>	<b>0.010</b>		
		<b>Beach Sand Max</b>	<b>12.119</b>	<b>0.168</b>	<b>0.000</b>	<b>0.001</b>	<b>0.002</b>	<b>0.094</b>	<b>0.255</b>	<b>3.884</b>	<b>10.909</b>	<b>0.467</b>	<b>0.257</b>	<b>0.000</b>	<b>441.160</b>	<b>0.015</b>	<b>10.241</b>	<b>0.096</b>	<b>0.000</b>	<b>91.348</b>	<b>15.021</b>	<b>65.670</b>	<b>0.001</b>	<b>0.029</b>		
		<b>Beach Sand StDev</b>	<b>3.381</b>	<b>0.027</b>	<b>0.000</b>	<b>0.000</b>	<b>0.001</b>	<b>0.010</b>	<b>0.072</b>	<b>1.171</b>	<b>3.585</b>	<b>0.017</b>	<b>0.043</b>	<b>0.000</b>	<b>130.005</b>	<b>0.004</b>	<b>1.885</b>	<b>0.028</b>	<b>0.000</b>	<b>15.910</b>	<b>3.868</b>	<b>4.314</b>	<b>0.001</b>	<b>0.005</b>		
<b>VADOSE ZONE</b>																										
KNKB-20110801-1.0	Yucatan	1.000	7.794	0.055	0.000	0.001	0.044	0.043	0.011	1.205	0.812	0.387	0.180	0.000	4.968	0.020	0.269	0.006	0.000	10.991	5.670	2.498	0.002	0.139		
KNKF-20110801-1.7	Yucatan	1.700	3.218	0.040	0.000	0.001	0.022	0.054	0.006	0.652	0.706	0.398	0.171	0.011	7.362	0.007	0.179	0.006	0.000	30.475	1.096	4.453	0.000	0.128		
KNKG-20110801-2.2	Yucatan	2.200	9.190	0.098	0.000	0.001	0.019	0.040	0.007	3.900	0.994	0.374	0.147	0.000	11.257	0.006	1.508	0.005	0.000	21.772	7.529	2.620	0.000	0.040		
KNKH-20110801-2.7	Yucatan	2.700	2.806	0.032	0.000	0.001	0.012	0.029	0.009	0.684	0.570	0.394	0.263	0.000	4.400	0.001	0.158	0.006	0.000	19.342	1.752	4.195	0.000	0.090		
KNKI-20110801-3.0	Yucatan	3.000	3.083	0.028	0.000	0.001	0.025	0.050	0.009	0.743	0.931	0.366	0.213	0.000	8.032	0.009	0.173	0.006	0.000	31.433	2.959	4.019	0.000	0.148		
KNKJ-20110801-3.5	Yucatan	3.500	1.805	0.020	0.000	0.001	0.018	0.026	0.006	0.596	0.473	0.387	0.207	0.000	4.473	0.008	0.210	0.006	0.000	21.516	1.723	3.222	0.000	0.109		
SIBI-20111211-0.0	Puerto Morelos	0.000	64.913	0.564	0.000	0.001	0.110	0.167	0.013	12.654	3.170	0.664	0.334	0.022	13.325	0.052	1.758	0.006	0.000	19.893	71.617	6.723	0.000	0.049		
SAS03-01-20111212-2.0	Leona Vicario	2.000	2.563	0.042	0.000	0.000	0.020	0.160	0.015	1.695	0.433	0.366	0.239	0.000	5.080	0.035	3.521	0.006	0.000	0.000	0.270	6.157	0.002	0.148		
SAS03-02-20111212-0.0	Leona Vicario	0.000	87.705	0.099	0.000	0.001	0.051	0.186	0.018	11.777	2.640	0.749	1.419	0.020	6.947	0.000	1.643	0.006	0.000	1.078	90.408	4.771	0.000	0.065		
SAS03-03-20111212-5.5	Leona Vicario	5.500	3.736	0.046	0.000	0.001	0.033	0.177	0.021	2.749	0.509	0.380	0.266	0.000	5.077	0.036	3.387	0.005	0.000	0.000	0.546	6.104	0.001	0.146		
SAS04-20111212-U6	Solferino	0.000	25.050	0.054	0.000	0.002	0.127	0.174	0.034	3.041	3.506	0.385	0.284	0.020	7.938	0.009	1.928	0.008	0.000	33.215	38.178	4.026	0.000	0.512		
SAS04-20111212-U5A	Solferino	0.000	5.889	0.031	0.000	0.000	0.336	0.147	0.014	2.676	0.354	0.359	0.607	0.000	5.961	0.028	2.592	0.006	0.000	3.545	3.712	1.554	0.000	0.064		
SAS04-20111212-U5B	Solferino	0.000	8.773	0.030	0.000	0.001	0.450	0.147	0.023	2.140	0.889	0.353	1.127	0.000	11.179	0.021	4.874	0.003	0.000	8.452	5.804	2.159	0.000	0.071		
SAS04-20111212-U4	Solferino	0.000	2.617	0.014	0.000	0.002	0.527	0.068	0.040	3.108	0.173	0.335	0.226	0.000	2.098	0.031	5.718	0.006	0.000	0.113	1.226	4.745	0.000	0.031		
SAS04-20111212-U3A	Solferino	0.000	49.820	0.053	0.000	0.002	0.068	0.235	0.021	7.428	1.427	0.571	0.284	0.014	4.657	0.048	2.105	0.007	0.000	3.154	50.948	4.463	0.000	0.108		
SAS04-20111212-U3B	Solferino	0.000	77.131	0.035	0.000	0.001	0.500	0.245	0.040	7.573	2.544	0.690	0.537	0.020	3.579	0.107	1.339	0.007	0.000	1.508	84.683	6.313	0.000	0.111		

ID	LOCATION	DEPTH (m)	Al	Ba	Be	Cd	Co	Cr	Cu	Fe	K	Li	Mn	Mo	Na	Ni	P	Pb	Rb	S	Si	Sr	Tl	V
SAS06-20111215-U2A-1.2	Kantunil Kin	1.200	9.143	0.030	0.000	0.000	0.015	0.066	0.016	1.081	0.771	0.392	0.183	0.002	4.327	0.005	0.322	0.004	0.000	23.252	8.253	3.941	0.000	0.201
SAS06-20111215-U2B-2.0	Kantunil Kin	2.000	19.305	0.127	0.000	0.000	0.080	0.064	0.023	1.723	2.101	0.380	0.233	0.000	7.775	0.000	0.627	0.003	0.000	12.768	29.736	3.068	0.005	0.150
SAS06-20111215-U3	Kantunil Kin	3.000	15.554	0.036	0.000	0.000	0.058	0.048	0.014	1.767	1.789	0.363	0.205	0.005	5.040	0.000	1.046	0.005	0.000	23.416	26.760	3.011	0.003	0.156
SAS06-20111215-U4	Kantunil Kin	4.000	4.388	0.019	0.000	0.001	0.023	0.123	0.007	1.352	0.529	0.327	0.366	0.000	2.499	0.032	0.208	0.005	0.000	6.504	3.925	2.196	0.000	0.058
SAS06-20111215-U5	Kantunil Kin	5.000	6.342	0.021	0.000	0.003	0.025	0.060	0.013	1.458	1.261	0.350	0.454	0.001	6.663	0.000	0.235	0.001	0.000	2.689	8.888	2.560	0.000	0.093
SAS06-20111215-U6B	Kantunil Kin	6.000	4.240	0.019	0.000	0.003	0.021	0.047	0.010	1.088	0.588	0.331	0.401	0.002	2.616	0.001	0.249	0.009	0.000	11.144	4.116	2.670	0.001	0.094
SAS06-20111215-U6C	Kantunil Kin	7.000	6.608	0.022	0.000	0.002	0.017	0.044	0.023	1.519	1.855	0.339	0.467	0.000	5.869	0.003	0.335	0.010	0.000	2.916	8.832	3.215	0.002	0.071
SAS06-20111215-U6D	Kantunil Kin	8.000	19.440	0.024	0.000	0.002	0.084	0.047	0.014	2.630	4.032	0.347	0.532	0.002	2.489	0.000	0.300	0.008	0.000	4.750	32.956	2.390	0.000	0.089
SAS06-20111215-U6G	Kantunil Kin	9.000	6.279	0.017	0.000	0.002	0.028	0.089	0.009	1.484	1.384	0.424	0.402	0.000	2.332	0.004	0.266	0.005	0.000	4.656	9.742	3.422	0.000	0.050
SAS8A-20130401	Valladolid	1.000	50.196	0.047	0.000	0.004	0.026	0.095	0.041	3.611	7.222	0.335	0.241	0.016	5.739	0.018	10.543	0.006	0.076	0.000	60.891	2.946	0.000	0.194
SAS8B-20130401	Valladolid	4.000	10.513	0.043	0.000	0.002	0.014	0.077	0.027	2.067	0.408	0.311	0.321	0.000	9.294	0.022	9.065	0.002	0.120	6.470	2.570	1.389	0.000	0.438
SAS8C-20130401	Valladolid	0.000	15.126	0.045	0.000	0.002	0.034	0.082	0.027	2.606	0.813	0.343	0.270	0.000	11.235	0.031	11.803	0.002	0.138	10.567	6.113	1.609	0.000	0.464
SAS8D-20130401	Valladolid	7.000	12.480	0.041	0.000	0.005	0.014	0.090	0.037	3.581	0.759	0.329	0.395	0.000	9.106	0.025	11.809	0.002	0.138	8.446	4.300	1.437	0.000	0.229
AKS01-20130803	Akumal	0.940	7.525	0.100	0.000	0.000	0.022	0.253	0.028	0.748	1.265	0.343	0.058	0.001	66.859	0.010	1.770	0.008	0.171	28.267	2.948	75.020	0.000	0.010
AKS02-20130803	Akumal	1.670	7.893	0.096	0.000	0.000	0.042	0.338	0.026	1.162	1.452	0.348	0.083	0.000	60.355	0.017	1.685	0.003	0.154	27.005	2.267	63.423	0.000	0.014
AKS03-20130803	Akumal	2.140	8.320	0.058	0.000	0.000	0.082	0.282	0.042	1.248	0.788	0.325	0.097	0.000	47.481	0.027	2.573	0.000	0.174	14.151	2.362	45.749	0.000	0.008
AKS04-20130803	Akumal	2.480	15.844	0.097	0.000	0.000	0.396	0.366	0.031	2.408	1.517	0.357	0.154	0.000	63.529	0.020	3.841	0.000	0.178	24.698	10.354	64.365	0.000	0.019
AKS05-20130803	Akumal	1.350	7.365	0.105	0.000	0.000	0.043	0.309	0.048	1.343	1.136	0.318	0.106	0.000	62.428	0.036	2.312	0.003	0.173	24.602	2.322	81.358	0.000	0.013
SAS2S07-20130804-01	Tulum	1.000	605.183	0.239	0.000	0.002	0.157	0.521	0.032	51.475	12.227	1.249	1.220	0.080	18.852	0.000	1.240	0.011	0.283	30.785	276.073	11.386	0.000	0.201
SAS2S07-20130804-02	Tulum	2.300	54.824	0.146	0.000	0.001	0.051	0.248	0.022	5.273	1.092	0.444	0.335	0.000	11.215	0.010	0.796	0.007	0.153	18.240	19.449	10.895	0.000	0.025
SAS2S07-20130804-03	Tulum	3.200	26.313	0.086	0.000	0.000	0.049	0.240	0.027	2.912	0.885	0.336	0.142	0.000	11.207	0.011	1.387	0.001	0.233	7.679	8.315	10.638	0.000	0.026
SAS2S07-20130804-04	Tulum	3.000	11.788	0.068	0.000	0.000	0.058	0.269	0.028	1.742	0.685	0.327	0.131	0.000	15.949	0.015	1.862	0.001	0.285	4.738	2.668	12.433	0.000	0.040
SAS2S07-20130804-05	Tulum	3.800	9.042	0.042	0.000	0.000	0.022	0.225	0.028	1.062	0.232	0.310	0.163	0.000	5.295	0.012	2.798	0.004	0.236	0.000	0.986	9.036	0.000	0.015
SAS2S07-20130804-06	Tulum	4.500	18.375	0.029	0.000	0.000	0.130	0.181	0.026	0.922	0.500	0.349	0.057	0.000	7.345	0.028	0.253	0.000	0.290	0.000	4.150	13.646	0.000	0.012
PMS11-20130805B	Puerto Morelos	0.000	69.782	0.193	0.000	0.000	0.486	0.311	0.061	3.385	1.783	0.349	0.279	0.000	65.618	0.016	1.523	0.000	0.283	11.271	19.720	26.575	0.001	0.039
PMS12-20130805A	Puerto Morelos	0.000	63.916	0.375	0.000	0.001	0.078	0.249	0.039	3.592	1.711	0.399	0.850	0.000	16.195	0.009	2.241	0.004	0.219	33.330	16.596	40.695	0.000	0.032
PMS12-20130805B	Puerto Morelos	0.000	369.283	0.392	0.000	0.001	0.038	0.417	0.038	15.469	3.830	0.618	1.444	0.030	35.669	0.000	1.396	0.007	0.302	24.480	115.403	29.830	0.000	0.067
SCH01-20130907	José M Morelos	0.000	11.323	0.098	0.000	0.003	0.016	0.112	0.037	0.990	0.431	0.280	0.066	0.000	2.044	0.016	0.151	0.004	0.235	8.354	3.527	1.930	0.000	0.263
SCH02-20130907	José M Morelos	0.000	10.704	0.095	0.000	0.004	0.026	0.114	0.035	0.666	0.342	0.276	0.083	0.000	2.144	0.013	0.156	0.005	0.295	16.673	4.161	1.909	0.000	0.134
SG2A-20131211-0.0	Ruta de Cenotes	0.000	38.382	0.099	0.000	0.004	0.025	0.151	0.006	5.033	1.145	0.472	0.389	0.009	5.799	0.035	2.157	0.005	0.000	5.680	33.583	8.824	0.000	0.036
SG2C-20131211-0.0	Ruta de Cenotes	0.000	3.337	0.065	0.000	0.002	0.019	0.091	0.012	1.097	0.274	0.365	0.119	0.000	9.024	0.014	1.583	0.005	0.000	2.855	1.306	6.657	0.000	0.019
SG2E-20131211-0.0	Ruta de Cenotes	0.000	9.160	0.062	0.000	0.001	0.014	0.111	0.009	1.906	0.635	0.380	0.087	0.003	6.445	0.018	0.936	0.006	0.000	2.050	6.796	14.914	0.000	0.015
SG2F-20131211-0.0	Ruta de Cenotes	0.000	39.533	0.108	0.000	0.000	0.041	0.169	0.005	4.083	1.405	0.633	0.254	0.010	14.018	0.059	0.635	0.006	0.000	9.498	35.958	11.091	0.000	0.049
SG3A-20131212-0.0	Ruta de Cenotes	0.000	11.168	0.081	0.000	0.000	0.070	0.036	0.006	1.227	1.728	0.389	0.108	0.000	159.014	0.019	0.670	0.000	0.000	52.884	4.709	90.617	0.000	0.010
SG3B-20131212	Ruta de Cenotes	0.000	22.486	0.223	0.000	0.000	0.022	0.118	0.006	2.704	1.219	0.443	0.098	0.007	23.406	0.008	1.059	0.008	0.000	19.510	18.556	38.554	0.000	0.015
SG3C-20131212-0.0	Ruta de Cenotes	0.000	81.386	0.163	0.000	0.001	0.010	0.145	0.005	13.378	4.073	0.594	0.622	0.024	33.666	0.000	1.526	0.006	0.000	16.791	85.539	42.273	0.000	0.039
SG3D-20131212	Ruta de Cenotes	0.000	10.940	0.097	0.000	0.000	0.022	0.060	0.011	1.168	0.830	0.380	0.051	0.000	43.490	0.008	1.448	0.006	0.000	18.095	1.474	63.651	0.000	0.012
SG3E-20131212-0.0	Ruta de Cenotes	0.000	7.830	0.178	0.000	0.000	0.034	0.085	0.008	1.661	0.598	0.395	0.288	0.000	20.964	0.007	0.839	0.001	0.000	15.532	4.699	25.106	0.000	0.011
SG4A-20131213-0.0	Playa del Carmen	0.000	2.653	0.093	0.000	0.000	0.014	0.078	0.013	0.978	0.405	0.398	0.093	0.000	9.526	0.009	0.525	0.006	0.000	8.529	1.452	12.023	0.000	0.010
SG4B-20131213-0.0	Playa del Carmen	0.000	40.285	0.220	0.000	0.002	0.040	0.101	0.014	5.366	2.132	0.587	0.391	0.007	12.507	0.000	0.620	0.007	0.000	24.192	44.870	4.955	0.000	0.025
SG4C-20131214-0.0	Playa del Carmen	0.000	2.507	0.153	0.000	0.000	0.014	0.075	0.016	0.244	1.016	0.379	0.025	0.000	61.471	0.011	2.208	0.007	0.000	19.407	0.762	82.782	0.002	0.007

ID	LOCATION	DEPTH (m)	Al	Ba	Be	Cd	Co	Cr	Cu	Fe	K	Li	Mn	Mo	Na	Ni	P	Pb	Rb	S	Si	Sr	Tl	V		
SG4D-20131214-0.0	Playa del Carmen	0.000	2.236	0.127	0.000	0.000	0.042	0.057	0.016	0.566	1.471	0.398	0.127	0.000	71.639	0.013	2.875	0.007	0.000	22.263	0.876	93.171	0.000	0.007		
SG4E-20131214-0.0	Playa del Carmen	0.000	7.179	0.189	0.000	0.000	0.025	0.044	0.015	1.000	0.802	0.446	0.036	0.000	28.511	0.007	2.140	0.004	0.000	19.240	5.265	50.236	0.001	0.017		
SG4F-20131214-0.0	Playa del Carmen	0.000	25.107	0.152	0.000	0.000	0.018	0.113	0.013	3.502	1.817	0.458	0.257	0.000	18.757	0.000	0.867	0.009	0.000	17.097	30.647	25.427	0.000	0.026		
SG4G-20131214-0.0	Playa del Carmen	0.000	11.544	0.144	0.000	0.001	0.031	0.168	0.012	3.391	0.834	0.422	0.310	0.000	11.484	0.001	1.121	0.002	0.000	13.307	10.709	10.451	0.004	0.035		
SG4H-20131214-0.0	Playa del Carmen	0.000	4.492	0.100	0.000	0.000	0.004	0.092	0.016	2.149	0.383	0.362	0.142	0.000	11.993	0.009	1.190	0.009	0.000	9.760	1.908	12.267	0.000	0.018		
SG4H2-20131214-0.0	Playa del Carmen	0.000	12.330	0.085	0.000	0.001	0.023	0.115	0.013	3.256	0.852	0.415	0.281	0.003	10.578	0.017	1.564	0.003	0.000	13.993	9.238	11.702	0.001	0.019		
SG4I-20131214-0.0	Playa del Carmen	0.000	47.415	0.125	0.000	0.001	0.063	0.136	0.014	6.330	2.026	0.574	0.194	0.008	12.205	0.000	1.647	0.007	0.000	12.969	50.885	13.577	0.000	0.023		
SAS04-20140626-A	Solferino	0.000	7.583	0.042	0.000	0.001	0.061	0.279	0.018	2.385	3.254	0.398	1.687	0.000	57.582	0.025	6.586	0.002	0.000	32.793	4.448	3.112	0.000	0.116		
SAS04-20140626-B	Solferino	0.000	11.120	0.044	0.000	0.001	0.053	0.193	0.019	2.800	1.028	0.406	1.593	0.000	19.465	0.016	6.599	0.003	0.000	22.178	4.876	2.803	0.000	0.115		
SAS04-20140626-C	Solferino	0.000	6.920	0.041	0.000	0.000	0.022	0.108	0.029	1.511	0.495	0.425	1.062	0.000	7.352	0.032	4.916	0.006	0.000	8.752	1.968	1.436	0.000	0.055		
SAS04-20140626-D	Solferino	0.000	20.343	0.074	0.000	0.000	0.060	0.359	0.025	3.890	1.466	0.478	1.415	0.000	15.631	0.036	5.352	0.000	0.000	16.899	15.065	2.543	0.000	0.122		
SAS04-20140626-E	Solferino	0.000	11.596	0.065	0.000	0.000	0.045	0.271	0.014	4.174	2.361	0.437	1.573	0.000	29.384	0.034	5.034	0.004	0.000	18.191	7.288	2.755	0.000	0.118		
SAS04-20140626-F	Solferino	0.000	15.633	0.058	0.000	0.001	0.148	0.201	0.019	4.738	3.852	0.452	1.434	0.000	59.036	0.024	4.930	0.002	0.000	25.114	14.666	2.829	0.000	0.105		
SAS02-20140626-A	Tulum	0.000	9.555	0.102	0.000	0.000	0.041	0.090	0.008	3.094	1.195	0.424	0.128	0.000	92.840	0.004	0.953	0.004	0.000	23.028	12.505	14.212	0.000	0.014		
SAS02-20140626-B	Tulum	0.000	399.375	0.234	0.065	0.002	0.013	0.772	0.019	103.900	32.594	4.870	1.003	0.184	24.517	0.000	0.613	0.047	0.025	38.995	696.262	6.589	0.001	0.299		
SAS02-20140626-C	Tulum	0.000	306.128	0.215	0.000	0.002	0.010	0.364	0.017	66.698	30.084	2.345	0.805	0.115	8.945	0.000	0.098	0.053	0.000	10.700	505.943	5.021	0.000	0.194		
SAS02-20140626-DR	Tulum	0.000	292.700	0.417	0.048	0.002	0.030	0.392	0.015	75.777	28.566	2.770	0.887	0.113	13.099	0.000	0.452	0.041	0.000	11.137	494.031	10.799	0.000	0.249		
SAS02-20140626-DW	Tulum	0.000	42.346	0.141	0.000	0.001	0.039	0.135	0.011	8.255	2.856	0.606	0.515	0.005	12.889	0.000	0.854	0.010	0.000	19.865	47.197	11.277	0.000	0.036		
PAK-20140626		0.000	3.482	0.075	0.000	0.001	0.045	0.170	0.011	1.526	0.404	0.377	0.231	0.000	7.468	0.008	0.709	0.003	0.000	14.156	1.091	7.399	0.000	0.042		
<b>Vadose Mean</b>			<b>43.947</b>	<b>0.104</b>	<b>0.001</b>	<b>0.001</b>	<b>0.074</b>	<b>0.166</b>	<b>0.020</b>	<b>6.852</b>	<b>2.702</b>	<b>0.537</b>	<b>0.427</b>	<b>0.010</b>	<b>20.871</b>	<b>0.016</b>	<b>2.195</b>	<b>0.006</b>	<b>0.055</b>	<b>15.050</b>	<b>42.383</b>	<b>16.971</b>	<b>0.000</b>	<b>0.092</b>		
<b>Vadose Min</b>			<b>1.805</b>	<b>0.014</b>	<b>0.000</b>	<b>0.000</b>	<b>0.004</b>	<b>0.026</b>	<b>0.005</b>	<b>0.244</b>	<b>0.173</b>	<b>0.276</b>	<b>0.025</b>	<b>0.000</b>	<b>2.044</b>	<b>0.000</b>	<b>0.098</b>	<b>0.000</b>	<b>0.000</b>	<b>0.000</b>	<b>0.270</b>	<b>1.389</b>	<b>0.000</b>	<b>0.007</b>		
<b>Vadose Max</b>			<b>605.183</b>	<b>0.564</b>	<b>0.065</b>	<b>0.005</b>	<b>0.527</b>	<b>0.772</b>	<b>0.061</b>	<b>103.900</b>	<b>32.594</b>	<b>4.870</b>	<b>1.687</b>	<b>0.184</b>	<b>159.014</b>	<b>0.107</b>	<b>11.809</b>	<b>0.053</b>	<b>0.302</b>	<b>52.884</b>	<b>696.262</b>	<b>93.171</b>	<b>0.005</b>	<b>0.512</b>		
<b>Vadose StDev</b>			<b>99.510</b>	<b>0.099</b>	<b>0.009</b>	<b>0.001</b>	<b>0.116</b>	<b>0.127</b>	<b>0.012</b>	<b>16.787</b>	<b>5.878</b>	<b>0.622</b>	<b>0.431</b>	<b>0.029</b>	<b>26.137</b>	<b>0.017</b>	<b>2.577</b>	<b>0.009</b>	<b>0.097</b>	<b>10.694</b>	<b>114.105</b>	<b>23.446</b>	<b>0.001</b>	<b>0.103</b>		
<b>PHREATIC ZONE</b>																										
ZAP10-20110731-48.5	Puerto Morelos	48.5	5.873	0.182	0.000	0.000	0.947	0.041	0.006	0.963	1.434	0.365	0.334	0.000	26.526	0.020	15.026	0.000	0.000	18.091	3.772	4.995	0.000	0.064		
CARA-20110804-12.1	Aktun Ha	12.1	2.079	0.029	0.000	0.000	0.144	0.108	0.018	2.666	0.212	0.335	0.150	0.000	5.872	0.012	1.818	0.004	0.000	5.555	1.211	9.374	0.000	0.036		
CARB-20110804-13.6	Aktun Ha	13.6	6.348	0.025	0.000	0.000	0.065	0.112	0.022	3.778	0.399	0.333	0.448	0.000	4.505	0.023	2.817	0.002	0.000	1.991	4.660	13.067	0.000	0.041		
CARC-20110804-10.9	Aktun Ha	10.9	45.865	0.194	0.000	0.000	0.447	0.056	0.032	7.249	2.389	0.560	0.211	0.011	20.954	0.036	1.914	0.000	0.000	8.955	42.205	3.821	0.000	0.033		
CARD-20110804-13.5	Aktun Ha	13.5	14.230	0.146	0.000	0.000	0.320	0.042	0.037	2.131	0.877	0.379	0.241	0.003	15.659	0.025	1.641	0.000	0.000	5.983	9.355	3.270	0.000	0.019		
CARE-20110804-11.5	Aktun Ha	11.5	6.062	0.021	0.000	0.000	0.116	0.087	0.020	1.619	0.247	0.329	0.178	0.001	3.923	0.021	3.341	0.002	0.000	1.985	3.051	12.154	0.000	0.024		
CARF-20110804-17.0	Aktun Ha	1.7	6.914	0.051	0.000	0.000	0.117	0.173	0.037	13.104	2.395	0.351	0.182	0.000	7.346	0.037	2.414	0.000	0.000	10.262	2.073	14.551	0.000	0.107		
CARA-20110809-17.0	Aktun Ha	17.0	26.052	0.044	0.000	0.000	0.060	0.120	0.023	8.972	1.502	0.428	0.346	0.004	6.075	0.034	2.103	0.003	0.000	4.226	19.196	10.037	0.000	0.068		
CARB-20110809-16.1	Aktun Ha	16.1	6.184	0.066	0.000	0.001	0.077	0.110	0.019	4.762	0.379	0.351	0.333	0.000	6.047	0.013	2.632	0.005	0.000	7.679	3.331	12.562	0.000	0.072		
CARC-20110809-15.3	Aktun Ha	15.3	8.434	0.157	0.000	0.000	0.786	0.025	0.021	1.177	0.582	0.356	0.105	0.000	9.615	0.032	4.054	0.000	0.000	5.690	3.730	3.359	0.000	0.015		
CARD-20110809-14.1	Aktun Ha	14.1	41.040	0.039	0.000	0.000	0.369	0.130	0.027	9.454	2.075	0.471	0.310	0.005	6.051	0.037	1.838	0.001	0.000	3.360	27.553	9.557	0.000	0.048		
CARE-20110809-13.2	Aktun Ha	13.2	15.529	0.020	0.000	0.000	0.066	0.068	0.023	2.666	1.162	0.358	0.197	0.000	4.115	0.016	2.644	0.000	0.000	2.168	7.410	13.403	0.000	0.029		
CASA-20110809-3.3	Manati	3.3	8.960	0.105	0.000	0.000	0.144	0.061	0.032	2.302	1.435	0.379	0.186	0.000	70.972	0.033	2.734	0.000	0.000	23.799	4.681	35.385	0.000	0.031		
CASB-20110809-2.9	Manati	2.9	5.081	0.210	0.000	0.000	0.271	0.008	0.023	1.115	0.907	0.381	0.443	0.000	27.816	0.028	2.351	0.000	0.000	12.300	3.108	18.580	0.000	0.019		
CASC-20110809-4.1	Manati	4.1	5.855	0.185	0.000	0.000	0.094	0.111	0.023	1.561	0.836	0.418	0.196	0.000	48.077	0.029	2.716	0.000	0.000	34.936	2.155	37.335	0.000	0.029		
CASD-20110809-3.9	Manati	3.9	33.664	0.024	0.000	0.000	0.588	0.027	0.033	6.200	2.665	0.354	0.484	0.003	56.266	0.106	5.015	0.000	0.000	4.674	16.227	15.860	0.000	0.048		
CASE-20110809-4.4	Manati	4.4	18.310	0.150	0.000	0.000	0.127	0.178	0.022	10.141	1.312	0.406	0.396	0.000	47.650	0.029	4.112	0.000	0.000	34.541	2.964	31.764	0.000	0.088		

ID	LOCATION	DEPTH (m)	Al	Ba	Be	Cd	Co	Cr	Cu	Fe	K	Li	Mn	Mo	Na	Ni	P	Pb	Rb	S	Si	Sr	Tl	V
CASF-20110809-6.3	Manati	6.3	4.037	0.038	0.000	0.000	0.043	0.120	0.035	0.542	1.022	0.337	0.222	0.000	40.649	0.021	3.464	0.003	0.000	9.119	1.614	20.172	0.000	0.012
CASG-20110809-7.6	Manati	7.6	6.740	0.043	0.000	0.000	0.085	0.108	0.033	0.622	1.701	0.349	0.210	0.000	69.460	0.027	3.401	0.002	0.000	15.428	2.177	21.782	0.000	0.013
EDEC-20110810-8.1	Ponderosa	8.1	2.699	0.018	0.000	0.000	0.169	0.040	0.023	0.465	0.562	0.330	0.191	0.000	19.278	0.019	2.407	0.002	0.000	3.264	0.483	11.694	0.000	0.032
EDED-20110810-9.7	Ponderosa	9.7	2.204	0.016	0.000	0.000	0.211	0.046	0.024	0.724	0.542	0.331	0.180	0.000	18.906	0.009	2.023	0.003	0.000	3.746	0.294	13.738	0.000	0.048
EDEA-20110810-10.7	Ponderosa	10.7	3.238	0.033	0.000	0.000	0.071	0.046	0.016	0.374	0.520	0.335	0.247	0.000	19.124	0.012	3.473	0.001	0.000	4.236	0.424	8.476	0.000	0.015
EDEB-20110810-11.2	Ponderosa	11.2	2.846	0.024	0.000	0.000	0.071	0.041	0.026	0.488	0.960	0.326	0.234	0.000	20.624	0.012	2.943	0.003	0.000	3.800	0.444	9.702	0.000	0.022
EDEE-20110810-12.8	Ponderosa	12.8	1.695	0.014	0.000	0.000	0.048	0.024	0.023	0.513	0.375	0.318	0.174	0.000	14.708	0.010	2.437	0.003	0.000	3.046	0.311	10.215	0.000	0.017
EDEF-20110810-13.2	Ponderosa	13.2	4.538	0.038	0.000	0.001	0.103	0.051	0.046	0.667	0.762	0.357	0.296	0.000	28.075	0.020	5.067	0.003	0.000	4.951	0.641	7.910	0.000	0.019
EDEA-20111209-16.9	Ponderosa	16.9	4.289	0.022	0.000	0.000	0.057	0.075	0.029	0.704	1.045	0.340	0.227	0.000	38.602	0.023	5.318	0.000	0.000	4.842	0.750	6.478	0.000	0.014
EDEB-20111209-17.4	Ponderosa	17.4	34.596	0.065	0.000	0.000	0.033	0.015	0.037	4.466	1.609	0.388	0.078	0.000	22.259	0.046	1.729	0.000	0.000	6.308	11.668	14.326	0.000	0.041
EDEC-20111209-13.5	Ponderosa	13.5	2.554	0.023	0.000	0.000	0.041	0.040	0.022	0.701	0.562	0.326	0.303	0.000	19.081	0.020	5.796	0.000	0.000	3.799	0.566	9.130	0.000	0.013
EDED-20111209-5.2	Ponderosa	5.2	10.781	0.024	0.000	0.000	0.036	0.054	0.029	1.603	0.560	0.361	0.236	0.000	10.016	0.021	2.550	0.001	0.000	3.842	3.723	9.883	0.000	0.030
EDEE-20111209-3.1	Ponderosa	3.1	20.205	0.100	0.000	0.000	0.093	0.003	0.033	0.576	0.359	0.340	0.874	0.000	11.960	0.015	1.172	0.000	0.000	6.512	1.911	13.045	0.000	0.009
ANGA-20111210-30.2	Tulum	30.2	7.120	0.059	0.000	0.000	0.091	0.302	0.049	0.937	0.536	0.330	0.268	0.000	14.219	0.019	4.772	0.001	0.000	2.505	23.391	9.480	0.000	0.037
ANGB-20111210-29.3	Tulum	29.3	7.875	0.060	0.000	0.000	0.051	0.291	0.021	1.294	0.569	0.326	0.356	0.000	7.455	0.023	5.268	0.000	0.004	1.601	24.895	8.989	0.000	0.039
ANGC-20111210-27.8	Tulum	27.8	12.421	0.043	0.000	0.000	0.083	0.210	0.029	1.213	0.557	0.330	0.247	0.000	4.932	0.033	7.588	0.000	0.000	0.918	25.780	13.321	0.000	0.030
ANGD-20111210-24.3	Tulum	24.3	31.278	0.065	0.000	0.000	0.108	0.241	0.040	9.787	0.644	0.363	0.602	0.000	4.057	0.026	10.742	0.001	0.000	2.403	30.077	11.283	0.000	0.029
ANGE-20111210-20.9	Tulum	20.9	14.088	0.051	0.000	0.000	0.090	0.176	0.024	1.461	0.364	0.334	0.175	0.000	4.252	0.020	10.135	0.000	0.000	2.073	27.054	8.977	0.000	0.024
ANGF-20111210-17.6	Tulum	17.6	5.739	0.082	0.000	0.000	0.107	0.129	0.017	1.413	0.491	0.326	0.220	0.000	4.920	0.025	4.715	0.000	0.000	6.779	19.770	9.908	0.000	0.032
ANGG-20111210-15.4	Tulum	15.4	6.366	0.086	0.000	0.000	0.052	0.091	0.021	1.169	0.243	0.320	0.153	0.000	6.796	0.012	3.474	0.001	0.000	4.852	19.256	9.630	0.000	0.030
ANGH-20111210-10.8	Tulum	10.8	126.580	0.116	0.000	0.000	0.062	0.225	0.041	15.056	3.118	0.716	0.460	0.005	8.569	0.047	3.909	0.006	0.000	6.648	66.585	14.089	0.000	0.197
ANGI-20111210-12.0	Tulum	12.0	5.790	0.118	0.000	0.000	0.081	0.153	0.024	4.445	1.114	0.404	0.496	0.003	7.379	0.014	2.356	0.005	0.000	6.366	34.282	11.318	0.000	0.086
ANGJ-20111210-8.2	Tulum	8.2	7.569	0.081	0.000	0.000	0.049	0.184	0.022	4.021	0.695	0.390	0.160	0.001	7.341	0.024	2.467	0.005	0.000	6.773	27.376	13.154	0.003	0.090
ANGK-20111210-5.8	Tulum	5.8	3.491	0.069	0.000	0.000	0.088	0.135	0.008	0.948	0.296	0.307	0.083	0.000	5.888	0.014	5.774	0.005	0.000	2.734	22.532	9.942	0.000	0.021
ANGL-20111210-1.0	Tulum	1.0	7.146	0.208	0.000	0.000	0.079	0.262	0.018	1.455	0.433	0.325	0.064	0.000	12.013	0.017	4.337	0.005	0.000	19.613	25.351	8.295	0.002	0.039
SIBJ-20111211-0.0	Puerto Morelos	0.0	108.651	0.157	0.000	0.000	0.090	0.234	0.004	20.279	2.279	1.270	0.227	0.039	18.046	0.016	0.970	0.010	0.000	37.883	120.251	21.029	0.000	0.085
PITA-20111217-31.2	Dos Ojos	31.2	1.504	0.014	0.000	0.000	0.086	0.096	0.028	0.354	0.614	0.339	0.169	0.000	19.612	0.016	3.481	0.006	0.000	2.144	1.074	11.274	0.002	0.020
PITB-20111217-28.5	Dos Ojos	28.5	5.223	0.016	0.000	0.000	0.142	0.099	0.022	0.803	0.767	0.361	0.181	0.000	13.439	0.019	3.658	0.003	0.000	1.826	5.265	11.384	0.000	0.030
PITC-20111217-25.0	Dos Ojos	25.0	2.951	0.019	0.000	0.000	0.047	0.056	0.012	0.755	0.839	0.347	0.235	0.000	26.624	0.011	2.721	0.007	0.000	2.911	1.743	10.335	0.000	0.018
PITD-20111217-23.1	Dos Ojos	23.1	4.886	0.024	0.000	0.000	0.052	0.067	0.021	1.435	0.941	0.364	0.153	0.000	16.755	0.023	2.775	0.006	0.000	2.808	4.445	9.289	0.000	0.012
PITE-20111217-20.0	Dos Ojos	20.0	41.766	0.027	0.000	0.000	0.108	0.128	0.028	5.749	4.080	0.615	0.123	0.010	7.914	0.090	5.025	0.000	0.000	1.588	42.837	7.034	0.000	0.046
PITF-20111217-16.2	Dos Ojos	16.2	1.733	0.022	0.000	0.000	0.050	0.071	0.034	1.160	0.470	0.361	0.147	0.000	14.724	0.014	2.506	0.005	0.000	3.157	1.109	7.148	0.000	0.017
PITG-20111217-14.4	Dos Ojos	14.4	3.993	0.019	0.000	0.000	0.091	0.073	0.033	2.046	0.387	0.341	0.145	0.000	6.820	0.015	2.468	0.004	0.000	1.798	2.276	7.305	0.000	0.029
PITH-20111217-11.7	Dos Ojos	11.7	10.255	0.030	0.000	0.000	0.192	0.056	0.021	2.041	0.709	0.384	0.109	0.000	4.070	0.023	2.223	0.005	0.000	2.655	9.596	7.785	0.000	0.026
PITI-20111217-4.0	Dos Ojos	4.0	4.712	0.014	0.000	0.000	0.074	0.034	0.015	1.032	0.249	0.338	0.106	0.000	5.793	0.012	1.745	0.007	0.000	1.964	2.238	12.226	0.000	0.022
PITJ-20111217-0.0	Dos Ojos	0.0	2.877	0.078	0.000	0.000	0.075	0.081	0.013	1.024	0.352	0.404	0.073	0.000	12.324	0.010	1.252	0.004	0.000	10.912	1.094	13.554	0.000	0.009
CHIA-20111218-13.8	Ponderosa	13.8	3.876	0.011	0.000	0.000	0.257	0.052	0.012	0.524	0.660	0.334	0.117	0.000	22.169	0.020	4.124	0.002	0.000	2.656	0.419	5.536	0.000	0.011
CHIB-20111218-13.0	Ponderosa	13.0	4.436	0.014	0.000	0.000	0.068	0.061	0.008	0.368	0.381	0.344	0.203	0.000	11.652	0.021	2.409	0.001	0.000	1.073	0.400	7.813	0.000	0.010
CHIC-20111218-12.5	Ponderosa	12.5	2.495	0.013	0.000	0.000	0.216	0.068	0.015	0.423	0.260	0.327	0.270	0.000	6.928	0.029	2.839	0.000	0.000	0.713	0.458	12.298	0.000	0.013
CHID-20111218-12.3	Ponderosa	12.3	3.636	0.029	0.000	0.000	0.045	0.080	0.008	0.546	0.421	0.349	0.200	0.000	13.399	0.019	2.234	0.002	0.000	3.157	0.545	8.466	0.001	0.012
CHIE-20111218-11.6	Ponderosa	11.6	7.945	0.027	0.000	0.000	0.048	0.089	0.021	0.668	0.569	0.338	0.396	0.000	18.246	0.020	2.335	0.000	0.000	2.383	0.879	9.075	0.000	0.010

ID	LOCATION	DEPTH (m)	Al	Ba	Be	Cd	Co	Cr	Cu	Fe	K	Li	Mn	Mo	Na	Ni	P	Pb	Rb	S	Si	Sr	Tl	V
CHIF-20111218-10.4	Ponderosa	10.4	7.686	0.074	0.000	0.000	0.036	0.093	0.022	1.024	0.536	0.340	0.541	0.000	5.190	0.030	3.618	0.001	0.000	1.038	20.418	19.881	0.000	0.019
CHIG-20111218-8.8	Ponderosa	8.8	7.535	0.022	0.000	0.000	0.029	0.072	0.013	1.264	0.587	0.344	0.823	0.000	4.710	0.026	3.581	0.002	0.000	1.074	4.369	14.992	0.000	0.014
CHIH-20111218-7.0	Ponderosa	7.0	10.088	0.035	0.000	0.000	0.049	0.150	0.022	1.237	0.743	0.391	0.279	0.001	10.855	0.031	4.768	0.000	0.000	3.020	8.176	10.971	0.000	0.020
EDENS06A-20130804-1.4	Edén	1.4	5.290	0.117	0.000	0.000	0.024	0.253	0.033	0.674	0.771	0.326	0.046	0.000	64.461	0.024	2.494	0.002	0.215	23.124	0.750	64.930	0.000	0.008
EDENS06B-20130804-1.5	Edén	1.5	7.968	0.097	0.000	0.000	0.068	0.229	0.029	0.611	0.869	0.380	0.066	0.000	67.781	0.046	5.425	0.000	0.182	20.155	1.064	62.096	0.000	0.016
EDENS06C-20130804-1.8	Edén	1.8	7.553	0.105	0.000	0.000	0.055	0.284	0.032	0.607	5.327	0.404	0.084	0.000	96.166	0.020	5.181	0.001	0.163	27.141	3.232	68.206	0.000	0.024
EDENS06D-20130804-0.4	Edén	0.4	10.052	0.108	0.000	0.000	0.038	0.262	0.023	0.804	0.732	0.330	0.056	0.000	63.839	0.010	2.324	0.003	0.244	24.142	1.229	70.049	0.000	0.013
NHAA-20131202-6.2	Tulum	6.2	8.397	0.123	0.000	0.000	0.038	0.116	0.034	0.833	0.401	0.284	0.480	0.000	11.909	0.010	1.338	0.005	0.234	0.000	1.728	8.040	0.000	0.011
NHAB-20131202-4.5	Tulum	4.5	51.014	0.111	0.000	0.000	0.072	0.136	0.032	2.803	0.988	0.351	0.202	0.000	13.117	0.021	2.107	0.004	0.251	0.000	12.342	9.276	0.000	0.034
NHAC-20131202-3.5	Tulum	3.5	24.156	0.109	0.000	0.000	0.048	0.125	0.037	1.447	0.332	0.298	0.097	0.000	9.033	0.015	1.040	0.003	0.261	0.000	1.930	8.493	0.000	0.026
NHAD-20131202-2.6	Tulum	2.6	22.851	0.120	0.000	0.000	0.050	0.139	0.039	2.742	0.338	0.316	0.187	0.000	11.007	0.018	1.268	0.006	0.204	2.709	3.090	12.425	0.000	0.027
NHAE-20131202-2.1	Tulum	2.1	154.777	0.121	0.000	0.000	0.059	0.154	0.050	5.607	2.919	0.475	0.137	0.007	13.204	0.036	1.275	0.006	0.232	0.456	47.111	7.176	0.000	0.034
JAH01-20131204-0.0	Tulum	0.0	111.625	0.191	0.000	0.000	0.032	0.172	0.036	4.209	2.522	0.398	0.146	0.001	56.111	0.003	0.945	0.001	0.247	18.647	33.103	53.762	0.000	0.033
JAH02-20131204-0.0	Tulum	0.0	15.778	0.283	0.000	0.000	0.134	0.126	0.002	4.043	1.474	0.407	0.208	0.009	44.775	0.016	1.068	0.000	0.000	27.265	14.771	47.907	0.000	0.034
JAHA-20131204-21.1	Tulum	21.1	4.189	0.122	0.000	0.000	0.068	0.143	0.012	1.777	1.251	0.453	0.148	0.001	39.544	0.020	1.733	0.000	0.000	8.157	4.430	9.991	0.000	0.023
JAHB-20131204-21.6	Tulum	21.6	4.559	0.103	0.000	0.000	0.069	0.106	0.010	1.406	1.015	0.430	0.132	0.000	22.096	0.017	1.457	0.002	0.000	4.154	3.633	10.875	0.000	0.016
JAHC-20131204-18.1	Tulum	18.1	3.406	0.107	0.000	0.000	0.058	0.121	0.011	2.202	1.172	0.347	0.177	0.002	36.253	0.020	1.937	0.004	0.000	5.551	2.433	11.316	0.000	0.023
JAHD-20131204-3.2	Tulum	3.2	4.953	0.152	0.000	0.000	0.380	0.152	0.014	2.011	1.038	0.404	0.176	0.000	61.506	0.011	1.856	0.000	0.000	13.002	6.324	33.901	0.000	0.093
BNGA-20131205-20.2	Tulum	20.2	8.639	0.100	0.000	0.000	0.960	0.145	0.013	2.709	1.883	0.383	0.299	0.000	39.658	0.032	2.150	0.004	0.000	5.601	8.446	10.324	0.000	0.042
BNGB-20131205-19.5	Tulum	19.5	5.288	0.112	0.000	0.000	0.032	0.135	0.019	2.263	0.851	0.365	0.186	0.000	9.341	0.018	2.939	0.007	0.000	4.661	4.063	9.009	0.001	0.030
BNGC-20131205-18.3	Tulum	18.3	3.984	0.119	0.000	0.000	0.128	0.123	0.018	2.844	0.586	0.366	0.289	0.000	7.038	0.023	1.756	0.001	0.000	3.787	2.067	10.310	0.000	0.047
BNGD-20131205-14.6	Tulum	14.6	5.635	0.058	0.000	0.000	0.077	0.086	0.019	5.592	0.591	0.374	1.625	0.000	7.732	0.063	1.629	0.006	0.000	3.275	5.335	9.203	0.000	0.086
BNGE-20131205-3.0	Tulum	3.0	42.226	0.229	0.000	0.000	0.062	0.061	0.006	5.768	2.519	0.588	0.714	0.014	21.660	0.016	2.348	0.006	0.000	15.213	44.345	14.722	0.000	0.040
ODYB-20131207-12.1	Tulum	12.1	8.558	0.049	0.000	0.000	0.069	0.026	0.008	1.216	0.659	0.363	0.178	0.000	13.637	0.009	0.552	0.005	0.000	10.281	5.662	16.899	0.001	0.009
ODYC-20131207-7.2	Tulum	7.2	1.836	0.038	0.000	0.000	0.056	0.028	0.000	0.215	0.402	0.325	0.073	0.000	12.089	0.010	1.024	0.001	0.000	1.982	0.224	8.141	0.000	0.009
ODYD-20131207-12.8	Tulum	12.8	2.834	0.042	0.000	0.000	0.189	0.087	0.002	1.265	1.013	0.363	0.160	0.000	31.349	0.017	2.397	0.000	0.000	4.092	1.591	9.083	0.000	0.028
ODYE-20131207-13.3	Tulum	13.3	1.481	0.049	0.000	0.000	0.088	0.090	0.012	0.760	0.860	0.368	0.124	0.000	19.412	0.014	2.054	0.004	0.000	2.965	1.122	7.457	0.000	0.021
ODYF-20131207-2.6	Tulum	2.6	1.464	0.051	0.000	0.000	0.095	0.059	0.005	0.753	0.619	0.360	0.163	0.000	18.268	0.013	1.478	0.005	0.000	3.350	0.626	11.575	0.000	0.023
TABA-20131208-4.8	Tulum	4.8	12.123	0.106	0.000	0.000	0.026	0.050	0.012	3.660	2.459	0.427	0.236	0.002	15.084	0.021	2.466	0.004	0.000	8.940	16.255	19.913	0.000	0.031
TABB-20131208-5.8	Tulum	5.8	9.198	0.074	0.000	0.000	0.055	0.085	0.016	2.666	1.827	0.407	0.508	0.000	14.504	0.034	4.162	0.007	0.000	16.867	12.016	10.694	0.000	0.026
TABC-20131208-8.2	Tulum	8.2	1.218	0.047	0.000	0.000	0.065	0.011	0.004	0.284	0.787	0.330	0.082	0.000	19.192	0.014	0.883	0.003	0.000	2.315	0.425	13.939	0.000	0.012
TABD-20131208-5.3	Tulum	5.3	85.252	0.072	0.000	0.001	0.036	0.146	0.017	19.924	7.075	1.027	0.995	0.026	11.859	0.030	5.173	0.010	0.000	2.525	114.787	13.643	0.000	0.084
<b>Phreatic Mean</b>			<b>16.166</b>	<b>0.077</b>	<b>0.000</b>	<b>0.000</b>	<b>0.129</b>	<b>0.109</b>	<b>0.022</b>	<b>2.888</b>	<b>1.106</b>	<b>0.389</b>	<b>0.306</b>	<b>0.002</b>	<b>20.877</b>	<b>0.023</b>	<b>3.152</b>	<b>0.003</b>	<b>0.025</b>	<b>7.416</b>	<b>12.331</b>	<b>15.386</b>	<b>0.000</b>	<b>0.034</b>
<b>Phreatic Min</b>			<b>1.218</b>	<b>0.011</b>	<b>0.000</b>	<b>0.000</b>	<b>0.024</b>	<b>0.003</b>	<b>0.000</b>	<b>0.215</b>	<b>0.212</b>	<b>0.284</b>	<b>0.046</b>	<b>0.000</b>	<b>3.923</b>	<b>0.003</b>	<b>0.552</b>	<b>0.000</b>	<b>0.000</b>	<b>0.000</b>	<b>0.224</b>	<b>3.270</b>	<b>0.000</b>	<b>0.008</b>
<b>Phreatic Max</b>			<b>154.777</b>	<b>0.283</b>	<b>0.000</b>	<b>0.001</b>	<b>0.960</b>	<b>0.302</b>	<b>0.050</b>	<b>20.279</b>	<b>7.075</b>	<b>1.270</b>	<b>4.084</b>	<b>0.039</b>	<b>96.166</b>	<b>0.106</b>	<b>15.026</b>	<b>0.010</b>	<b>0.261</b>	<b>37.883</b>	<b>120.251</b>	<b>70.049</b>	<b>0.003</b>	<b>0.197</b>
<b>Phreatic Stdev</b>			<b>27.329</b>	<b>0.059</b>	<b>0.000</b>	<b>0.000</b>	<b>0.171</b>	<b>0.070</b>	<b>0.011</b>	<b>3.834</b>	<b>1.081</b>	<b>0.133</b>	<b>0.460</b>	<b>0.005</b>	<b>18.987</b>	<b>0.015</b>	<b>2.174</b>	<b>0.002</b>	<b>0.071</b>	<b>8.293</b>	<b>20.578</b>	<b>13.798</b>	<b>0.000</b>	<b>0.028</b>

Table VII-2 Information on geography, characteristics of sites, coordinates, and weight (mg) used in the multi-elemental quantification by ICP-OES analyzes for a selection of 185 samples. Depth means meters above ground for vadose sample rocks, and meters below water table for phreatic sample rocks.

#	ID	DATE COLLECTED	SITE	LOCATION	PLACE / NOTES	LAT	LON	ELEVATION/ DEPTH (m)	Weight (mg)
1	AKS01-20130803	03/Aug/13	Outcrop	Akumal	Quintana Roo	20.400	-87.322	0.9	100.9
2	AKS02-20130803	03/Aug/13	Outcrop	Akumal	Quintana Roo	20.400	-87.322	1.7	103.8
3	AKS03-20130803	03/Aug/13	Outcrop	Akumal	Quintana Roo	20.400	-87.322	2.1	104.5
4	AKS04-20130803	03/Aug/13	Outcrop	Akumal	Quintana Roo	20.400	-87.322	2.5	103.8
5	AKS05-20130803	03/Aug/13	Outcrop	Akumal	Quintana Roo	20.400	-87.322	1.4	102.5
6	ANGA-20111210-30.2	10/Dec/11	Angelita	Tulum	pit cenote	20.138	-87.578	30.2	111.08
7	ANGB-20111210-29.3	10/Dec/11	Angelita	Tulum	pit cenote	20.138	-87.578	29.3	102.14
8	ANGC-20111210-27.8	10/Dec/11	Angelita	Tulum	pit cenote	20.138	-87.578	27.8	107.95
9	ANGD-20111210-24.3	10/Dec/11	Angelita	Tulum	pit cenote	20.138	-87.578	24.3	111.57
10	ANGE-20111210-20.9	10/Dec/11	Angelita	Tulum	pit cenote	20.138	-87.578	20.9	99.70
11	ANGF-20111210-17.6	10/Dec/11	Angelita	Tulum	pit cenote	20.138	-87.578	17.6	111.46
12	ANGG-20111210-15.4	10/Dec/11	Angelita	Tulum	pit cenote	20.138	-87.578	15.4	106.53
13	ANGH-20111210-10.8	10/Dec/11	Angelita	Tulum	pit cenote	20.138	-87.578	10.8	106.46
14	ANGI-20111210-12.0	10/Dec/11	Angelita	Tulum	pit cenote	20.138	-87.578	12.0	106.38
15	ANGJ-20111210-8.2	10/Dec/11	Angelita	Tulum	pit cenote	20.138	-87.578	8.2	106.30
16	ANGK-20111210-5.8	10/Dec/11	Angelita	Tulum	pit cenote	20.138	-87.578	5.8	106.23
17	ANGL-20111210-1.0	10/Dec/11	Angelita	Tulum	pit cenote	20.138	-87.578	1.0	106.15
18	BNGA-20131205-20.2	05/Dec/13	Bang	Tulum	Quintana Roo	20.210	-87.501	20.2	104.75
19	BNGB-20131205-19.5	05/Dec/13	Bang	Tulum	Quintana Roo	20.210	-87.501	19.5	103.48
20	BNGC-20131205-18.3	05/Dec/13	Bang	Tulum	Quintana Roo	20.210	-87.501	18.3	103.61
21	BNGD-20131205-14.6	05/Dec/13	Bang	Tulum	Quintana Roo	20.210	-87.501	14.6	110.69
22	BNGE-20131205-3.0	05/Dec/13	Bang	Tulum	Quintana Roo	20.210	-87.501	3.0	101.91
23	CARA-20110804-12.1	04/Aug/11	Carwash	Aktun Ha	upstream	20.274	-87.486	12.1	103.90
24	CARA-20110809-17.0	09/Aug/11	Carwash	Aktun Ha	downstream	20.274	-87.486	17.0	104.40
25	CARB-20110804-13.6	04/Aug/11	Carwash	Aktun Ha	upstream	20.274	-87.486	13.6	129.50
26	CARB-20110809-16.1	09/Aug/11	Carwash	Aktun Ha	downstream	20.274	-87.486	16.1	119.90
27	CARC-20110804-10.9	04/Aug/11	Carwash	Aktun Ha	upstream	20.274	-87.486	10.9	101.20
28	CARC-20110809-15.3	09/Aug/11	Carwash	Aktun Ha	downstream	20.274	-87.486	15.3	104.90
29	CARD-20110804-13.5	04/Aug/11	Carwash	Aktun Ha	upstream	20.274	-87.486	13.5	106.70
30	CARD-20110809-14.1	09/Aug/11	Carwash	Aktun Ha	downstream	20.274	-87.486	14.1	110.30
31	CARE-20110804-11.5	04/Aug/11	Carwash	Aktun Ha	upstream	20.274	-87.486	11.5	106.00
32	CARE-20110809-13.2	09/Aug/11	Carwash	Aktun Ha	downstream	20.274	-87.486	13.2	103.80
33	CARF-20110804-17.0	04/Aug/11	Carwash	Aktun Ha	upstream	20.274	-87.486	17.0	119.30
34	CASA-20110809-3.3	09/Aug/11	Casa Cenote	Manati	upstream	20.266	-87.391	3.3	102.50
35	CASB-20110809-2.9	09/Aug/11	Casa Cenote	Manati	upstream	20.266	-87.391	2.9	105.80
36	CASC-20110809-4.1	09/Aug/11	Casa Cenote	Manati	upstream	20.266	-87.391	4.1	120.40
37	CASD-20110809-3.9	09/Aug/11	Casa Cenote	Manati	upstream	20.266	-87.391	3.9	103.60
38	CASE-20110809-4.4	09/Aug/11	Casa Cenote	Manati	upstream	20.266	-87.391	4.4	105.10
39	CASF-20110809-6.3	09/Aug/11	Casa Cenote	Manati	upstream	20.266	-87.391	6.3	119.10
40	CASG-20110809-7.6	09/Aug/11	Casa Cenote	Manati	upstream	20.266	-87.391	7.6	104.60
41	CHIA-20111218-13.8	18/Dec/11	Chikin Ha	Ponderosa	Carretera 307	20.500	-87.261	13.8	112.30
42	CHIB-20111218-13.0	18/Dec/11	Chikin Ha	Ponderosa	Carretera 307	20.500	-87.261	13.0	103.70

#	ID	DATE COLLECTED	SITE	LOCATION	PLACE / NOTES	LAT	LON	ELEVATION/ DEPTH (m)	Weight (mg)
43	CHIC-20111218-12.5	18/Dec/11	Chikin Ha	Ponderosa	Carretera 307	20.500	-87.261	12.5	104.50
44	CHID-20111218-12.3	18/Dec/11	Chikin Ha	Ponderosa	Carretera 307	20.500	-87.261	12.3	104.00
45	CHIE-20111218-11.6	18/Dec/11	Chikin Ha	Ponderosa	Carretera 307	20.500	-87.261	11.6	101.80
46	CHIF-20111218-10.4	18/Dec/11	Chikin Ha	Ponderosa	Carretera 307	20.500	-87.261	10.4	107.30
47	CHIG-20111218-8.8	18/Dec/11	Chikin Ha	Ponderosa	Carretera 307	20.500	-87.261	8.8	108.80
48	CHIH-20111218-7.0	18/Dec/11	Chikin Ha	Ponderosa	Carretera 307	20.500	-87.261	7.0	108.20
49	EDEA-20110810-10.7	10/Aug/11	El Eden	Ponderosa	downstream	20.492	-87.255	10.7	110.60
50	EDEA-20111209-16.9	09/Dec/11	El Eden	Ponderosa	downstream	20.492	-87.255	16.9	107.10
51	EDEB-20110810-11.2	10/Aug/11	El Eden	Ponderosa	downstream	20.492	-87.255	11.2	104.80
52	EDEB-20111209-17.4	09/Dec/11	El Eden	Ponderosa	downstream	20.492	-87.255	17.4	108.50
53	EDEC-20110810-8.1	10/Aug/11	El Eden	Ponderosa	downstream	20.492	-87.255	8.1	105.70
54	EDEC-20111209-13.5	09/Dec/11	El Eden	Ponderosa	downstream	20.492	-87.255	13.5	103.60
55	EDED-20110810-9.7	10/Aug/11	El Eden	Ponderosa	downstream	20.492	-87.255	9.7	102.00
56	EDED-20111209-5.2	09/Dec/11	El Eden	Ponderosa	downstream	20.492	-87.255	5.2	112.10
57	EDEE-20110810-12.8	10/Aug/11	El Eden	Ponderosa	downstream	20.492	-87.255	12.8	125.90
58	EDEF-20111209-3.1	09/Dec/11	El Eden	Ponderosa	downstream	20.492	-87.255	3.1	104.20
59	EDEF-20110810-13.2	10/Aug/11	El Eden	Ponderosa	downstream	20.492	-87.255	13.2	107.40
60	EDENS06A-20130804-1.4	04/Aug/13	Entrance	Edén	Quintana Roo	20.489	-87.250	1.4	101.30
61	EDENS06B-20130804-1.5	04/Aug/13	Entrance	Edén	Quintana Roo	20.489	-87.250	1.5	102.90
62	EDENS06C-20130804-1.8	04/Aug/13	Entrance	Edén	Quintana Roo	20.489	-87.250	1.8	109.40
63	EDENS06D-20130804-0.4	04/Aug/13	Entrance	Edén	Quintana Roo	20.489	-87.250	0.4	104.10
64	JAH01-20131204-0.0	04/Dec/13	Jailhouse	Tulum	Quintana Roo	20.188	-87.490	0.0	102.18
65	JAH02-20131204-0.0	04/Dec/13	Jailhouse	Tulum	Quintana Roo	20.188	-87.490	0.0	101.75
66	JAHA-20131204-21.1	04/Dec/13	Jailhouse	Tulum	Quintana Roo	20.188	-87.490	21.1	102.93
67	JAHB-20131204-21.6	04/Dec/13	Jailhouse	Tulum	Quintana Roo	20.188	-87.490	21.6	101.33
68	JAHC-20131204-18.1	04/Dec/13	Jailhouse	Tulum	Quintana Roo	20.188	-87.490	18.1	105.32
69	JAHD-20131204-3.2	04/Dec/13	Jailhouse	Tulum	Quintana Roo	20.188	-87.490	3.2	102.13
70	KNKB-20110801-1.0	01/Aug/11	Kantunilkin	Yucatan	Road	21.182	-87.477	1.0	113.78
71	KNKF-20110801-1.7	01/Aug/11	Kantunilkin	Yucatan	Road	21.182	-87.477	1.7	102.65
72	KNKG-20110801-2.2	01/Aug/11	Kantunilkin	Yucatan	Road	21.182	-87.477	2.2	100.81
73	KNKH-20110801-2.7	01/Aug/11	Kantunilkin	Yucatan	Road	21.182	-87.477	2.7	106.94
74	KNKI-20110801-3.0	01/Aug/11	Kantunilkin	Yucatan	Road	21.182	-87.477	3.0	105.29
75	KNKJ-20110801-3.5	01/Aug/11	Kantunilkin	Yucatan	Road	21.182	-87.477	3.5	101.17
76	NHAA-20131202-6.2	02/Dec/13	Niete Ha	Tulum	Quintana Roo	20.323	-87.380	6.2	114.61
77	NHAB-20131202-4.5	02/Dec/13	Niete Ha	Tulum	Quintana Roo	20.323	-87.380	4.5	110.05
78	NHAC-20131202-3.5	02/Dec/13	Niete Ha	Tulum	Quintana Roo	20.323	-87.380	3.5	102.05
79	NHAD-20131202-2.6	02/Dec/13	Niete Ha	Tulum	Quintana Roo	20.323	-87.380	2.6	112.70
80	NHAE-20131202-2.1	02/Dec/13	Niete Ha	Tulum	Quintana Roo	20.323	-87.380	2.1	107.74
81	ODYB-20131207-12.1	07/Dec/13	Odissey	Tulum	Quintana Roo	20.173	-87.472	12.1	105.06
82	ODYC-20131207-7.2	07/Dec/13	Odissey	Tulum	Quintana Roo	20.173	-87.472	7.2	104.84
83	ODYD-20131207-12.8	07/Dec/13	Odissey	Tulum	Quintana Roo	20.173	-87.472	12.8	107.11
84	ODYE-20131207-13.3	07/Dec/13	Odissey	Tulum	Quintana Roo	20.173	-87.472	13.3	110.08
85	ODYF-20131207-2.6	07/Dec/13	Odissey	Tulum	Quintana Roo	20.173	-87.472	2.6	101.74
86	PAK-20140626	26/Jun/14	Paamul	Surface road		20.527	-87.199	0.0	104.11
87	PITA-20111217-31.2	17/Dec/11	The Pit	Dos Ojos	Carretera 307	20.323	-87.410	31.2	107.24
88	PITB-20111217-28.5	17/Dec/11	The Pit	Dos Ojos	Carretera 307	20.323	-87.410	28.5	106.41
89	PITC-20111217-25.0	17/Dec/11	The Pit	Dos Ojos	Carretera 307	20.323	-87.410	25.0	122.06

#	ID	DATE COLLECTED	SITE	LOCATION	PLACE / NOTES	LAT	LON	ELEVATION/ DEPTH (m)	Weight (mg)
90	PITD-20111217-23.1	17/Dec/11	The Pit	Dos Ojos	Carretera 307	20.323	-87.410	23.1	123.13
91	PITE-20111217-20.0	17/Dec/11	The Pit	Dos Ojos	Carretera 307	20.323	-87.410	20.0	134.36
92	PITF-20111217-16.2	17/Dec/11	The Pit	Dos Ojos	Carretera 307	20.323	-87.410	16.2	109.35
93	PITG-20111217-14.4	17/Dec/11	The Pit	Dos Ojos	Carretera 307	20.323	-87.410	14.4	102.86
94	PITH-20111217-11.7	17/Dec/11	The Pit	Dos Ojos	Carretera 307	20.323	-87.410	11.7	103.45
95	PITI-20111217-4.0	17/Dec/11	The Pit	Dos Ojos	Carretera 307	20.323	-87.410	4.0	104.16
96	PITJ-20111217-0.0	17/Dec/11	The Pit	Dos Ojos	Carretera 307	20.323	-87.410	0.0	111.85
97	PMS11-20130805B	05/Aug/13	Ruta de Cenotes	Puerto Morelos	Quintana Roo	20.851	-87.003	0.0	102.15
98	PMS12-20130805A	05/Aug/13	Ruta de Cenotes	Puerto Morelos	Quintana Roo	20.857	-86.952	0.0	123.35
99	PMS12-20130805B	05/Aug/13	Ruta de Cenotes	Puerto Morelos	Quintana Roo	20.857	-86.952	0.0	99.61
100	SAK01-20140316	16/Mar/14	Beach sand	Akumal	Akumal beach	20.396	-87.314	0.0	151.21
101	SAK02-20140316	16/Mar/14	Beach sand	Akumal	Akumal beach	20.396	-87.314	0.0	121.84
102	SAK03-20140316	16/Mar/14	Beach sand	Akumal	Akumal beach	20.396	-87.314	0.0	108.56
103	SAK04-20140316	16/Mar/14	Beach sand	Akumal	Akumal beach	20.396	-87.314	0.0	144.34
104	SAK05-20140316	16/Mar/14	Beach sand	Akumal	Akumal beach	20.396	-87.314	0.0	153.40
105	SAK06-20140316	16/Mar/14	Beach sand	Akumal	Akumal beach	20.396	-87.314	0.0	134.38
106	SAK07-20140316	16/Mar/14	Beach sand	Akumal	Akumal beach	20.396	-87.314	0.0	121.67
107	SAK08-20140316	16/Mar/14	Beach sand	Akumal	Akumal beach	20.396	-87.314	0.0	111.57
108	SAK09-20140316	16/Mar/14	Beach sand	Akumal	Akumal beach	20.396	-87.314	0.0	131.30
109	SAK10-20140316	16/Mar/14	Beach sand	Akumal	Akumal beach	20.396	-87.314	0.0	105.40
110	SAS02-20140626-A	26/Jun/14	Sascabera 2	Tulum	Quintana Roo	20.269	-87.411	0.0	110.71
111	SAS02-20140626-B	26/Jun/14	Sascabera 2	Tulum	Quintana Roo	20.269	-87.411	0.0	106.70
112	SAS02-20140626-DR	26/Jun/14	Sascabera 2	Tulum	Quintana Roo	20.269	-87.411	0.0	111.41
113	SAS02-20140626-DW	26/Jun/14	Sascabera 2	Tulum	Quintana Roo	20.269	-87.411	0.0	107.16
114	SAS03-01-20111212-2.0	12/Dec/11	Sascabera 3	Leona Vicario	Ruta de Cenotes	20.979	-87.190	2.0	104.97
115	SAS03-02-20111212-0.0	12/Dec/11	Sascabera 3	Leona Vicario	Ruta de Cenotes	20.979	-87.190	0.0	103.88
116	SAS03-03-20111212-5.5	12/Dec/11	Sascabera 3	Leona Vicario	Ruta de Cenotes	20.979	-87.190	5.5	105.69
117	SAS04-20111212-U3A	12/Dec/11	Sascabera 4	Solferino	Carretera 180	20.899	-87.548	0.0	122.10
118	SAS04-20111212-U3B	12/Dec/11	Sascabera 4	Solferino	Carretera 180	20.899	-87.548	0.0	112.50
119	SAS04-20111212-U4	12/Dec/11	Sascabera 4	Solferino	Carretera 180	20.899	-87.548	0.0	107.90
120	SAS04-20111212-U5A	12/Dec/11	Sascabera 4	Solferino	Carretera 180	20.899	-87.548	0.0	101.40
121	SAS04-20111212-U5B	12/Dec/11	Sascabera 4	Solferino	Carretera 180	20.899	-87.548	0.0	122.80
122	SAS04-20111212-U6	12/Dec/11	Sascabera 4	Solferino	Carretera 180	20.899	-87.548	0.0	104.80
123	SAS04-20140626-A	26/Jun/14	Sascabera 4	Solferino	Carretera 180	20.899	-87.548	0.0	107.97
124	SAS04-20140626-B	26/Jun/14	Sascabera 4	Solferino	Carretera 180	20.899	-87.548	0.0	101.50
125	SAS04-20140626-C	26/Jun/14	Sascabera 4	Solferino	Carretera 180	20.899	-87.548	0.0	109.51
126	SAS04-20140626-D	26/Jun/14	Sascabera 4	Solferino	Carretera 180	20.899	-87.548	0.0	102.31
127	SAS04-20140626-E	26/Jun/14	Sascabera 4	Solferino	Carretera 180	20.899	-87.548	0.0	108.45
128	SAS04-20140626-F	26/Jun/14	Sascabera 4	Solferino	Carretera 180	20.899	-87.548	0.0	104.23
129	SAS06-20111215-U2A-1.2	15/Dec/11	Sascabera 6	Kantunil Kin	Quintana Roo	21.073	-87.499	1.2	104.37
130	SAS06-20111215-U2B-2.0	15/Dec/11	Sascabera 6	Kantunil Kin	Quintana Roo	21.073	-87.499	2.0	102.07
131	SAS06-20111215-U3	15/Dec/11	Sascabera 6	Kantunil Kin	Quintana Roo	21.073	-87.499	3.0	112.32
132	SAS06-20111215-U4	15/Dec/11	Sascabera 6	Kantunil Kin	Quintana Roo	21.073	-87.499	4.0	105.44
133	SAS06-20111215-U5	15/Dec/11	Sascabera 6	Kantunil Kin	Quintana Roo	21.073	-87.499	5.0	102.43
134	SAS06-20111215-U6B	15/Dec/11	Sascabera 6	Kantunil Kin	Quintana Roo	21.073	-87.499	6.0	102.55
135	SAS06-20111215-U6C	15/Dec/11	Sascabera 6	Kantunil Kin	Quintana Roo	21.073	-87.499	7.0	109.46
136	SAS06-20111215-U6D	15/Dec/11	Sascabera 6	Kantunil Kin	Quintana Roo	21.073	-87.499	8.0	106.81

#	ID	DATE COLLECTED	SITE	LOCATION	PLACE / NOTES	LAT	LON	ELEVATION/ DEPTH (m)	Weight (mg)
137	SAS06-20111215-U6G	15/Dec/11	Sascabera 6	Kantunil Kin	Quintana Roo	21.073	-87.499	9.0	114.63
138	SAS2S07-20130804-01	04/Aug/13	Sascabera 2	Tulum	Quintana Roo	20.269	-87.411	1.0	114.70
139	SAS2S07-20130804-02	04/Aug/13	Sascabera 2	Tulum	Quintana Roo	20.269	-87.411	2.3	134.30
140	SAS2S07-20130804-03	04/Aug/13	Sascabera 2	Tulum	Quintana Roo	20.269	-87.411	3.2	110.70
141	SAS2S07-20130804-04	04/Aug/13	Sascabera 2	Tulum	Quintana Roo	20.269	-87.411	3.0	101.10
142	SAS2S07-20130804-05	04/Aug/13	Sascabera 2	Tulum	Quintana Roo	20.269	-87.411	3.8	113.20
143	SAS2S07-20130804-06	04/Aug/13	Sascabera 2	Tulum	Quintana Roo	20.269	-87.411	4.5	101.00
144	SAS8A-20130401	01/Apr/13	Sascabera 8	Valladolid	Yucatán	20.685	-88.052	1.0	103.07
145	SAS8B-20130401	01/Apr/13	Sascabera 8	Valladolid	Yucatán	20.685	-88.052	4.0	100.36
146	SAS8C-20130401	01/Apr/13	Sascabera 8	Valladolid	Yucatán	20.685	-88.052	0.0	104.33
147	SAS8D-20130401	01/Apr/13	Sascabera 8	Valladolid	Yucatán	20.685	-88.052	7.0	114.15
148	SCH01-20130907	07/Sep/13	Chunhuhub	José M Morelos	Quintana Roo	19.571	-88.594	0.0	104.08
149	SCH02-20130907	07/Sep/13	Chunhuhub	José M Morelos	Quintana Roo	19.571	-88.594	0.0	99.80
150	SG2A-20131211-0.0	11/Dec/13	Pozos	Ruta de Cenotes	Puerto Morelos	20.914	-87.131	0.0	110.99
151	SG2C-20131211-0.0	11/Dec/13	Pozos	Ruta de Cenotes	Puerto Morelos	20.933	-87.132	0.0	106.34
152	SG2E-20131211-0.0	11/Dec/13	Pozos	Ruta de Cenotes	Puerto Morelos	20.978	-87.106	0.0	112.18
153	SG2F-20131211-0.0	11/Dec/13	Pozos	Ruta de Cenotes	Puerto Morelos	20.993	-87.090	0.0	114.69
154	SG3A-20131212-0.0	12/Dec/13	Torres	Ruta de Cenotes	Puerto Morelos	20.873	-86.931	0.0	101.81
155	SG3B-20131212	12/Dec/13	Torres	Ruta de Cenotes	Puerto Morelos	20.884	-86.926	0.0	108.76
156	SG3C-20131212-0.0	12/Dec/13	Torres	Ruta de Cenotes	Puerto Morelos	20.884	-86.926	0.0	106.59
157	SG3D-20131212	12/Dec/13	Torres	Ruta de Cenotes	Puerto Morelos	20.884	-86.926	0.0	105.29
158	SG3E-20131212-0.0	12/Dec/13	Torres	Ruta de Cenotes	Puerto Morelos	20.882	-86.926	0.0	113.64
159	SG4A-20131213-0.0	13/Dec/13	Sacbé	Playa del Carmen	Quintana Roo	20.704	-87.078	0.0	110.49
160	SG4B-20131213-0.0	13/Dec/13	Sacbé	Playa del Carmen	Quintana Roo	20.709	-87.086	0.0	103.77
161	SG4C-20131214-0.0	14/Dec/13	Amaneciendo	Playa del Carmen	Quintana Roo	20.760	-86.970	0.0	105.67
162	SG4D-20131214-0.0	14/Dec/13	Amaneciendo	Playa del Carmen	Quintana Roo	20.760	-86.970	0.0	106.49
163	SG4E-20131214-0.0	14/Dec/13	Amaneciendo	Playa del Carmen	Quintana Roo	20.745	-86.994	0.0	119.79
164	SG4F-20131214-0.0	14/Dec/13	Amaneciendo	Playa del Carmen	Quintana Roo	20.757	-87.019	0.0	114.49
165	SG4G-20131214-0.0	14/Dec/13	Amaneciendo	Playa del Carmen	Quintana Roo	20.760	-87.033	0.0	103.21
166	SG4H-20131214-0.0	14/Dec/13	Amaneciendo	Playa del Carmen	Quintana Roo	20.771	-87.051	0.0	118.13
167	SG4H2-20131214-0.0	14/Dec/13	Amaneciendo	Playa del Carmen	Quintana Roo	20.780	-87.071	0.0	118.04
168	SG4I-20131214-0.0	14/Dec/13	Amaneciendo	Playa del Carmen	Quintana Roo	20.783	-87.078	0.0	102.71
169	SIBA-20111211-11.8	11/Dec/11	Siete Bocas	Puerto Morelos	pit cenote	20.877	-87.044	11.8	106.07
170	SIBB-20111211-10.6	11/Dec/11	Siete Bocas	Puerto Morelos	pit cenote	20.877	-87.044	10.6	106.00
171	SIBC-20111211-4.7	11/Dec/11	Siete Bocas	Puerto Morelos	pit cenote	20.877	-87.044	4.7	105.92
172	SIBD-20111211-7.3	11/Dec/11	Siete Bocas	Puerto Morelos	pit cenote	20.877	-87.044	7.3	105.69
173	SIBE-20111211-18.9	11/Dec/11	Siete Bocas	Puerto Morelos	pit cenote	20.877	-87.044	18.9	105.61
174	SIBF-20111211-21.4	11/Dec/11	Siete Bocas	Puerto Morelos	pit cenote	20.877	-87.044	21.4	103.80
175	SIBG-20111211-24.7	11/Dec/11	Siete Bocas	Puerto Morelos	pit cenote	20.877	-87.044	24.7	105.60
176	SIBH-20111211-16.9	11/Dec/11	Siete Bocas	Puerto Morelos	pit cenote	20.877	-87.044	16.9	117.30
177	SIBI-20111211-0.0	11/Dec/11	S01	Puerto Morelos	Road	20.867	-87.047	0.0	114.80
178	SIBJ-20111211-0.0	11/Dec/11	S02	Puerto Morelos	Road	20.857	-87.002	0.0	108.90
179	TABA-20131208-4.8	08/Dec/13	Tábano	Tulum	Quintana Roo	20.169	-87.456	4.8	103.26
180	TABB-20131208-5.8	08/Dec/13	Tábano	Tulum	Quintana Roo	20.169	-87.456	5.8	101.48
181	TABC-20131208-8.2	08/Dec/13	Tábano	Tulum	Quintana Roo	20.169	-87.456	8.2	102.85
182	TABD-20131208-5.3	08/Dec/13	Tábano	Tulum	Quintana Roo	20.169	-87.456	5.3	103.11
183	ZAP10-20110731-48.5	31/Jul/11	Zapote	Puerto Morelos	Hell Bells	20.854	-87.125	48.5	100.50

## VIII Vita

### EMILIANO MONROY RÍOS

Born and raised in Mexico City. Moved to the Caribbean and became a cave diver.

PhD. Karst Geochemistry and Hydrogeology. Earth & Planetary Sciences Department, Northwestern University. Evanston, IL.

MSc. Marine Sciences and Limnology. Instituto de Ciencias del Mar y Limnología, UNAM, Mexico.  
Dissertation: “Hidrología del embalse de Valle de Bravo, México” [Hydrology of the Valle de Bravo Reservoir, Mexico].

BSc. Chemistry. Faculty of Chemistry, Universidad Nacional Autónoma de México, UNAM.  
Dissertation: “Propiedades electrónicas y estructurales del sistema Fe(n)-NO. Un estudio teórico” [Electronic and structural properties of the system Fe(n)-NO. A theoretical approach].

 @mantarrayo

EVANSTON, IL, USA.

TEPOZTLÁN, MORELOS, MÉXICO.